

# Plasma Diagnostics and Modelling of Nanosecond Pulsed Surface Dielectric Barrier Discharge Actuators

THÈSE N° 6282 (2014)

PRÉSENTÉE LE 29 SEPTEMBRE 2014

À LA FACULTÉ DES SCIENCES ET TECHNIQUES DE L'INGÉNIEUR  
LABORATOIRE DE THERMIQUE APPLIQUÉE ET DE TURBOMACHINES  
PROGRAMME DOCTORAL EN ENERGIE

ÉCOLE POLYTECHNIQUE FÉDÉRALE DE LAUSANNE

POUR L'OBTENTION DU GRADE DE DOCTEUR ÈS SCIENCES

PAR

**Sami GOEKCE**

acceptée sur proposition du jury:

Prof. F. Maréchal, président du jury  
Dr P. Ott, directeur de thèse  
Dr C. Hollenstein, rapporteur  
Prof. C. Laux, rapporteur  
Dr T. Unfer, rapporteur



ÉCOLE POLYTECHNIQUE  
FÉDÉRALE DE LAUSANNE

Suisse  
2014



A Tim et Gabrielle.



# Acknowledgements

J'aimerais remercier les personnes qui m'ont entouré durant ces presque 5 ans de thèse. Tout d'abord mon directeur de thèse, le Dr Peter Ott, qui m'a permis d'entreprendre cette thèse avec une grande liberté et dont la bonne humeur et la gentillesse ont été constantes. Ensuite mon superviseur pour la physique des plasmas, le Dr Christoph Hollenstein, qui m'a aidé à me familiariser avec les outils de diagnostic et la haute tension (en mettant une main dans la poche) et grâce à qui j'ai pu effectuer les expériences décrites dans la thèse. Un merci tout particulier au Dr Pénélope Leyland, avec qui j'ai effectué mon premier projet dans le domaine des plasmas et qui m'a permis d'aller en Australie pour mon projet de Master, ce qui a été une expérience très enrichissante. Son dynamisme et sa volonté de découvrir de nouveaux sujets ont été très motivants tout au long de ma thèse (et même après !).

Je tiens à remercier ensuite les acteurs externes de cette thèse, le Professeur Christophe Laux et le Dr Thomas Unfer qui ont généreusement accepté d'être les experts externes pour ma défense de thèse, ainsi que le Professeur François Maréchal pour avoir accepté de présider mon jury de thèse. Leurs remarques durant la défense de thèse ainsi que les discussions sur la spectroscopie et la modélisation des plasmas durant les workshops ATW m'ont été d'une aide précieuse.

Les expériences réalisées durant cette thèse n'ont été possible que grâce au concours précieux de Steve Couturier, Jérémie Dubray et Damien Fasel au CRPP, qui ont assemblé et amélioré le générateur plasma. Enfin je voudrais remercier mes collègues passés et présents du LTT/GTT et mes presque collègues de l'IAG, du CRPP et des autres labos pour leur aide, les discussions intéressantes (ou non) et leur gentillesse, en particulier: Annick, Stina, Cécile, Elia, Virginie, Margarita (merci pour les nombreux chocolats !), Romain, Ojas, Angelo, Pierre, Sébastien, Oleg, Rik et Gennady pour les travaux au CRPP, Philippe Guittienne, Ralf, David Granges, David Martinet, Alan, Michael, Yanis Andrebe pour son aide avec la calibration du spectromètre, Vincent pour son aide en programmation et pour l'amélioration de mon code, et Marc-Antoine pour l'opportunité de donner l'assistantat dans son cours, qui m'a appris beaucoup de choses.

Les étudiants qui ont participé à mes travaux durant leur travail de semestre ou de master m'ont beaucoup apporté et m'ont permis de prendre du recul : Merci à Marina, Timothy, Luis et en particulier à Fouad, qui a développé la version Fortran du code de simulation. Un mot particulier pour mes collègues doctorants du LTT/GTT avec qui j'ai passé ces 5 ans : to Alex : thanks for the good times and for making me discover PAOK. Je suis reconnaissant à Achim

## Acknowledgements

---

pour les Tandems-pizza et pour le temps consacré à répondre à mes questions. Philip : merci pour tout, en particulier les relectures de la thèse.

Je voudrais ensuite remercier ma belle-famille et mes amis qui m'ont soutenu et qui m'ont écouté parler de mon sujet passionnant : la vitesse des électrons. Je remercie particulièrement Yoann, Carina, Vincent, Eric, Yacine, Nadia et Fabien pour leur amitié. Je suis reconnaissant à mon frère David pour sa présence et sa sagesse durant la thèse et avant: morf.

Je dois la plus grande gratitude à mes parents qui ont soutenu mes choix tout au long de mes longues études et qui m'ont permis d'atteindre mes buts, qui semblaient à certains moments inaccessibles.

Enfin, je remercie Gabrielle qui m'a soutenu tout au long de la thèse et en particulier durant la dernière année, qui a été très riche en émotions. Merci pour ton amour, pour ta patience et pour m'avoir donné un avenir plein de bonheur avec Tim.

*Lausanne, 11 Juillet 2014*

Sami Goekce

# Abstract

During the past years, an increasing number of studies have been conducted on the use of electrical discharges for the stabilization of airflows (plasma flow control). Electrical gas discharges transfer energy and momentum to the gas through collisions of free electrons with atoms and molecules. Chemically active species such as ions, radicals and excited species are produced due to these collisions. The use of plasma actuators, notably surface dielectric barrier discharges (SDBD), for flow control applications has been largely investigated, and it has been demonstrated to effectively control the flow at low flow speed (below 30 m/s). Nowadays, the research in this area focuses on ways to improve the plasma actuators for flow speeds relevant to real flight conditions. One promising device for plasma flow control at high flow speed is the nanosecond pulsed surface dielectric barrier discharge. Nanosecond pulsed plasmas in general have also drawn attention from other fields, such as plasma assisted combustion, due to their ability to produce a large amount of active species and producing substantial overheating in a very short time.

In this thesis an investigation of nanosecond pulsed SDBD is presented, with a focus on flow-control applications, but also on the production of active species, which are of great interest for plasma-assisted combustion and for other fields. The experimental characterization of the plasma created for different conditions, such as the operating pressure, the polarity and the amplitude of the applied voltage, is conducted. Important plasma parameters such as the gas temperature, the excited species produced, the reduced electric field or the electron density are either directly measured or inferred from emission spectroscopy using existing and novel diagnostic methods. The validity of the diagnostic methods is demonstrated using a numerical model of the plasma. The numerical modelling of the plasma also allows determining the influence of the plasma on the flow for several conditions. The experimentally studied conditions are simulated and compared with experimental results to show the strengths and limitations of the numerical model.

**Keywords:** surface dielectric barrier discharge, SDBD, plasma actuator, plasma flow control, plasma assisted combustion, streamer, plasma diagnostics, emission spectroscopy, plasma modelling.





# Zusammenfassung

In den vergangenen Jahren wurde mit zunehmender Intensität die Anwendung von elektrischen Entladungen, sogenannten Plasmen, zur Strömungskontrolle im Bereich der Luftfahrt untersucht. Bei einer Entladung kollidieren freie Elektronen mit Molekülen und übertragen so Energie und Impuls auf das neutrale Gas. Durch die Kollisionen werden chemisch aktive Ionen, Radikale und angeregte Spezies erzeugt.

Bisher wurden insbesondere dielektrischen Barriereentladungen (engl.: surface dielectric barrier discharges, kurz SDBD) für Anwendungen bei niedrigen Strömungsgeschwindigkeiten (bis 30 m/s) untersucht. Obwohl dabei zum Teil grosse Erfolge erzielt wurden zielen viele jüngere Studien darauf ab die Wirksamkeit auf höhere, flugrelevante Geschwindigkeiten auszuweiten. Eine vielversprechender Ansatz dafür sind SDBD Aktoren bei welchen das Plasma durch Hochspannungspulse mit einer Dauer von einigen Nanosekunden erzeugt wird. Neben der Strömungskontrolle wurden auch andere Anwendungen für die gepulsten SDBD untersucht wie z.B. die plasmaunterstützte Verbrennung, da diese Form der Entladung besonders viele aktive Spezies in kurzer Zeit erzeugt.

In dieser Dissertation wird eine Studie zu gepulsten SDBD vorgestellt. Im Mittelpunkt stehen sowohl Anwendungen zur Strömungskontrolle als auch die Erzeugung von aktiven Spezies für die plasmaunterstützte Verbrennung. Der Einfluss von verschiedenen Randbedingungen wie der Umgebungsdruck, die Polarität und die Spannung auf die Eigenschaften des Plasmas werden experimentell untersucht. Dabei werden die wichtigsten Parameter wie die Gastemperatur, die produzierten aktiven Spezies, das reduzierte elektrische Feld und die Elektronen Dichte direkt gemessen oder basierend auf spektroskopischen Messungen mit einer neu entwickelten Methode berechnet. Mittels eines numerischen Modells wird die Gültigkeit dieses Verfahrens überprüft. Darüber hinaus zeigt das Modell den Einfluss des Plasmas auf die Strömung. Ein Vergleich der numerischen und experimentellen Ergebnisse zeigt die Möglichkeiten und Grenzen beider Ansätze.

Stichwörter: dielektrische Barriereentladung, SDBD, Plasma Aktor, Strömungskontrolle, plasmaunterstützte Verbrennung, Plasmadiagnostik, Emmisionsspektroskopie, Plasmamodellierung



# Résumé

Durant les dernières années, un nombre croissant de recherches ont été conduites sur l'utilisation de décharges électriques pour la stabilisation d'écoulement d'air (contrôle d'écoulement par plasma). Les décharges électriques ont la propriété de pouvoir transférer de l'énergie et de la quantité de mouvement au gaz par l'intermédiaire des collisions entre les électrons libres et les atomes ou molécules du gaz. Des espèces chimiquement actives comme les ions, les radicaux ou les espèces excitées sont produites grâce à ces collisions. Les applications concrètes des décharges électriques supposent donc l'utilisation d'espèces chimiquement actives ou la déposition d'énergie et de quantité de mouvement. L'utilisation d'actuateurs plasma pour le contrôle d'écoulement, notamment les décharges à barrière diélectrique de surface (SDBD), a été largement investiguée durant les vingt dernières années, et a prouvé son efficacité notamment pour des écoulements lents (moins de 30 m/s). Actuellement, la recherche dans ce domaine se concentre sur des manières d'améliorer les actuateurs plasma dans le but de leur implémentation pour des conditions réelles de vol. Un type d'actuateur prometteur pour le contrôle d'écoulement par plasma pour de hautes vitesses d'écoulement est la SDBD alimentée par des impulsions de tension de très courte durée (de l'ordre de la dizaine de nanosecondes), appelées impulsions nanosecondes. Les plasmas produits par impulsions nanosecondes en général ont aussi attiré l'attention dans d'autres domaines, comme la combustion assistée par plasma, due à leur capacité de produire de grandes quantités d'espèces actives et de provoquer une grande augmentation de la température du gaz en des temps très courts. L'investigation de SDBD alimentée par des impulsions nanosecondes est présentée dans cette thèse, qui se focalise avant tout sur les applications dans le domaine du contrôle d'écoulement, mais aussi sur la production d'espèces actives, qui sont primordiales pour la combustion assistée par plasma entre autre. La caractérisation du plasma produit par la SDBD pour différentes conditions comme la pression du gaz, la polarité de l'impulsion de tension, et l'amplitude de la tension appliquée a été faite. Des paramètres importants du plasma comme la température du gaz, l'identification des espèces excitées produites, le champ électrique réduit ou encore la densité électronique ont été soit directement mesurés, soit déterminés par des méthodes existantes ou spécialement développées durant la thèse. La modélisation numérique du plasma généré est effectuée en utilisant une approche fluide pour le transport des espèces chargées couplée de façon auto-consistante avec l'équation régissant le champ électrique (l'équation de Poisson). Le plasma produit aux conditions étudiées expérimentalement est simulé numériquement et comparé aux résultats expérimentaux. La validation des méthodes diagnostiques est effectuée sur la base des résultats numériques.

## Acknowledgements

---

**Mots-clés :** décharge à barrière diélectrique, SDBD, actuateur plasma, contrôle d'écoulement par plasma, combustion assistée par plasma, streamer, diagnostic plasma, spectroscopie d'émission, modélisation du plasma.

# Contents

<b>Acknowledgements</b>	<b>v</b>
<b>Abstract (English/Français)</b>	<b>vii</b>
<b>List of figures</b>	<b>xiv</b>
<b>List of tables</b>	<b>xx</b>
<b>Nomenclature</b>	<b>xxiii</b>
<b>1 Introduction</b>	<b>1</b>
1.1 Context and motivation . . . . .	1
1.2 Objectives and structure of the thesis . . . . .	4
<b>2 Plasma Physics</b>	<b>7</b>
2.1 Introduction . . . . .	7
2.2 Gas discharge physics . . . . .	7
2.3 Physical model . . . . .	11
2.3.1 Electromagnetic fields . . . . .	11
2.3.2 Boltzmann equation and conservation equations . . . . .	11
2.3.3 Kinetic processes modeled . . . . .	17
2.3.4 EHD force and heat release . . . . .	22
2.4 Optical diagnostics of the plasma . . . . .	23
2.4.1 Excited species . . . . .	25
2.4.2 Reduced electric field and active species determination . . . . .	29
2.5 Optical emission spectroscopy . . . . .	32
2.5.1 Introduction . . . . .	32
2.5.2 Spectra of Diatomic Molecules: Basic Concepts . . . . .	33
2.5.3 Spectra of Diatomic Molecules: Finer Details . . . . .	37
2.6 Conclusions . . . . .	44
<b>3 Experimental Characterization of the Plasma</b>	<b>47</b>
3.1 Introduction . . . . .	47
3.1.1 Literature review . . . . .	47
3.2 Experimental setups . . . . .	49

## Contents

---

3.3	Experimental results . . . . .	54
3.3.1	Global characteristics of the SDBD . . . . .	54
3.3.2	Effect of the voltage on streamer propagation . . . . .	61
3.3.3	Temporal and spatial evolution of positive streamers . . . . .	65
3.3.4	Effect of the plasma on the gas temperature . . . . .	73
3.3.5	Effect of the polarity on streamer propagation . . . . .	76
3.3.6	Effect of pressure on streamer propagation . . . . .	80
3.3.7	Comparison with sinusoidal applied voltage . . . . .	92
3.4	Conclusions . . . . .	93
<b>4</b>	<b>Numerical Model of the Plasma</b>	<b>97</b>
4.1	Introduction . . . . .	97
4.1.1	Literature review for plasma modelling . . . . .	98
4.2	Numerical Model . . . . .	100
4.2.1	Numerical Discretization . . . . .	100
4.2.2	Numerical Schemes . . . . .	104
4.2.3	Non-uniform Grid . . . . .	107
4.2.4	Solver . . . . .	107
4.2.5	Validation of the Numerical schemes . . . . .	108
4.3	Numerical Results . . . . .	112
4.3.1	Positive Pulse . . . . .	112
4.3.2	Influence of the Polarity . . . . .	112
4.3.3	Influence of the Applied Voltage . . . . .	113
4.3.4	Influence of the Pressure . . . . .	116
4.3.5	EHD Force and Heat Released by the Actuator . . . . .	123
4.4	Comparison with the Experiments . . . . .	126
4.5	Conclusions . . . . .	140
<b>5</b>	<b>Final Conclusions</b>	<b>143</b>
<b>A</b>	<b>Appendix</b>	<b>147</b>
	<b>Bibliography</b>	<b>157</b>
	<b>Curriculum Vitae</b>	<b>159</b>

# List of Figures

2.1	Mean free path (a) and electron-neutral collision frequency (b) in $N_2$ as a function of the electron energy normalized to 1 bar. The mean energy gained by an electron during one collision is shown for $N_2$ , for 100 Td (e) and 1000 Td (f) The scattering cross section is that of [Tabata et al., 2006]. . . . .	16
2.2	Comparison of $\alpha$ in air with different models. Bolsig+ with modified cross sections and electron-electron collisions ( $10^{-5}$ ionization) (blue solid line) Bolsig+ with electron-electron collisions ( $10^{-4}$ ionization) (black solid line), Bolsig+, without electron-electron collisions (red solid line) . . . . .	18
2.3	Comparison of $\alpha$ in air with different models. Bolsig+ with modified cross sections (blue solid line), Raizer's model (red solid line), Morrow's model (green dashed line) and $\alpha$ derived from Kossyi's model (black solid line) . . . . .	19
2.4	Comparison of $\alpha$ and $\eta$ in air with different models. Bolsig+ with modified cross sections (blue solid line), Raizer's model (black solid line), Morrow's model (green dashed line) and $\alpha$ derived from Kossyi's model (red dashed-dotted line) . . . . .	20
2.5	Comparison of $\mu p$ in air with different models. Bolsig+ with modified cross sections (blue solid line), mobility inferred from Grigoriev's drifts velocities (red dashed-dotted line), Morrow's model (green dashed line). . . . .	21
2.6	Excitation cross sections by electron-impact for the production of excited species listed in table 2.2. . . . .	28
2.7	Ratio of vibrational populations $N_2(C^3\Pi_u, \nu = 0 - 4)$ normalized to $N_2(C^3\Pi_u, \nu = 0)$ corresponding to the red, blue and black solid lines and to the green and orange dash-dotted lines respectively. Computation performed for a constant reduced electric field of 700 Td. Vibrational relaxation taken into account (a) and vibrational relaxation not taken into account (b). . . . .	30
2.8	Fit (red solid line) of a typical experimental spectrum (blue solid line) using Specair (units are in $mWcm^{-2}sr^{-1}$ )(a) and the in-house code (b). . . . .	43
2.9	Fit (red solid line) of a typical experimental spectrum (blue solid line) using Specair (a) and the in-house code (b). . . . .	44
3.1	Sketch of the SDBD. . . . .	50
3.2	Sketch of the push-pull switch in positive pulse mode. . . . .	51
3.3	Typical current (left) and voltage (right) between the electrodes of the SDBD. . . . .	51
3.4	Sketch of the optical setup. . . . .	53

## List of Figures

---

3.5	Computed current difference between plasma on and plasma off(insulated). Filtered data (see text) for: 2 kV (a) and 7 kV (b). . . . .	55
3.6	Difference between energy input and output to the SDBD. With plasma (red solid line) and without plasma (blue solid line). . . . .	56
3.7	Fast camera images of the streamer propagation. The applied voltage is 7kV and pressure is 1 atm, the gate exposure is 5 ns and the image is an average over 5000 cycles. The time at which images are taken corresponds to the trigger time $t_{ref}$ (a) plus 5 and 10 ns respectively for (b,c) for the ascending phase. The images for the decaying phase (right) are delayed by 160 ns with respect to the ascending phase. The edge of the upper electrode is located at 5.2 mm. . . . .	57
3.8	Low resolution spectrum acquired with the 150 g/mm grating of the spectrometer (150 mm focal length). . . . .	58
3.9	Medium resolution spectrum acquired with the 1200 g/mm grating of the spectrometer (150 mm focal length). . . . .	59
3.10	Low resolution spectrum acquired with the 600 g/mm grating of the spectrometer (750 mm focal length). . . . .	59
3.11	Energy input in the plasma in function of the applied voltage. The value of the series resistor is: 33 $\Omega$ (red solid line), 68 $\Omega$ (blue solid line) and 150 $\Omega$ (black solid line). . . . .	61
3.13	Effect of the applied voltage on the population of excited species during the ascending phase (a) and decaying phase (b). The excited species correspond to : $N_2(C^3\Pi_u, v' = 0, 1, 2, 3)$ and $N_2^+(B^2\Sigma_u^+, v' = 0)$ . Optical fibers placed parallel to the electrodes (see text). . . . .	62
3.12	Effect of the applied voltage on the spectrum. Recorded spectra (blue solid line) and computed spectra (red solid line). . . . .	63
3.14	Effect of the applied voltage on the spatial distribution of excited species. The red, blue and black solid lines and the green, orange, light blue and bronze dash-dotted lines correspond to voltages from 10 kV to 2 kV respectively. The excited species correspond to : $N_2(C^3\Pi_u, v' = 1)$ (a), $N_2^+(B^2\Sigma_u^+, v' = 0)$ (b), $N_2(B^3\Pi_u, v' = 2)$ (c) and $O(^5P)$ (d). . . . .	64
3.15	Temporal evolution of the excited species populations, for the ascending phase (left) and the decaying phase (right) for a 7 kV pulse at 1 bar. The excited species are inferred from emission spectroscopy in the 400 nm spectral zone (a) and in the 760 nm spectral zone (b). . . . .	66
3.16	Temporal evolution of the ratio of vibrational levels $N_2(C^3\Pi_u, v)/N_2(C^3\Pi_u, v = 0)$ for the ascending phase (a) and the decaying phase (b) compared to the theoretical distribution (c) for a 7 kV pulse at 0.25 bar. The curves corresponding to the vibrational levels $v = 0, 1, 2, 3, 4$ are the red, blue and black solid lines, green and orange dash-dotted lines respectively. . . . .	68
3.17	Spatial profile of the excited species populations, for the ascending phase (a) and the decaying phase (b). The applied voltage is 7 kV and the pressure is 1 bar. . . . .	69



3.18 Measurement (blue solid line) and fit (red solid line) of the spectrum recorded at 2 mm from the upper electrode during the decaying phase. The conditions are 7 kV applied voltage and atmospheric pressure. . . . .	70
3.19 Spatial profile of the averaged electric field and normalized electron density for the axial direction, for the ascending phase (a) and the decaying phase (b). The applied voltage and corresponding pressure are: 7 kV, 1 bar. . . . .	71
3.20 Spatial profile of the averaged electron density, the averaged electron density obtained from the exponential fit and the population density of metastable states in the direction of propagation of the streamer, for the ascending phase (a) and the decaying phase (b). The applied voltage and corresponding pressure are: 7kV, 1 bar. . . . .	72
3.21 Fit of (0-0) band of the FNS using Specair (a) and the in-house code (b) for the ascending phase. The different curves in (a) are for rotational temperature 300 K (red solid line), 350 K (blue solid line) and 400 K (green solid line). The rotational temperature for (b) is 350 K. . . . .	74
3.22 Fit of the (2-5) band of the FPS using Specair (a) and the in-house code (b) for the decaying phase (after 1 $\mu$ s). The different curves in (a) are for rotational temperature 300 K (red solid line), 400 K (blue solid line) and 500 K (green solid line). The rotational temperature for (b) is 400 K. . . . .	75
3.23 Emission spectra recorded during the ascending phase at different times with respect to the reference time $t_{ref}$ . $t = t_{ref} + 2.5$ ns (a), $t = t_{ref} + 5$ ns (b) and $t = t_{ref} + 10$ ns (c). The fit of the spectra is performed with a rotational temperature of 300 K and FWHM of 0.3 nm. The light is recorded during 2 ns. . . . .	76
3.24 Spatial profile of the excited species populations for a negative nanosecond pulsed applied voltage, for the ascending phase (a) and the decaying phase (b). The applied voltage and corresponding pressure are: -7 kV, 1 bar. Comparison with the positive pulse is shown in (c) and (d). . . . .	77
3.25 Spatial profile of the averaged electric field and normalized electron density for the axial direction, for the ascending phase (a) and the decaying phase (b). The applied voltage and corresponding pressure are: -7 kV, 1 bar. Comparison with the positive pulse is shown in (c) and (d). . . . .	78
3.26 Spatial profile of the averaged electron density, the averaged electron density obtained from the exponential fit and the population density of metastable states in the direction of propagation of the streamer, for the ascending phase (a) and the decaying phase (b). The applied voltage and corresponding pressure are: -7kV, 1 bar. . . . .	79
3.27 Fast camera images of the streamer propagation. The applied voltage is 3.5 kV, the pressure is 0.5 bar and the gate exposure is 5 ns. The time at which images are taken correspond to the trigger time $t_{ref}$ (a) plus 5 and 10 ns respectively for (b,c) for the ascending phase. The images for the decaying phase (right) are delayed by 165 ns with respect to the ascending phase. The edge of the upper electrode is located at 5.2 mm. . . . .	81

## List of Figures

---

3.28	Fast camera images of the streamer propagation. The applied voltage is 7 kV, the pressure is 0.5 bar and the gate exposure is 5 ns. The time at which images are taken correspond to the trigger time $t_{\text{ref}}$ (a) plus 5 and 10 ns respectively for (b,c) for the ascending phase. The images for the decaying phase (right) are delayed by 165 ns with respect to the ascending phase. The edge of the upper electrode is located at 5.2 mm. . . . .	82
3.29	Fast camera images of the streamer propagation. The applied voltage is 3.5 kV, the pressure is 0.25 bar and the gate exposure is 5 ns. The time at which images are taken correspond to the trigger time $t_{\text{ref}}$ (a) plus 5 and 10 ns respectively for (b,c) for the ascending phase. The images for the decaying phase (right) are delayed by 155 ns with respect to the ascending phase. The edge of the upper electrode is located at 5.2 mm. . . . .	83
3.30	Temporal evolution of the excited species populations, for the ascending phase (left) and the decaying phase (right) for a 3.5 kV pulse at 0.25 bar. The excited species are inferred from emission spectroscopy in the 400 nm spectral zone (a) and in the 760 nm spectral zone (b). . . . .	85
3.31	Temporal evolution of the ratio of vibrational levels $N_2(C^3\Pi_u, \nu)/N_2(C^3\Pi_u, \nu = 0)$ for the ascending phase (a) and the decaying phase (b) compared to the theoretical distribution (c) for a 3.5 kV pulse at 0.25 bar. The curves corresponding to the vibrational levels $\nu = 0, 1, 2, 3, 4$ are the red, blue and black solid lines, green and orange dash-dotted lines respectively. . . . .	86
3.32	Spatial profile of the excited species populations, for the ascending phase (left) and the decaying phase (right). The applied voltage and corresponding pressure are: 1 bar, 7 kV (a), 0.5 bar, 3.5 kV (b) and 0.5 bar, 7 kV (c). . . . .	87
3.33	Spatial profile of the excited species populations, for the ascending phase (left) and the decaying phase (right). The applied voltage and corresponding pressure are: 0.3 bar, 4.2 kV (a), 0.25 bar, 3.5 kV (b) and 0.2 bar, 2.8 kV (c). . . . .	88
3.34	Spatial profile of the averaged electric field and normalized electron density in the direction of propagation of the streamer, for the ascending phase (left) and the decaying phase (right). The applied voltage and corresponding pressure are: 7kV, 1 bar (a) and 3.5 kV, 0.5 bar (b). . . . .	90
3.35	Spatial profile of the averaged electric field and normalized electron density in the direction of propagation of the streamer, for the ascending phase (left) and the decaying phase (right). The applied voltage and corresponding pressure are: 7kV, 0.5 bar (a), 3.5 kV, 0.25 bar (b), 2.8 kV, 0.2 bar (c). . . . .	91
3.36	Spatial profile of the excited species populations, for one cycle. The applied voltage and corresponding pressure are: 1 bar, 10 kV p-p and 2.5 kHz (a), 0.25 bar, 2.5 kV p-p and 10 kHz (b). . . . .	93
3.37	Spatial profile of the averaged electric field and normalized electron density, in the direction of propagation of the streamer, for one cycle. The applied voltages and corresponding pressures are: 1 bar, 10 kV p-p and 2.5 kHz (a), 0.25 bar, 2.5 kV p-p and 10 kHz (b). . . . .	93

---

4.1 Computational cell with dielectric-gas interface located at the node. . . . .	101
4.2 Computational cell with dielectric-gas interface located at the cell's boundary. . . . .	101
4.3 Computational cell with dielectric-gas interface located at the node. . . . .	102
4.4 Representation of the computational cells implemented in the numerical model	105
4.5 Typical non-uniform grid used for the computations. . . . .	108
4.6 Computational domain used for the validation calculations. . . . .	109
4.7 Density contours of the electron density computed at $t=5, 15, 45$ and $60$ ns. Uniform grid $200 \times 100$ (a) and non-uniform grid $200 \times 45$ (b). . . . .	110
4.8 Conduction current computed for the uniform grid. . . . .	111
4.9 Voltage applied to the upper electrode in function of time. . . . .	112
4.10 Contour plot of the electron density (a) and the potential (b) at time $t=13$ ns (ascending phase). Enlarged view of the electron density (c) and of the reduced electric field (d). The conditions for the computation are: $7$ kV applied voltage at $1$ bar. . . . .	113
4.11 Contour plot of the electron density and reduced electric field for different times during the ascending (a) and decaying (b) phases. The conditions for the computation are: $7$ kV applied voltage at $1$ bar. . . . .	114
4.12 Contour plot of the electron density and reduced electric field for different times during the ascending (a) and decaying (b) phases. The conditions for the computation are: $-7$ kV applied voltage at $1$ bar. . . . .	115
4.13 Influence of the voltage slope on the reduced electric field (left) and on the electron density (right). . . . .	117
4.14 Maximum reduced electric field and total number of electrons as a function of the voltage slope (a). Maximum power density in the streamer (b). . . . .	118
4.15 Maximum streamer velocity (a) and starting times of the streamer (b) as a func- tion of the voltage slope. . . . .	118
4.16 Conduction current collected at the anode for applied voltages: $4, 7, 10$ and $14$ kV.	119
4.17 Contour plot of the electron density and reduced electric field for different ap- plied voltages during the ascending (a) and decaying (b) phases. The conditions for the computation are: $4, 7, 10$ and $14$ kV applied voltages at $1$ bar. . . . .	120
4.18 Contour plot of the electron density for different pressures and voltages. Left figures correspond to the ascending phase, $20$ ns after the pulse and right figures to the decaying phase, $240$ ns after the pulse. The pressures and applied voltages are: $0.5$ bar, $7$ kV, $0.3$ bar, $4.2$ kV and $0.2$ bar, $2.8$ kV. . . . .	121
4.19 Contour plot of the electron density and reduced electric field for different voltages and pressures during the ascending (a) and decaying (b) phases. . . . .	122
4.20 Temporal evolution of the time and space integrated parallel EHD force (a) and energy density (b) in function of the applied voltage. . . . .	125
4.21 Temporal evolution of the time and space integrated parallel EHD force (a) and energy density (b) for different voltages and pressures. . . . .	125
4.22 Temporal evolution of the time and space integrated parallel EHD force (a) and energy density (b) for positive and negative voltages. . . . .	126

## List of Figures

---

4.23	Response of the optical system to a point source in the 385-415 nm wavelength range. . . . .	127
4.24	Temporal evolution of the excited species as would be recorded with a gate width of 2 ns. Ascending phase (a) and decaying phase (b). . . . .	128
4.25	Temporal evolution of the excited species populations, for the ascending phase (left) and the decaying phase (right) for a 7 kV pulse at 1 bar. The excited species are inferred from emission spectroscopy in the 400 nm spectral zone (a) and in the 760 nm spectral zone (b). . . . .	129
4.26	Contour plot of the density of $N_2(C^3\Pi_u, \nu = 0)$ (a) and $N_2^+(B^2\Sigma_+, \nu = 0)$ (b). . . .	130
4.27	Comparison of the spatial profiles of the excited species computed with the numerical model (left) and measured during the experiments (right). Ascending phase (a) and decaying phase (b). . . . .	131
4.28	Comparison of the spatial profile of the reduced electric field computed with the numerical code (left) and measured during the experiments (right). Ascending phase (a) and decaying phase (b). . . . .	132
4.29	Spatial evolution of the average electron density and average metastable states $N_2(A^3\Sigma_u^+)$ and $O_2(a^1\Delta_g)$ . The comparison is made between population densities estimated and directly computed. Ascending phase (a) and decaying phase (b). . . . .	133
4.30	One dimensional profile of the electron density and reduced electric field along the streamer. . . . .	133
4.31	Spatial evolution of the average electron density and average metastable states $N_2(A^3\Sigma_u^+)$ and $O_2(a^1\Delta_g)$ for the ascending phase. Comparison between population densities estimated with the exponential fit and directly computed (a). Comparison between population densities estimated with equation 2.24 and directly computed (b). . . . .	135
4.32	Comparison of the spatial profiles of the excited species populations, for the ascending phase. Numerical model (left) and the experiments (right). The applied voltages and corresponding pressures are: 1 bar, 7 kV (a), 0.5 bar, 3.5 kV (b) and 0.5 bar, 7 kV (c). . . . .	136
4.33	Comparison of the spatial profiles of the excited species populations, for the ascending phase. Numerical model (left) and the experiments (right). The applied voltages and corresponding pressures are: 0.25 bar, 3.5 kV (a) and 0.2 bar, 2.8 kV (b). . . . .	137
4.34	Comparison of the spatial profiles of the excited species populations, for the decaying phase. Numerical model (left) and the experiments (right). The applied voltages and corresponding pressures are: 1 bar, 7 kV (a), 0.5 bar, 3.5 kV (b) and 0.5 bar, 7 kV (c). . . . .	138
4.35	Comparison of the spatial profiles of the excited species populations, for the decaying phase. Numerical model (left) and the experiments (right). The applied voltages and corresponding pressures are: 0.25 bar, 3.5 kV (a) and 0.2 bar, 2.8 kV (b). . . . .	139

# List of Tables

2.1	Important fast processes occurring in cold air plasmas at atmospheric pressure.	18
2.2	Electron-impact excitations and references for the corresponding excitation cross sections and quenching rates . . . . .	27
2.3	Rotational matrix elements . . . . .	42
2.4	Comparison of population densities in $\text{cm}^{-3}$ as computed with Specair and the in-house code. . . . .	44
4.1	Amplification coefficient $\int \alpha_{\text{eff}} dr$ for the SDBD configuration at atmospheric pressure . . . . .	119
4.2	Breakdown pressure for the SDBD configuration for different values of $U_0/p$ . .	123
A.1	Fitting coefficients for $\text{N}_2$ computed with Bolsig+ . . . . .	147
A.2	Fitting coefficients for Air computed with Bolsig+ . . . . .	148



# Nomenclature

## Abbreviations

Symbol	Description	Dimensions	Units
E/N	Reduced electric field		Td
EEDF	Electron energy distribution function		$\text{eV}^{-3/2}$
EHD	Electrohydrodynamic (force)		$\text{N} \cdot \text{cm}^{-3}$
FNS	First negative system of $\text{N}_2^+$		
FPS	First positive system of $\text{N}_2$		
FWHM	Full width at half maximum		
HWHM	Half width at half maximum		
LFA	Local field approximation		
LTE	Local thermodynamic equilibrium		
OES	Optical emission spectroscopy		
SDBD	Surface dielectric barrier discharge		
SPS	Second positive system of $\text{N}_2$		

## Constants

Symbol	Description	Dimensions	Units
$\epsilon_0$	Permittivity of vacuum	$8.854187 \cdot 10^{-12}$	$\text{C}^2 \cdot \text{J}^{-1} \cdot \text{m}^{-1}$
$\mu_0$	Permeability of vacuum	$4\pi \cdot 10^{-7}$	$\text{H} \cdot \text{m}^{-1}$
$e$	Elementary charge	$1.602176 \cdot 10^{-19}$	C
$k_B$	Boltzmann constant	$1.380648 \cdot 10^{-23}$	$\text{J} \cdot \text{K}^{-1}$
$m_e$	Mass of the electron at rest	$9.109382 \cdot 10^{-31}$	kg

## Nomenclature

---

$c$	Speed of light	$2.997924 \cdot 10^8$	$\text{m} \cdot \text{s}^{-1}$
$h$	Planck's constant	$6.626068 \cdot 10^{-34}$	$\text{J} \cdot \text{s}$

### Physical quantity

Symbol	Description	Dimensions	Units
$\alpha$	Ionization coefficient		$\text{cm}^{-1}$
$\beta_{ei}$	Electron-ion recombination coefficient		$\text{cm}^3 \cdot \text{s}^{-1}$
$\beta_{ii}$	Ion-ion recombination coefficient		$\text{cm}^3 \cdot \text{s}^{-1}$
$\eta$	Attachment coefficient		$\text{cm}^{-1}$
$\gamma$	Secondary emission coefficient		-
$\Gamma_e$	Electron flux		$\text{cm}^2 \cdot \text{s}^{-1}$
$\Gamma_n$	Negative ion flux		$\text{cm}^2 \cdot \text{s}^{-1}$
$\Gamma_p$	Positive ion flux		$\text{cm}^2 \cdot \text{s}^{-1}$
$\lambda_{\text{mfp}}$	mean free path		$\text{cm}$
$\mu_e$	Mobility of electrons		$\text{cm}^2 \cdot \text{V}^{-1} \cdot \text{s}^{-1}$
$\mu_n$	Mobility of negative ions		$\text{cm}^2 \cdot \text{V}^{-1} \cdot \text{s}^{-1}$
$\mu_p$	Mobility of positive ions		$\text{cm}^2 \cdot \text{V}^{-1} \cdot \text{s}^{-1}$
$\nu$	Frequency of light		$\text{s}^{-1}$
$\sigma_i^{es}$	Scattering cross section		$\text{cm}^2$
$\sigma_i^e$	Excitation cross section		$\text{cm}^2$
$\tau_{ne}$	Electron-neutral collision frequency		$\text{s}^{-1}$
$\tau_{nn}$	Neutral-neutral collision frequency		$\text{s}^{-1}$
$B$	Magnetic field		$\text{A} \cdot \text{cm}^{-1}$
$D_e$	Diffusion coefficient of the electrons		$\text{cm}^2 \cdot \text{s}^{-1}$
$D_n$	Diffusion coefficient of the negative ions		$\text{cm}^2 \cdot \text{s}^{-1}$
$D_p$	Diffusion coefficient of the positive ions		$\text{cm}^2 \cdot \text{s}^{-1}$
$E$	Electric field		$\text{V} \cdot \text{cm}^{-1}$
$E_{ph}$	Energy of a photon		$\text{J}$



$E_{th}$	Breakdown electric field	$V \cdot cm^{-1}$
$f$	Electro-hydrodynamic force	$N \cdot cm^{-3}$
$j$	Current density	$A \cdot cm^{-2}$
$N$	Gas number density	$cm^{-3}$
$n_e$	Electron density	$cm^{-3}$
$n_n$	Negative ion density	$cm^{-3}$
$n_p$	Positive ion density	$cm^{-3}$
$n_i$	Density of species $i$	$cm^{-3}$
$p$	Gas pressure (static pressure)	bar, Torr
$q_{A,v' \rightarrow B,v''}$	Franck-Condon factor	-
$V$	Potential	V
$v_e$	Electron drift velocity	$cm \cdot s^{-1}$
$v_n$	Negative ion drift velocity	$cm \cdot s^{-1}$
$v_p$	Positive ion drift velocity	$cm \cdot s^{-1}$
$V_{th}$	Breakdown voltage	V
$v_{th,j}$	Thermal velocity of species $j$	$cm \cdot s^{-1}$
$W$	Heat source density	$W \cdot cm^{-3}$

**Units**

<b>Symbol</b>	<b>Description</b>	<b>Dimensions</b>	<b>Units</b>
eV	Electron volt	$1.602217 \cdot 10^{-19}$	J
Td	Townsend	$10^{-17}$	$V \cdot cm^2$



# 1 Introduction

## 1.1 Context and motivation

Aircraft and turbomachines are machines relying on the transfer of momentum from the airflow to the airfoil or from the airfoil to the air. The momentum is efficiently transferred to or from the flow if the flow is said to be *attached* to the surface. If the flow undergoes a perturbation, it can detach from the surface and lead to a loss of efficiency and in the worst case, to a stalled flow. The stalled flow leads to a sudden loss of lift in an airplane. These situations are generally avoided by designing the airplane to fly at a certain speed and with a certain angle with respect to the wind, in such a manner that small variations in the external flow do not lead to stalled flow. If, however, the flow can be controlled, the airplane can be both safer and more efficient.

In order to act on the airflow, several flow control techniques exist, among which a novel technique emerged since the mid 90's, which gained broad interest from the scientific community, plasma flow control. The flow-control device is called a *plasma actuator*. The plasma is a general term used to describe a certain type of ionized gas. In this thesis the precise meaning implied by the word plasma is not retained, and is to be understood as a general denomination for a partially ionized gas. The plasma is produced by applying a large potential difference between two electrodes. The ionized gas formed can transfer momentum and energy to the neutral gas in which it is taking place. It is this transfer that is used in plasma flow-control applications.

Different configurations of plasma actuators can be found, but they all have some basic properties in common, which make them desirable from the aerodynamic point of view. They are relatively simple to manufacture, simple to operate and generally light weight. The most important features are the absence of moving parts which could be a source of failure, and their ability to be operated at very high frequency (>100 kHz) and fast response times, which makes them suitable for real time flow control.

The different types of plasma actuators and their applications were reviewed in [Moreau, 2007].

## Chapter 1. Introduction

---

The basic principle used in the beginning of plasma flow-control was exclusively based on the momentum transfer due to the acceleration of charges in the applied electric field. This effect is called the *ionic wind*.

The most common actuators are the corona discharge actuator and the surface dielectric barrier discharge (SDBD) actuator. In both actuators, the ionic wind is generated, reaching maximum values of induced-flow velocity of approximately 8 m/s. This value might seem small, but is sufficient in some applications to modify the flow beneficially. A well known example of such an application is the reattachment of stalled flow over an airfoil, as first studied by Roth et al. [Roth et al., 1998] in 1998. The experiments conducted on actuators were usually investigated by measurement techniques typical for fluid mechanics (pitot tubes, PIV), complemented by integral measurement techniques such as thrust measurements and current-voltage measurements. While these measurement are well suited to determine the effectiveness of the actuator, the parameters to be varied in order to achieve the optimization of the actuator are too numerous. The parameters important for flow-control applications are for example: the geometry and material of the electrodes, the thickness and material of the dielectric (for SDBD), the shape of the applied voltage, the frequency of the applied voltage and so on. To diminish the number of degrees of freedom, the understanding of the physical processes occurring in the plasma and its coupling to the flow field are necessary. Corke et al. [Orlov et al., 2006] addressed the problem in a different manner. They used an electrical circuit to model the plasma. This approach was successful to derive basic parameters of the plasma such as its extent, the power converted to mechanical work, etc. This allowed to reduce the complexity associated with the operation of the SDBD. However, this type of approach gives little information on the physics of the actuators. While the basic principle of charge acceleration by an electric field and momentum transfer to a neutral molecule of the gas is easy to understand, it does not encompass the physics of the plasma actuators. Indeed, the ions are not provided by some external generator but produced in the plasma. The understanding of the mechanisms underlying the formation of the plasma is therefore important. The formation of the plasma and the amount of momentum transferred to the gas were studied numerically and experimentally by Boeuf et al, for the case of an AC driven SDBD. [Boeuf and Pitchford, 2005, Lagmich et al., 2007]. In these references, the modelling of the plasma is performed by a fluid approximation of the charged species, which are coupled to Poisson's equation self-consistently. The numerical model happened to describe accurately experimental data on the plasma actuators, notably the current-voltage characteristics. The magnitude of the ionic wind determined was also in accordance with the experiments.

Since the successful demonstration of the ability of the plasma actuators to control a low speed flow, developments were conducted aiming at increasing the induced flow velocity, in order to increase the range of applicability of the plasma actuators, notably at higher flow velocities. The implementation of plasma actuators in high speed airflows was investigated by several authors, among which [Grundmann and Tropea, 2007] can be cited. The approach followed by these authors demonstrated the use of a SDBD plasma actuator integrated in a feedback control loop in order to suppress Tollmien-Schlichting waves, which are an in-

stability developing in the laminar flow which leads to the transition to turbulence and to separation. When considering the implementation of the plasma actuators for real airplanes (or turbomachines), the influence of real flight conditions on the performances of plasma actuators have to be investigated. The investigation of the pressure level and the humidity has been conducted in [Benard et al., 2008]. Their findings indicate that the plasma actuator can be operated in humid air without problems, and that the pressure has a major effect on the ionic wind produced. They found that a maximum ionic wind was produced for a pressure of 0.6 atm. The reason for this maximum was however not explained.

A recent approach to address the problem of high speed flow control by plasma actuators was the use of a very short high voltage pulse applied to a SDBD to produce the plasma [Roupassov et al., 2009]. These so-called *nanosecond pulsed* plasma actuators are the topic of this thesis. The nanosecond pulsed SDBD used in [Roupassov et al., 2009] allowed to delay the leading edge separation occurring over an airfoil at  $M=0.74$ . In the case of the nanosecond pulsed SDBD, the physical principle for flow actuation is the fast relaxation of thermal energy released in the gas by the plasma, leading to a pressure wave. This pressure wave can interact with the flow in a beneficial way for certain conditions. Before the work of Roupassov, the possibility to use nanosecond pulsed SDBD actuators was investigated experimentally by Opaits [Opaits et al., 2008a]. The numerical modelling of this actuator was conducted by Likhanskii [Likhanskii et al., 2007] in parallel to experimental investigations. These authors proposed to enhance the ionic wind produced by the nanosecond pulsed SDBD by applying a voltage bias in addition to the voltage pulse, which has the effect of accelerating the charges produced during the pulse, as for normal AC driven SDBD. The idea behind the use of nanosecond pulses for ionic wind generation is that the streamers can be controlled and operated more often than naturally occurring in an AC driven SDBD. Thus the high density of charged species produced can be efficiently accelerated by a DC bias. The experiments were conducted with nanosecond pulses of 4 ns FWHM duration and up to 10 kV amplitude of the applied voltage. The nanosecond pulse generator was capable of delivering pulses at frequencies up to 100 kHz. The resulting ionic wind was found to be reduced by the charge build-up of the dielectric by the successive pulses. In order to overcome this problem, a square or sinusoidal low frequency bias was superimposed on the nanosecond pulses, which effectively removed the charges on the surface periodically. The overall flow-control capability of this actuator was found to be increased compared to the sinusoidal driven SDBD.

For the optimization of the nanosecond pulsed actuators operating as a pressure wave generator, the understanding of the fast heat release mechanism is necessary. This problem has been addressed experimentally in [Starikovskii et al., 2009] and numerically in [Unfer and Boeuf, 2009]. Both experiments and numerical simulations showed that the nanosecond pulsed SDBD was efficient for heat release but not for the generation of ionic wind, due to the short time during which the charges are exposed to the electric field. The numerical modelling seems therefore to be a tool well suited for the understanding of the plasma. The main problem with numerical modelling is their validation with experimental data. As long as global features are examined, good agreement is generally observed. But more advanced features

such as the precise chemical reactions occurring in the plasma are more challenging. These questions were addressed in [Aleksandrov and Bazelyan, 1996, Pancheshnyi et al., 2000, Popov, 2001] for example. The further investigation of plasma components and characteristics makes the link between the plasmas used for flow-control applications and the general investigation of cold plasmas.

### 1.2 Objectives and structure of the thesis

The main objective of this thesis is the understanding of the basic processes taking place in the plasma in view of its use as actuator for flow-control on real aircrafts, flying in air at different altitudes.

The investigation of the plasma is restricted to plasma produced by a nanosecond pulsed SDBD. This configuration was chosen at the beginning of this PhD thesis on the basis of the results of a previous PhD thesis conducted on the topic of plasma flow-control at EPFL [Pavón et al., ]. The use of nanosecond pulsed SDBD was believed to be beneficial in the context of transonic flows, influencing notably the shock-boundary layer interaction, thus allowing the reduction of detrimental oscillations produced at transonic velocities encountered over airfoils. In determining the objectives of this thesis, the detailed understanding of the physics of the plasma was lacking, directing the research onto simplified actuators from the standpoint of physical processes. Such an approach has been successfully applied in [Lagmich, 2007] by using nitrogen and air at lower pressures, allowing simpler diagnostics and interpretations. Here the approach was different, based on the simplification of the processes with respect to time. Indeed, gas and surface processes in air at high pressure can be overwhelmingly difficult to model due to the large number of reactions occurring in cold air plasmas [Kossyi et al., 1992]. The use of short pulses allows to restrict the study of the kinetic processes occurring to retain only the fastest reactions, which are easier to model.

The choice of the type of voltage pulse was motivated by the following considerations: The advantages of having a very high power input to the gas are evident: the possible effects on the flow will be stronger and therefore easier to characterize. Drawbacks are also associated with the use of very powerful generators. The main drawbacks are the necessity of a more complex system to provide the high voltage and power, which is considerably more expensive. Larger electromagnetic interferences will also be generated, which is a very important aspect for aerodynamics applications. The larger generation of pollutant, such as NO, is also probable. In this thesis and the parallel thesis conducted by Ph. Peschke in the context of the project PLASMAERO, the same pulse generator was used. The goal was to come closer to real needs of aerodynamics applications with light, affordable and energy efficient plasma actuators.

While the focus of the thesis is set on flow-control, other aspects of the SDBD are important in the context of aeronautics. One of the most important aspects is plasma-assisted combustion, which uses the ability of the SDBD to produce chemically reactive species, such as radicals (mainly oxygen), metastable excited species, ozone and more (see [Starikovskiy and

Aleksandrov, 2013]). Another application of the plasma's ability to produce active species lies in medicine, for the treatment of skin disease [Babaeva and Kushner, 2013] and for the killing of pathogenic agents. The other main application of the DBD is the production of ozone for decontamination purposes, which could also benefit from the use of a nanosecond pulsed plasma actuator.

The path that this thesis follows consists in the characterization of the plasma at different operating conditions, in order to deduce their influence on the flow actuation capabilities of the plasma. Indeed, the flow control capabilities of the actuator depend certainly on the electric field applied, the number of charged species and the energy released in the gas.

The plasma is characterized by its composition, its thermodynamic state and its dimensions. In order to determine these characteristics, the two most important quantities driving all electron-impact processes, i.e. the electron density and the reduced electric field, are required. As a first step, the momentum transferred from the plasma to the gas is assumed to be proportional to the total number of positive ions and to the applied electric field. The number of positive ions is then assumed to be equal to the number of electrons. Indeed, the total number of positive ions should be larger than the total number of electrons, but in the same order of magnitude. The effective electric field accelerating the charges should also be proportional to the applied electric field. The energy released to the gas can be estimated by electrical measurements and is also proportional to the positive ion density times the square of the electric field. With these assumptions, the influence of the operating parameters on the actuation capabilities of the actuator can be determined. The determination of the concentration of active species produced by the actuators is also possible with this approach.

The numerical modelling of the plasma is performed in order to verify the assumptions made and to quantify the actual momentum and heat transferred to the gas. The experiments serve also to validate the numerical model.

This thesis is divided into 5 chapters. Chapters two to four have a short introduction and the main findings are summarized in a conclusions section. Chapter 2 describes the physics of the cold plasmas typically encountered in SDBDs and forms the theoretical basis for the rest of the thesis. The principles of the plasma diagnostics used are explained and the spectral code developed for the interpretation of the emission spectroscopy are notably presented.

Chapter 3 presents the experimental investigation of the actuators. The electrical and optical diagnostics of the plasma is performed to determine the main characteristics of the actuators. Variation of parameters such as the voltage, the polarity and the pressure is performed and analyzed. Determination of the reduced electric field, the average electron density and the production of active species is discussed.

The numerical investigation of the plasma is presented in chapter 4. The plasma is simulated for the operating conditions of the experiments. The experimental diagnostic methods are applied to the numerical simulation of the plasma and are analyzed.

## **Chapter 1. Introduction**

---

Chapter 5 summarizes the findings and conclusions of the thesis and proposes future investigations.



## 2 Plasma Physics

### 2.1 Introduction

The concepts necessary for the understanding of the plasma are presented in this chapter. General plasma physics concepts are exposed mainly to explain the findings of this thesis and to place them in their context. The physics of the cold plasma is introduced in an elementary and intuitive way, for the purpose of understanding the main aspects and characteristics of the plasma. More advanced topics are limited to the background necessary to interpret the results. The interested reader can find more general informations on the physics of cold plasmas in the two main references used during this thesis: [Lieberman, 2005] and [Raizer, 1991].

The general description of gas discharges is presented in section 2.2 with a focus on the pressure effects on the development of the discharge. The physical model of the plasma and the assumptions associated with it are discussed in section 2.3. Section 2.4 presents a short overview of the different diagnostic methods available for the characterization of the plasma. The description of the excitation of neutral and ionized particles (molecules and atoms) in relation with plasma diagnostics purposes is also made. The last section describes the physics of emission spectroscopy and the numerical model developed for its interpretation.

### 2.2 Gas discharge physics

#### Qualitative description of the discharges

When an electrical field is applied to a neutral weakly ionized gas, its free charged particles are accelerated and gain kinetic energy. In a cold weakly ionized gas, the electrons will gain energy from the field much faster than the ions, which are on the order of a thousand times heavier. The electrons will accelerate until they collide with another particle. The average distance after which this collision occurs is called the *mean free path*  $\lambda_{\text{mfp}}$  and is equal to  $1/N\sigma_{\text{es}}$ , where  $N$  is the gas number density in  $\text{cm}^{-3}$  of the target particle (usually the gas density),  $\sigma_{\text{es}}$  is the scattering cross section in  $\text{cm}^2$ . Therefore, an electron will gain on average  $E\lambda_{\text{mfp}}$  energy per

collision. The scattering cross section is a function of the electron energy and of the particular gas in which the discharge takes place, but not of the electric field nor the gas density. The average energy gained by an electron from the field is therefore proportional to the *reduced electric field* ( $E/N$ ).

The computation of the actual electron energy distribution function (EEDF) in a variable electric field is discussed in section 2.3.2. The knowledge of this distribution is of utmost importance for the plasma, since all electron-impact processes are controlled by it. For example, ionizing collisions involve only electrons having energy higher than the ionization threshold (e.g. 15 eV for  $N_2$  and 13 eV for  $O_2$ ).

### Similarity laws

The scaling laws for streamers are discussed in [Ebert et al., 2010, Liu and Pasko, 2006] for example. If the reduced electric field  $E/N$  is kept constant between two different operating conditions, and the product pressure times distance  $p \cdot d$  is kept constant, then the discharge or plasma is said to be similar. As an example, consider a constant electric field  $E_1$  applied between two parallel electrodes in a gas with density  $N_1$  separated by a distance  $d_1$ . The number of collisions will be proportional to  $d_1/\sigma_{es}N_1$  and the reduced electric field to  $E_1/N_1$ . If a different value of the electric field  $E_2$  is applied between two electrodes separated by a distance  $d_2$  in the same gas of density  $N_2$ , and that the reduced electric field  $E_2/N_2$  and the number of collisions  $d_2/\sigma_{es}N_2$  are equal to the previous case, a similar behavior of the plasma can be expected. This allows easier comparison between different configurations of discharges.

As the mean free path scales as  $\propto 1/N$ , where  $N$  is the gas density, the characteristic lengths of the plasma scales as  $\propto 1/N$ . Electron's velocities are a function of the reduced electric field, therefore the characteristic times have to scale as  $1/N$  as well. The electron density present in the head of the streamer must screen the electric field (see below, 2.2) and thus the electron density integrated over the length of the streamer head must scale as the electric field, which scales as  $N$ . The electron density thus scales as  $N^2$ . The total number of electrons, as observed with spectroscopy (see 3.3.6), scales therefore as  $N^2/N^3 = 1/N$ . Breakdown of similarity is expected and observed for processes not governed by the reduced electric field. These are for example the three-body attachment, recombination or heating effects.

### Breakdown voltage

The question of how the discharge begins and evolves is of particular interest for the determination of the domain of application of the nanosecond pulsed SDBD for flow control operating at different pressures.

**Townsend breakdown** The main mechanism for the formation of the discharge is usually explained by the Townsend breakdown mechanism [Raizer, 1991] p.72 and 130-131. The theory for the development of the discharge takes place for an electrode configuration consisting in two plane electrodes separated by the distance  $d$ , to which a potential difference  $V$  is applied, the *anode* being the electrode with positive potential and the *cathode* being the electrode with negative potential. The gap is filled with a non-attaching gas at pressure  $p$ . An initial photocurrent  $i_0$  is generated by a UV lamp (or some other external source), and every electron is accelerated by the field and produces  $\exp(\alpha(E)d)$  additional electrons and their corresponding ions, where  $\alpha(E)$  is the first Townsend coefficient and represent the ionization per cm produced by one electron placed in the electric field  $E = V/d$ . This exponential growth is known as an *electron avalanche*, and if diffusion is taken into account, it is also expanding in the direction normal to the field to give a Gaussian distribution of electron density. The electron avalanche is the primary element of any discharge. At steady state, the current at the anode is equal to that to the cathode and is equal to  $i = i_0 \exp(\alpha d)$ . The positive ions created are eventually pulled toward the cathode and the collision of the ions with the material of the cathode might generate so-called *secondary electrons*, at the rate  $i_{\text{ions}}\gamma$ , with  $i_{\text{ions}} = i_{\text{el}}(\exp(\alpha d) - 1)$  the ionic current and with  $\gamma$  being the *secondary emission coefficient*, the value of which depends on the material of the cathode. The newly created current add to the photocurrent and the total electronic current reads  $i_{\text{el}} = i_0 + i_{\text{el}}\gamma(\exp(\alpha d) - 1)$  and the total current reads:

$$i = i_{\text{el}} \exp(\alpha d) = i_0 \exp(\alpha d) / (1 - \gamma(\exp(\alpha d) - 1)) \quad (2.1)$$

This formula is valid for the so-called non-self sustained discharges, in which the externally applied photocurrent still controls the current. The idea of this analysis is that when the denominator of equation 2.1 is equal to zero, and the current will grow at a rapid rate, leading to a different type of discharge, the self-sustained discharge. The condition  $(1 - \gamma(\exp(\alpha d) - 1)) = 0$  can therefore be used to determine the critical electric field at which the breakdown will occur. The actual value of the breakdown voltage  $V_{\text{th}}$  and its corresponding breakdown field  $E_{\text{th}}$  can be found if the ionization coefficient assumes the form  $\alpha = A p \exp(-B p / E)$ . One finds  $V_{\text{th}} = B p d / (\ln(p d) + \ln(A / \ln(\gamma^{-1} + 1)))$  and thus  $E_{\text{th}} / p = B / (\ln(p d) + \ln(A / \ln(\gamma^{-1} + 1)))$ . There the product  $p d$  appears as a similarity number once again. With these formula, the Paschen curves, which gives  $V_{\text{th}}(p d)$  experimentally, can be approximated and better understood. The formulas above show that the voltage threshold will increase almost linearly with  $p \cdot d$  and that the electric field threshold will decrease logarithmically with  $p \cdot d$  (for high  $p \cdot d$ ).

For attaching gases, i.e. gases in which the attachment of electrons occurs, for example  $\text{O}_2$ , the effective ionization coefficient  $\alpha_{\text{eff}} = \alpha - \eta$  must be used.

This breakdown mechanism describes how the avalanches grow due to the secondary emission.

It is to be noted that the time necessary for the secondary electrons to be emitted from the surface has a lag with respect to avalanche creating the ions, this lag being the time necessary for the ions to cross the distance from the anode to the cathode. Therefore if the mechanism is not secondary emission but photoemission, the formation time of the breakdown will depend on the drift time of the electrons, not the ions, and is thus accelerated about 100 times.

**Streamer breakdown** If the overvoltage (i.e. the voltage above the breakdown voltage) is sufficient, a so-called *streamer* can be formed. The streamer forms when the avalanche involves such a large number of electrons and ions that the electric field produced by the charge difference, i.e. the *space charge*, within the avalanche starts to influence the applied electric field. The electric field produced by the space charge adds up vectorially to the applied electric field and becomes larger in front of the anode directed avalanche. This produces substantially more ionization owing to the steep dependence of the ionization coefficient on the electric field. On the contrary, at the cathode side of the avalanche, the total electric field is reduced with respect to the applied electric field. This situation leads to a very high electric field at the head, with strong ionization, and a low electric field region with no ionization at the tail, where a weakly ionized (quasineutral) plasma is formed. The transition from an electron avalanche to a streamer can be computed with *Meek's criterion* (or Meek-Raether criterion), which states that the multiplication factor  $\exp(\alpha d) \approx 20$ . A detailed review of this condition taking into account of the diffusion was made in [Montijn and Ebert, 2006] to find a variable criterion in function of the applied electric field, with values from  $\exp(\alpha d) = 21$  (for  $E_{th}$ ) to  $\exp(\alpha d) = 16$  ( $> 2E_{th}$ ). This theory is valid for plane gap geometries, but must be modified for non-uniform electric field configurations. The criterion for streamer formation is then  $\int \alpha(E(x))dx = 16 - 21$  (in 1D). If the distance between the anode and the cathode is not too high, and the overvoltage not too large, the transition has not the time to occur, and thus the avalanche reaches the anode, leaving only positive charges behind. This large positive space charge is then able to directly initiate a streamer, which will be directed from the anode to the cathode. This streamer is said to be a positive streamer, or a cathode-directed streamer. If the transition to streamer occurs before reaching the anode, the streamer develops in both directions. If the transition occurs close to the cathode, then the streamer develops mostly toward the anode, and the streamer is said to be a negative streamer, or an anode-directed streamer. The mechanism of growth of the positive streamer is as follows: when the positive space charge is formed, free electrons ahead of it (in the direction of the cathode) will get accelerated and a new, *secondary* avalanche will develop and reach the streamer head, neutralizing partly the positive charge and leaving behind it a positive trail, which will become the new streamer head. A debate exists for the mechanism of production of the free electrons (also called *seed* electrons) necessary for the development of the positive streamer. The theory on positive streamer propagation involves photoionization, i.e. excitation of molecules taking place in the high electric field region of the head of the streamer de-excite to a lower energy level by emitting a photon which is able to ionize the gas. However the question of the validity of this theory is not yet ascertained, especially for the case of nitrogen for example, in which

the excited species cannot emit photons with energy higher than the ionization threshold, thus discarding photoionization as the mechanism for the production of seed electrons. This question is discussed in several papers, notably in [Pancheshnyi, 2005] where the level of seed electrons coming from other mechanisms than photoionization is investigated thoroughly.

## 2.3 Physical model

Most aspects of the plasma can be described accurately using the classical laws of physics. The equations and approximations used to derive them are presented in this section. These equations are solved numerically in chapter 4.5 in a Cartesian grid.

### 2.3.1 Electromagnetic fields

The dynamics of the electromagnetic fields is described by Maxwell's equations<sup>1</sup>:

$$\begin{aligned}\nabla \times \mathbf{E} &= -\epsilon_0 \frac{\partial \mathbf{B}}{\partial t} \\ \nabla \times \mathbf{B} &= -\mu_0 \frac{\partial \mathbf{E}}{\partial t} \\ \nabla \cdot \epsilon \mathbf{E} &= \rho \\ \nabla \cdot \epsilon \mathbf{B} &= 0\end{aligned}$$

where  $\epsilon = \epsilon_r \epsilon_0$  is the dielectric constant associated with the material in which the fields evolve. However, it is assumed that the magnitude of the variation in time of the current involved in the discharge is relatively small when compared to the applied voltage, thus allowing to write  $\nabla \times \mathbf{E} = 0$ . The electric field can thus be expressed in its potential form  $\mathbf{E} = -\nabla V$ . The equation for the potential reads then:

$$\nabla \cdot \epsilon (-\nabla V) = \rho \tag{2.2}$$

This equation is easier to solve in practice due notably to the implementation of the boundary conditions, which are much easier in the potential form. This approximation is widely applied, even though its validity might be questioned.

### 2.3.2 Boltzmann equation and conservation equations

The dynamics of gas species can be treated using the kinetic theory. In this framework, the velocities and positions of the particles of interests (electrons, ions, neutrals) are treated as independent variables, described in a six-dimensional phase space  $(\mathbf{r}, \mathbf{v})$ . The distribution function  $f(\mathbf{r}, \mathbf{v}, t)$  is equal to the number of particles in a infinitesimal phase space volume

<sup>1</sup>Bold italic characters are employed to represent vectors, e.g.  $\mathbf{f}$  is a vector while  $f$  is its norm.

( $d^3r d^3v$ ) at  $\mathbf{r}$ ,  $\mathbf{v}$  and at time  $t$  [Lieberman, 2005]. The total derivative of the distribution function can be written as:

$$\frac{\partial f(\mathbf{r}, \mathbf{v}, t)}{\partial t} + \mathbf{v} \cdot \nabla_{\mathbf{r}} f(\mathbf{r}, \mathbf{v}, t) + \mathbf{a} \cdot \nabla_{\mathbf{v}} f(\mathbf{r}, \mathbf{v}, t) = \left. \frac{\partial f(\mathbf{r}, \mathbf{v}, t)}{\partial t} \right|_c \quad (2.3)$$

where  $\mathbf{a}$  is the acceleration  $\equiv \partial \mathbf{v} / \partial t$  and  $\left. \frac{\partial f(\mathbf{r}, \mathbf{v}, t)}{\partial t} \right|_c$  is a *collision term* which takes into account the variation of velocities and production/destruction of particles due to collisions. The collisions are assumed to change the velocities instantaneously. The LHS of equation 2.3 is simply the total derivative of the distribution function and the RHS is basically a source term.

In the case of a neutral gas at thermodynamic equilibrium, without time variation, acceleration or spatial gradients (the total derivative equals to zero), this equation can be solved analytically and the Maxwell-Boltzmann distribution function is obtained:

$$f(v) = n_{\text{gas}} \left( \frac{m_{\text{gas}}}{2\pi k_B T_{\text{gas}}} \right)^{3/2} \exp \left( -\frac{m_{\text{gas}} v^2}{2k_B T_{\text{gas}}} \right) \quad (2.4)$$

where  $v$  is the magnitude of the velocity and  $f(v)$  is the velocity distribution function for the case of a homogeneous medium. This distribution is very useful for determining equilibrium properties, but does not apply to time-varying, spatially-inhomogeneous fluid mixture such as the plasma investigated in this study.

If the gas is assumed to be weakly ionized and that the neutral species are not much perturbed by the plasma, then the neutral species can be said to be at thermal equilibrium which is well described by one temperature  $T_{\text{gas}}$ . Boltzmann's equation needs to be solved only for charged particles.

If we use equation 2.3 to describe for example electrons, in a weakly ionized gas in which only an electric field  $\mathbf{E}$  is acting, the acceleration term can be evaluated as  $\mathbf{a} = -\frac{e\mathbf{E}}{m_e}$ , where  $m_e$  is the mass of the electron.

In order to solve this equation in a more general case, several simplifications are necessary [Hagelaar and Pitchford, 2005]. The first one is to assume that the electric field and the collision term are uniform in space. The second one is to assume that the distribution function varies only in the direction of the field (taken to be along the  $z$  coordinate here). With these simplifications, equation 2.3 is written, expressing the velocity in spherical coordinates:

$$\frac{\partial f}{\partial t} + v \cos(\theta) \frac{\partial f}{\partial z} - \frac{eE}{m_e} \left( \cos(\theta) \frac{\partial f}{\partial v} + \frac{\sin^2(\theta)}{v} \frac{\partial f}{\partial \cos(\theta)} \right) = \frac{\partial f}{\partial t} \Big|_c \quad (2.5)$$

where the distribution function  $f$  is a function of  $(z, v, \theta, t)$ ,  $v$  being the magnitude of the velocity. It is independent of  $\phi$  because  $\mathbf{E} = E(\cos(\theta)\mathbf{e}_v - \sin(\theta)\mathbf{e}_\theta + \mathbf{e}_\phi \cdot 0)$  is chosen as the axis of symmetry.  $\nabla_v = \mathbf{e}_v \frac{\partial}{\partial v} + \mathbf{e}_\theta \frac{1}{v} \frac{\partial}{\partial \theta} + \mathbf{e}_\phi \frac{1}{v \sin(\theta)} \frac{\partial}{\partial \phi}$

This equation can be solved using an expansion series, the *two-term* expansion. Following [Hagelaar and Pitchford, 2005], the two term expansion is constructed in function of the two first Legendre polynomials (1 and  $x$ ) with  $x = \cos(\theta)$ . The function is then assumed to be a product of two functions, one for the spatial and temporal dependence and the other for the dependence on the velocity:

$$f(z, v, \cos(\theta), t) = \frac{1}{2\pi(2e/m_e)^{3/2}} n(z, t) (F_0(\varepsilon) + \cos(\theta)F_1(\varepsilon)) \quad (2.6)$$

where  $\varepsilon = 1/(2e)m_e v^2 = (v/\gamma)^2$  is the kinetic energy of the electron in eV.

If moments of Boltzmann's equation are taken, a set of equations describing the macroscopic properties of the fluid of charged species can be obtained, giving the hydrodynamic description of the ionized gas [Ferreira and Loureiro, 2000]. These equations are the well known equations for the conservation of mass, momentum and energy.

In order to model the discharge's formation phase, the momentum conservation equation for electrons and ions in the fluid description of the plasma is simplified to yield the classical **drift-diffusion** approximation. In this approximation, the equation for the conservation of momentum (see for example [Lieberman, 2005] equation 2.3.15) is simplified assuming negligible inertial terms (valid for high pressures<sup>2</sup>) and therefore linking the fluid velocity to the electric field with a pressure term, which can be related to diffusion through the ideal gas law. The equation reads:

$$m_e n_e \left[ \frac{\partial \mathbf{v}_e}{\partial t} + \mathbf{v}_e \cdot \nabla \mathbf{v}_e \right] = -en_e \mathbf{E} - \nabla(k_B T_e n_e) - m_e n_e \mathbf{v}_m \mathbf{v}_e \quad (2.7)$$

where  $\mathbf{v}_e$  is the drift velocity of the electron gas. If the total derivative of the drift velocity is assumed to be zero, the electron flux ( $\mathbf{J}_e = n_e \mathbf{v}_e$ ) is then:

<sup>2</sup>In the context of cold plasma physics, atmospheric pressure is considered high.

$$n_e \mathbf{v}_e = \frac{-en_e \mathbf{E}}{m_e \nu_m} - \frac{1}{m_e \nu_m} \nabla(k_B T_e n_e)$$

for an isothermal electron gas, the flux can be written:  $\mathbf{J}_e = -\mu_e \mathbf{E} n_e - D_e \nabla n_e$ , where  $\mu_e = e/m_e \nu_m$ ,  $D_e = k_B T_e / m_e \nu_m$  are the mobility and the diffusion coefficient respectively.

The flux of charged species being determined, the equation for the conservation of mass, i.e. the continuity equation can be solved.

In the simplest approach, no equation for the conservation of energy is solved. Therefore, an additional assumption must be made in order to determine the coefficient which depend on the electron energy. This assumption is known as the local field approximation (LFA), which assumes that the electron energy distribution function (EEDF) is fully determined by the local electric field. The EEDF is then computed separately with a Boltzmann solver (usually Bolsig+ [Hagelaar and Pitchford, 2005]), which solves Boltzmann's equation for electrons in the two-term approximation. The LFA is equivalent to assuming that all energy gained by the electron from the electric field is lost in collisions. This assumption is usually good at high pressures where the electron-neutral collision frequency is high. It is to be noted that these assumptions are widely used in the literature on streamer modelling. The continuity equations to be solved in this drift-diffusion form are:

$$\frac{\partial n_e}{\partial t} + \nabla \cdot \vec{\Gamma}_e = n_e(\alpha - \eta) |\vec{\Gamma}_e| - n_e n_p \beta_{ei} \quad (2.8)$$

$$\frac{\partial n_p}{\partial t} + \nabla \cdot \vec{\Gamma}_p = n_p \alpha |\vec{\Gamma}_e| - n_e n_p \beta_{ei} - n_n n_p \beta_{ii} \quad (2.9)$$

$$\frac{\partial n_n}{\partial t} + \nabla \cdot \vec{\Gamma}_n = n_e \eta |\vec{\Gamma}_e| - n_n n_p \beta_{ii} \quad (2.10)$$

$$(2.11)$$

where  $\mathbf{\Gamma}_i = n_i \mu_i \mathbf{E} - \nabla(D_i n_i)$  with  $i = e, n, p$ . The RHS terms in equations 2.11 are the sources for the corresponding charged species.  $\alpha$  and  $\eta$  are the ionization coefficient and the attachment coefficient. As the mobility and the diffusion coefficient, they are functions of the reduced electric field and are determined in the Boltzmann solver.  $\beta_{ei}$  and  $\beta_{ii}$  are the electron-ion and ion-ion recombination coefficients. The source parameters are described in more details in subsection 2.3.3.



At the walls, the flux is expressed as [Boeuf et al., 2007, Hagelaar et al., 2000]:

$$\mathbf{\Gamma}_j \cdot \mathbf{n} = (-a(q_j / |q_j|) \mu_j \mathbf{E} \cdot \mathbf{n} - \frac{1}{4} v_{\text{th},j}) n_j + \gamma_{\text{m,d}} \mathbf{\Gamma}_j \cdot \mathbf{n} \quad (2.12)$$

where  $\mathbf{\Gamma}_j$  is the flux vector of the corresponding species (electrons, positive and negative ions),  $\mathbf{n}$  is the vector normal to the surface (pointing away from it). They represent the flux of charged species to the wall or from the wall. The flux from the wall is not null in the case of electrons, due to the secondary emissions, taken to be due exclusively to ions impacting the electrode (or the dielectric) and releasing an electron (see [Raizer, 1991]). The number of secondary electrons entering the gas is proportional to the number of incident positive ions. This fraction is determined experimentally and is written  $\gamma_{\text{m,d}}$  in equation 2.12, the subscripts standing for the metal (electrode) or dielectric surfaces. Other secondary emissions could have an important effect, such as secondary electron emission (SEE) due to electrons impacting a surface and releasing one or more electrons [Henrist, Bernard et al., 2002]. This effect can be treated qualitatively by using a reflection coefficient ([Hagelaar et al., 2000]). Here this has not been made since the calculations performed in chapter 4.5 were not sensitive to this parameter. The second term in the RHS of equation 2.12 is the thermal velocity of the species and is associated with the isotropic distribution of speed.  $a$  is equal to one if the electric field is directed toward the wall (drift velocity directed away from the wall) and to zero otherwise. This formula models the fact that when the drift velocity is directed toward the wall, the total flux is the sum of an isotropic part (the thermal flux) and a drift part. If however the drift velocity is directed away from the wall, the thermal flux will be diminished or canceled.

**Typical conditions and validity of the model** There are many assumptions made in the above model, starting with the Boltzmann equation, which assumes that the mean free path is small compared to the characteristics length of the problem. The mean free path is computed as  $\lambda_{\text{mfp}} = 1/(N\sigma_{\text{es}})$ , where  $N$  is the density of the gas into which the particle of interest moves, and  $\sigma_{\text{es}}$  is the total scattering cross section of the particle at energy  $\epsilon$  in the gas. The mean free path for collisions between neutral gas particles at atmospheric pressure is on the order of  $\lambda_{\text{mfp}} \approx 10^{-7}$  m and the collision frequency associated with it is on the order of  $\tau_{\text{nn}} = \nu/\lambda_{\text{mfp}} \approx 10^9$  s<sup>-1</sup>. Free electrons have a mean free path which depends on the velocity. For the two-term approximation to hold, the energy gained by the electrons from the field must be small compared to their mean energy. The mean energy transmitted to an electron during one average collision depends therefore on the electron velocity (=to its kinetic energy) and is proportional to the field strength.

The mean free path is plotted as a function of the energy of electrons normalized to the atmospheric pressure (1 bar) in figure 2.1 (a). For electrons in the typical range 1-200 eV, the mean free path must be smaller than the grid size for the Boltzmann equation to be meaningful, this implies grid sizes larger than about 1  $\mu\text{m}$  for atmospheric pressure. As the

mean free path increases linearly with decreasing pressure ( $\propto 1/P$ ), the minimal grid size must be larger than  $10 \mu\text{m}$  at 100 mbar. Another issue is the collision time between electrons and neutrals, which must be very short when compared to the characteristic time of the problem. The inverse of the collision time, the collision frequency can be approximated by  $\tau_{ne} = N\sigma_{es}v_e$  ( $v_e$  is the electron velocity) or can be computed via a Boltzmann solver such as Bolsig+ (shown in figure 2.1 (b)). The mean energy gained per collision in an uniform reduced electric field of 100 and 1000 Td is shown in figure 2.1 (c) and (d).

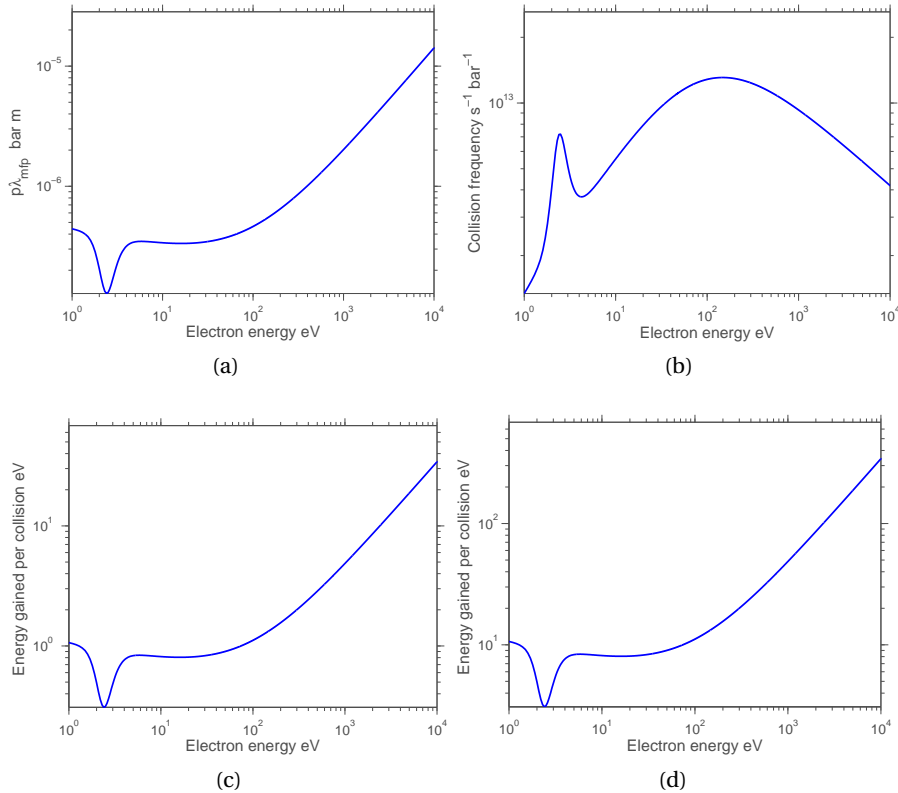


Figure 2.1: Mean free path (a) and electron-neutral collision frequency (b) in  $\text{N}_2$  as a function of the electron energy normalized to 1 bar. The mean energy gained by an electron during one collision is shown for  $\text{N}_2$ , for 100 Td (e) and 1000 Td (f) The scattering cross section is that of [Tabata et al., 2006].

The second strong assumption is the electron growth model in Bolsig+, which assumes either a steady state and spatial variation of the electron density, or a spatially homogeneous but an exponential growth of the electron density in time. For the case of streamer modelling, none of these assumptions are justified, since the electron density varies both in time and space. The main outcome of the choice of the growth model is the change in the ionization rate, which is a very important parameter of the discharge, as will be seen in detail in section 2.3.3.

### 2.3.3 Kinetic processes modeled

The kinetic processes taking place in the plasma are numerous and can be classified as follows:

- Electron-impact processes
- Heavy species processes
- Surface processes

Electron-impact processes involve collision of an electron with one or more heavy species and are characterized by the kinetic energy of the electron, which is much larger than the kinetic energy of heavy species in a non-equilibrium plasma. This feature would make the rate of heavy species processes lower than for electron-impact processes, but they are counterbalanced by the normally larger cross sections associated with the size of the heavy species. Therefore, one can normally make the following ranking for the rates at which the different processes occur. First electron-impact processes involving neutrals, then ion-neutral processes and finally three-body processes at high pressure. A notable exception is the three body charge exchange reactions, which are very fast at high pressures. The other processes such as electron-ion, electron-excited species, ion-ion impacts are generally considerably less important at low ionization degree. Note that low ionization means here  $< 10^{-5}$ , which makes the streamer like plasmas candidates for step processes such as electron-excited species ionization (notably vibrational excitation), step-ionization.

For the purpose of modelling a nanosecond pulsed plasma at atmospheric pressure, the following reasoning is used to reduce the number of reactions: during formation phases such as the formation of a streamer, the short duration allows discarding processes with slow dynamics. For longer times, the reduced electric field is much weaker, allowing to discard high threshold processes such as ionization.

#### **Electron-impact processes**

The most important processes taking place in air plasmas are the two-body electron-impact ionization, the two and three-body attachment, the two and three-body ion-ion recombination and the two and three-body electron-ion recombination. These processes are especially important because they involve a change in the number of free charged species present in the plasma. A selection of the possible forms of these processes taking place in cold air plasmas [Kossyi et al., 1992] is shown in table 2.1:

Ionization and two and three-body attachment are discussed below. Other processes are computed using rates from [Kossyi et al., 1992].

A comparison of the ionization coefficients  $\alpha$  for air computed with Bolsig+ using three

Table 2.1: Important fast processes occurring in cold air plasmas at atmospheric pressure.

Process	succinct scheme
electron-impact ionization	$e + O_2, N_2 \rightarrow O_2^+, N_2^+ + 2e$
two-body attachment	$e + O_2 \rightarrow O_2^-$
three-body attachment	$e + O_2 + O_2, N_2 \rightarrow O_2^- + O_2, N_2$
dissociative recombination	$e + O_4^+, N_4^+ \rightarrow 2O_2, 2N_2$
two-body ion-ion recombination	$O_2^+, N_2^+ + O_2^- \rightarrow O_2, N_2 + O_2$
three-body ion-ion recombination	$O_2, N_2^+ + O_2^- + O_2, N_2 \rightarrow O_2, N_2 + O_2 + O_2, N_2$

different sets of parameters and assumptions is performed. The electron growth mechanism selected in Bolsig+ is the spatial growth, due to the strong ionization taking place in the head of the streamer, which can be imagined as a moving high voltage electrode producing a strong electric field, which attracts electrons. This assumption is of course not very satisfactory in the body of the streamer, but fortunately the electric field is very weak in it, reducing ionization to a negligible value. The different assumptions concern the role of the electron-electron collisions and the level of ionization of the plasma, which modify the results significantly at high reduced electric fields. In order to include electron-electron collisions, the ionization level must be specified. This ionization level can only be estimated and is varying in space, thus making estimation difficult. To summarize, the three parameters tested were electron-electron collisions with  $10^{-5}$  level of ionization, electron-electron collisions with  $10^{-4}$  ionization level and no electron-electron collisions taken into account. The difference can be seen in figure 2.2.

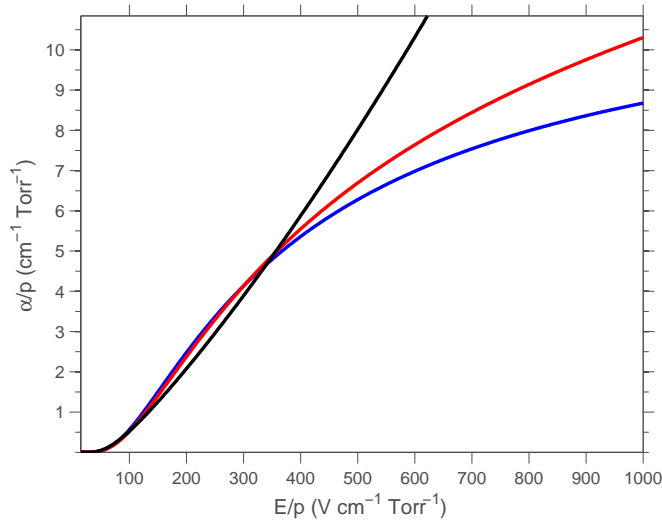


Figure 2.2: Comparison of  $\alpha$  in air with different models. Bolsig+ with modified cross sections and electron-electron collisions ( $10^{-5}$  ionization) (blue solid line) Bolsig+ with electron-electron collisions ( $10^{-4}$  ionization) (black solid line), Bolsig+, without electron-electron collisions (red solid line)

It can be seen that significant difference occurs for values higher than  $350 \text{ V} \cdot \text{cm}^{-1} \cdot \text{Torr}^{-1}$  ( $\cong 1000 \text{ Td}$ ). Incidentally, the accuracy of the solution of the two-term approximation used in Bolsig+ is significantly reduced for values of the reduced electric field higher than  $1000 \text{ Td}$ . This comparison is made, because in streamer modelling, the electric field often reaches values of  $3000 \text{ Td}$ , which makes the two-term approach incorrect and therefore the ionization rate incorrect for high reduced electric field regions. Due to the necessity to use a Boltzmann solver for the determination of excited species (see section 2.4.1), the validity of the ionization coefficient for high reduced electric field is compared to other models, notably the model described in [Raizer, 1991] which is based on experimental data.

The two other models compared are those described in [Morrow and Lowke, 1997] and [Kossyi et al., 1992]. The ionization coefficient for the four models is shown in figure 2.3.

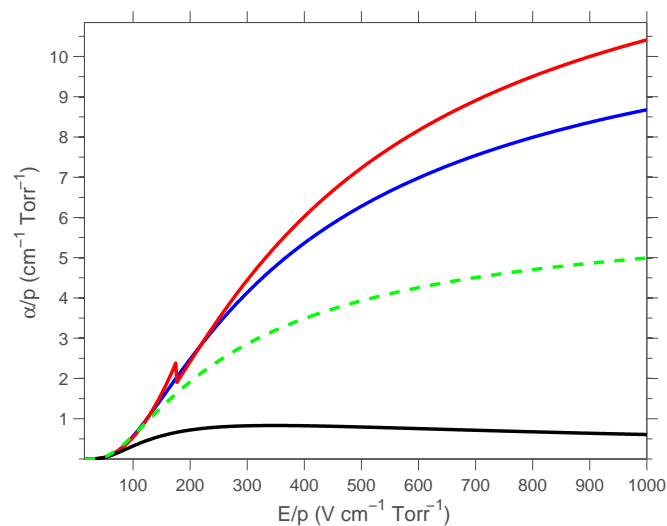


Figure 2.3: Comparison of  $\alpha$  in air with different models. Bolsig+ with modified cross sections (blue solid line), Raizer's model (red solid line), Morrow's model (green dashed line) and  $\alpha$  derived from Kossyi's model (black solid line)

Surprisingly, the fit for the ionization coefficient of Raizer gives very similar values compared to the computation made with Bolsig+. It also seems not physical that the ionization coefficient keeps increasing as the reduced electric field increases, as it should reach a maximum value and decrease at some point ([Raizer, 1991] p. 57). Morrow's model performs rather poorly at high reduced electric field, but this was to be expected since the fits given in [Morrow and Lowke, 1997] are valid only up to  $800 \text{ Td}$  (graph in [Lowke and Morrow, 1995]). The values of  $\alpha$  determined from Kossyi's model were obtained by using the formula (20-21) of [Kossyi et al., 1992] giving the reaction rates of ionization by electron impact from  $\text{N}_2$  and  $\text{O}_2$  and multiplying by  $N/\mu E$ , with the mobility  $\mu$  obtained from Bolsig+. It can be seen that this fit is not consistent with Bolsig+ or Raizer's ionization coefficients for high reduced electric fields. This also is not a surprise since Kossyi's data are valid up to  $300 \text{ Td}$  only.

If we take a look at what happens for lower reduced electric fields, we can see that the fits of

Morrow and based on Kossyi perform rather well when compared to Bolsig+ results. On the other hand, Raizer's fit does not provide a very satisfactory results, and is supplemented by another formula for lower reduced electric fields, which is then combined to the former fit in order to obtain a satisfactory model for  $\alpha$ . This is made for example in [Macheret et al., 2002, Likhanskii et al., 2007].

In figure 2.4, the fits obtained from Bolsig+ calculations and from Morrow, Raizer and Kossyi (equation 45 and 46) are shown for both the ionization and attachment coefficients. Here, the fits corresponding to Raizer's model is obtained by using the two available fits, one valid for the whole range of reduced electric fields which is used whenever the other is not valid, that is, outside the region  $44\text{-}176 \text{ V} \cdot \text{cm}^{-1} \cdot \text{Torr}^{-1}$ . It is noted that no explicit fit is given for two-body attachment in [Raizer, 1991]. The values of the attachments coefficients of Morrow are not following the trends of the other models. The somehow surprising fact is that the data from [Lowke and Morrow, 1995] from which Morrow's are supposed to be based does look similar to the other fits. It is also noted that Bolsig's three-body attachment is supposed to be multiplied by the gas density  $N_g$  in  $\text{cm}^{-3}$  as stated in the input file, but the multiplication with  $O_2 = 0.21N_g$  seems to agree best with the other fits, and looks very similar to [Lowke and Morrow, 1995].

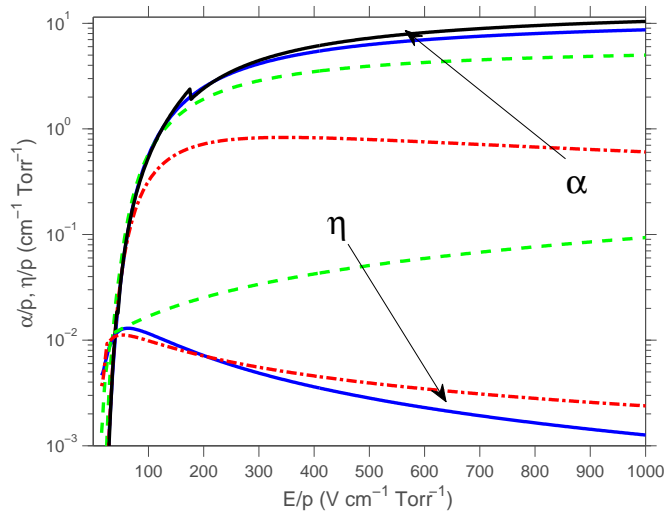


Figure 2.4: Comparison of  $\alpha$  and  $\eta$  in air with different models. Bolsig+ with modified cross sections (blue solid line), Raizer's model (black solid line), Morrow's model (green dashed line) and  $\alpha$  derived from Kossyi's model (red dashed-dotted line)

**Transport coefficients** The mobility and diffusion of the charged species depend on the type of the gas in which the species of interest evolve, the reduced electric field and the pressure and temperature of the gas. Mobilities for ions were assumed to change only with respect to pressure in this thesis, although they are known to vary with the reduced electric field. This parameter is very important for models in which the seed electrons are only produced by

ion-impacts to the surface, which is not the case here since photoionization is assumed as a the generation mechanism for seed electrons. The comparison of the mobility for electrons for different models is shown in 2.5. The data used in [Likhanskii et al., 2007, Macheret et al., 2002] give the drift velocities of the electrons for  $N_2$  and  $O_2$ , from 0.07 to 1000 Td. It was assumed that the mobility for air can be computed as (from Blanc's law) :

$$\frac{1}{\mu_{air}} = \frac{0.78}{\mu_{N_2}} + \frac{0.21}{\mu_{O_2}} \quad (2.13)$$

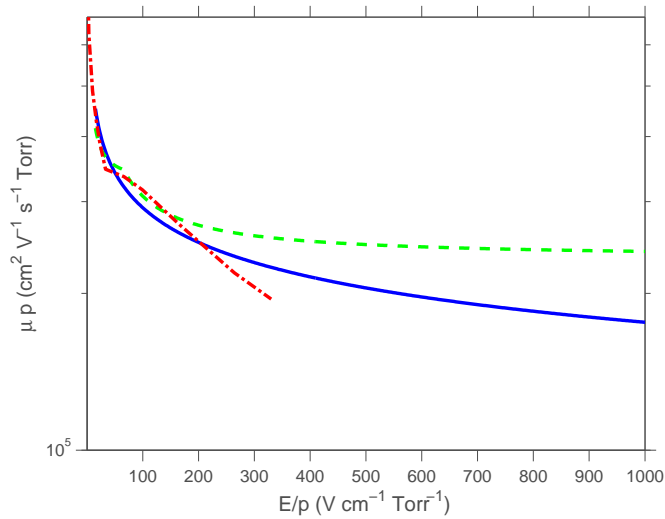


Figure 2.5: Comparison of  $\mu p$  in air with different models. Bolsig+ with modified cross sections (blue solid line), mobility inferred from Grigoriev's drifts velocities (red dashed-dotted line), Morrow's model (green dashed line).

It can be seen that mobilities are consistent between different authors and methods.

### Surface processes

The only surface processes taken into account are the recombination of positive and negative charged species at the solid surface (on the dielectric), which is assumed to be instantaneous, and the charging of the surface by charged species. These processes are especially important for streamer simulations because they modify significantly the electric field distribution and thus the whole streamer simulation.

### 2.3.4 EHD force and heat release

The momentum equation 2.7 for charged species was described in section 2.3.2, which is noted once more here, only slightly rearranged:

$$\left[ \frac{\partial \mathbf{v}_e}{\partial t} + \mathbf{v}_e \cdot \nabla \mathbf{v}_e \right] = \frac{-e\mathbf{E}}{m_e} - \frac{\nabla(k_B T_e n_e)}{m_e n_e} - \nu_m \mathbf{v}_e$$

The last term of the LHS of this equation contains  $\nu_m$  which is the momentum exchange frequency between neutral and charged species  $i$ . This expression can be used also to determine the amount of momentum transferred from the charged species to the neutral gas, which is of interest in the context of aerodynamic flow control. The assumptions made to compute this momentum transfer are described in [Boeuf and Pitchford, 2005]. The main assumptions made are the same as for the drift-diffusion approximation described in section 2.3.2. The total momentum transfer is expressed as a force acting on the neutral gas. It is called the electro-hydrodynamic force (EHD). It reads:

$$\mathbf{f} = e(n_i - n_e - n_n)\mathbf{E} + (m_e \mathbf{u}_e - m_i \mathbf{u}_i + m_n \mathbf{u}_n)S - \nabla(n_i k_B T_i) - \nabla(n_e k_B T_e) - \nabla(n_n k_B T_n)$$

Where  $S$  is the source term for charged species.

In this thesis, the order of magnitude of this force is of interest, and only the largest term, the Coulomb term is retained. The EHD force is then expressed by:

$$\mathbf{f} = e(n_i - n_e - n_n)\mathbf{E} \tag{2.14}$$

in  $\text{Ncm}^{-3}$ .

The maximum heating density that can be released in the gas by charged particles is simply the Joule heating [Soloviev and Krivtsov, 2009], which is an upper estimates of the heat deposition in the gas:

$$W = |\mathbf{j} \cdot \mathbf{E}| = e |(n_p \mu_p - n_e \mu_e - n_n \mu_n)| E^2 \tag{2.15}$$

in  $\text{Wcm}^{-3}$ .

The actual heat released by the plasma in the gas will occur through transfer of energy from

---

<sup>3</sup>The electric field must be taken in V/m in equation 2.14 to yield  $\text{N/cm}^3$



the electrons, ions and excited species (including vibrational and rotational excitation) to the translational energy of the gas. This process is complicated and is outside the scope of this thesis. If this problem is of interest to the reader, a phenomenological approach can be employed, as was performed in [Unfer and Boeuf, 2009].

## 2.4 Optical diagnostics of the plasma

**General considerations** Plasma diagnostics techniques allow the determination of plasma parameters such as the temperatures (translational, rotational, vibrational and electronic), the density of species, the electric field, the magnetic field, etc. The techniques available depend largely on the type of plasma, which is characterized mainly by its pressure, the ionization degree, the temperature and its dimensions.

If the dimensions of the plasma are small when compared to the mean free path of the charged species, then the charged species do not encounter enough collisions to reach a statistical equilibrium. In the extreme case of no interaction between particles, every particle is independent and no collective behavior can be characterized by a single quantity such as the temperature. For the case of an ionized gas, long range forces come into play, and interactions between distant particles arise through Maxwell laws of electrodynamics. This is typically encountered in space plasmas. When the mean free path between particles diminishes, collisions occur, exchanging energy and momentum, thereby modifying their states. These changes can be the transfer of momentum or energy through modifications of the electronic structure, which can lead to excitation or to ionization.

If the number of collisions between electrons and heavy species is high, the energy transfer tends to equilibrate the average kinetic energy between different species, until thermodynamic equilibrium is attained. A plasma is said to be at thermodynamic equilibrium or at local thermodynamic equilibrium (LTE), when one global temperature describes every degree of freedom. In this case most of the properties of the plasma can be computed knowing the temperature (e.g *Saha* equation). This is usually true for high temperature and high pressure plasmas such as encountered for example in an arc discharge. For intermediate cases where the thermodynamical equilibrium is realized only partially, for example in a shock tube experiment, several temperatures arise, each describing a different degree of freedom of the system. These can be the translational, rotational, vibrational and electronic temperatures.

**Overview of existing diagnostic methods** For low pressures, an electrostatic probe or Langmuir probe can be used. A potential difference is applied between two (for the simplest case) wires which are placed in the plasma. At the negative tip, the electrons are repelled and the positive ions are attracted. Due to the high kinetic energy of the electrons, a fraction of the electrons is able to cross the potential barrier and reach the electrode. At the positive tip on the other hand, the electrons are attracted and the ions repelled. By measuring the total current and the voltage between the two ends of the wire, the ionic current and information

on the EEDF can be determined. However, when the pressure increases, collisional processes come into play and makes the interpretation of the data more complicated. Moreover, the maximum temporal resolution of such a technique is of the order of the  $\mu\text{s}$  (e.g. triple probe technique [Chen and Sekiguchi, 1965]), which would be too slow for nanosecond pulses. The most important restriction of this technique is its intrusive nature. The intrusion of a metallic wire on the path of the streamer would completely change its properties, thus excluding the use of such a technique.

Surface measurements of the electric field are possible in high-pressure plasmas such as shown in [Tanaka et al., 2009] using so-called Pockel's effect. This effect is the change in polarization of light in a crystal occurring in the presence of an electric field. This technique is very interesting in itself, but provides no information on the electric field above the surface, in the gas. This electric field is the determining one for most processes in the plasma.

The measurement of surface charges remaining after the plasma has been switched off is also possible using an electrostatic voltmeter. The measurement of the surface charges is of interest due to the saturation provoked by these charges on the ionic wind produced by SDBD. This has been performed in [Opaits et al., 2008b].

Optical methods are most often used in plasmas. Optical methods can be either non-intrusive (emission) or slightly intrusive (absorption).

Emission techniques are based on the observation of the light naturally emitted by the plasma (or another source). They are usually easy to implement depending on the conditions, but the quality of the results obtained depend on the power of the light source investigated. If the source produces sufficient light, the colors can be separated using a dispersive element, such as in a spectrometer for example, and a spectrum of the frequency composing the light can be recorded. The structure of this spectrum can be analyzed using the methods of emission spectroscopy, which relies on the understanding of the internal configuration of the molecules and atoms (see section 2.5). If the optical system used to record the light is calibrated in intensity, then the absolute amount of light emitted can be determined. The intensity of light allows to determine the population density (number of particle per unit volume) of radiating particles (molecules, atoms or electrons). In addition to the population densities of radiative particles, numerous informations on the state of the plasma can be inferred from emission spectroscopy, such as the rotational, vibrational and electronic temperatures and the electron density (using the Stark broadening effect) provided some conditions are fulfilled.

The main disadvantage of emission spectroscopy is that it can be applied only if the source emits sufficient light. When the plasma is unexcited, such as in regions with low electric fields, it does not emit light and no information on the plasma can be gathered. An overview of the methods of emission spectroscopy for plasma diagnostics in air at atmospheric pressure is given in [Laux et al., 2003]. Emission spectroscopy is the main tool of investigation used during this thesis, and is further developed in section 2.5.

Absorption-based techniques use a light source which illuminates a section of the plasma.

The molecules of the plasma react by absorbing the light or by stimulated emission of a photon (*fluorescence*). These techniques are similar to emission spectroscopy, as they rely on the understanding of the electronic structure of particles. The photons of the light at a specific frequency provoke the excitation of a particle to a higher energy level, which might or might not de-excite by the release of a photon (it *fluoresce*). The main advantage when compared to pure emission spectroscopy is the ability to gather information on the plasma even when it does not radiate by itself and to provide information about the ground states of the molecules and atoms of the gas. The disadvantages apart from their intrusive nature is the implementation and especially the need of a well defined, stable source of light. For this purpose most techniques use a laser as the light source. Among these techniques, accurate methods to measure the population density of a species are the laser induced fluorescence (LIF) and the cavity ring-down spectroscopy (CRDS) for example. Finally, the Thomson scattering effect, which is the scattering of the light by free charges, can be used to determine the electron density. These techniques are usually more difficult to implement than emission spectroscopy, and have therefore not been used during this thesis.

### 2.4.1 Excited species

A molecule or an atom is said to be in an *excited state* when its electronic structure is not in the ground (most stable) state. The molecule's electronic structure can reach an excited state via several interactions with other molecules or atoms, electrons or photons. For example, consider the *electron-impact* excitation of molecule M into an electronic state having higher energy  $M^*$  by electron impact:



The electron perturbs the electronic structure of the molecule. If the energy associated with the electronic structure of the molecule remains unchanged, the collision is said to be elastic, the electron and the molecule conserve their respective energy while their momentum may change. If the energy of the molecule is increased (or decreased), then the collision is said to be inelastic (or superelastic). In that case the molecule remains in an excited state after the collision. The molecule can then be de-excited to a lower state (not necessarily the ground state) by radiative decay, which occurs mainly by electric dipole radiation, or by collisions with another particle (molecule or electron). The radiative decay reaction is:



The second de-excitation process is called collisional de-excitation or *quenching* of the excited state M by a particle p which is called the *quencher*.



In the high pressure air plasma produced with the nanosecond pulsed SDBD, excited species are assumed to be produced mainly by electron-impacts from the ground state of neutral air species ( $N_2, O_2, H_2O, Ar$ ), due to the short time scale of the streamer propagation. This assumption is verified in the head of the streamer, but is not very good in the body of the streamer (see section 3.3.3), where the population of excited species is high and the target species cannot be considered as only ground state air. The excited species are assumed to be de-excited only by spontaneous radiative decay and two-body collisional de-excitation. These assumptions are standard and form a so called *collisional-radiative* model. The populations of excited species can be computed using equation 2.19.

$$\frac{dn_i}{dt} = n_e X_i K_i(E/N) - \frac{n_i}{\tau_i} \quad (2.19)$$

where  $K_i(E/N)$  is the production rate for the electron-impact excitation process  $i$ , which depends on  $E/N$ .  $X_i$  is the target species density.  $\tau_i$  is the total lifetime of the excited state  $i$ , calculated as  $\tau_i = 1/\tau_0^i + Q_{N_2}^i N_2 + Q_{O_2}^i O_2$ , where  $\tau_0^i$  is the radiative lifetime of the species  $i$  and  $Q_M^i$  is the quenching rate of the  $i$  state by the quencher M. The radiative lifetimes are taken from [Gilmore et al., 1992] and [Chang and Setser, 1978]. The production rates are computed as follows:

$$K_i(E/N) = \frac{2e}{m_e} \int_0^\infty \varepsilon \sigma_i^e F_0 d\varepsilon$$

where  $\varepsilon = 1/(2e)mv^2$  is the kinetic energy of the electron in eV,  $F_0$  is the electron energy distribution function (EEDF), which is discussed in section 2.3.2, and  $\sigma_i^e$  is the *excitation cross section* in  $cm^2$ .

Excitation cross sections are sometimes available only for the whole excited state, and not for

Table 2.2: Electron-impact excitations and references for the corresponding excitation cross sections and quenching rates

Process	Reference for e-impact	Reference for quenching
$O_2(X^3\Sigma_g^-) + e \rightarrow O_2(a^1\Delta_g) + e$	[Phelps and Pitchford, 1985]	[Zhdanov et al., 2001]
$N_2(X^1\Sigma_g^+) + e \rightarrow N_2(A^3\Sigma_u^+) + e$	[Tabata et al., 2006]	[Cartwright, 1978]
$N_2(X^1\Sigma_g^+) + e \rightarrow N_2(B^3\Pi_g) + e$	[Tabata et al., 2006]	[Piper, 1992]
$N_2(X^1\Sigma_g^+) + e \rightarrow N_2(C^3\Pi_u) + e$	[Tabata et al., 2006]	[Dilecce et al., 2007, Pancheshnyi et al., 1998]
$N_2(X^1\Sigma_g^+) + e \rightarrow N_2^+(B^2\Sigma_u^+, \nu = 0) + 2e$	[Tabata et al., 2006]	[Valk et al., 2010]
$N_2^+(X^2\Sigma_g^+) + e \rightarrow N_2^+(B^2\Sigma_u^+, \nu = 0) + e$	[Tabata et al., 2006]	[Valk et al., 2010]
$Ar(\text{ground}) + e \rightarrow Ar(2p_1) + e$	[Boffard et al., 2007]	[Sadeghi et al., 2001]

a particular vibrational level of this electronic state. In this case it was assumed that the vibrational levels are populated according to the Franck-Condon principle (see 2.5). The vibrational populations can therefore be estimated as  $N_i(\nu') = q_{X,0 \rightarrow i,\nu'} N_i(\Sigma \nu')$  (see for example [Bibinov et al., 1998]), where  $q_{X,0 \rightarrow i,\nu'}$  is the Franck-Condon factor from the first vibrational state of the ground electronic state (X) to a particular  $\nu'$  vibrational state of an excited electronic state  $i$ . The Franck-Condon factors for every molecules were taken from [Gilmore et al., 1992].

The energy threshold of the excitation cross section was also shifted by the vibrational energy of the vibrational level, with vibrational constants taken from [Laher and Gilmore, 1991]. The excited species of use in the present thesis are shown in table 2.2 together with the references corresponding to the excitation cross sections and quenching rates of the excited species.

The excitation cross sections used are summarized in figure 2.6.

It can be seen that the excitation cross sections have a threshold below which no excitation is possible. This corresponds to the energy associated with the electronic configuration of the excited state with respect to the ground state of that molecule. A high lying state has a high energy, such as the  $N_2^+(B^2\Sigma_u^+)$  which has an energy of about 18 eV. In the remainder of the thesis,  $O_2(a^1\Delta_g)$ ,  $N_2(A^3\Sigma_u^+)$  and  $N_2(B^3\Pi_g)$  are considered the low lying states, while the rest are considered high.

For  $N_2(B^3\Pi_g)$  and  $N_2(C^3\Pi_u)$ , the quenching rates used correspond to the  $\nu = 3$  and  $\nu = 0$  vibrational state respectively. The value of the quenching rate chosen for the process  $N_2^+(B^2\Sigma_u^+, \nu = 0) + M \rightarrow \text{products}$  where  $M = N_2, O_2$ , is critical as the overall quenching rate can vary by a factor 3 according to the source (see [Dilecce et al., 2010]). The quenching rates chosen here are intermediate. Only two-body quenching rates have been used in this study, as suggested in [Valk et al., 2010]. The cross sections for the electron-impacts processes involved agree normally very well between authors, apart perhaps for the  $N_2(C^3\Pi_u)$  state which peak excitation cross section is  $9.75 \cdot 10^{-17} \text{cm}^2$  according to [Phelps and Pitchford, 1985] and  $3.86 \cdot 10^{-17} \text{cm}^2$  according to [Tabata et al., 2006]. The latter reference being more recent, was preferred. The excitation cross section for argon  $2p_1$  state differs also significantly according to [Boffard et al., 2007] or to [Hayashi, 2003]. The former was chosen as it was obtained from emission measurements.

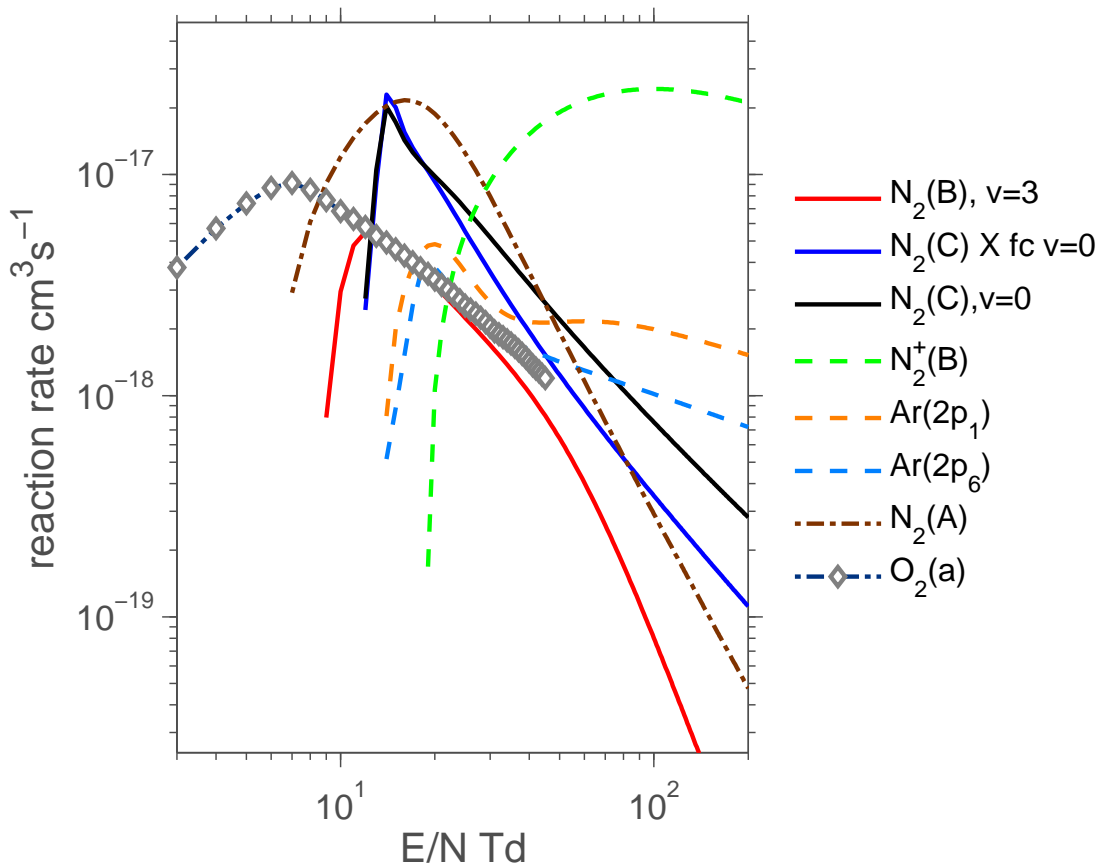


Figure 2.6: Excitation cross sections by electron-impact for the production of excited species listed in table 2.2.

The reaction rates were computed for several reduced electric fields (from 1 to 1500 Td) with the freeware Bolsig+ [Hagelaar and Pitchford, 2005] and a fit has been performed (facility of Bolsig+) which takes the form:

$$K_i = \exp \left( A + B \cdot \ln(E/N) + \frac{C}{E/N} + \frac{D}{(E/N)^2} + \frac{E}{(E/N)^3} \right)$$

The computations were performed with the cross sections available in Bolsig+'s package [Phelps and Pitchford, 1985] with the exception of the cross sections for electronic excitation described in table 2.2 which have been used instead.

### 2.4.2 Reduced electric field and active species determination

If equation 2.19 describes correctly the evolution of excited species, the experimental determination of E/N in a gas discharge can be performed by comparing the relative population of excited species. Indeed, by dividing two equations such as 2.19 applied for two different transitions, the electron density simplifies and as a result, equation 2.20 is obtained in which only E/N is unknown.

$$\frac{X_j n_i \tau_j}{X_i n_j \tau_i} = \frac{K_i(E/N)}{K_j(E/N)} \quad (2.20)$$

In [Paris et al., 2005], the ratio of excited species is compared directly to the known applied electric field, and provide a formula that fits the experimental data. This method is straightforward and does not depend on reaction rates, a Boltzmann solver or quenching rates (at atmospheric pressure). However, in [Paris et al., 2005], the ratio of intensities is determined for two different vibrational bands of the SPS to the first vibrational band of the FNS. This feature is most interesting in the framework of streamer dynamics due to the possibility to perform the measurement of intensity ratio in a single measurement. If the ( $v'=2-v''=5$ ) band of the SPS is chosen instead of the (0-0) band, possible overpopulation by vibrational relaxation is possible. In order to take into account the vibrational relaxation, the collisional radiative model for  $N_2(C^3\Pi_u)$  should be updated to equation 2.21.

$$\frac{dn_v}{dt} = n_e N_2 q_{X,0 \rightarrow C,v} K(E/N) - \frac{n_v}{\tau_v} + \sum_{w=v+1}^4 k_{wv} N_2 n_w \quad (2.21)$$

Where  $k_{wv}$  is the vibrational relaxation rate of the vibrational level  $w$  to the vibrational level  $v$ . The relaxation rate constants are taken from [Dilecce et al., 2007]. The ratio of vibrational states normalized to the first vibrational state is shown in figure 2.7. The change of the relative value is important when the steady state is compared to the Franck-Condon factors, and increases with pressure. It is also independent of the reduced electric field and of the electron density. That means the reduced electric field estimated with the ratio of  $N_2^+(B^2\Sigma_u^+, v=0)$  to  $N_2(C^3\Pi_u, v=2)$  will be underestimated by a factor up to 1.64 for the case of short pulses if it is computed using Paris's method. Even in the pulsed case of [Paris et al., 2004], where the discharge was excited by a pulsed laser of 33 ns half-width duration, the  $N_2(C^3\Pi_u)$  vibrational states have time to equilibrate. This observation also explains the pressure-dependent behavior of the ratio 391/394 of Paris, which was unexplained. To summarize, the method of [Paris et al., 2005]

can be applied provided only the first vibrational bands are used, in the context of temporal variations faster than about 5 ns. There is also a contribution from vibrational relaxation to the first vibrational state, which could affect both the experimental and the theoretical method. The overestimation can be computed as 1.0696 times higher than without vibrational relaxation at atmospheric pressure, which is well below than the typical error associated with such methods. The same effect is of course affecting the  $N_2^+(B^2\Sigma_u^+, \nu = 0)$  state, but is believed to be even smaller owing to the small Franck-Condon factors of the vibrational states  $\nu > 0$ . This effect for the  $N_2(B^3\Pi_g)$  state should be the largest, but its evaluation was not possible due to the lack of experimental data available in the literature on vibrational relaxation of this state.

The population of the  $N_2(B^3\Pi_g, \nu = 2 - 4)$  states can also be influenced by the  $N_2(A^3\Sigma_u^+, \nu = 7 - 12)$  states and by the  $N_2(W^3\Delta_u, \nu = 1 - 5)$  as discussed in [Benesch and Fraedrich, 1984, Bachmann et al., 1992, Kirillov, 2008] and is therefore difficult to model accurately.

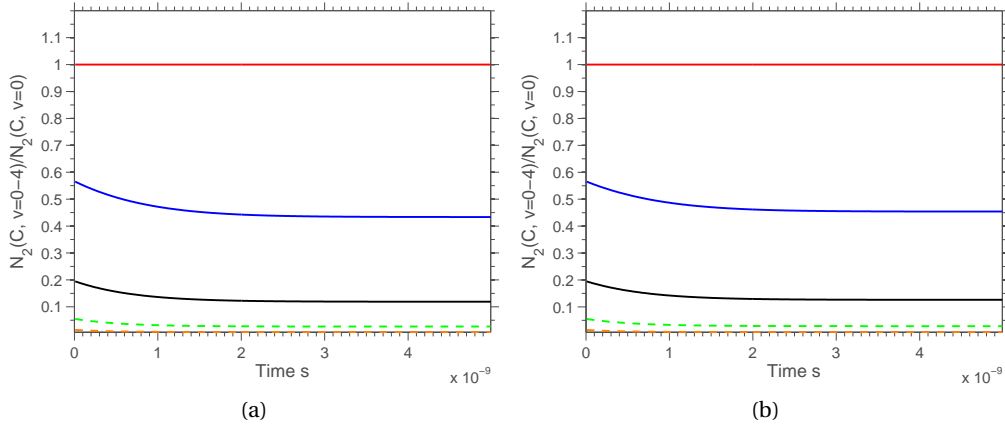


Figure 2.7: Ratio of vibrational populations  $N_2(C^3\Pi_u, \nu = 0 - 4)$  normalized to  $N_2(C^3\Pi_u, \nu = 0)$  corresponding to the red, blue and black solid lines and to the green and orange dash-dotted lines respectively. Computation performed for a constant reduced electric field of 700 Td. Vibrational relaxation taken into account (a) and vibrational relaxation not taken into account (b).

If the plasma is rapidly varying in time and/or inhomogeneous, equation 2.20 must be integrated over the spatial resolution of the optical system, taking into account its sensitivity, and for the duration of light collection chosen for the experiment. In the case of streamers, the plasma passes in front of the optical system and the light recorded presents itself in the form of a pulse. If the light is collected for a sufficiently long duration in order to capture the whole pulse, then equation 2.20 can be integrated in time to remove the temporal dependence. The equation reads then 2.22:



$$\frac{\int_{-\infty}^{\infty} \int_{\Omega} T n_i d\Omega dt}{\int_{-\infty}^{\infty} \int_{\Omega} T n_j d\Omega dt} = \frac{\Delta\Omega \bar{n}_i}{\Delta\Omega \bar{n}_j} = \frac{\tau_i X_i K_i(\hat{E})}{\tau_j X_j K_j(\hat{E})} \quad (2.22)$$

where  $\Omega$  is the volume of the discharge and  $T$  is the optical response factor of the optical system.  $\bar{n}_i$  is the time and space averaged excited population species, with  $\Delta\Omega$  the volume.  $\hat{E}$  represents an average reduced electric field for the whole pulse, taking into account also variations of the electron density. Once the reduced electric field strength is evaluated, the averaged electron density can be evaluated, provided that the system is properly calibrated in intensity (equation 2.23).

$$\bar{n}_e = \frac{\bar{n}_i}{\tau_i X_i K_i(\hat{E})} \quad (2.23)$$

This electron density is representative of the streamer head, where the excited species are produced.

To compute these averages, the assumption was made that the excited species density reaches zero after a short time  $t_{max}$  due to the strong quenching, which in practice is of the order of 50 ns. If the reverse situation of no significant quenching is assumed to occur, which is representative of metastable states, then the estimate becomes:

$$\frac{\int_0^t \int_{\Omega} T \frac{\partial n_i}{\partial t} + \frac{n_i}{\tau_i} d\Omega dt}{\int_0^t \int_{\Omega} T \frac{\partial n_j}{\partial t} + \frac{n_j}{\tau_j} d\Omega dt} = \frac{X_i K_i(\hat{E})}{X_j K_j(\hat{E})}$$

if the  $i$ 's state is assumed to be metastable, and state  $j$  is assumed to quench rapidly, then the previous equation becomes 2.24:

$$\bar{n}_i(\Delta t) = \frac{X_i K_i(\hat{E})}{X_j K_j(\hat{E})} \frac{\bar{n}_j \Delta t}{\tau_j} \quad (2.24)$$

where the  $\bar{\phi}$  is the spatial average of the function  $\phi$ . The determination of the density of non-radiating species can therefore be evaluated by recording the light emitted by radiating excited species.

Another estimate for the electron density is based on the assumption that the reduced electric field and the electron density can be approximated by exponentials of a one-dimensional variable representing the direction of propagation of the plasma. The developments are presented in section 4.5.

The electron density is estimated with this approximation with equation 2.25.

$$N_{e0} = \frac{\bar{n}_i}{\tau_i \left( \int_0^{x_{\max}} \exp(-sx) X_i K_i(E_0 \exp(x)) dx / x_{\max} \right)} \quad (2.25)$$

where the parameters  $E_0$  and  $s$  are determined from two equations involving ratios of transitions such as equation 2.20.

These approximations will be assessed in section 4.4 with a numerical simulation of the plasma.

## 2.5 Optical emission spectroscopy

### 2.5.1 Introduction

When recording the emission spectrum from a gas, generally displayed on an intensity (arbitrary units) vs wavelength [nm] graph, it is not straightforward to determine which emitter contributes to a particular spectral region of the recorded emission spectrum. Indeed, there is often more than one radiating species emitting in the same spectral range. In addition, there is a broadening and a shifting of the lines due to instrumental finite resolution or to physical reasons (Stark shifting and broadening, Doppler broadening, etc). Moreover, due to the resolving power of the spectrograph, it is not always possible to separate two lines (narrow peaks in the spectrum) from one another because they will appear “merged” in the spectrum.

If the rotational energy levels are at equilibrium, it is possible to relate the intensity emitted by every rotational line within a vibrational band with the number of species being in that particular vibrational state. If vibrational energy levels are also at equilibrium, it is possible to relate the intensity of every vibrational band within a system (electronic transition) to the number of species in that electronic transition. If the plasma is completely at equilibrium (LTE), it is then possible to relate the intensity of every electronic transitions with the number of species present in the gas.

In the case of a non-equilibrium cold plasma, only the assumption of rotational equilibrium is reasonable. Therefore, it is necessary to simulate separately the emission spectrum due to a single vibrational band for a particular electronic transition and compare them with the experimental emission spectrum in order to determine the amount of species in a particular vibrational level present in the gas. This was one of the motivations to develop an in-house

spectral code.

## 2.5.2 Spectra of Diatomic Molecules: Basic Concepts

### Introduction and nomenclature

The light recorded by a spectrometer or by the eye is the sum of many photons emitted from particles undergoing a **transition** from one energetic **state** (quantum configuration) to a less energetic state. The excess amount of energy is ejected from the system as a photon.

The energy of one atom or several bounded atoms (a molecule) is quantized, that is to say the energy can take only discrete values. The photon emitted will therefore have only a quantized amount of energy, which correspond to quantized frequencies ( $E_{\text{ph}} = h\nu$ ,  $\nu$  being the frequency and  $h$  Planck's constant).

The energy levels (or just levels) in which a diatomic molecule can be separated are:

- The electronic energy  $T_e$  (tens of thousands of  $\text{cm}^{-1}$ <sup>4</sup>)
- The vibrational energy  $G_v$  (thousands of  $\text{cm}^{-1}$ )
- The rotational energy  $F_j$  (a few  $\text{cm}^{-1}$ )

which can be summarised as, in wave-number units  $T = \frac{E_{\text{ph}}}{100hc}$  [ $\text{cm}^{-1}$ ]:

$$T = T_e + G_v + F_j$$

Two elements are necessary to determine the spectra emitted by diatomic molecules. First the frequency at what a particular transition occurs (its "location"), then the **intensity** at which it radiates (the "power" emitted). To determine both elements is very important in order to identify the features of the measured spectrum with a particular concentration of species at a particular condition (temperature, density, etc.).

The knowledge of the **electronic state** (also called **electronic configuration**) in which the molecule is before undergoing a transition to a lower energy state is important to determine its properties. The difference in energy between the electronic configurations of the upper and lower state determines the amount of emitted energy during the transition. This determines the frequency of the light emitted, also called *line*, corresponding to this transition.

<sup>4</sup>a  $\text{cm}^{-1}$  is an energy unit used in spectroscopy which is equal to  $1.239842 \cdot 10^{-4}$  [eV]

## Chapter 2. Plasma Physics

---

To determine the intensity of the transition, it is necessary to know what is the probability for the transition to occur. Indeed, the higher the probability is, the higher the number of spontaneous transitions per time unit will occur.

The number of transitions is proportional to two quantities. The probability for the transition to occur and the number of molecules in the upper state.

The probability of occurrence of a transition is determined through quantum mechanical calculations and the probability of having a certain number of molecule in the upper state is described by statistical considerations, if the energy levels in question are said to be at *thermal equilibrium*. Most of the time, the rotational levels are assumed to be in equilibrium with translational levels.

The electronic configurations are designated according to the quantum numbers characterizing them, such as:

- The *principal quantum number*,  $\Lambda$ , which is the projection of the electronic orbital angular momentum  $\vec{L}$  on the internuclear axis, and which values can be 0, 1, 2, ... and are represented by the Greek letters  $\Sigma$ ,  $\Pi$ ,  $\Delta$ , etc. in analogy with the states s, p, d, etc. of an atom.
- The spin  $S$ , which is the sum of the spins of all electrons in the molecule, it can have the values  $0, \frac{1}{2}, 1, \frac{3}{2}, 2, \dots$

These two quantities ( $\Lambda$ ,  $S$ ) can interact (they are then **coupled**) and form slightly different states with very slightly different energy levels (splitting).

### Determination of the rotational lines

The energy associated with an electronic configuration is computed via quantum mechanics. It is generally available in the literature (see the table at the end of [Herzberg, 1950]), and will not be discussed here.

The vibrational states of a molecule can be described as an anharmonic oscillator. The upper electronic state can be in any vibrational state and the transition can occur to any vibrational state of the lower electronic state. The energy levels are located in the spectral domain according to the following formula (see [Herzberg, 1950]):

$$G = \omega_e \left( v + \frac{1}{2} \right) - \omega_e x_e \left( v + \frac{1}{2} \right)^2 + \omega_e y_e \left( v + \frac{1}{2} \right)^3 \quad (2.26)$$

Where  $\nu$  is the vibrational quantum number having values 0, 1, 2, 3, ... and  $\omega_e$ ,  $x_e$  and  $y_e$  are physical constants describing the quantum oscillator.

The rotational states can be described as a quantum rotator (symmetric top) which energy spacing can be calculated by (same reference):

$$F = B_\nu J(J+1) - D_\nu J^2(J+1)^2 \quad (2.27)$$

Where  $J$  is the rotational quantum number having values 0, 1, 2, 3, ... and  $B_\nu$  and  $D_\nu$  are physical constants describing the quantum rotator. The subscript  $\nu$  reflects the fact that the rotational constants B and D are dependent on the vibrational state of the upper state.

Combining these formula with the electronic energies corresponding to each configuration of the transition between an upper state (prime) and a lower state (double prime), we obtain:

$$T' - T'' = T'_e - T''_e + G' - G'' + F' - F''$$

This gives rise to several groups of lines regularly spaced, forming the **bands** structure typical of vibrational-rotational spectra.

For the purpose of simulating the band structure of the spectrum, it is not always necessary to take into account all details. Therefore, it is sufficient to retain only the first order terms in the preceding formula:

$$\begin{aligned} T' - T'' &= T'_e - T''_e + G' - G'' + F' - F'' \\ G' - G'' &= \omega'_e(v' + \frac{1}{2}) - \omega''_e(v'' + \frac{1}{2}) \\ F' - F'' &= B'_\nu J'(J' + 1) - B''_\nu J''(J'' + 1) \end{aligned} \quad (2.28)$$

The selection rules to determine which rotational transition is allowed are determined from quantum mechanical considerations, the results being:  $\Delta J = 0, -1, +1$ . That means that only transitions with  $\Delta J = J' - J''$  equal to  $-1, 0, 1$  are possible. This corresponds to three *rotational branches* R, Q and P.

### Intensity of the rotational lines

The power emitted per unit volume by the spontaneous radiative transition from an upper  $J'$  level to a lower  $J''$  level is defined by the following formula (see [Laux, 2002] for example):

$$\epsilon(\nu) = \frac{1}{4\pi} n_{e'v'J'} A_{e'v'J'-e''v''J''} h\nu_{e'v'J'-e''v''J''}$$

in  $[\text{W m}^{-3} \text{ sr}^{-1}]$ .

Where  $n_{e'v'J'}$  is the density of particles in the upper state in  $[m^{-3}]$ ,  $\nu_{e'v'J'-e''v''J''}$  is the frequency of the light emitted during the transition in  $[s^{-1}]$ .  $A_{e'v'J'-e''v''J''}$  is the emission coefficient (also called Einstein coefficient) in  $[s^{-1}]$ , representing the probability of transition per second. It can be decomposed in (from [Laux, 2002], [Schadee, 1978] and [Whiting et al., 1980]):

$$A_{e'v'J'-e''v''J''} = \frac{S_{J'J''}}{(2J'+1)(2-\delta_{0,\Lambda'+\Lambda''})(2S+1)} A_{v'v''}.$$

$A_{v'v''}$  is the vibrational emission coefficient, it is the probability of transition from a vibrational upper state to a vibrational lower state, irrespective of the rotational state. The factor  $S_{J'J''}$  is the probability that a transition occurs between two rotational states, irrespective of the vibrational state, it is called the **rotational line strength** [Laux, 2002]. The other terms are statistical weighting factors accounting for the sub-states within a rotational state.

The expression for  $A_{v'v''}$  is [Schadee, 1978] and [Gilmore et al., 1992]:

$$A_{v'v''} = \frac{64\pi^4 \nu_{v'v''}^3}{(4\pi\epsilon_0)3hc^3} \frac{(2-\delta_{0,\Lambda'+\Lambda''})}{(2-\delta_{0,\Lambda'})} q_{v'v''} |R_e|^2$$

Where  $q_{v'v''}$  is the Franck-Condon factor (dimensionless),  $R_e$  is the electronic transition moment in  $[Cm]$ ,  $\nu$  is the band origin frequency in  $[s^{-1}]$ .

The intensity is then [Whiting et al., 1980]:

$$\epsilon = \frac{1}{4\pi} n_{e'v'J'} \frac{S_{J'J''}}{(2J'+1)(2-\delta_{0,\Lambda'+\Lambda''})(2S+1)} A_{v'v''} h\nu_{e'v'J'-e''v''J''}$$

**Effect of nuclear spin** In order to obtain the correct expression for the emission of rotational lines, it is necessary to take into account the parity properties of the molecules. Additional selection rules apply arising from the interaction between the nuclear spin and the electron wavefunctions. The intensity will be affected in a significant way. To be more specific, these additional selection rules affect the intensity of lines usually in the form of an alternation, every other line is either weaker than the previous or even totally absent. Because of the complicated way of finding the proper alternating factor for every type of transition, it has been chosen to implement this alternation factor for each electronic transition manually,

using the parity properties summarized in [Herzberg, 1950] p.135, p.247 and p.271 for example.

The alternation factor is thus  $Altern(I, J) = \frac{(I+1)}{2I+1} = \frac{2}{3}$  for even  $J$  and  $Altern(I, J) = \frac{I}{2I+1} = \frac{1}{3}$  for odd  $J$  ( $I$  being the nuclear spin, = 1 for molecular nitrogen) for the transition  $N_2^+(B^2\Sigma_u^+ - X^2\Sigma_g^+)$  and no alternation for  $N_2(C^3\Pi_u - B^3\Pi_g)$ .

If we assume moreover that the frequency does not vary significantly over the band, we find the expression for the intensity of a rotational line:

$$\epsilon = \frac{1}{4\pi} n_{e'v'} \frac{S_{J'J''}}{(2J'+1)(2-\delta_{0,\Lambda'+\Lambda''})(2S+1)} A_{v'v''} h\nu_{e'v'-e''v''} Altern(I, J)$$

If the rotational levels are at thermal equilibrium, that is, they follow a Boltzmann distribution, the population of the  $J$ -th rotational level is proportional to  $n_J = n_{e'v'} \frac{(2J+1)}{Q_r} e^{-\frac{B_v hc J'(J'+1)}{kT}}$ , where  $Q_r$  is the rotational partition function.  $Q_r \cong \frac{kT}{hcB_v}$  if the temperature is sufficiently high (see [Tatum, 1967] for more details). The intensity takes then the form:

$$\epsilon = \frac{1}{4\pi} n_{e'v'} \frac{S_{J'J''}}{(2-\delta_{0,\Lambda'+\Lambda''})(2S+1)\sigma Q_r} A_{v'v''} h\nu_{e'v'-e''v''} e^{-\frac{B_v hc J'(J'+1)}{kT}} Altern(I, J) \quad (2.29)$$

### 2.5.3 Spectra of Diatomic Molecules: Finer Details

This section is based on the books by Kovács [Kovacs, 1969] and Herzberg [Herzberg, 1950].

#### Modelling of a diatomic molecule

To model the energy levels and electronic functions of a diatomic molecule, several choices are possible. One of them ([Hougen, 1970], or [Kovacs, 1969], for Hund's coupling case a) consists of a molecule-fixed coordinates, where the  $z$  axis (or zeta axis) is fixed along the internuclear axis. In this framework, the equations to be solved to correctly predict the behavior of the system composed of the two nuclei and of one or more electrons, is the time-independent Schrödinger equation. To make the computation tractable, several simplifications and assumptions are made. The first is the assumption that the motion of the nuclei is not affected (or slightly affected) by the motion of electrons (Born Oppenheimer approximation). This means that the vibrational and rotational motion of the molecule are considered to be unaffected by the motion of electrons.

Note however that the motions of electrons are still coupled to the motion of the nuclei. This will usually be taken into account with a parameter being the internuclear distance  $r$  (at equilibrium) for vibrational motion and rotational angular momentum for rotational motion.

Schrödinger equation defines how the probability function for a certain object to be at a certain location in space (not in time, because the time-independent Schrödinger equation is applied) evolve under the action of potential and kinetic energy. The operators found in this equation are hence applied to a standing wave-like function, which will have different modes associated with different quantum numbers. These quantum numbers are simply the eigenvalues of the equation divided by a constant (ex:  $J$  is the quantum number associated to the eigenvalue  $\hbar J$ ), to which a particular eigenfunction corresponds.

If a quantum number is said to be “good” [Hougen, 1970], that means that the eigenfunction associated with it is an eigenfunction of a particular operator. For example,  $\Lambda$  is said to be a good quantum number if the function associated with it is also the eigenfunction of the operator of resultant angular momentum of electrons,  $L_z$ . The usage of good quantum numbers can thus greatly simplify the calculation, as every “good” operator can be replaced by its eigenvalue, a scalar.

**Hund’s coupling cases** In the coordinates chosen the so called Hund’s coupling case a) is describing a particular case of a molecule in which the resultant orbital angular momentum of the electrons  $\vec{L}$  (the sum of the angular momenta of the electrons in a molecule) is strongly coupled to the internuclear axis (the vector  $\vec{L}$  is rotating with the molecule) and in which the resultant spin momentum  $\vec{S}$  (the sum of the spins of the electrons) is also strongly coupled to the internuclear axis because of the electromagnetic interactions between  $\vec{L}$  and  $\vec{S}$ . Hund’s case b) is characteristic of a decoupling of the resultant spin from the internuclear axis.

In case a),  $\vec{L}$  will precess<sup>5</sup> about the internuclear axis because of the electric field and thus cannot be taken as a constant quantity describing the state. Instead, its projection on the internuclear axis  $\Lambda$  is used as a quantum number ( $\hbar\Lambda$  is the eigenvalue of the operator  $L_z$ ). The same will happen also for the resultant spin, but the precessing is due to the magnetic field created by  $\vec{L}$  rather than by the electric field due to the nuclei (see for example Kovács p.25). The quantum number  $\Sigma$  is the projection of  $\vec{S}$  onto the internuclear axis and it is the quantum number associated with the operator  $S_z$  in the Schrodinger equation.

---

<sup>5</sup>Precession is the motion of an angular momentum vector under the action of a force (Herzberg p.116 [Herzberg, 1950])



### Singlet states rotational energies

In a molecule with angular momentum different from zero and zero spin, solutions for the energy levels of different modes of rotation (rotational modes) are known to be the solution of the so called **symmetric top**. The symmetric top models a system comprised of two large mass in revolution and a non zero moment of inertia on the axis. In the actual molecule, these are the inertia due to the two nuclei and the inertia due to the electrons (the order of magnitude of the angular momentum is, however, the same due to the high velocity of the electrons, [Herzberg, 1950] p.115). This simple system has the following eigenvalues:

$$B[J(J+1) - \Lambda^2] \quad (2.30)$$

where  $B$  is the rotational constant and  $J$  is the rotational quantum number ([Kovacs, 1969] p.21 for example). This expression is similar to the first terms in 2.27. The vector  $\vec{J}$  is equal to  $\vec{R} + \vec{\Lambda} + \vec{S}$  (case a) that is to  $\vec{R} + \vec{\Lambda}$  in this case (singlet state). This quantum number can take the values  $J = |\Lambda|, |\Lambda| + 1, \dots$ . If the energy associated with the electronic configuration and vibrational level is known, the total energy of the rotational level can be determined.

### Multiplet states rotational energies

The resultant spin vector  $\vec{S}$  can be coupled more or less strongly to the orbital angular momentum, and therefore to the internuclear axis (in Hund's case a)). Because of this interaction (a magnetic field created by the orbital motion of the electrons), the spin will also precess about the internuclear axis. The projection of the spin on the internuclear axis will therefore represent best a constant of the motion than the spin itself. It can take only the quantised values:  $\Sigma = S, S-1, \dots, -S = 2S+1$ . Depending on how the spin combines to the orbital angular momentum, the value of the projection of  $\vec{L}$  and  $\vec{S}$  will change (see figure in [Herzberg, 1950] p.215), and with it, the total angular momentum  $\vec{J}$  as well. That means that for the same magnitude of the vectors  $\vec{L}$  and  $\vec{S}$ , there will be a different total angular momentum and therefore a different rotational energy. This phenomenon is known as spin splitting because the energy level is "split" into  $2S+1$  levels with slightly different energies. The formula giving as a first approximation the splitting of the terms is ([Herzberg, 1950] p.215):  $T_e = T_0 + A\Lambda\Sigma$  where  $A$  is a constant for a given multiplet term and is called the spin-orbit coupling constant (as an example, it is  $42.253 [cm^{-1}]$  for  $N_2(B-A)$  transition).

Further, if a more accurate value for the term multiplet is needed, it is possible to take into account the effect of spin-spin interaction and spin-rotation interaction, which are respectively giving rise to the terms  $\epsilon[3\Sigma^2 - S(S+1)]$  and  $\gamma[\Sigma^2 - S(S+1)]$ , as well as centrifugal terms, which are of relatively small magnitude.

For a non-sigma state ( $\Lambda \neq 0$ ), the spin-spin coupling can give rise to a lambda-type doubling, which intensity is proportional to the spin ( $\propto \alpha S(S+1)$ ). All formula are taken from [Kovacs, 1969] and are also summarized in [Hornkohl et al., 2005].

### States intermediate between Hund's coupling case a) and b)

So far, the multiplet energy values corresponding to pure Hund's coupling case can be computed (only the formulae for case a) have been given here). However, a pure Hund's coupling case is rarely representative of a real state. Therefore, it is necessary to take into account the effects of the terms arising whenever the assumptions for the coupling case do not hold strictly. This is realised with a perturbation method, which yields very good results for molecular transitions that can be described by a coupling case intermediate between a) and b).

The whole idea to find the correct eigenfunctions with the perturbed Hamiltonian, is to write the eigenfunctions as a linear combination of basis functions (Kovacs p.48) which then are multiplied by their conjugate and integrated over the configuration space to find either the energy of the mode (a scalar) or either zero (orthogonal functions).

$$\begin{aligned}\langle \Lambda S \Sigma | H_0 | \Lambda' S' \Sigma' \rangle &= 0 \\ \langle \Lambda S \Sigma | H_0 | \Lambda S \Sigma \rangle &= E_{\Lambda S \Sigma}\end{aligned}$$

This will give rise to a matrix equation which elements are computed by solving a problem of the form  $\langle \Lambda S \Sigma | H_0 + H_{\text{perturbed}} | \Lambda' S' \Sigma' \rangle$ , involving basis functions and the perturbed Hamiltonian, which is easily solved (eigenvalue problem). An example with a state characterised by  $\Lambda = 1$  and  $S = 1/2$ :

$$\begin{pmatrix} \langle 1, 0.5, 1/2 | H_0 + H_p | 1, 0.5, 1/2 \rangle & \langle 1, 0.5, 1/2 | H_0 + H_p | 1, 0.5, -1/2 \rangle \\ \langle 1, 0.5, -1/2 | H_0 + H_p | 1, 0.5, 1/2 \rangle & \langle 1, 0.5, -1/2 | H_0 + H_p | 1, 0.5, -1/2 \rangle \end{pmatrix} \begin{pmatrix} \alpha \\ \beta \end{pmatrix} = \begin{pmatrix} E_{1,0.5,1/2} \\ E_{1,0.5,-1/2} \end{pmatrix} \quad (2.31)$$

The diagonal terms of this equation are the energies associated with the basis functions and the non-diagonal terms are responsible for the coupling of two basis functions, which allows to describe accurately a state intermediate between case a) and b). Thus, the eigenvalues of this equation are the energy levels of the (real) state characterised by  $\Lambda, \Sigma$ .

To summarise, the terms forming the effective Hamiltonian matrix  $H_{eff}$  to compute the

rotational energy levels are:

$$B_v[J(J+1) - \Omega^2 + S(S+1) - \Sigma^2] + A_v\Lambda\Sigma + \epsilon_v[3\Sigma^2 - S(S+1)] \quad (2.32)$$

for diagonal terms and

$$B_v([J(J+1) - \Omega(\Omega+1)][S(S+1) - \Sigma(\Sigma+1)])^{1/2} \quad (2.33)$$

for non-diagonal terms.

The matrix 2.34 shows an example of the matrix diagonalised for the computation of a  $^3\Pi$  state's lines and rotational factors ( $\Lambda = 1$ ,  $S = 1$  thus  $\Sigma = -1, 0, 1$  and  $\Omega = 0, 1, 2$ ).

$$H_{eff} = \begin{pmatrix} B_v[J(J+1) + 1] - A_v + \epsilon_v & B_v(2J(J+1))^{1/2} & 0 \\ B_v(2J(J+1))^{1/2} & B_v[J(J+1) + 1] - 2\epsilon_v & B_v(2[J(J+1) - 2])^{1/2} \\ 0 & B_v(2[J(J+1) - 2])^{1/2} & B_v[J(J+1) - 3] + A_v - \epsilon_v \end{pmatrix} \quad (2.34)$$

### Rotational intensity factors

To compute the intensity of a rotational line, the probability of the transition between two states must be computed. This computation involves the eigenfunctions characterizing the states before and after the transition ( $\Psi_{upper}$  and  $\Psi_{lower}$  in emission) and an operator  $R$ , characterizing the physical interaction which couples the two states  $\text{Probability} = \int \Psi_{lower}^* R \Psi_{upper}$ .

It is thus necessary to determine the eigenfunctions. These eigenfunctions can be written as a product of eigenfunctions characterizing the electronic state of the fixed-molecule, its vibrational state and its rotational state.

The two formers can be computed and are available in the literature ([Gilmore et al., 1992], [Laux, 2002], [Nicholls et al., 2001] or [Laux et al., 2003]).

The probability for the transition between rotational states in pure coupling case a) can be computed exactly, as depicted in [Hougen, 1970]. Whiting (see [Whiting and Center, 1973] or [Whiting and Nicholls, 1974]) has developed a computer code based on the method described in [Hougen, 1970] by Hougen to compute the real state's rotational transition probability.

It uses basis functions characteristic of Hund's coupling case (a) and (c) to compute transition probability for either spin allowed ( $S' = S''$ , characterized by basis functions (a)) or spin forbidden ( $S' \neq S''$ , characterized by basis functions (c)) transitions. To find the correct way to mix the basis state to form a real state 2.31, the matrix of the transformation matrix

that diagonalizes the basis functions' Hamiltonian to transform the rotational matrix. If all probabilities corresponding to basis function are grouped in a **rotational matrix**, this matrix can be transformed by the transformation matrix and give the rotational transition probability corresponding to the real state. This method was already used by Kovács [Kovacs, 1969] but the difference here is that the diagonalization is performed numerically, which simplifies considerably the procedure and removes the need for approximations, introduced to make analytical calculations tractable.

The code briefly described in [Hornkohl et al., 2005] applies this principle to find eigenfunctions characteristic of the upper and lower states of a transition, then uses them to find a transformation matrix which enables to pass from the basis function representation to the real function representation of the multiplets terms. This is used further to transform the rotational matrix which takes into account the effect of rotation on the transition probability for each multiplet term which is a diagonal matrix for spin allowed transitions.

The rotational matrix, for spin allowed transitions, is:

Table 2.3: Rotational matrix elements, in function of the quantum number  $\Omega$

R Branch	Q Branch	P Branch
$\frac{2[(J+\Omega)(J-\Omega)]^{\frac{1}{2}}}{[4J]^{\frac{1}{2}}}$	$\frac{2\Omega}{[4J(J+1)/(2J+1)]^{\frac{1}{2}}}$	$\frac{2[(J+1+\Omega)(J+1-\Omega)]^{\frac{1}{2}}}{[4(J+1)]^{\frac{1}{2}}}$

The rotational intensity factor is then :

$$\langle S_{J'J''} \rangle = q_{v'v''} R_e^2 |T'^{-1} \langle \phi'_a | \alpha | \phi''_a \rangle T''|^2$$

Where  $q_{v'v''}$  is the Franck-Condon factor,  $R_e$  is the electronic transition moment,  $T'$  and  $T''$  are the upper and lower transformation matrices, formed with the eigenvectors of the corresponding Hamiltonians.  $\phi'_a$  and  $\phi''_a$  are Hund's case (a) basis eigenfunctions.

The code proposed by Hornkohl [Hornkohl et al., 2005] uses also directly the eigenvalues of the perturbed matrix to find the location of the lines, which is very efficient as it is a completely automated process and permits to avoid mistakes in the transcription of analytical formula.

The code developed in this work uses a slightly simplified method:  $\Lambda$  type doubling is not taken into account (apart for the FPS) and it is restricted to spin-allowed transitions. Also, it is not suited for polarized radiation.

Atomic transitions are modeled within the code, each term of a multiplet being computed separately. The intensity  $\epsilon$  is linked to the density of excited atoms  $n$  by:

$$\epsilon(\nu) = \frac{1}{4\pi} n A_{u-1} h \nu_{u-1}$$

with  $A_{u-1}$  representing the emission coefficient.

The slit function used to convolve the rotational and atomic lines was assumed to be a gaussian. The full width at half maximum (FWHM) is used to determine its width.

**Comparison with Specair** The comparison of a fitted spectrum computed with the present in-house code with the fit obtained using the software Specair [Laux, 2002] using the same resolution is shown in figure 2.8. The parameters used for the fit in Specair were:  $T_e = 7900 K$ ,  $T_{rot} = T_{trans} = 300 K$  and  $T_{vib} = 3000$ , and the mole fractions were  $[N_2] = 0.88$  and  $[N_2^+] = 6.5 \cdot 10^{-6}$ . The slit function was triangular with a base of 0.6 nm. No better fit could be performed with Specair. This is due to the non-equilibrium vibrational distribution function. The non-equilibrium of the vibrational levels is one of the reasons for the development of an in-house spectral code, as stated above, in order to allow for vibrational-specific population densities to be determined.

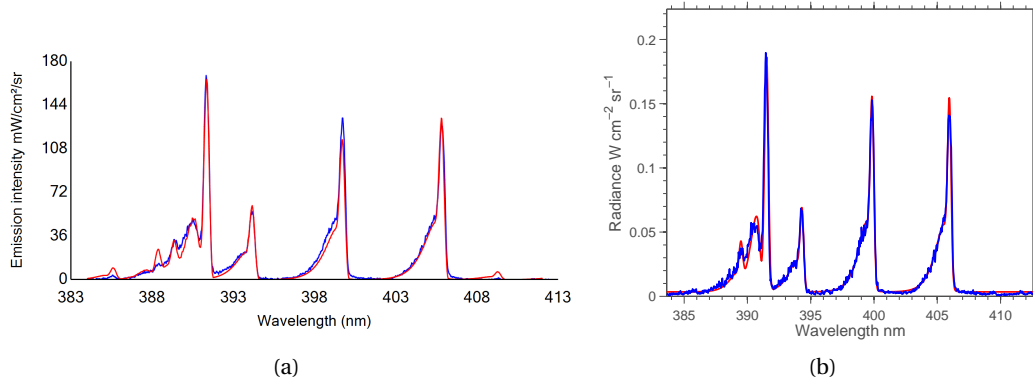


Figure 2.8: Fit (red solid line) of a typical experimental spectrum (blue solid line) using Specair (units are in  $mWcm^{-2}sr^{-1}$ ) (a) and the in-house code (b).

If the vibrational temperature in Specair is set to 200 (a low value), then only the first band of each electronic transition will occur. The following spectrum was obtained: The other temperatures were set to  $T_e = 7700 K$ ,  $T_{rot} = T_{trans} = 300 K$ , and the mole fractions were  $[N_2] = 0.88$  and  $[N_2^+] = 6.5 \cdot 10^{-6}$ .

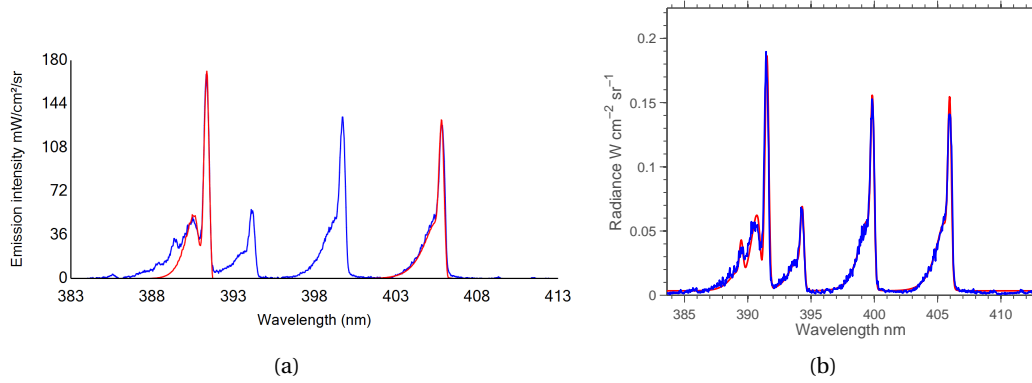


Figure 2.9: Fit (red solid line) of a typical experimental spectrum (blue solid line) using Specair (a) and the in-house code (b).

Table 2.4: Comparison of population densities in  $\text{cm}^{-3}$  as computed with Specair and the in-house code.

Species	Specair	in-house code
$\text{N}_2(\text{C}^3\Pi_u, v = 0)$	$8.39 \cdot 10^{13}$	$8.29 \cdot 10^{13}$
$\text{N}_2^+(\text{B}^2\Sigma_u^+, v = 0)$	$8.54 \cdot 10^{12}$	$8.31 \cdot 10^{12}$

## 2.6 Conclusions

The basic properties of electrical discharges were reviewed. Similarity laws for gas discharges were presented and showed that two parameters have to be kept constant in order to have a similar discharge, namely the reduced electric field  $E/N$  and the pressure times distance product  $p \cdot d$ . The breakdown of gases by the Townsend and streamer mechanism was described, with an emphasis on the criterion for streamer breakdown. In the next section, the physical model for the description of the plasma was depicted. The drift-diffusion approximation for the transport of the charged species was described. The two-term approximation for Boltzmann's equation for the electrons and the LFA approximation which replaces the energy equation were presented. A short analysis of the validity of these approximation was made, and showed that they were correct provided that the size of the plasma considered is not too small. The different kinetic processes used by different authors in the literature were reviewed, and showed large differences notably in the ionization coefficient, at very high reduced electric fields. In the fourth section, the diagnostics of the plasma was discussed. The reasoning behind the choice of the diagnostic method to be used was presented. It showed that the use of optical methods were the most suited for the diagnostics of the plasma. The formation and decay of excited species, together with the data from the literature necessary for the calculation of their populations was described. The method used during this thesis to determine the reduced electric field and averaged quantities such as the electron density

was presented. In the fifth section, the theory necessary to understand the modelling of the spectra emitted by excited species was presented. The approximation made and the method to compute the different parameters were explained. These calculations were implemented in a numerical code which purpose was to determine the population of excited species present in the plasma, based on emission spectroscopy. The code was validated against the software Specair, which is a reference for spectral simulations.





# 3 Experimental Characterization of the Plasma

## 3.1 Introduction

The experimental determination of plasma characteristics is presented in this chapter. The temporal and spatial evolution of the thermodynamic state of the plasma, its composition, the electric field inside the plasma are measured. The variation of these characteristics with respect to the operating parameters such as the applied voltage, the polarity and the ambient air pressure are investigated. These valuable informations allow to determine the optimal configuration of the actuators, depending on the application needs. First a short review of the literature on plasma diagnostics applied to high pressure, high voltage plasmas is given.

The chapter is structured as follows: In section 3.2, the different experimental setups are described. In section 3.3, the principal experimental results of this thesis are presented. The global characteristics of the SDBD actuator are described. The influence of different operating conditions on the measured plasma parameters are analyzed. Section 3.4 summarizes the findings of the chapter.

### 3.1.1 Literature review

Experimental determination of plasma characteristics in the case of a SDBD is largely based on optical methods, as discussed in section 2.4. This is mostly due to the highly transient nature of the plasma investigated, its very small size ( $\approx 5\text{mm} \times 200\mu\text{m} \times 200\mu\text{m}$ ) and to the high voltages and currents involved. Such studies have been performed in similar experiments in the recent past by a number of authors.

The common feature of these investigations is the use of OES for the characterization of the plasma. The plasma was generated in different geometries (notably point-to-plane geometry) and at different pressures. While the conclusions drawn in these configurations are difficult to apply to other cases, they give useful insights on the physics of the plasma and on the experimental methods employed.

### Chapter 3. Experimental Characterization of the Plasma

---

The determination of the reduced electric field based on experimental data was already presented in section 2.4.2. Methods to determine the reduced electric field in streamers are reviewed in [Starikovskaia et al., 2010], with an example given for the determination of the reduced electric field for the case of a SDBD driven by a sinusoidal voltage at 12 kV p-p operated in a  $N_2 - O_2 = 95:5$  mixture at atmospheric pressure. The method employed relies on the method given in [Paris et al., 2005]. This method is similar to the method employed here.

Absolute emission spectroscopy was performed in [Starikovskaia et al., 2002] for the determination of the electric field and electron density at different pressures (0.1-30 Torr) and for high voltage pulse. These conditions lead to a so-called fast ionization wave, which reaches velocities of up to  $10^{10}$  cm/s. It is interesting to note that the EEDF is inferred from the solution to the Boltzmann equation for electrons in the two-term approximation. This solution is considered accurate only for values of the reduced electric field of about 1000 Td (see section 2.3.2). This fact poses the question of the validity of the method for very high electric fields such as encountered in streamers.

The measurement of the reduced electric field was performed also for pressures above the atmospheric pressure (1-5 atm) in [Kosarev et al., 2012], which is very important for combustion applications. It was found that the average reduced electric field is decreasing linearly with increasing pressures. The feasibility of using a SDBD for plasma-assisted combustion is demonstrated. As higher than atmospheric pressures were not the topic of this thesis, they were not investigated, but this reference shows that implementation of the SDBD in a turbo-machine or in a combustion chamber could be envisaged for future work.

In [Pancheshnyi et al., 2000], the determination of active particles produced in a cathode directed streamer, namely  $N_2(C^3\Pi_u)$ ,  $N_2^+(B^2\Sigma_u^+)$  and  $NO(A^2\Sigma^+)$  was conducted. The main differences, when compared to the SDBD investigated here, is the point-to-plane geometry and the high voltage pulse of 18 kV. The linear densities of the active particles are recorded. The reduced electric field is determined.

In a latter publication [Pancheshnyi et al., 2005], the same author investigated the influence of the pressure on the propagation of the streamers in the range 760 to 300 Torr and its impact on the production of active particles. The experimental setup was similar to the previous publication (point-to-plane, 12 kV). Several parameters of the streamers were measured: the velocity, the diameter inferred from spectroscopy and the reduced electric field. Comparisons with direct simulation were also provided. The influence of the pressure on the production of active particles was deduced from calculations and was found to increase with the inverse of the square of the pressure. The reduced electric field was found to vary insignificantly with the pressure. The velocity of the streamer was found to increase with decreasing pressure. It was noted that the similarity laws such as described in section 2.2 do not hold for most parameters of the streamers and this was attributed to non-linear dynamics caused by the photoionization and strongly coupled chemical kinetics. The question of the similarity laws is discussed in this

reference, and poses the question of their validity for certain types of processes. This question is important since similarity relations would be of great interest for the deduction of the flow actuation properties of the actuator at different pressures.

The experimental investigation of nanosecond pulsed SDBD has been conducted in [Starikovskii et al., 2009, Nudnova et al., 2010, Roupasov et al., 2009], investigating the characteristics of the plasma generated by means of a fast camera, optical emission spectroscopy, air density measurements (Schlieren technique) and pressure measurements. Positive and negative pulses of high voltage up to 50 kV and duration down to 7 ns with extremely fast rise time down to 1.3 ns were investigated. Different setups were investigated in different gases (influence of the heating in N<sub>2</sub>, Ar, CO<sub>2</sub>, He and Air), at different pressures (150-1350 Torr). The reduced electric field was determined by OES using the first bands of the SPS and FNS for both polarities and at different pressures. The increase in gas temperature was measured by spectroscopy and the energy input to the plasma was determined by electrical measurements for different pressures. The deductions made during these series of experiments explain most of the properties of the plasma generated by a nanosecond pulsed SDBD. The comparison of these experiments with the present configuration of SDBD driven by a voltage pulse which is shorter and has a smaller voltage amplitude is of interest.

## 3.2 Experimental setups

The surface dielectric barrier discharge (SDBD) and the nanosecond voltage pulse generator used throughout this thesis are described here.

The SDBD is made of dielectric material  $Al_2O_3$  (alumina) and the electrodes are made of copper strips (see figure 3.1). The upper electrode is exposed and the lower electrode is encapsulated with Kapton. The electrodes are soldered to high voltage cables and connected to the voltage generator.

The high voltage pulse generator is composed of a high voltage power supply connected to a switching unit ( $\equiv$  high power transistor).

The high voltage generator is a TREK power generator PM 04015-H-CE (600 VA max) which can provide +/- 10 kV in either AC or DC modes. The TREK is used in DC mode for pulsed experiments and provides the high voltage to the switching unit.

Two switching units were used: MOSFET push-pull switches HTS 151-03-GSM and HTS 111-06-GSM from Behlke. The first one was used for the first experiments and optimized for shortest transition times (rise and fall time), by varying the series and parallel resistors (see figure 3.2). As the SDBD behaves like a capacitor, it is important to have a very small resistor in series with it to allow for a fast transition time, but at the same time the MOSFET switch used needs protective resistor in order not to overheat. As both a fast transition time (for efficient plasma generation) and a high frequency of operation are necessary for optimal flow-control

### Chapter 3. Experimental Characterization of the Plasma

abilities, the second switching unit was purchased. This switch allows a high-voltage input up to +/- 11 kV and 60 A peak current, with a continuous frequency operation of 100 kHz with the cooling fins option selected. The theoretical rise and fall time are 19 ns assuming a 200 pF capacitance.

The very good repeatability of the voltage pulses is one of the major assets of the pulse generator used. It allows the interpretation of single pulse's characteristics on the basis of measurements performed on an accumulation of several thousand pulses. The accumulation of the light for optical measurements for example, is necessary due to the low level of light emitted by the plasma.

Whenever short-circuit occurred, the circuit was operated with too high currents, therefore damaging the MOSFET switches. In order to circumvent this problem and to allow for higher power deposition in the plasma, a MOSFET switch equipped with cooling fins and a cooling ventilator was developed by the electrical team at CRPP. A protective system was designed in order to cut the command signal to the MOSFET whenever a too high current is measured (with a Rogowsky ring) and an integrated voltage divider permits to measure the voltage.

The switching unit needs to be triggered by an external signal, which is provided by a ROHDE & SCHWARZ pulse generator SCF-AL-018 in pulsed mode.

Positive pulses were generated with a duration of 200 ns and a repetition frequency of 1 kHz unless otherwise stated. Typical voltage and current signals are displayed in figure 3.3. The rise and fall time of the input signal depend on the switching unit and on the electrical circuit parameters.

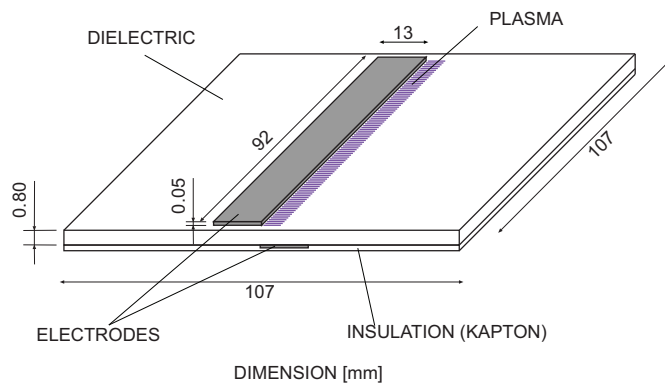


Figure 3.1: Sketch of the SDBD.

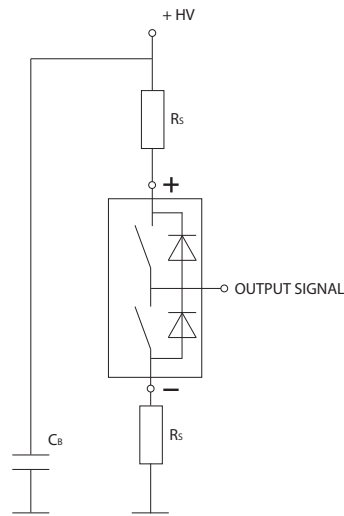


Figure 3.2: Sketch of the push-pull switch in positive pulse mode.

The temporal evolution of the discharge can be depicted using figure 3.3, which represents typical voltage and current graphs for a 7 kV applied voltage.

A plasma forms at the voltage rise (ascending phase) and at the voltage fall (decaying phase), according to electrical and optical measurements. During each phase, the plasma emits light.

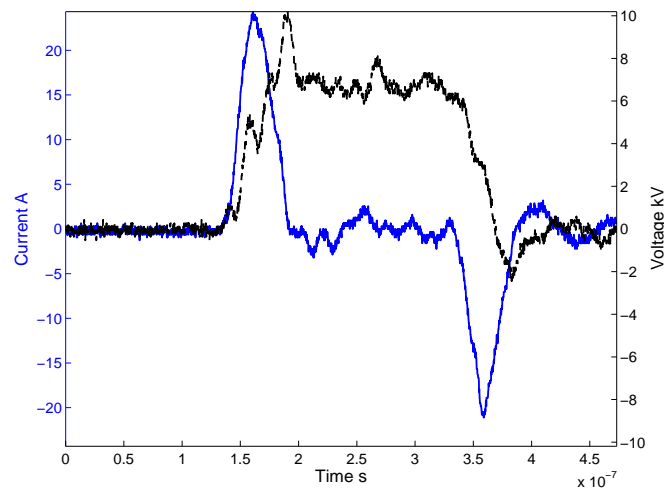


Figure 3.3: Typical current (left) and voltage (right) between the electrodes of the SDBD.

**Ambient pressure experiments** These experiments correspond to early measurements for which the calibration of the optical setup was not yet performed. The light from the SDBD was collected directly by a rack of 16 quartz optical fibers of 200  $\mu\text{m}$  core diameter. They are spaced by 0.5 mm and their numerical aperture is 0.22. The fibers were placed along the direction of propagation of the streamer, i.e. perpendicular to the electrodes, with the first

### Chapter 3. Experimental Characterization of the Plasma

---

fiber being located 1 mm before the edge of the upper electrode. The fibers were placed 13 mm above the SDBD which allowed to record the light from a 8 mm long region with full intensity (14 mm in total). An Acton SP2750 spectrometer coupled to a intensified CCD (1340 × 400 pixels, Spec-10:400 B from Roper Scientific) cooled with liquid nitrogen were used to record the spectra. The spectrometer is equipped with three gratings of 300, 600 and 1800 g/mm. The 1800 g/mm was used for measurements shown in this thesis.

**Vacuum chamber experiments** The SDBD was placed in the vacuum chamber at pressures in the range 0.2 bar to atmospheric pressure, in order to measure characteristics relevant for aerodynamics application (0-10 km altitude). The pressure was reduced using a pre-pump from Pfeiffer Vacuum and the pressure was measured using a MKS Baratron pressure gauge 626 A (1-1000 mbar).

The optical setup used to collect the light is shown in figure 3.4. The light coming from the plasma is collected through a converging lens of 50 mm focal length to the optical fibers rack, which comprises 16 fibers in a row. An Acton SP2750 spectrometer coupled to an ICCD (1024 × 1024 pixels) fast camera PI-MAX 2 from Princeton instruments was used to record the spectra emitted from the plasma. The fast camera was triggered by the ROHDE & SCHWARZ pulse generator triggering the switch. The 600 g/mm grating was used for measurements shown in this thesis, with linear dispersion of 2.16 nm/mm, giving a resolution of approximately 0.3 nm (inferred from emission spectra). The optical system was focused by shining white light into the fibers at the spectroscopy entrance slit in order to see the image of the fibers on the SDBD. The rack was oriented parallel to the upper electrode of the SDBD in order to perform a spatial average in that direction. The size of the image was then made as small as possible while retaining the highest possible intensity. The size of the images from the fibers was smaller than 1 mm, which is an estimate of the spatial resolution of the measurements. The tube holder for the fibers rack and the converging lens was mounted on micrometer screws to allow spatial resolution.

Two spectral zones were recorded, a 400 nm zone (384-412 nm) and a 760 nm zone (744-772 nm). In order to record the spectra in the long wavelength region (about 760 nm), a low-pass filter has been used in order to cut-off the light below 400 nm, to avoid second order spectra.

The system was calibrated in frequency with an Avantes argon-mercury lamp and in intensity with a NIST traceable Avantes AvaLight-DH-BAL-CAL calibrated light source.

An optical fiber was connected to the calibration lamp and the output was placed at the location of the SDBD inside the vacuum chamber, in order to ensure the correct calibration of the whole optical system for the conditions of operation.

The absolute calibration of the system was made with an integrating sphere from Labsphere,

### 3.2. Experimental setups

which was performed after the experiments due to the impossibility to fit the Labsphere into the vacuum chamber. The difference in relative population of excited species computed using both calibrations was smaller than 2 percent within a spectral range (400 nm or 760 nm) and better than 10 percent for the comparison between spectral ranges, which is the uncertainty associated with the absolute intensity of the AvaLight-DH-BAL-CAL. The results presented in this section are obtained using the calibration data from the Labsphere. The calibration of the system was performed with an exposure time of 50 ns. It should be noted that the intensity response of the CCD is not necessarily the same for exposures of different duration. Therefore time-resolved intensities with temporal resolution of 2 or 5 ns presented in the following sections must be taken as estimates.

The intensity measured was divided by the integration time in order to obtain radiance in units  $\text{Wcm}^{-3}\text{sr}^{-1}$ . The intensity was further divided by the number of accumulations performed on the CCD in order to obtain an intensity in radiance representative of one single pulse.

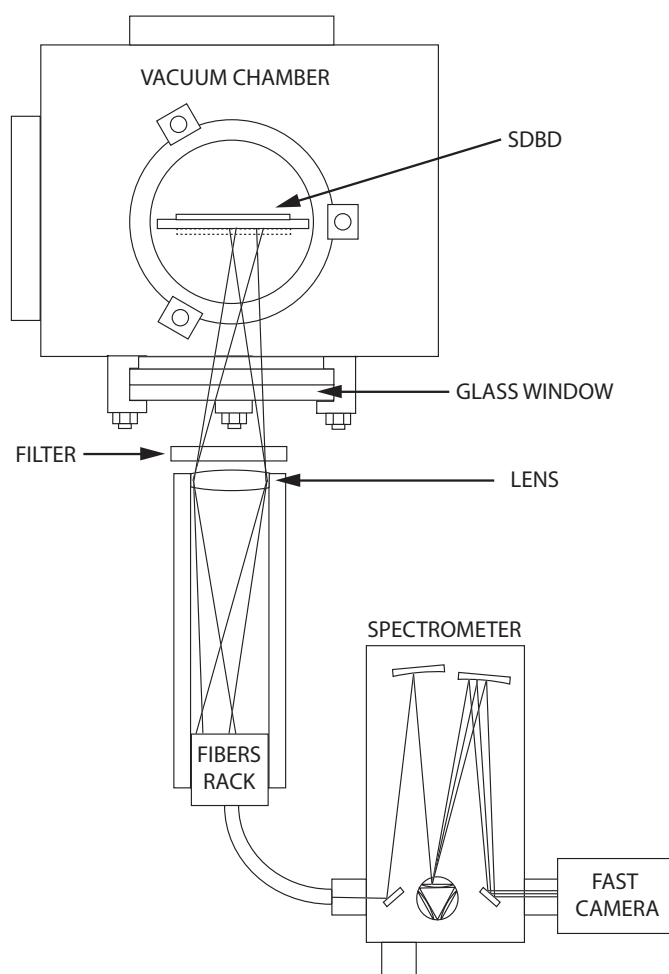


Figure 3.4: Sketch of the optical setup.

### 3.3 Experimental results

In this section, the experimental results obtained for the influence of several parameters on the plasma are presented. First, the global characteristics of the plasma produced by a SDBD with nanosecond pulsed applied voltage are described in subsection 3.3.1. The influence of the applied voltage on the plasma is discussed in subsection 3.3.2, the temporal and spatial evolution of the streamer at atmospheric pressure for a positive pulse in subsection 3.3.3, the influence of the polarity and of the pressure on the propagation of the streamers in subsections 3.3.5 and 3.3.6 respectively. A comparison with measurements performed with the sinusoidal applied voltage is presented in subsection 3.3.7.

#### 3.3.1 Global characteristics of the SDBD

The general experimental characterization of the plasma is performed and used to describe the different diagnostics used and their limitations. Electrical measurements monitor integral quantities such as the current and the energy in the plasma, time-resolved plasma imaging serves to identify the general spatio-temporal structure of the light emitted by the plasma. The analysis of the different species present in the plasma is made using time-averaged emission spectroscopy.

#### Electrical diagnostics

The voltage set to the SDBD was measured between the two electrodes with a high-voltage probe, a Tektronix P6015 (75 MHz bandwidth, max 20 kV) and the current was measured either with a LeCroy current clamp or a Rogowsky ring. The current measured is composed of the *displacement* (or capacitive) current and the current passing in the plasma. For this reason it is difficult to perform measurement of the current flowing in the plasma with sufficient accuracy. The time response of the voltage probe can be calculated as  $0.35/75$  MHz, which gives 4.7 ns. Thus features in the signal which vary faster than 5 ns cannot be tracked.

Two methods have been used to measure either the current or the total energy released into the plasma. The first consists in the measurement of the current in the SDBD while the plasma was ignited subtracted to the current measured after having encapsulated both electrodes with an insulating material (Kapton), to completely suppress the plasma. The resulting current should corresponds to the current flowing in the plasma. This method is of course not very accurate as there are variations in the current flowing through the SDBD from one test to the other and moreover there is possibly a modification of the SDBD properties by adding an insulating material. This method was also used in [Lagmich, 2007] for example.

The first results shown in figure 3.5 are obtained for a  $1 \mu\text{s}$  pulse at 2 kV when there is no plasma (or really weak) and at 7 kV when the plasma is well formed. The raw data being very noisy, it was filtered (function `filter` in Matlab, window = 50). It can be seen that the order



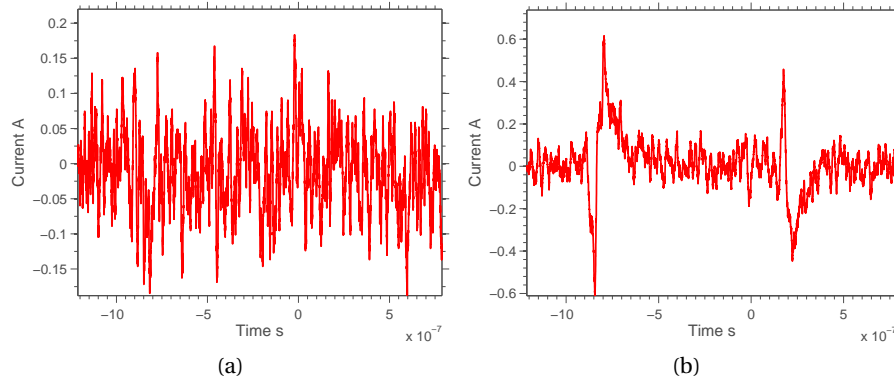


Figure 3.5: Computed current difference between plasma on and plasma off (insulated). Filtered data (see text) for: 2 kV (a) and 7 kV (b).

of magnitude of the current estimated with this technique is of the order of 500 mA for these conditions.

The method to compute the total energy flowing into the plasma over one complete cycle is as follows: the current is multiplied with the voltage to yield instantaneous power and then integrated over time during one voltage pulse. Because the capacitor is essentially a non dissipative device, the total energy over a complete pulse should be zero. The energy loss is then assumed to be due to energy consumption in the plasma (momentum transfer, heating, radiative transfer, etc.).

The integrated power over one pulse is  $E = 1.12$  mJ for the 7 kV case. The energy input to the plasma measured with the same method in [Starikovskii et al., 2009] for a similar geometry and applied voltage, is approximately 3 mJ, which is in of the same order of magnitude.

However, the accuracy of this technique is limited because the measurements of the voltage and current exhibit a strong noise, which is voltage dependent. The energy difference between pulses could then be simply due to the noise of the signal. In order to validate this method, the energy was calculated from the experimental data for the case with plasma and for the case without plasma, in the condition of figure 3.5. The results are shown in figure 3.6. The difference in energy calculated for the case without plasma (insulated) is at most (7 kV case) 30 percent lower than the case with plasma. This shows that the validity of the energy input calculations is highly dependent on the quality of the voltage and current measurements. With the present electrical setup, the energy input in the plasma is strongly overestimated.

### Plasma imaging

The overall propagation of the plasma is best pictured using fast camera images. The fast camera is the PI MAX 2 described in 3.2. It was placed above the SDBD and focused with

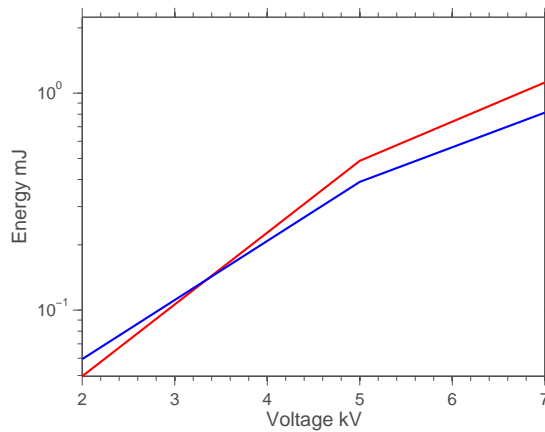


Figure 3.6: Difference between energy input and output to the SDBD. With plasma (red solid line) and without plasma (blue solid line).

a camera lens at a distance of approximately 130 mm from the SDBD. Due to the high repeatability of the experiments, it was possible to perform phase-averaged acquisitions. The camera was triggered with the ROHDE & SCHWARZ pulse generator, and the recorded light was accumulated on the CCD for several thousand pulses. Two phases during which light was emitted were found, corresponding to the ascending and decaying phase. The temporal resolution was chosen in such a manner as to allow a visualization of the propagation of the plasma. For these experiments, the gate exposure was 5 ns and 5000 pulses were accumulated on the CCD, unless otherwise stated.

The plasma propagates in the form of small filaments from the upper electrode toward the lower electrode direction, for both phases. The plasma propagates further in the ascending phase, with branching phenomena occurring at the end of the propagation. For the decaying phase, the plasma develops also in the form of filaments, but propagates less far and slower. No branching is observed for this phase. The filamentary structure, the speed of propagation and the high intensity emitted allow to conclude that the plasma forms as streamers. The streamers propagating always from the upper electrode to the lower electrode, regardless of the phase (and of the *polarity*, see [Peschke, 2014]), it can be concluded that the streamer during the ascending phase is a positive streamer and the one during the decaying phase a negative streamer. The difference in the type of streamers also explains why a different behavior of the plasma is observed between the ascending and decaying phases.

It is to be noted that the repeatability of the plasma is such that it allows the visualization of single streamers. The streamers always start at the same location, corresponding probably to locations on the electrode where was situated a small protrusion, enhancing the local electric field.

### 3.3. Experimental results

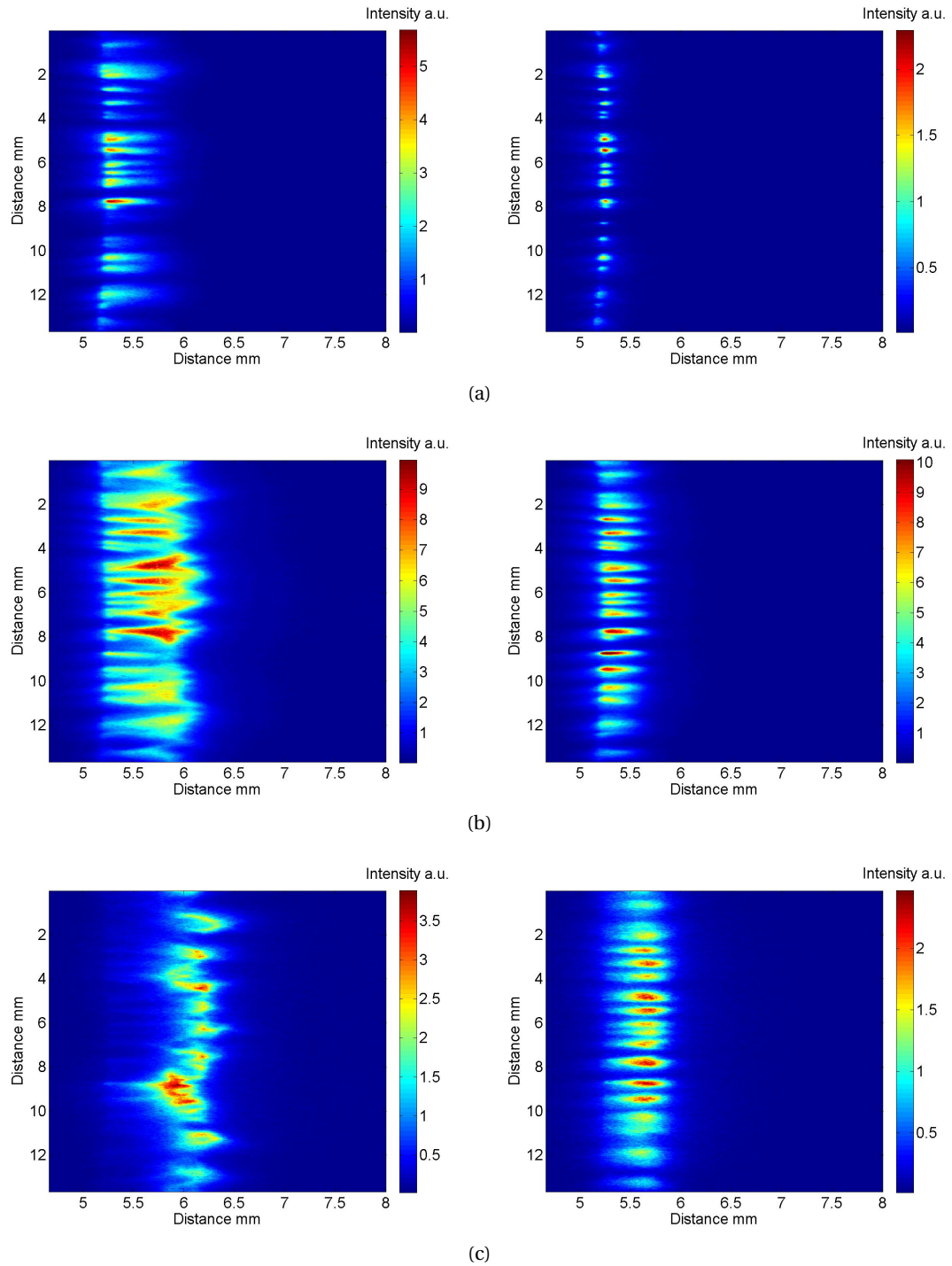


Figure 3.7: Fast camera images of the streamer propagation. The applied voltage is 7kV and pressure is 1 atm, the gate exposure is 5 ns and the image is an average over 5000 cycles. The time at which images are taken corresponds to the trigger time  $t_{ref}$  (a) plus 5 and 10 ns respectively for (b,c) for the ascending phase. The images for the decaying phase (right) are delayed by 160 ns with respect to the ascending phase. The edge of the upper electrode is located at 5.2 mm.

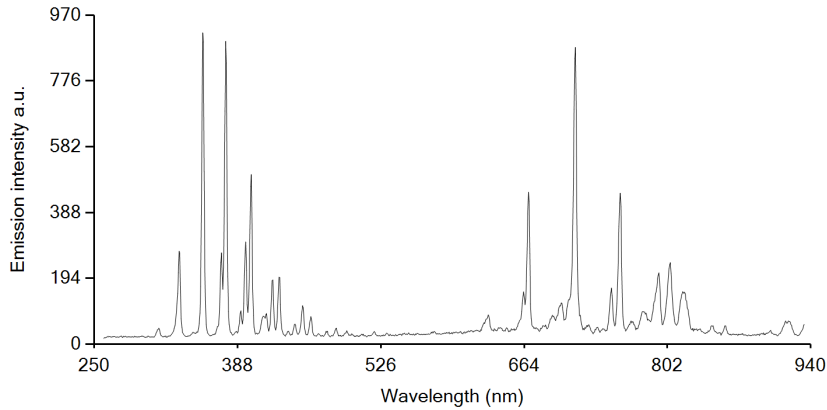


Figure 3.8: Low resolution spectrum acquired with the 150 g/mm grating of the spectrometer (150 mm focal length).

### Radiating species

The identification of excited species produced in the plasma was performed by optical emission spectroscopy. An example of a low resolution spectrum is shown in figure 3.8. It was obtained using a 150 g/mm grating of an Acton 2150 spectrometer. The left part of the spectrum, from 300 to 500 nm belongs to the transition  $N_2(C^3\Pi_u - B^3\Pi_g)$ , which is called the second positive system of  $N_2$  (SPS) (see section 2.5). The right part of the spectrum looks very similar to the left part: it is the so-called second order spectrum which can arise when using a grating; it is the short wavelength spectrum with doubled wavelength. In order to remove this feature, a short-wavelength filter can be used.

If a higher resolution is used for the left part (by using the 1200 g/mm grating), finer details can be observed, notably the presence of the first band of the transition  $N_2^+(B^2\Sigma_u^+ - X^2\Sigma_g^+)$ , the first negative system of  $N_2^+$  (FNS) whose head is located at 391.2 nm. If a filter is used to remove the second order spectra coming from the SPS, the features of the spectrum in the right part of figure 3.8 can be investigated. An example of what is observed is shown in figure 3.10 for a grating of 600 g/mm of the 2750 Acton spectrometer. The spectrum observed in this spectral region is due to the transition  $N_2(B^3\Pi_g - A^3\Sigma_u^+)$ , which is called the first positive system of  $N_2$  (FPS) and of atomic lines due to Ar(ground -  $2p_{1,5,6}$ ) (in Paschen's notation) at 750.39, 751.47, 763.51 nm and to  $O(^5S^{deg} - ^5P)$  at 777 nm.

Some features of the spectrum were absent or weak, which prevented the use of some diagnostic technique as presented in section 2.4, making the plasma particularly difficult to analyze. The electron density can be inferred from the  $H_\alpha$  at 656.3 nm and the  $H_\beta$  at 486.1 nm using the measurement of the Stark broadened line width. Both lines were too weak to be distinguished from the background. The hydrogen coming from the water vapor dissociation is normally used for such a purpose, and its content should be present between 1 and 2 percent in humid air. The excitation cross section for the  $H_\alpha$  is an order of magnitude larger

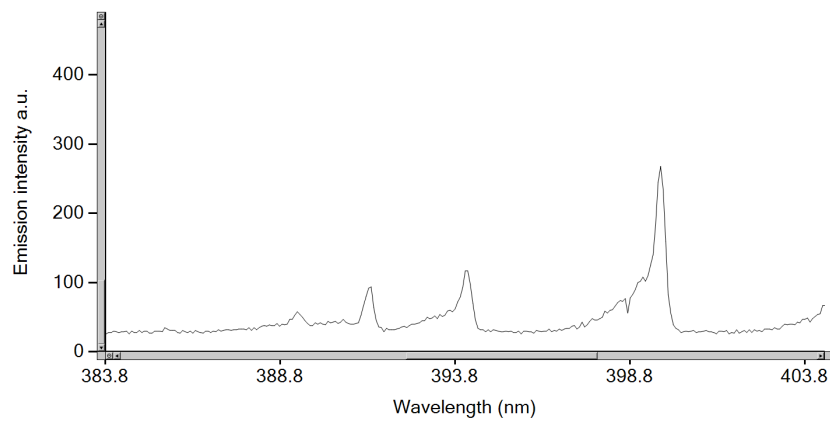


Figure 3.9: Medium resolution spectrum acquired with the 1200 g/mm grating of the spectrometer (150 mm focal length).

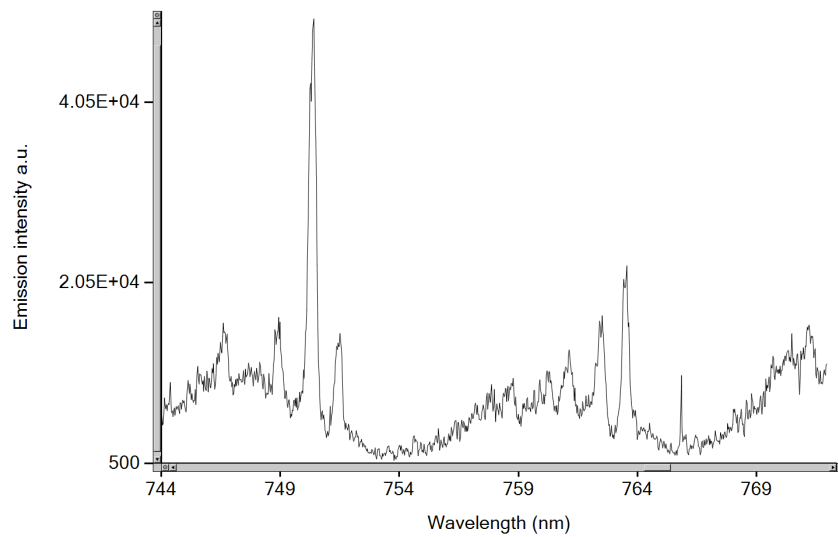


Figure 3.10: Low resolution spectrum acquired with the 600 g/mm grating of the spectrometer (750 mm focal length).

than the excitation cross section for  $H_\beta$ . Consequently, a long exposure was used to detect the  $H_\alpha$  line. It was too weak to be distinguished in the background. In order to determine why this line is absent, the comparison can be made with the most intense argon line ( $2p_1$ ) possessing an emission coefficient of the same magnitude as that of  $H_\alpha$ . The  $2p_1$  state is produced from electron-impact excitation of ground state argon, representing 1 percent of the dry air content. Its excitation cross section peaks at  $5.3 \cdot 10^{-18} \text{ cm}^{-2}$  for an electron energy of 20 eV (see figure 2.6). Comparatively, the  $H_\alpha$  peaks at  $0.204 \cdot 10^{-18} \text{ cm}^{-2}$  for an electron energy of 20 eV rising to a maximum value of  $3.55 \cdot 10^{-18} \text{ cm}^{-2}$  at 100 eV, as reported in [Itikawa, 2005]. This lower excitation cross section could explain the absence of this line. Moreover, the  $\text{OH}(A^2\Sigma_+, v' = 0 - X^2\Pi_i, v'' = 0)$  band at 306-310 nm was very weak and difficult to identify among the background indicating a low dissociation of water vapor. Atomic lines from N atoms were not observed, nor was the  $\text{N}_2^+(A^2\Pi_u - X^2\Sigma_g^+)$  Meinel system of  $\text{N}_2^+$ , despite long exposures.

The diagnostics of the plasma presented in section 2.4.2 is based on the determination of the reduced electric field. Most of the authors determining the reduced electric field do so by comparing the relative intensities of the FNS and the SPS. In this thesis, other transitions are analyzed for the determination of the reduced electric field, for several reasons. The first one is to determine the validity of this approach experimentally, as there is no reliable comparison available for the value of the reduced electric field apart from the comparison made in [Starikovskaia et al., 2002] with a capacitive gauge, which gave reasonable agreement for a positive pulse and a factor of 2 discrepancy for a negative pulse. The second one is to allow for the determination of the reduced electric field in special conditions, such as when the electric field is too low to provide sufficient intensity of the FNS or when the recording system cannot perform measurements below 400 nm, as was encountered during this thesis (measurement behind a Plexiglas window). The third one is to allow for the reconstruction of the shape of the streamer front, as discussed in section 4.4. This last point is the most distinctive feature of this thesis.

In order to provide different transitions for the purpose of determining the reduced electric field, argon lines are suitable, since they most probably are populated by electron-impact from the ground state of argon. Another candidate is the FPS, which can be populated by numerous other sources, as described in section 2.4.1. Another transition would be the strong oxygen lines at 777 nm. This last candidate is difficult to assess, since the main production mechanism could be direct electron impact dissociative excitation, but also by electron-impact from atomic oxygen [Germany et al., 1988], which might be produced efficiently in the plasma. For this reason this transition was discarded.

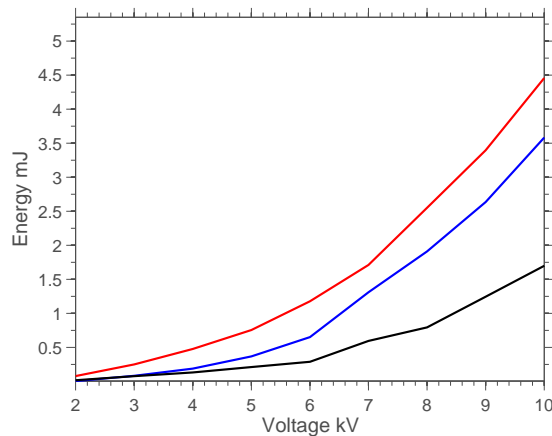


Figure 3.11: Energy input in the plasma in function of the applied voltage. The value of the series resistor is: 33  $\Omega$  (red solid line), 68  $\Omega$  (blue solid line) and 150  $\Omega$  (black solid line).

### 3.3.2 Effect of the voltage on streamer propagation

The experiments presented in this section were performed using the experimental setup in ambient air described in subsection 3.2.

The applied voltage has a high impact on the produced plasma because it changes the strength of the applied electric field driving the processes in the plasma. However, raising the voltage does not necessarily mean an increase in the reduced electric field in the plasma once a streamer is initiated, but it will certainly speed the breakdown process as discussed in section 2.2. Other parameters such as the rate of the voltage increase in time have also a large influence on the plasma. If the electrical circuit behaves linearly with input voltages, then the effect of a rise in voltage is equivalent to an increase in the slope of the voltage pulse (higher  $dV/dt$ ).

Once a streamer is initiated, its propagation length will depend on the applied voltage, which acts as the energy supply necessary to overcome the losses occurring in the plasma channel, but also on other processes such as the charging of the dielectric by positive or negative charges. Thus a higher applied voltage should generate longer streamers and consume more energy than for lower voltages. To investigate these effects, the electrical diagnostics described in section 3.3.1 is first used to determine the input energy in the plasma. As noted in section 3.3.1, the accuracy of the electrical measurements is questionable, but is believed to give valuable insight on the trend of the overall energy consumption of the plasma for different applied voltages.

The energy transmitted from the electrical circuit to the plasma is estimated for voltages from 2 to 10 kV, and for different values of the resistor (series), 33, 68 and 150  $\Omega$ . The energy increase follows the trend of the power input, which is about quadratic with respect to the voltage ( $P=U^2/R$ ). Since the length of the upper electrode is 9 cm, the specific energy is 0.5 mJ/cm at 10 kV for the 33  $\Omega$  case.

### Chapter 3. Experimental Characterization of the Plasma

Secondly, the optical diagnostics described in section 3.3.1 is used to determine the spatial extension of the plasma as a function of the applied voltage, together with the different production of active species. The light emitted by the plasma was recorded for applied voltages from 1 to 10 kV and the relative populations of radiating species associated with it were determined using the spectral code described in section 2.5. The integration time was varied between 30 and 250 s and averaged over that time allowing comparison, the plasma was pulsed at a frequency of 100 Hz. No light was detected for the 1 kV case, it is thus not shown. Both recorded and fitted spectra are shown in figure 3.12. The experimental spectra are very well fitted by the code for all conditions.

The spatial evolution of the excited species populations is shown in figure 3.14. The length of the plasma does seem to vary appreciably with varying applied voltage. It is to be noted that due to the optical setup consisting of optical fibers directly placed over the SDBD, the intensity of the light emitted at a certain location was measured by fibers placed also further ahead or behind, thus producing a certain spread of in the recorded intensities. Consequently, the intensity recorded increases due to both an increase in intensity due to the higher voltage but also due to the longer extent of the plasma. Indeed, a longer plasma produces more overall light, as recorded by this setup. This interpretation is supported by measurements performed with a different experimental setup: the fibers were placed parallel to the electrodes and closer to them, and time-resolved spectroscopy was performed. The results exhibit an almost linear increase of the populations of excited species with the increase of applied voltage (see figure 3.13).

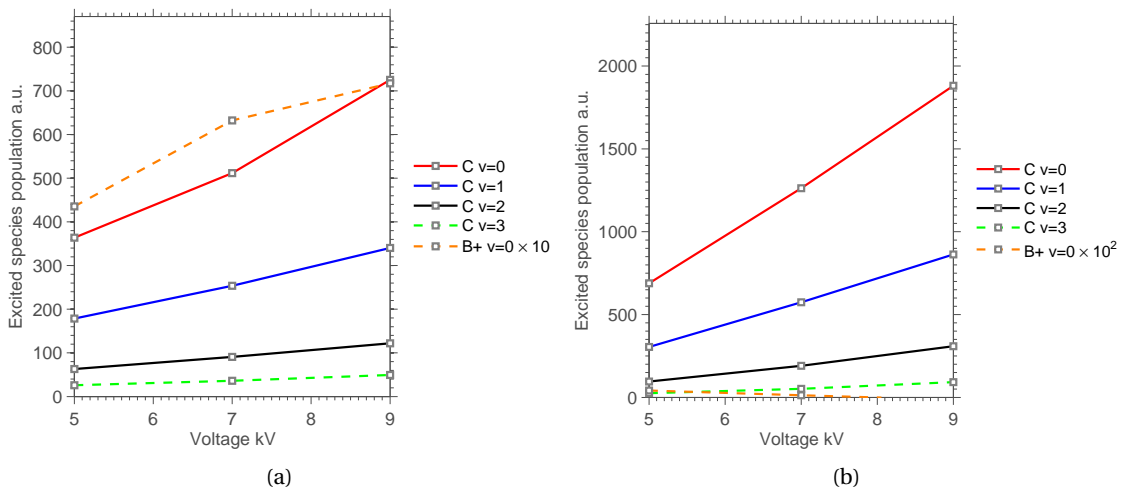


Figure 3.13: Effect of the applied voltage on the population of excited species during the ascending phase (a) and decaying phase (b). The excited species correspond to :  $N_2(C^3\Pi_u, v' = 0, 1, 2, 3)$  and  $N_2^+(B^2\Sigma_u^+, v' = 0)$ . Optical fibers placed parallel to the electrodes (see text).

There exists a difference between the shapes of different excited species profile. This is readily interpreted as the contribution of the decaying phase to the emission, as will be



### 3.3. Experimental results

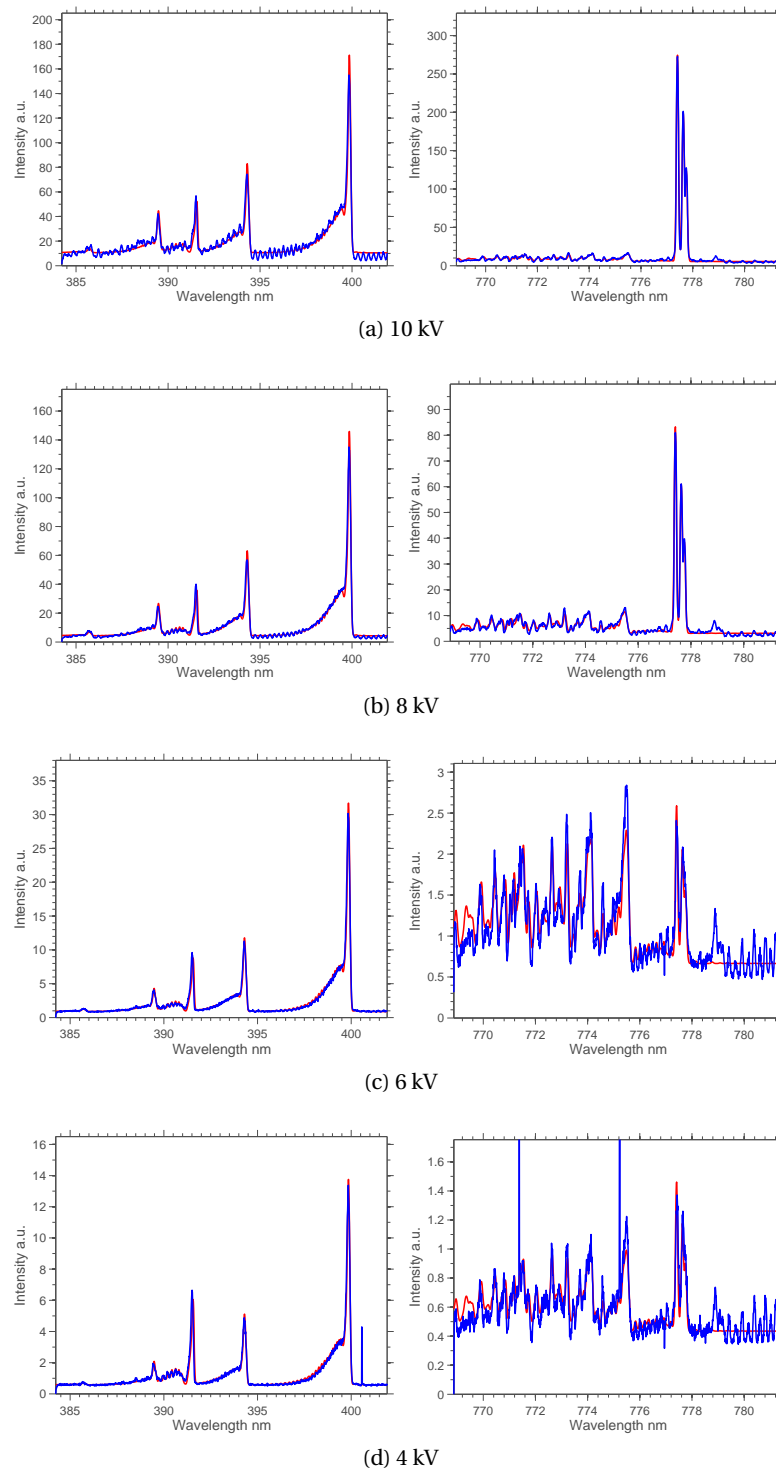


Figure 3.12: Effect of the applied voltage on the spectrum. Recorded spectra (blue solid line) and computed spectra (red solid line).

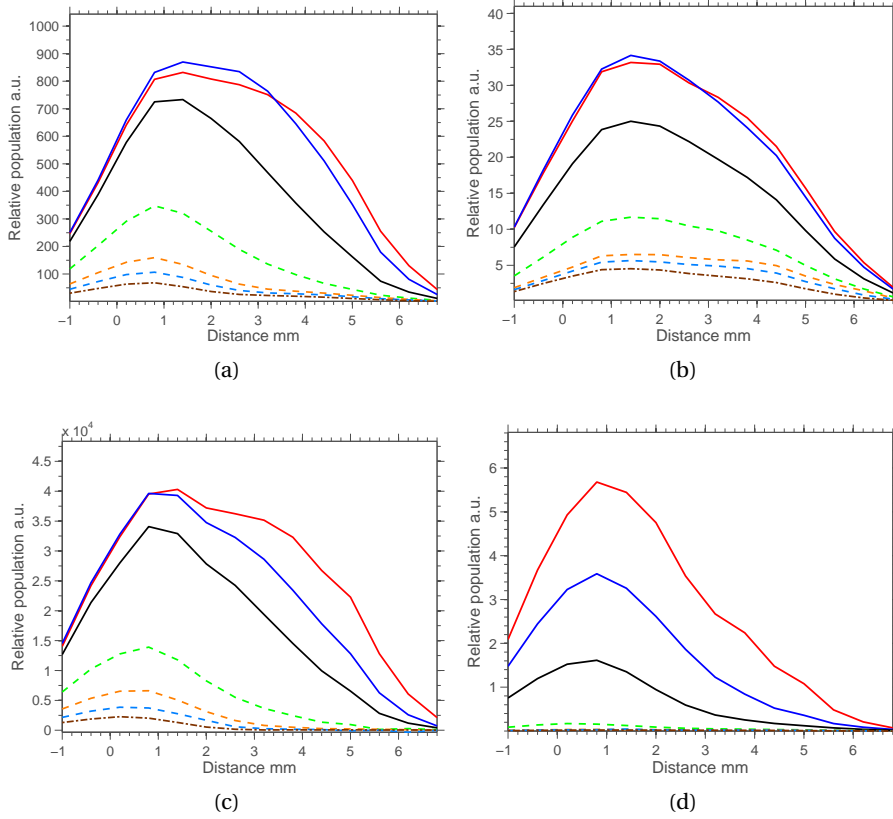


Figure 3.14: Effect of the applied voltage on the spatial distribution of excited species. The red, blue and black solid lines and the green, orange, light blue and bronze dash-dotted lines correspond to voltages from 10 kV to 2 kV respectively. The excited species correspond to :  $N_2(C^3\Pi_u, v' = 1)$  (a),  $N_2^+(B^2\Sigma_u^+, v' = 0)$  (b),  $N_2(B^3\Pi_u, v' = 2)$  (c) and  $O(^5P)$  (d).

discussed in the next subsection. Low lying species are efficiently produced during the decaying phase, whereas high lying states are not. Therefore the population density profile of the  $N_2^+(B^2\Sigma_u^+, v' = 0)$  state (figure 3.14 (b)), which is almost flat (contribution from the ascending phase only). Comparatively, the  $N_2(B^3\Pi_u, v' = 2)$  state (figure 3.14 (c)) presents a larger intensity at short distances (for voltages below 7 kV). This larger intensity comes from a contribution from the decaying phase, during which the streamer propagates for a shorter distance. The maximum distance at which significant light is recorded reaches a maximum value of 6 mm, depending on the transition observed.

### 3.3.3 Temporal and spatial evolution of positive streamers

The experimental setup for the experiments presented in the remainder of this section corresponds to the vacuum chamber experiment described in section 3.2.

The spectral code described in chapter 2.6 was used to determine the population of excited species using the following parameters: rotational temperature  $T_{\text{rot}} = 300$  K and resolution of 0.3 nm FWHM. The populations are given in  $\text{cm}^{-3}$ , which assumes that the plasma is 1 cm thick. However, the actual thickness of the plasma is unknown, and should be very difficult to measure accurately in a SDBD configuration. Thickness for the SDBD configuration has been estimated by measuring the profile of the light intensity from the dielectric surface in function of the pressure in [Starikovskii et al., 2009]. Thicknesses for other geometries were measured by several authors, and can be estimated with the formula  $p \cdot d_{\text{min}} = 0.2$  mm bar, which gives the diameter of the streamer as function of the pressure (see [Briels et al., 2008]). The two estimates give similar figures. The actual population densities can thus be estimated as  $p/0.02$  times the populations densities displayed in the following figures. The accuracy of this approach is investigated in section 4.4.

A note on the designation of the excited species used in the graphs: excited species  $\text{N}_2(C^3\Pi_u, v = 0, 1, 2, 3)$ ,  $\text{N}_2^+(B^2\Sigma_u^+, v = 0)$ ,  $\text{N}_2(B^3\Pi_g, v = 2, 3, 4)$  and  $\text{Ar}(2p_{1,5,6})$  are denoted simply by C  $v = 0, 1, 2, 3$ , B +  $v = 0$ , B  $v = 2, 3, 4$  and  $2p_{1,5,6}$  for simplicity.

**Temporal evolution of the streamer** For time-resolved spectroscopy, the recorded intensity of light can be written as:

$$\bar{I} = \int_{t_k}^{t_{k+1}} \int_{-\infty}^{\infty} \int_{-\infty}^{\infty} I(x, y, t) \cdot s(x, y) dx dy dt \quad (3.1)$$

where  $I(x, t)$  is the intensity of light emitted by the plasma and  $s(x, y)$  is the sensitivity of the optical system.

The inverse problem of estimating  $I(x, y, t)$  on the basis of the recorded intensity  $\bar{I}$  is impractical since deconvolution methods are very sensitive to noise. Moreover, as the light collected is the sum of light coming from several fibers monitoring different streamers, which are not necessarily exactly synchronized (see the camera footage in section 3.3.1), the interpretation of the data would be difficult.

However, most insight is gained by solving the direct problem described by equation 3.1, i.e. convolving the light emitted by a numerically simulated streamer with the sensitivity of the optical system, as is made in section 4.4. This analysis allows for better understanding of the results presented in this section. The temporal evolution of the excited species determined

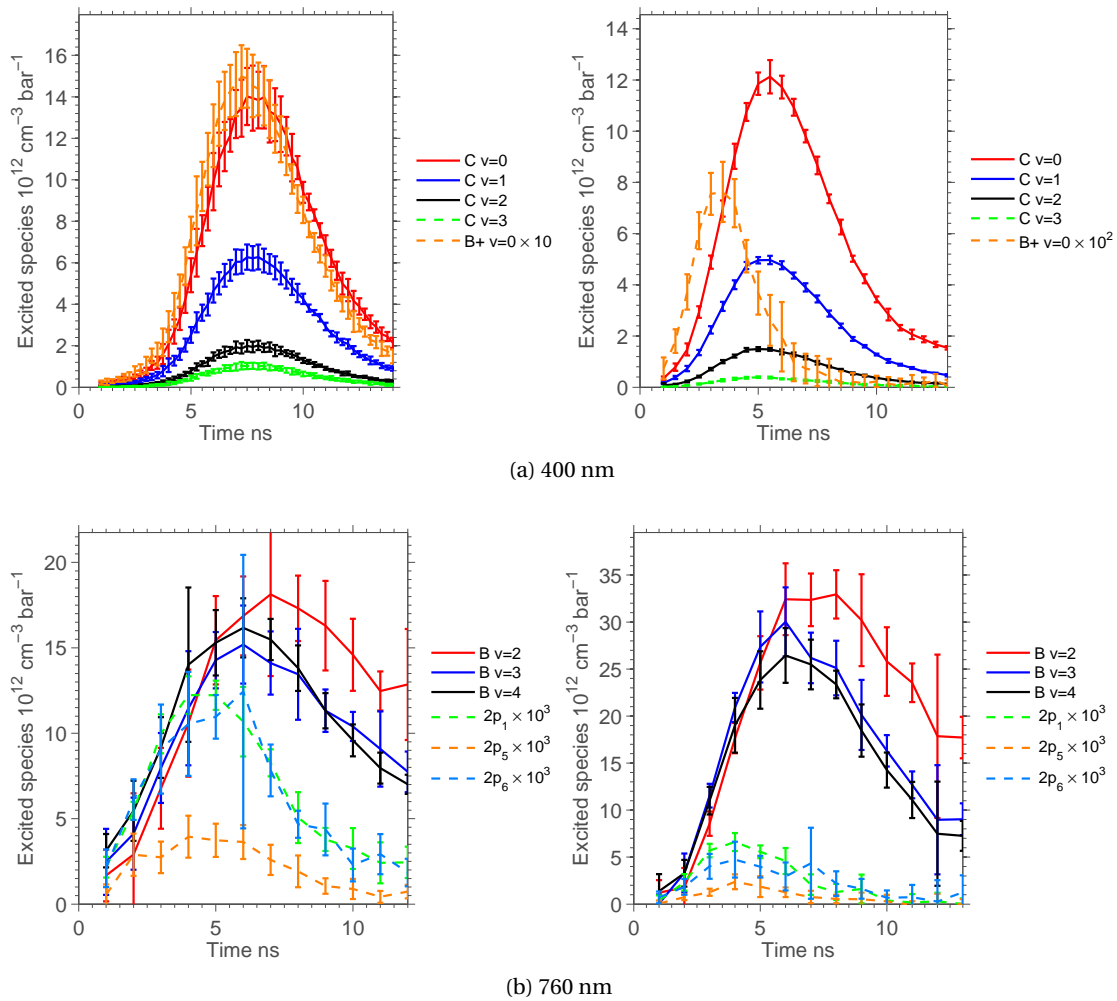


Figure 3.15: Temporal evolution of the excited species populations, for the ascending phase (left) and the decaying phase (right) for a 7 kV pulse at 1 bar. The excited species are inferred from emission spectroscopy in the 400 nm spectral zone (a) and in the 760 nm spectral zone (b).

from time-resolved spectroscopy obtained with a gate width of 2 ns is shown in figure 3.15 for the two spectral zones investigated. The optical system was focused at 0.5 mm from the edge of the upper electrode. In order to allow a better comparison between different operating pressures (see below), the excited species populations is normalized to the pressure in bar.

The evolution in time of the excited species increases and decreases due to the passing of the streamer in the collecting area seen by the optical system. The width (in time) of the pulse seen is of course a function of the optical system sensitivity and of the velocity of the streamer but also of other parameters such as the spread of the excited species. It can be seen that the qualitative behavior for every excited species is similar for the same phase. The higher lying states appear to attain their peak value earlier (=more to the left) when compared

to lower lying states. This effect is much more pronounced for the decaying phase. The magnitude of the excited species population is most interesting, since a clear difference exists between the ascending and decaying phase. This difference lies in the population density of the  $N_2^+(B^2\Sigma_u^+, \nu = 0)$  state, which is about 20 times lower in the decaying phase than in the ascending phase. The magnitude of  $N_2(C^3\Pi_u)$  is similar between phases. The maximum value of the  $N_2(B^3\Pi_g)$  population density increases by a factor 2 in the decaying phase while the  $Ar(2p_1)$  decreases by a factor 2. These differences indicates that the high lying states are much weaker in the decaying phase, indicating a weaker reduced electric field, as is shown in the following. The interpretation of these results is discussed in more detail in section 4.4.

It is interesting to plot the ratio of vibrational levels of  $N_2(C^3\Pi_u)$ , in order to compare to the vibrational population expected from theoretical analysis. If the excitation mechanism is only electron impact from the ground state, the distribution should follow the Franck-Condon factors at the beginning and change slightly over time due to different quenching rates for different vibrational states. The comparison of the ratio of vibrational states for the ascending and decaying phase are compared to the theoretical case (with vibrational relaxation, see section 2.4.1) in figure 3.16. The vibrational distribution starts very close to the Franck-Condon ratio (1, 0.5651, 0.1945, 0.0550) and relaxes to values below what was found from computations, considering a constant electric field. The difference between the ascending and decaying phase is not very pronounced, which allows to conclude that the excitation occurs from the ground state of  $N_2$  even in the case of the decaying phase, although the small difference could be attributed to a non-negligible excitation of the  $\nu = 1$  vibrational level (Franck-Condon ratio: 1, 0.2282, 0.7695, 0.5274).

For the 760 nm spectral zone, the measurement of the excited species population is more problematic since the  $N_2(B^3\Pi_g, \nu' = 2) \rightarrow N_2(A^3\Sigma_u^+, \nu'' = 0)$  and  $N_2(B^3\Pi_g, \nu' = 4) \rightarrow N_2(A^3\Sigma_u^+, \nu'' = 2)$  bands are not completely resolved. Moreover the spectra recorded are much fainter than for the 400 nm zone, which gives less confidence in the fitted values (which is also reflected by the error bars). The ratio of the population of vibrational states cannot give information on the process of population of this state. The Franck-Condon factors for this state are 0.195, 0.190 and 0.151 for vibrational states  $\nu = 2, 3, 4$  respectively. The quenching rates as taken from the literature increase slightly with vibrational level, therefore they should only decrease vibrational populations of higher vibrational levels. This distribution does not seem to be respected, as the  $\nu = 4$  state is overpopulated. The effect of the vibrational relaxation is difficult to evaluate, but should increase vibrational populations of lower levels. The fact that the population of vibrational levels does not seem to follow the Franck-Condon factors does cast some doubt on the mechanism of population of the  $N_2(B^3\Pi_g)$  state.

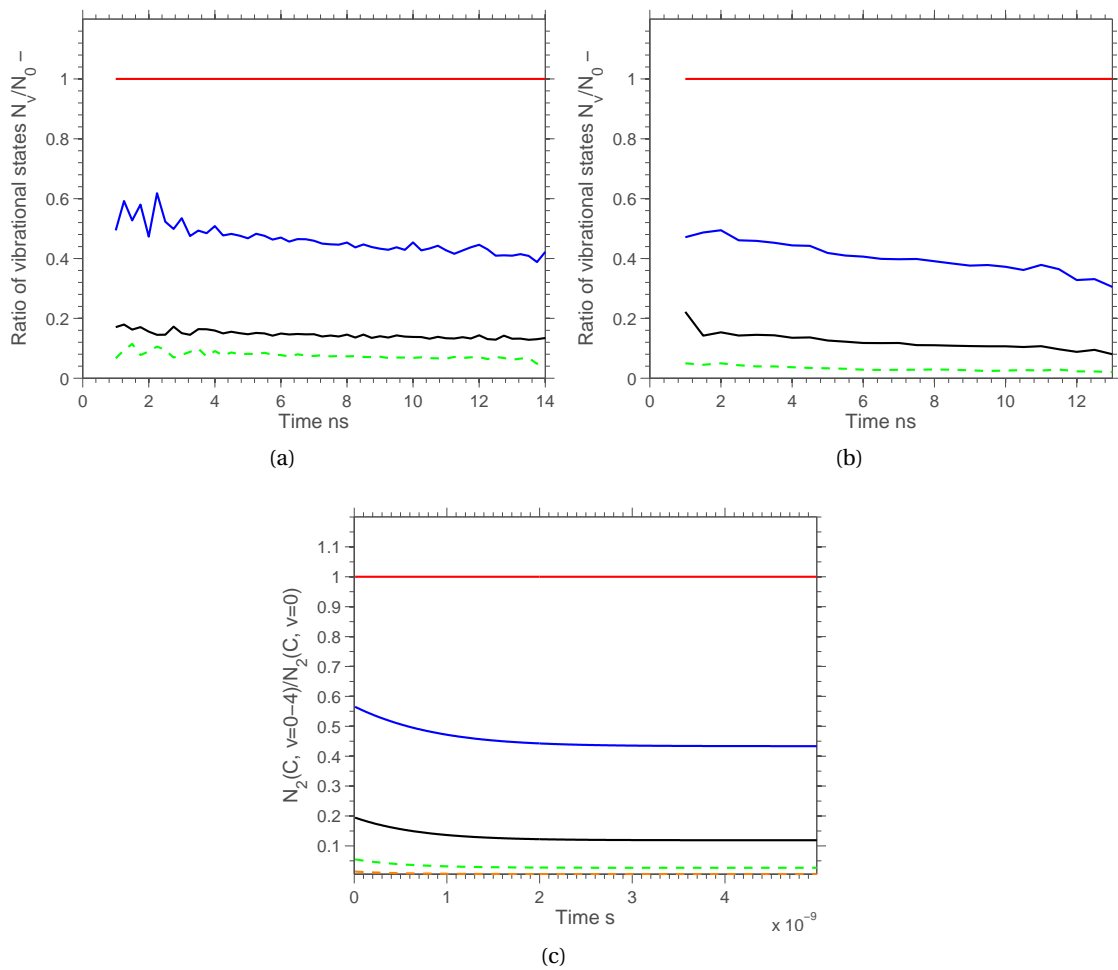


Figure 3.16: Temporal evolution of the ratio of vibrational levels  $N_2(C^3\Pi_u, v)/N_2(C^3\Pi_u, v = 0)$  for the ascending phase (a) and the decaying phase (b) compared to the theoretical distribution (c) for a 7 kV pulse at 0.25 bar. The curves corresponding to the vibrational levels  $v = 0, 1, 2, 3, 4$  are the red, blue and black solid lines, green and orange dash-dotted lines respectively.

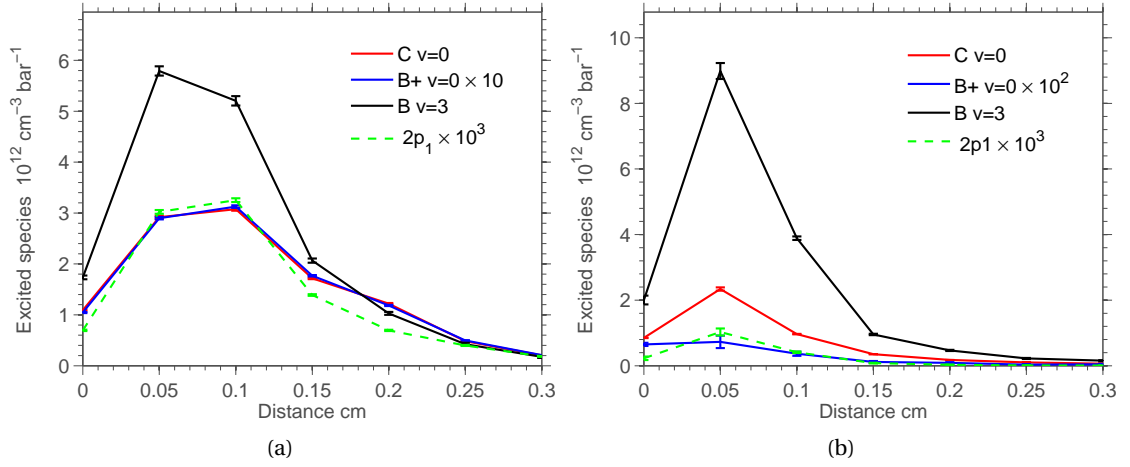


Figure 3.17: Spatial profile of the excited species populations, for the ascending phase (a) and the decaying phase (b). The applied voltage is 7 kV and the pressure is 1 bar.

**Spatial resolution of the streamers** The light is recorded for each phase (ascending and decaying) for a time long enough to ensure that all the light from the passing streamer is collected. The method to determine the average electron density and active species described in section 2.4.1 is applied.

The spectra associated with the streamers formed during the ascending and decaying phase are recorded during 50 ns starting at the beginning of the phase, as determined from time-resolved measurements. The optical system is then moved by steps of 0.5 mm in the direction of the propagation of the plasma, i.e. perpendicular to the electrodes, for 3 mm. The error bars shown represent the error made during the fit of the computed spectra to the experimental one, apart for the case of the 0.5 mm position, which has been performed five times in order to give an idea of the repeatability of the experiment. The error for this case is the sum of the standard deviation associated with the five experiments and the error induced by the fit.

**Excited species populations** Figure 3.17 shows the spatial evolution of the average population density of 4 excited species, namely  $N_2(C^3\Pi_u, \nu = 0)$ ,  $N_2(B^3\Pi_g, \nu = 3)$ ,  $N_2^+(B^2\Sigma_u^+, \nu = 0)$  and  $Ar(2p_1)$ . The differences already noted between ascending and decaying phases are also seen for other distances than 0.5 mm (time-resolved case). During the ascending phase, the excited species produced in the streamer start by a steep increase followed by a longer decay. The same is observed during the decaying phase, except that the decay is faster, and thus the plasma appears to go less far, as seen with the fast camera images 3.7.

**Reduced electric field estimation** The average reduced electric field as described by equation 2.20 is calculated for different combination of excited species and shown in figure 3.19. Ratios denoted C/B, Ar/B, B+/B, Ar/C, B+/C in the legends represent values of the electric

### Chapter 3. Experimental Characterization of the Plasma

field determined using the ratio of excited species' populations  $N_2(C^3\Pi_u, \nu = 0)/N_2(B^3\Pi_g, \nu = 3)$ ,  $Ar(2p_1)/N_2(B^3\Pi_g, \nu = 3)$ ,  $N_2^+(B^2\Sigma_u^+, \nu = 0)/N_2(B^3\Pi_g, \nu = 3)$ ,  $Ar(2p_1)/N_2(C^3\Pi_g, \nu = 0)$  and  $N_2^+(B^2\Sigma_u^+, \nu = 0)/N_2(C^3\Pi_g, \nu = 0)$  respectively.

It is to be noted that for the case of the decaying phase, the quality of the fits of the 760 nm zone are not very satisfactory for the larger distances. The determination of the population of argon excited species in the FPS background, which is very noisy, are not very reliable. The spectra recorded for the 2 mm position is shown in figure 3.18.

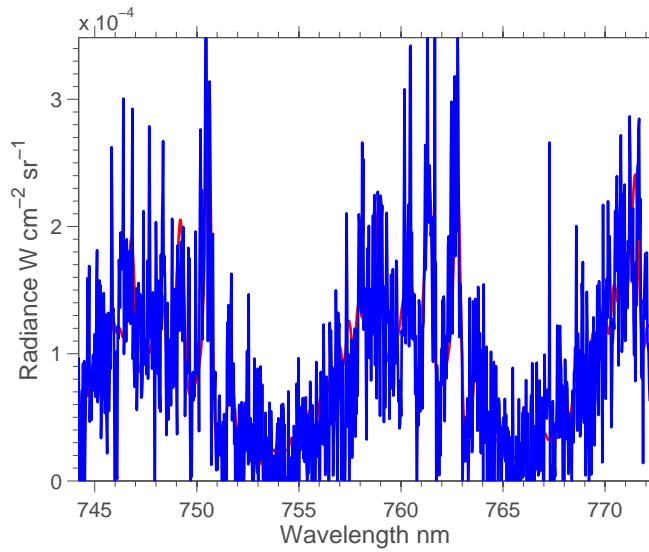


Figure 3.18: Measurement (blue solid line) and fit (red solid line) of the spectrum recorded at 2 mm from the upper electrode during the decaying phase. The conditions are 7 kV applied voltage and atmospheric pressure.

The quality of the fits for the other measurement points were satisfactory. The reduced electric field determined does not vary significantly with respect to the distance, apart for reduced electric fields determined from transitions involving the  $N_2(B^3\Pi_g)$  state, which increase as the distance increases.

This effect is attributed to the overpopulation of this state by processes other than electron-impact from the ground state, and is more pronounced during the ascending phase.

The reduced electric field was found to be much stronger during the ascending phase compared to the decaying phase. The reduced electric fields determined from different transitions were found to have very different values, especially in the case of the ascending phase.



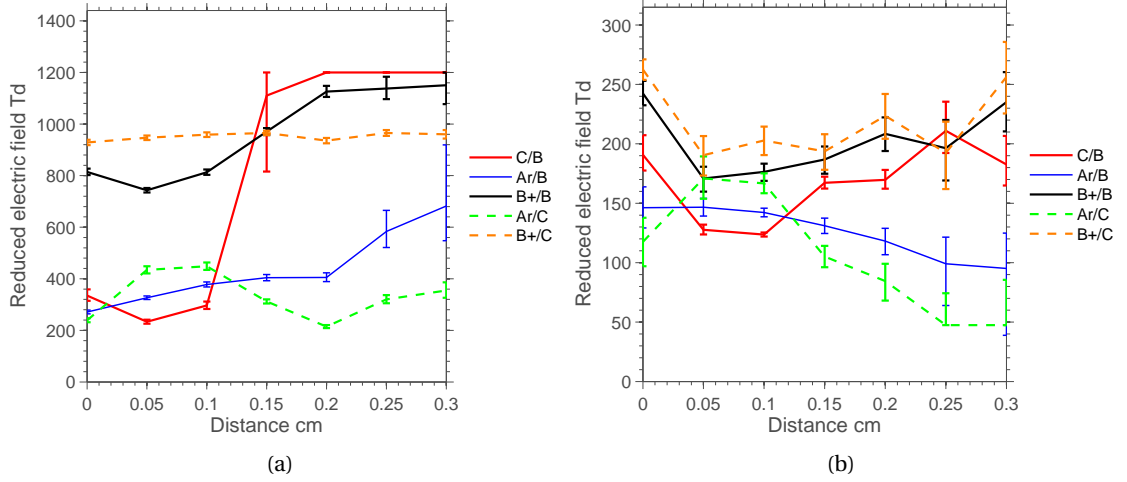


Figure 3.19: Spatial profile of the averaged electric field and normalized electron density for the axial direction, for the ascending phase (a) and the decaying phase (b). The applied voltage and corresponding pressure are: 7 kV, 1 bar.

**Averaged electron and metastable species densities estimation** The averaged electron density as computed with equation 2.23 using the averaged reduced electric field  $\hat{E}$  and the averaged electron density using the exponential fit as computed with equation 2.25, using transitions from the FPS,SPS,FNS and argon, are shown in figure 3.20. The population densities of two metastable excited states,  $N_2(A^3\Sigma_u^+)$  and  $O_2(a^1\Delta_g)$ , are also shown.

There is more than an order of magnitude difference between the two different averages for the electron density estimated for the ascending phase. If the thickness of the plasma is assumed to be 200  $\mu\text{m}$ . They are estimated as  $3.5 \cdot 10^{13} \text{ cm}^{-3}$  for the average electron density computed with equation 2.23 and  $2.0 \cdot 10^{15} \text{ cm}^{-3}$  for the average electron computed using the exponential fit. This difference is discussed in section 4.4 and is attributed to the location in space that the electron density represents. The exponential fit gives a value which is supposed to be closer to the electron density in the body of the streamer, just behind the head. It is consequently much higher than the electron density computed with 2.23 which is representative of the head of the streamer. For the decaying phase, maximum values of the averages are  $2.0 \cdot 10^{14} \text{ cm}^{-3}$  and  $5.0 \cdot 10^{15} \text{ cm}^{-3}$  respectively. For the ascending phase, the maximum value of the absolute densities of the  $N_2(A^3\Sigma_u^+)$  is estimated as  $2.0 \cdot 10^{16} \text{ cm}^{-3}$  and of the  $O_2(a^1\Delta_g)$  as  $8.6 \cdot 10^{15} \text{ cm}^{-3}$ , if the thickness of the plasma is supposed to be  $p \cdot d = 0.02 \text{ cm}$ . For the decaying phase, the tendency is reversed, with a maximum value of the absolute densities of the  $N_2(A^3\Sigma_u^+)$  estimated as  $8.5 \cdot 10^{15} \text{ cm}^{-3}$  and of the  $O_2(a^1\Delta_g)$  as  $3.2 \cdot 10^{16} \text{ cm}^{-3}$ . This seems natural since the excitation cross section of  $N_2(A^3\Sigma_u^+)$  is higher than that of  $O_2(a^1\Delta_g)$  for high electron energies.

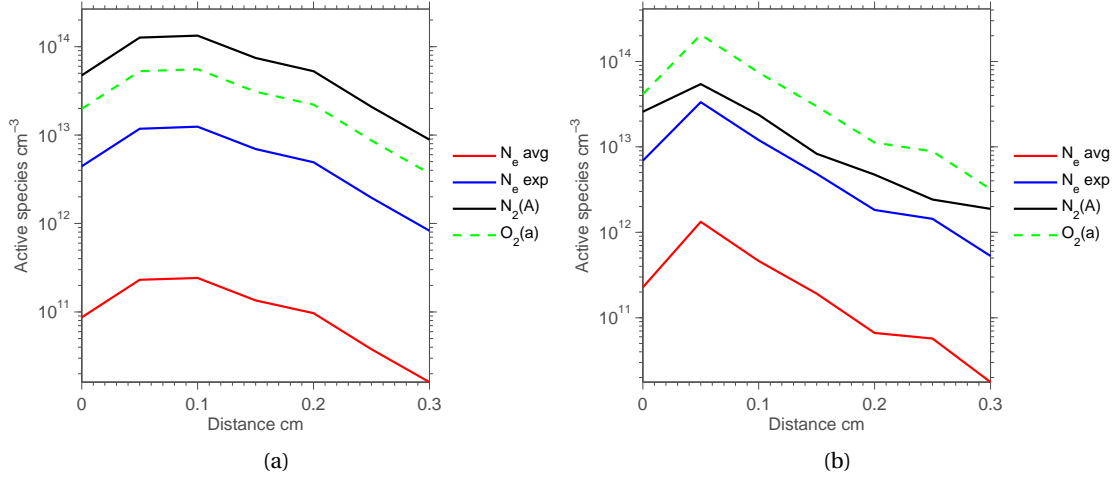


Figure 3.20: Spatial profile of the averaged electron density, the averaged electron density obtained from the exponential fit and the population density of metastable states in the direction of propagation of the streamer, for the ascending phase (a) and the decaying phase (b). The applied voltage and corresponding pressure are: 7kV, 1 bar.

The measurement of the electron density produced by a 5 to 8 kV and 10 nanosecond pulsed experiment at atmospheric pressure in heated air (1000 K) was performed in [Rusterholtz et al., 2013]. The electron density is measured using the Stark broadening of  $H_{\alpha}$  and was ranging from  $2.0 \cdot 10^{14}$  to  $2.1 \cdot 10^{15} \text{ cm}^{-3}$  as a function of time. In the same experimental setup, the production of  $N_2(A^3\Sigma_u^+)$  was investigated experimentally in [Stancu et al., 2010] with the cavity ring-down spectroscopy (CRDS) technique and the average density during the 100 ns after the nanosecond pulse onset was found to be of  $5 \cdot 10^{14} \text{ cm}^{-3}$ . This measurement is of the same order of magnitude as the present estimate. The smaller value found in the CRDS experiment is believed to be due to the higher quenching rate occurring in heated air due to the larger amount of oxygen atoms which are efficient quencher of the  $N_2(A^3\Sigma_u^+)$  state and due to the time averaging over the 100 ns. An analytical and numerical investigation was carried in [Naidis, 2010] on the topic of  $N_2(A^3\Sigma_u^+)$  generation by streamers in  $N_2$  gas with small admixture of oxygen. This investigation gives an estimate on the order of  $10^{15} \text{ cm}^{-3}$ .

The main advantage of the present technique over absorption based techniques is that it enables to take into account the whole volume of the plasma provided the collection area of the optical system is large enough. The determination of the volume of the plasma being not trivial in a SDBD configuration, this asset is important. This enables the measurement of total numbers of molecules for a particular geometry.

Experimental data on the production of  $O_2(a^1\Delta_g)$  by nanosecond high-voltage pulses in air could not be found in the literature and would be of great interest for the experimental validation of the diagnostic method.

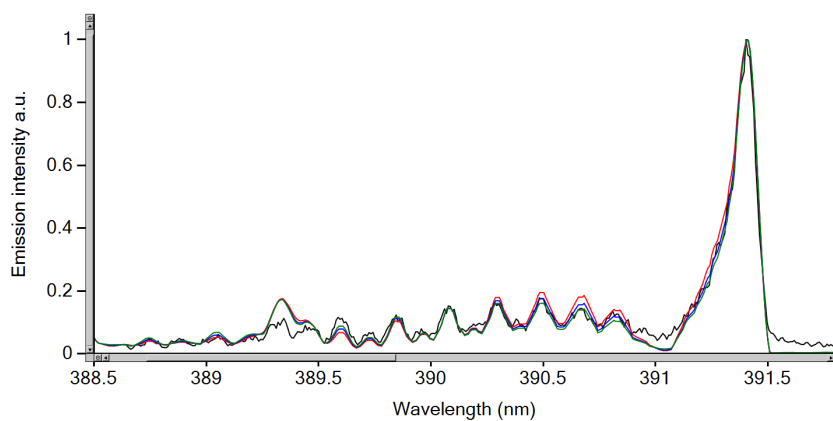
#### 3.3.4 Effect of the plasma on the gas temperature

The temperature of the gas can be determined provided that the rotational levels are at equilibrium. Indeed, the population of rotational states depends on the rotational temperature (see section 2.5), and can thus be determined from the shape of the bands. The rotational temperature is then assumed to represent the translational temperature owing to the fact that electron collisions do not change appreciably the angular momentum of the molecules. The temperature determined with Specair and with the in-house spectral code (see section 2.5) is shown for an applied voltage of 7 kV. The parameters for the fit in Specair are: trapezoidal slit of 0.15 nm width for the base and 0.025 width for the top. Resolution of the in-house code is 0.08 nm FWHM (Gaussian) for this computation. The accuracy of the in-house code is good for the FNS apart for the larger rotational lines, which is probably due to the inaccurate spectroscopic model used for location of the lines in the frequency domain. The accuracy for the SPS is not as satisfactory, probably due to the neglect of lambda doubling occurring in this case.

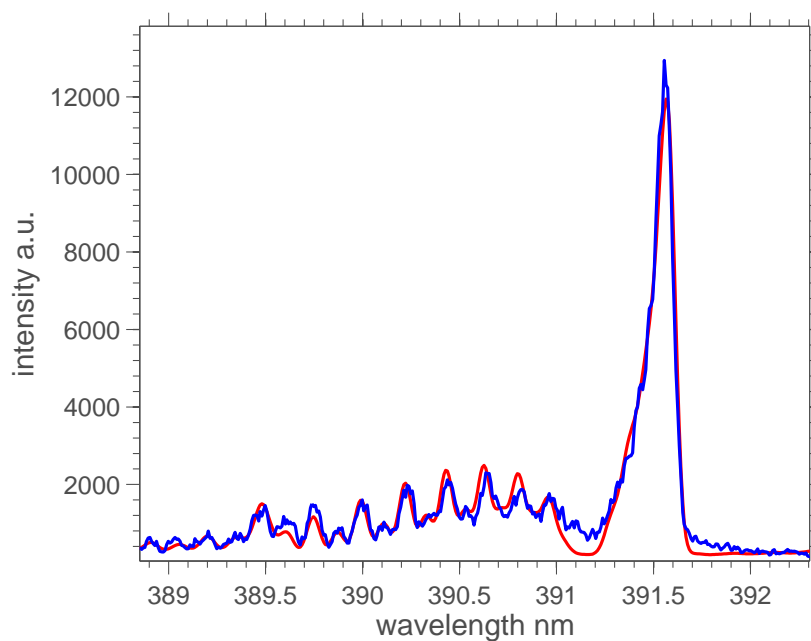
The temperature for the ascending phase can be estimated as  $350 \pm 50$  K and for the decaying phase, occurring after 1  $\mu$ s in this case, at  $400 \pm 50$  K.

The increase of temperature in the decaying phase is believed to be due to the release of heat during the ascending phase. The temperature during the ascending phase is, however, explained only by a long term heating of the gas (the light is collected for several thousand cycles). The amount of heat released in the gas during one pulse is therefore even lower.

These measurements are to be compared with the experiments conducted in [Starikovskii et al., 2009], where the temperature increase due to high voltage pulses was measured by means of emission spectroscopy during the pulse. A secondary pulse was sent in the plasma 1  $\mu$ s after the first pulse, enabling the measurement of the increase in temperature after 1  $\mu$ s. The measurements show a similar trend for the lower voltage (14 kV), with a rotational temperature of 330 K for the first pulse and a temperature of 380 K for the second pulse. They claim that the first temperature measured is increased with respect to room temperature (290 K) of 40 K. The low repetition rate of their experiment (1-100 Hz) suggests that the global temperature increase at the beginning of the pulse is solely due to energy transfer from electrons to rotational energy directly and ultrafast heating during the pulse, as investigated in [Rusterholtz et al., 2013]. Their measurement of the rotational temperature is made using 2000 accumulation of 0.25 nm FWHM resolution spectra of the first band of the second positive system. As shown in figure 3.22, the accuracy of such a measurement is difficult to assess and is probably not better than 50 K. Time resolved measurements performed in the present thesis (see figure 3.23) show that even at the beginning of the pulse recorded, corresponding to the head of the streamer, the temperature is already similar to the temperature measured in the whole streamer and no increase can be detected. The fast equilibration of the rotational levels of the excited species with the rotational levels of the neutral gas can be estimated (see [Rusterholtz et al., 2013]) as



(a)



(b)

Figure 3.21: Fit of (0-0) band of the FNS using Specair (a) and the in-house code (b) for the ascending phase. The different curves in (a) are for rotational temperature 300 K (red solid line), 350 K (blue solid line) and 400 K (green solid line). The rotational temperature for (b) is 350 K.

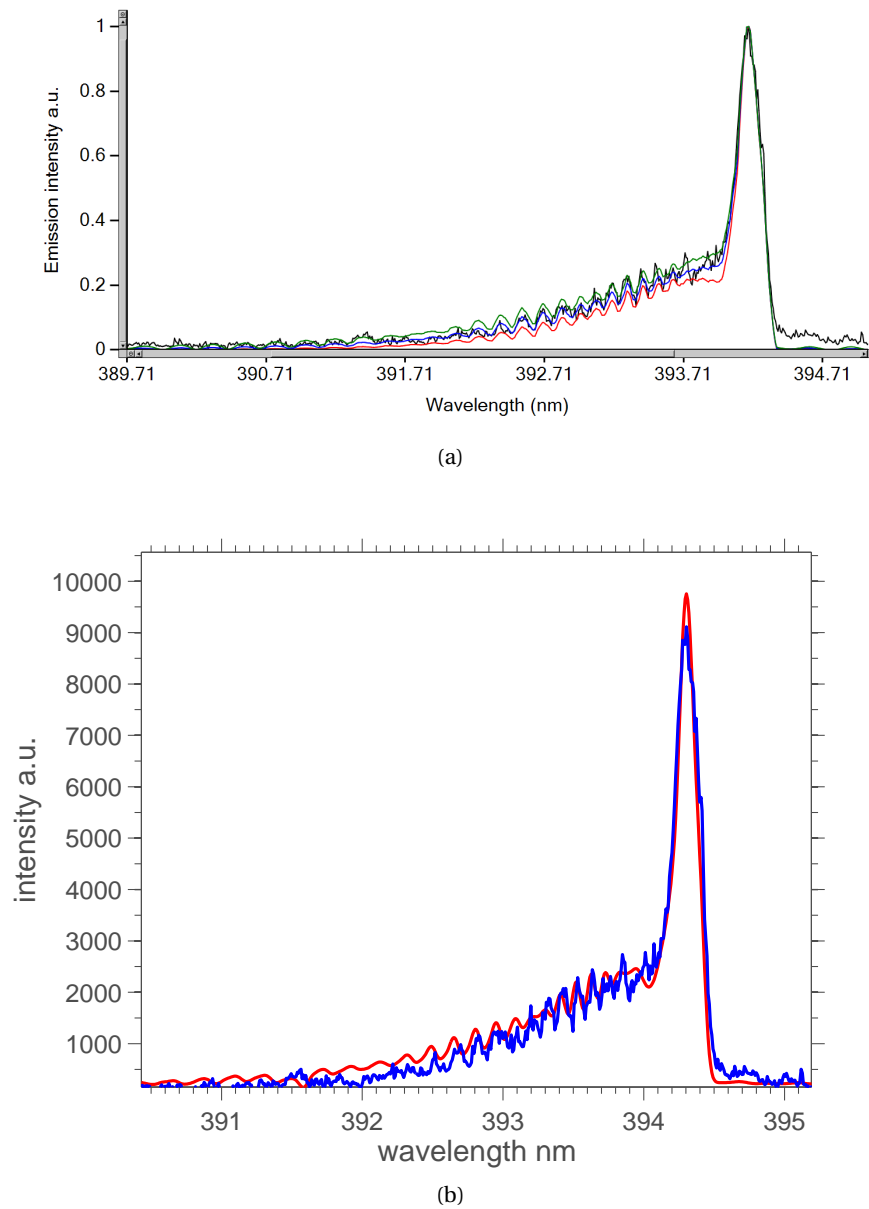


Figure 3.22: Fit of the (2-5) band of the FPS using Specair (a) and the in-house code (b) for the decaying phase (after  $1 \mu\text{s}$ ). The different curves in (a) are for rotational temperature 300 K (red solid line), 400 K (blue solid line) and 500 K (green solid line). The rotational temperature for (b) is 400 K.

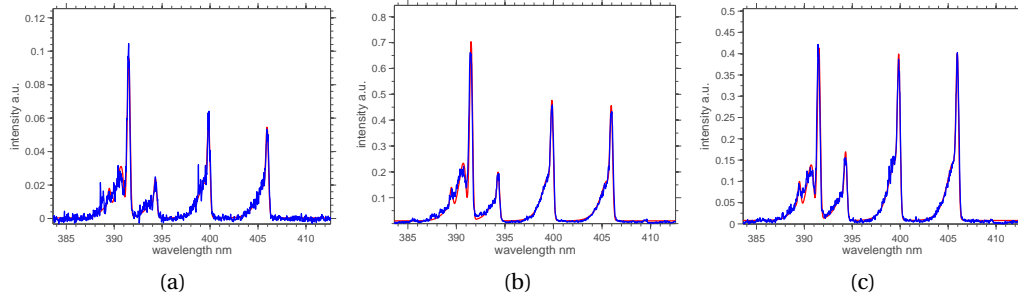


Figure 3.23: Emission spectra recorded during the ascending phase at different times with respect to the reference time  $t_{ref}$ .  $t = t_{ref} + 2.5$  ns (a),  $t = t_{ref} + 5$  ns (b) and  $t = t_{ref} + 10$  ns (c). The fit of the spectra is performed with a rotational temperature of 300 K and FWHM of 0.3 nm. The light is recorded during 2 ns.

1 ns, which supports the use of OES for gas temperature measurements.

For conditions typical of the other experiments performed in this thesis, the duration of the pulse was 200 ns, and generally the resolution of the spectra was fitted with a resolution of 0.3 nm FWHM and with a rotational temperature of 300 K. At this resolution, the uncertainty on the temperature is worse than  $\pm 50$  K, which makes accurate measurements of the rotational temperature not feasible. However, the rotational temperature can be ascertained to be less than 500 K for all conditions tested.

In addition, the global energy released to the gas can also be visualized by the compression wave sent in the gas, as can be seen with Schlieren experiments. Such experiments were performed with the same actuator in [Peschke et al., 2011].

#### 3.3.5 Effect of the polarity on streamer propagation

The high-voltage was connected to the lower electrode and the ground was connected to the upper electrode. All other characteristics were kept identical.

**Excited species populations** The evolution of the excited species with respect to the distance of propagation is shown in figure 3.24. The decrease in voltage is associated with the decaying phase, and the increase in voltage occurring after is associated with the ascending phase. If these phases are compared to the corresponding phases for the positive pulse, a similar behavior is observed. The population density of the  $N_2^+(B^2\Sigma_u^+, v = 0)$  state is slightly less than an order of magnitude lower in the decaying phase than in the ascending phase, which is to be compared with the positive pulse case in which the ratio between phases is of about 40. The population density of every excited species is approximately 3 times larger for the negative pulse than for the positive pulse during the decaying phase. During the ascending phase, the population density is a factor 2 to 3 lower for the negative pulse compared to the positive one,

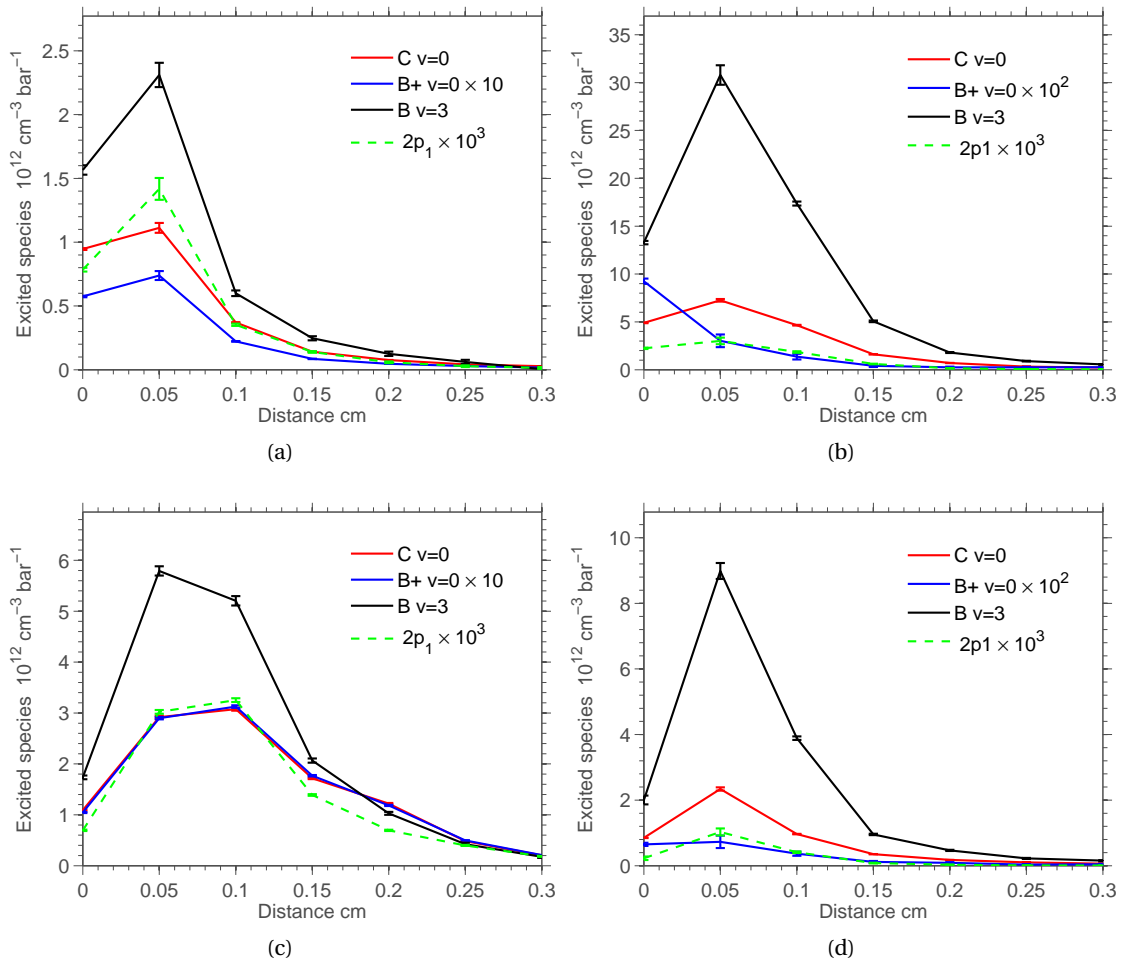


Figure 3.24: Spatial profile of the excited species populations for a negative nanosecond pulsed applied voltage, for the ascending phase (a) and the decaying phase (b). The applied voltage and corresponding pressure are: -7 kV, 1 bar. Comparison with the positive pulse is shown in (c) and (d).

depending on the species.

**Reduced electric field estimation** The reduced electric fields determined from several transitions are shown in figure 3.25 in function of the distance of propagation of the streamer. The ascending phase exhibits again a substantially higher reduced electric field when compared to the decaying phase. The difference is however less marked than for the positive pulse. The values of the reduced electric fields are lower than for the positive pulse for the ascending phase and higher than for the positive pulse during the decaying phase.

These differences are intuitively easy to interpret. The negative streamer which arises during the decaying phase is formed due to a large voltage difference applied between the electrodes,

### Chapter 3. Experimental Characterization of the Plasma

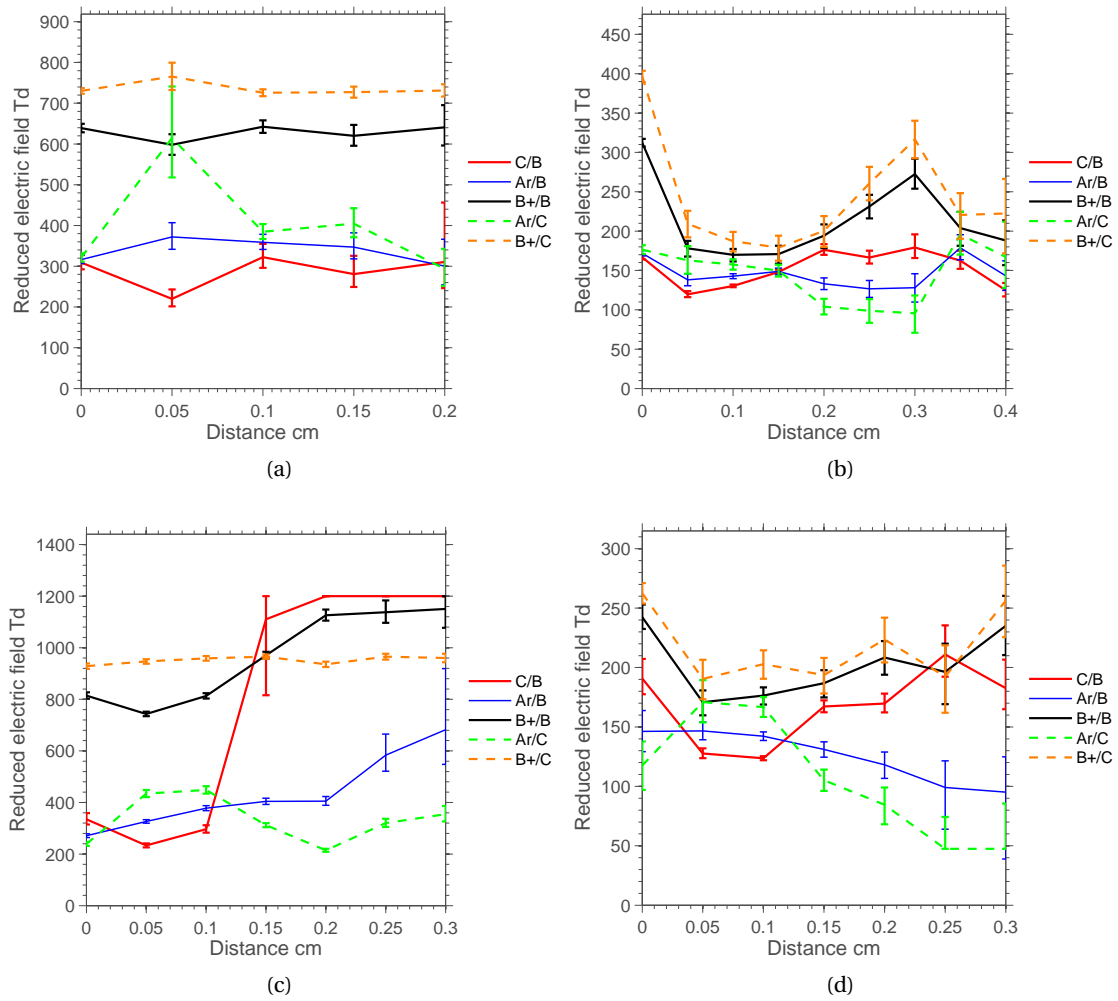


Figure 3.25: Spatial profile of the averaged electric field and normalized electron density for the axial direction, for the ascending phase (a) and the decaying phase (b). The applied voltage and corresponding pressure are: -7 kV, 1 bar. Comparison with the positive pulse is shown in (c) and (d).



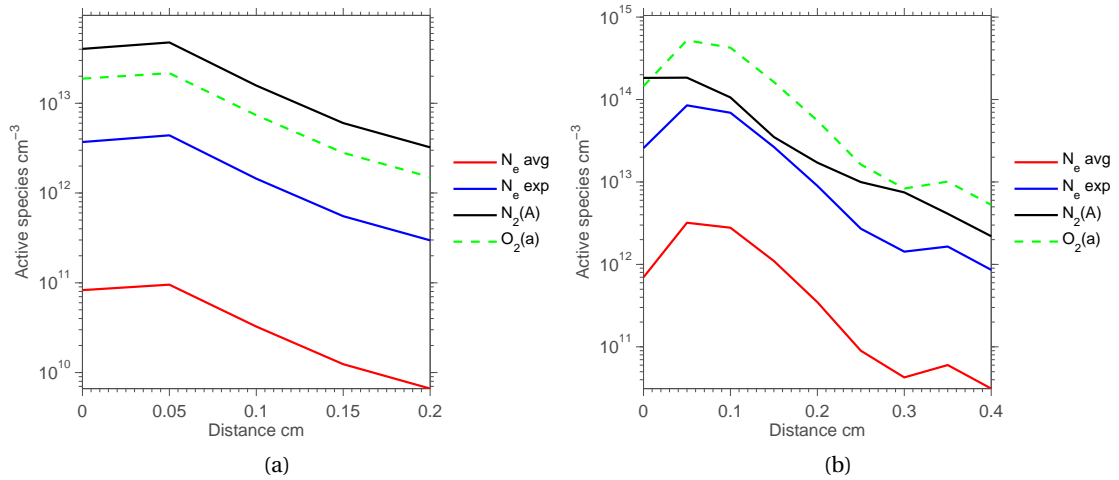


Figure 3.26: Spatial profile of the averaged electron density, the averaged electron density obtained from the exponential fit and the population density of metastable states in the direction of propagation of the streamer, for the ascending phase (a) and the decaying phase (b). The applied voltage and corresponding pressure are: -7kV, 1 bar.

and a strong electric field appears around the upper electrode. On the other hand, the positive streamer formed during the ascending phase occurs due to the electric field which sets between the increasing positive voltage at the electrode and the negative voltage due to negative charges remaining in the gas and on the surface of the dielectric. These charges are distributed in the vicinity of the upper electrode, closer than the lower electrode. The applied electric field is thus less intense for the case of a negative pulse than for a positive pulse.

**Averaged electron and metastable species densities estimation** The averaged electron density and average metastable population densities are shown in figure 3.26. The trend compared to the positive pulse follows from the trend for the excited species.

### 3.3.6 Effect of pressure on streamer propagation

The comparison is made between the ascending and decaying phase for a positive pulse at different pressures, and different voltages. The streamer should be similar (= follow similarity rules) for a same ratio of voltage over pressure  $V/p$ , which can be related to the reduced electric field  $E/N$ , and with a same product pressure times distance  $p \cdot d$  as discussed in section 2.2. While keeping a constant  $V/p$  is trivial to achieve experimentally, a constant  $p \cdot d$  is more difficult since it would involve the changing of the dielectric thickness, changing the capacitance and therefore changing the electric properties of the electrical setup. Moreover, the alignment of the SDBD with the optical setup would have been more difficult as well. It was thus chosen not to change the dielectric thickness, even if this makes the interpretation of the results more difficult.

The streamer can develop only according to Meek's criterion as discussed in section 2.2, i.e. the streamer develops only after a certain pressure for a given  $V/p$ . The values at which the streamer should develop were calculated in section 4.3.4 and give for example a value of 3.5 kV at atmospheric pressure, which is clearly overestimated with respect to the experiments. As seen in section 3.3.2, the plasma was developing already at 2 kV, although it was very weak and might not ignite for every pulse. This discrepancy can be explained by local enhancement of the electric field at the electrode's edge due to inhomogeneity coming from the manufacturing process or developing over time due to etching. During the experimental campaign in the vacuum chamber, the plasma was found to be not very stable (it was intermittent) for applied voltages of less than about 2.5 kV at 0.2 bar. For this reason, the lowest applied voltage at 0.2 bar was 2.8 kV. Even at this rather high applied voltage, the plasma appeared to be weaker at the end of the campaign, after several hours of operation, and affects measurements taken in the 760 nm zone. Due to this restriction, the lower voltage selected was 2.8 kV and to respect the  $V/p$  ratio, the applied voltage at 1 bar would have been 14 kV, which was not possible with the high-voltage generator used (max. 10 kV). Therefore, a compromise has been made and two  $V/p$  ratios were taken, 7 kV/bar at 1 and 0.5 bar and 14 kV/bar at 0.5, 0.3, 0.25 and 0.2 bar. Additionally, this allowed to determine the influence of the increase in  $V/p$  at 0.5 bar.

**Temporal evolution of the streamer** Fast camera images were acquired at pressures 0.5 bar and 3.5 kV, 0.5 bar and 7 kV and 0.25 bar and 3.5 kV. They are shown in figures 3.27, 3.28 and 3.29. Time-resolved spectroscopy is performed at 0.25 bar and 3.5 kV. The excited species population densities determined from the time-resolved spectroscopy are shown in figure 3.30.

### 3.3. Experimental results

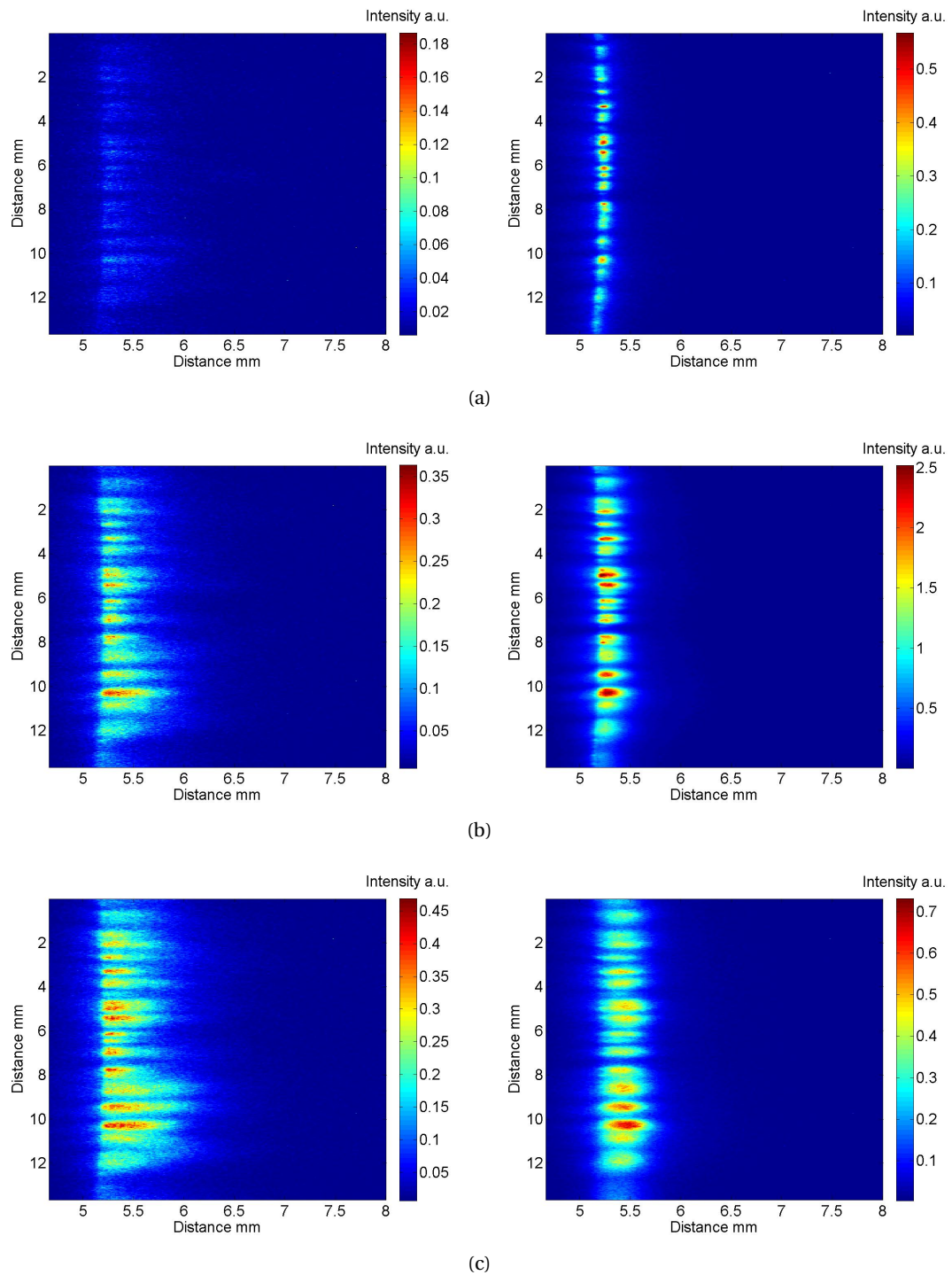


Figure 3.27: Fast camera images of the streamer propagation. The applied voltage is 3.5 kV, the pressure is 0.5 bar and the gate exposure is 5 ns. The time at which images are taken correspond to the trigger time  $t_{\text{ref}}$  (a) plus 5 and 10 ns respectively for (b,c) for the ascending phase. The images for the decaying phase (right) are delayed by 165 ns with respect to the ascending phase. The edge of the upper electrode is located at 5.2 mm.

### Chapter 3. Experimental Characterization of the Plasma

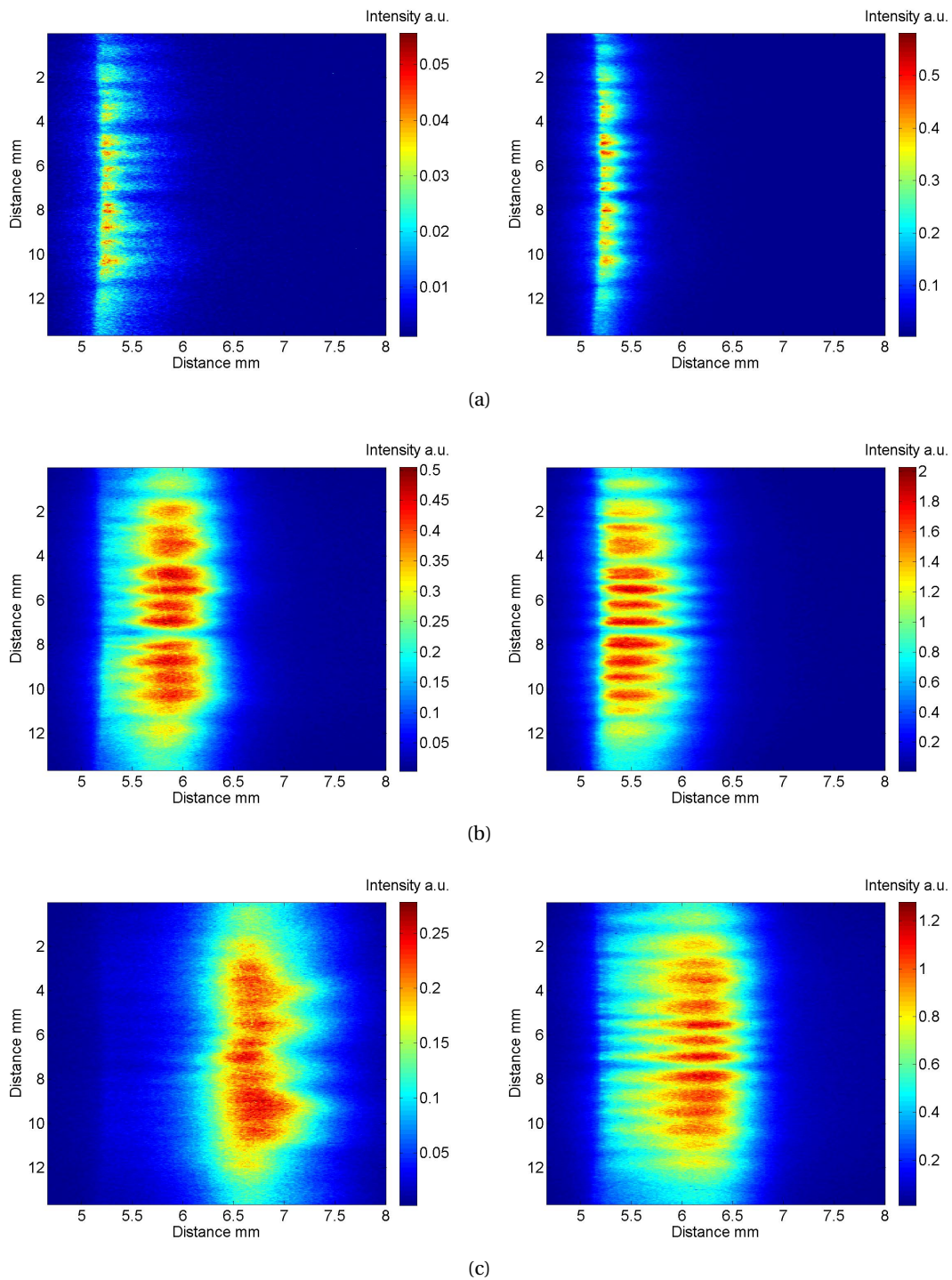


Figure 3.28: Fast camera images of the streamer propagation. The applied voltage is 7 kV, the pressure is 0.5 bar and the gate exposure is 5 ns. The time at which images are taken correspond to the trigger time  $t_{\text{ref}}$  (a) plus 5 and 10 ns respectively for (b,c) for the ascending phase. The images for the decaying phase (right) are delayed by 165 ns with respect to the ascending phase. The edge of the upper electrode is located at 5.2 mm.

### 3.3. Experimental results

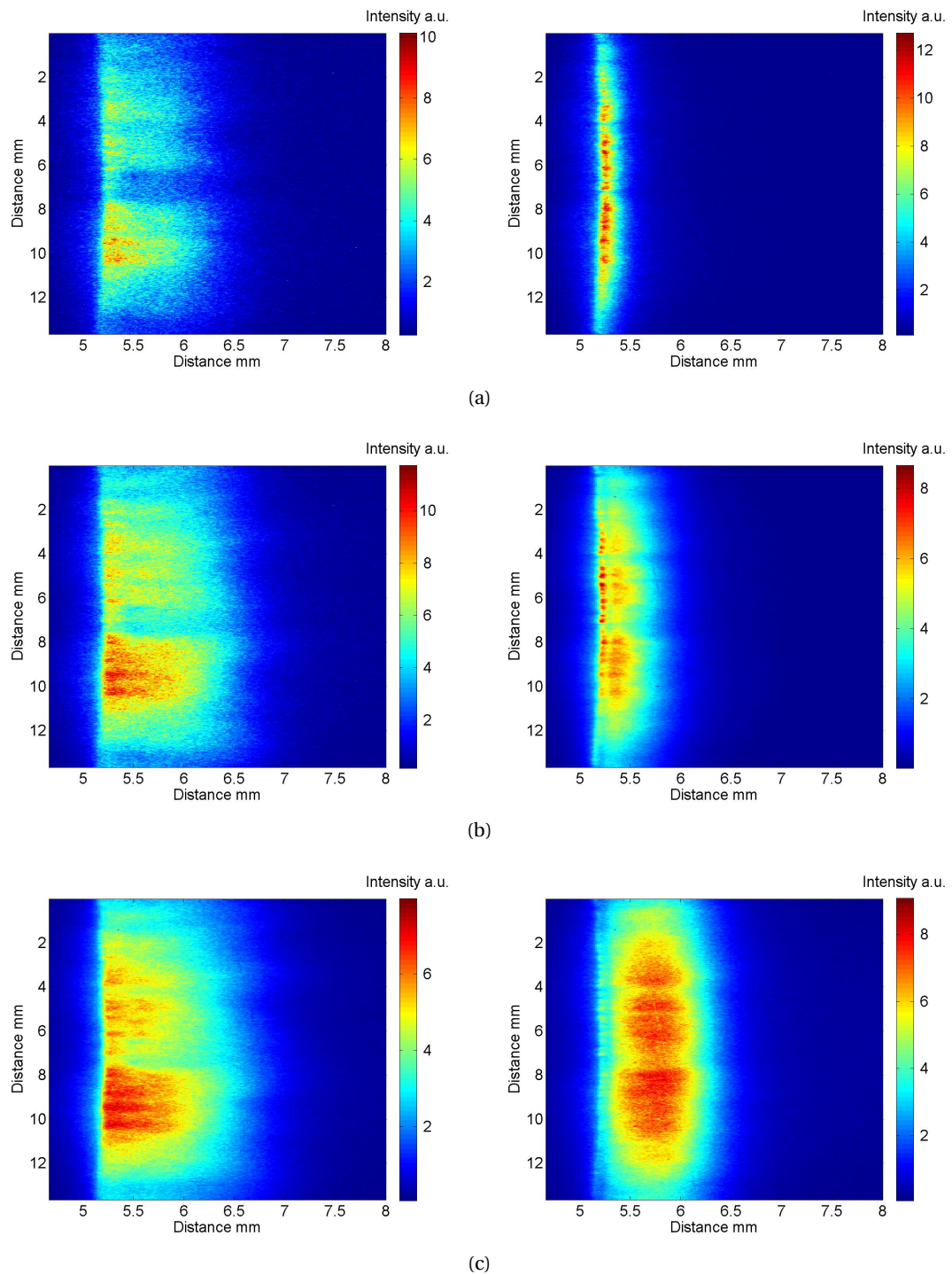


Figure 3.29: Fast camera images of the streamer propagation. The applied voltage is 3.5 kV, the pressure is 0.25 bar and the gate exposure is 5 ns. The time at which images are taken correspond to the trigger time  $t_{\text{ref}}$  (a) plus 5 and 10 ns respectively for (b,c) for the ascending phase. The images for the decaying phase (right) are delayed by 155 ns with respect to the ascending phase. The edge of the upper electrode is located at 5.2 mm.

### Chapter 3. Experimental Characterization of the Plasma

---

The streamer produced during the ascending phase is again propagating further and faster than the streamer produced during the decaying phase. However, the intensity of light is larger during the decaying phase. The aspect of the plasma seems more diffuse at lower pressures, and propagates further. The analysis of the fast camera images shows that the plasma propagates the farthest for the 0.5 bar and 7 kV case. For the same  $V/p$  and a pressure of 0.25 bar, the plasma propagates less far than for the 0.5 bar case. Since the product  $p \cdot d$  is twice lower at 0.25 bar compared to 0.5 bar, it is expected that the number of collisions between free electrons and neutrals are twice as few. The effect on the streamer will be as follows. The reduced electric field  $E/N(\mathbf{x})$  is constant for a same point  $\mathbf{x}$  in space due to the same  $V/p$ . Therefore if the streamer developing at lower pressure is enlarged by a factor  $\alpha$ , it will see a lower reduced electric field  $E/N(\alpha\mathbf{x})$  at the scaled location  $\alpha\mathbf{x}$  (for the SDBD geometry). This effect reduces the propagation of the streamer in the case of the lower pressure when compared to the higher pressure, and the larger the reduction the larger the inhomogeneity of the electric field is. Thus it can be concluded that in a plane parallel geometry, there is no such effect and for a corona actuator for example (wire-to-wire geometry) the effect is larger.

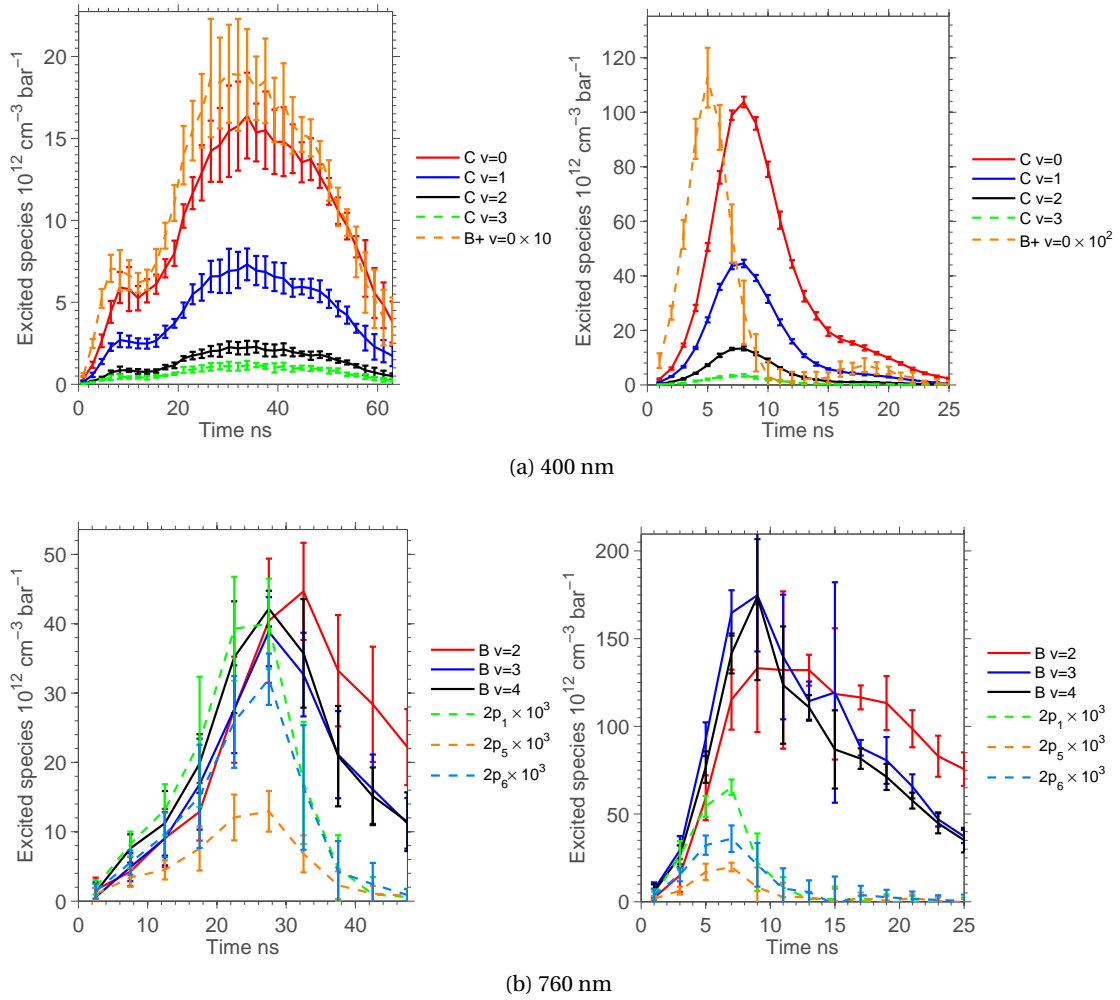


Figure 3.30: Temporal evolution of the excited species populations, for the ascending phase (left) and the decaying phase (right) for a 3.5 kV pulse at 0.25 bar. The excited species are inferred from emission spectroscopy in the 400 nm spectral zone (a) and in the 760 nm spectral zone (b).

The time-resolved spectra recorded to obtain the evolution of the excited species shown in figure 3.30 were acquired with a gate width of 2 ns for all but the 760 nm zone during the ascending phase, due to the very long exposures required and to the very long duration of the light emitted during this phase. Indeed, the plasma formed during the ascending phase was found to be more complex than for the other cases (pressures and phases), displaying two waves of propagation which are best pictured with the fast camera images. The first wave seems to ignite the plasma, and then a second one develops again from the electrode but much stronger. This is also seen in the evolution of the excited species. A similar difference between the ascending and decaying phase compared to the atmospheric pressure is seen. The population density of the  $\text{N}_2^+(B^2\Sigma_u^+, v=0)$  state, is however only about half during the decaying phase than in the ascending phase. The same trend is followed by the other species. Overall,

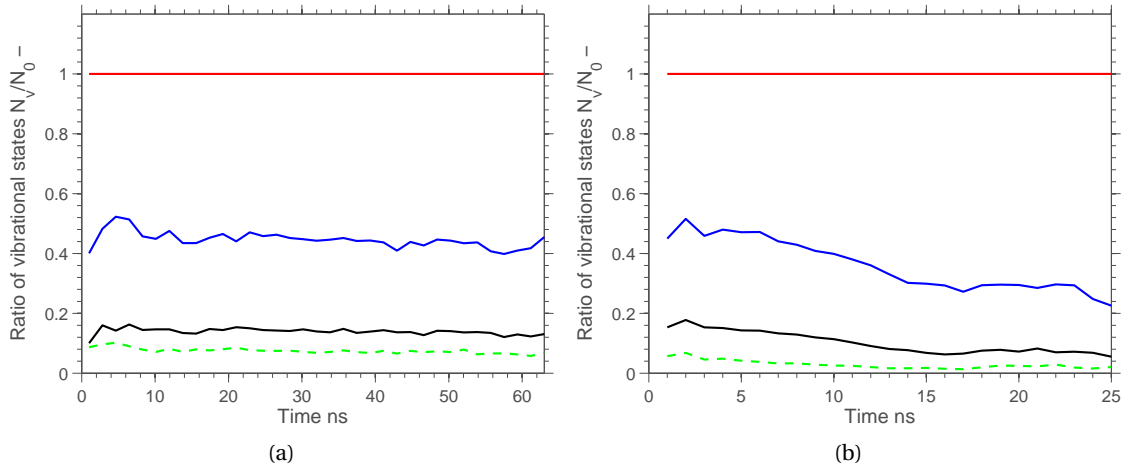


Figure 3.31: Temporal evolution of the ratio of vibrational levels  $N_2(C^3\Pi_u, \nu)/N_2(C^3\Pi_u, \nu = 0)$  for the ascending phase (a) and the decaying phase (b) compared to the theoretical distribution (c) for a 3.5 kV pulse at 0.25 bar. The curves corresponding to the vibrational levels  $\nu = 0, 1, 2, 3, 4$  are the red, blue and black solid lines, green and orange dash-dotted lines respectively.

the maximum intensity is considerably higher during the decaying phase. This is attributed to the higher applied reduced voltage  $V/p$  compared to the atmospheric pressure case. The ratio of vibrational levels of  $N_2(C^3\Pi_u)$  are also populated according to the Franck-Condon factors, as can be seen in figure 3.31

**Spatial evolution of the streamer** The comparison of the propagation of the streamer at different pressures are shown in figures 3.32 and 3.33 for  $V/p = 7\text{kV}/\text{bar}$  and  $14\text{ kV}/\text{bar}$  respectively. The overall behavior follows the same trend observed with the fast camera images, but is more clearly visualized with the spatial evolution of the excited species. An interesting feature is the evolution of the population density of the  $N_2(C^3\Pi_u)$  state compared with that of the  $N_2^+(B^2\Sigma_u^+, \nu = 0)$  state. During the ascending phase, the ratio remains more or less constant. During the decaying phase on the contrary, the maximum population density of the  $N_2^+(B^2\Sigma_u^+, \nu = 0)$  state increases with respect to that of the  $N_2(C^3\Pi_u)$  state with decreasing pressure. This is related with an increased reduced electric field as is shown in the following.



### 3.3. Experimental results

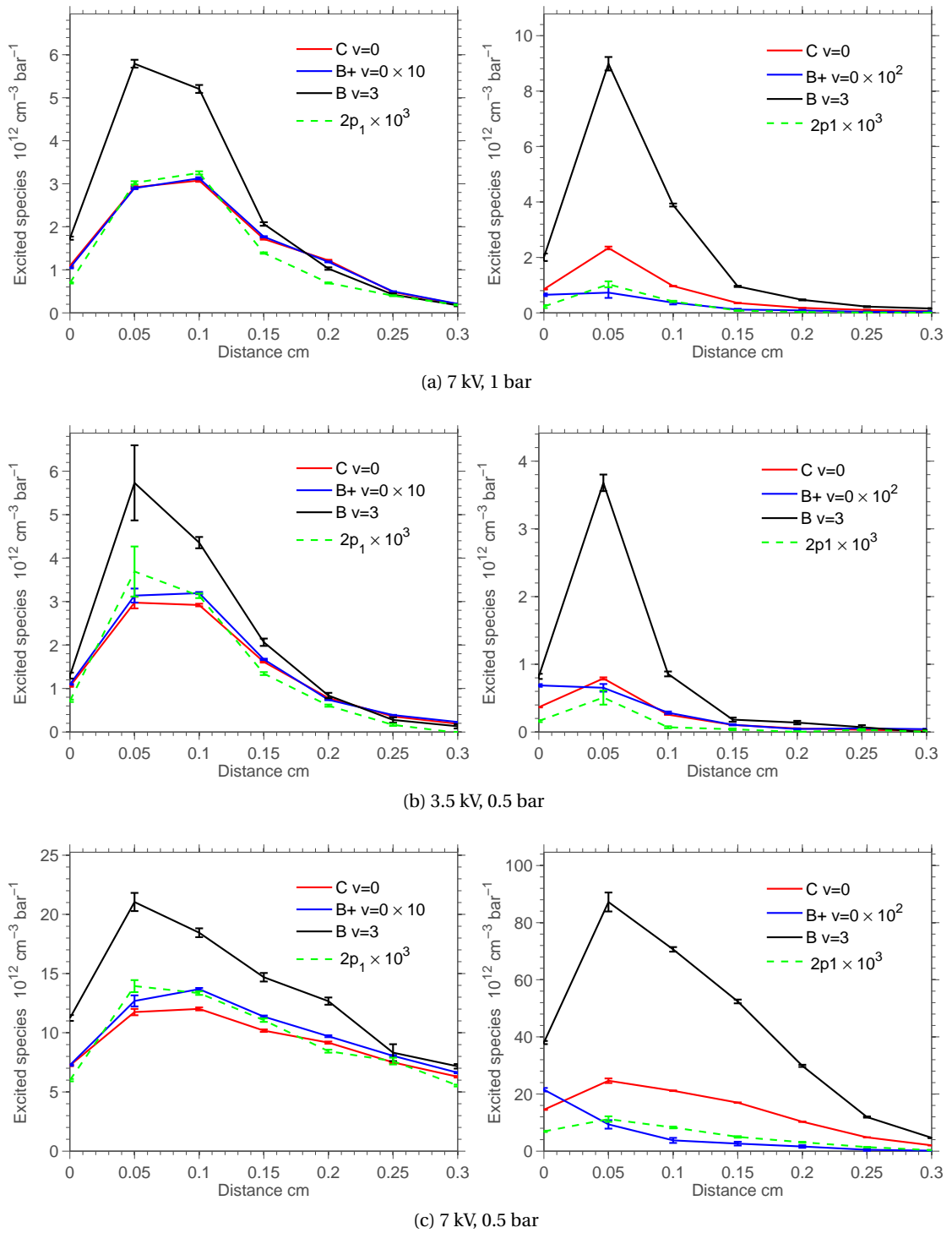


Figure 3.32: Spatial profile of the excited species populations, for the ascending phase (left) and the decaying phase (right). The applied voltage and corresponding pressure are: 1 bar, 7 kV (a), 0.5 bar, 3.5 kV (b) and 0.5 bar, 7 kV (c).

### Chapter 3. Experimental Characterization of the Plasma

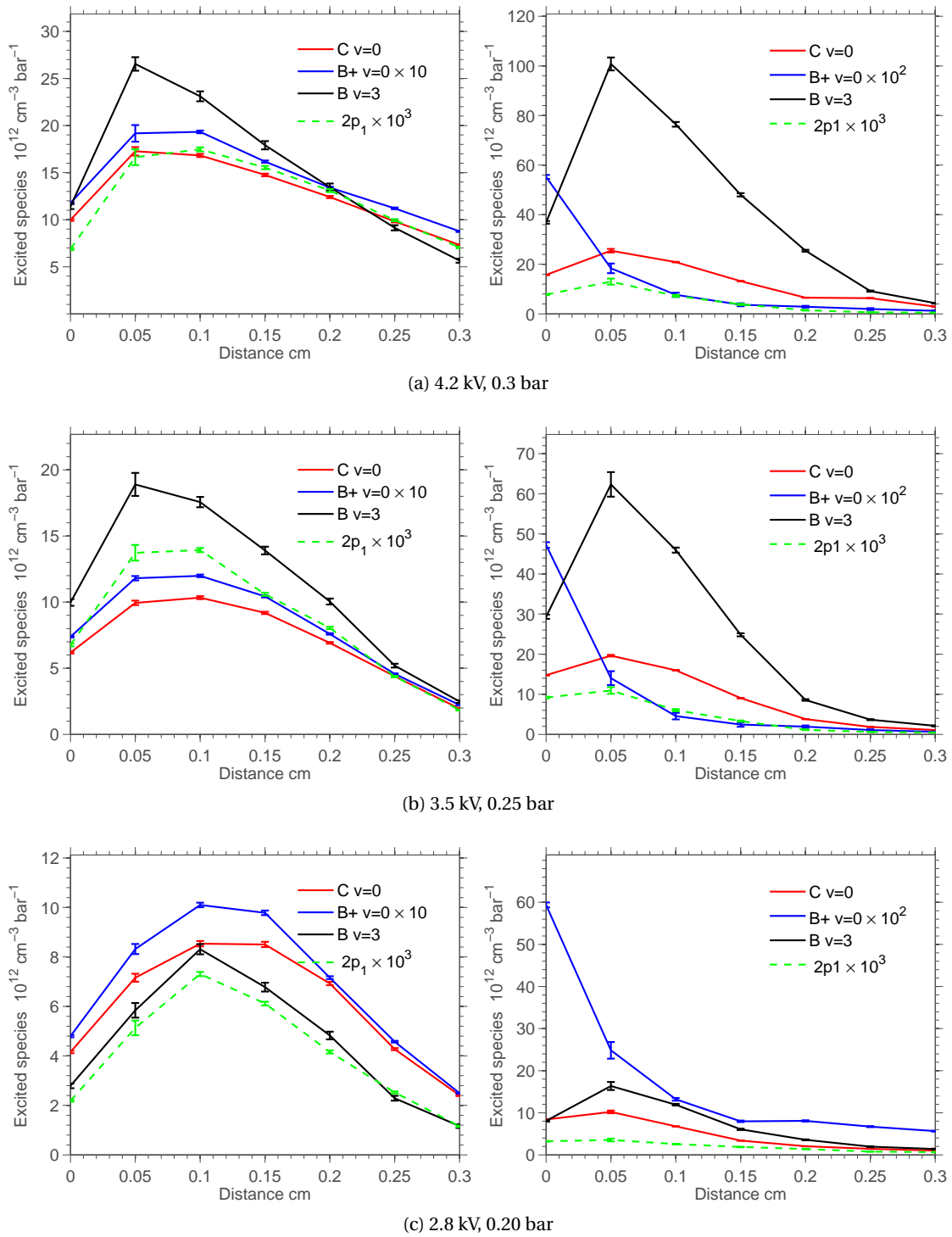


Figure 3.33: Spatial profile of the excited species populations, for the ascending phase (left) and the decaying phase (right). The applied voltage and corresponding pressure are: 0.3 bar, 4.2 kV (a), 0.25 bar, 3.5 kV (b) and 0.2 bar, 2.8 kV (c).

**Reduced electric field and averaged electron density estimation** The reduced electric field as computed with transitions B+/C and the average electron density obtained using the exponential fit are shown in figures 3.34 and 3.35. The electron density scales linearly with the pressure (or the density  $N$ ) for the ascending phase, despite that the  $p \cdot d$  value was not kept constant. It can be seen that it does not follow the same scaling for the decaying phase, with more than quadratic decrease in density with the pressure. The length of the streamer does not follow a simple scaling for both phases. The length of the streamers during the ascending phase increases mainly with the applied voltage, thus diminishes with pressure for a same reduced electric field, as discussed in the beginning of this section. The length of the streamers for the decaying phase remains more or less constant for all conditions, with values between 3 and 5 mm. At 0.2 bar, the decaying phase exhibits a much larger reduced electric field. As said above, the plasma was not very stable at this pressure. However, the ratio of the FNS and FPS 0 bands used for the determination of the reduced electric field plotted here were recorded simultaneously, thus discarding a possible difference between measured excited species populations performed at different moments. This tendency of increased reduced electric field was also noted at a pressure of about 0.3 bar for a negative streamer in [Starikovskii et al., 2009].

### Chapter 3. Experimental Characterization of the Plasma

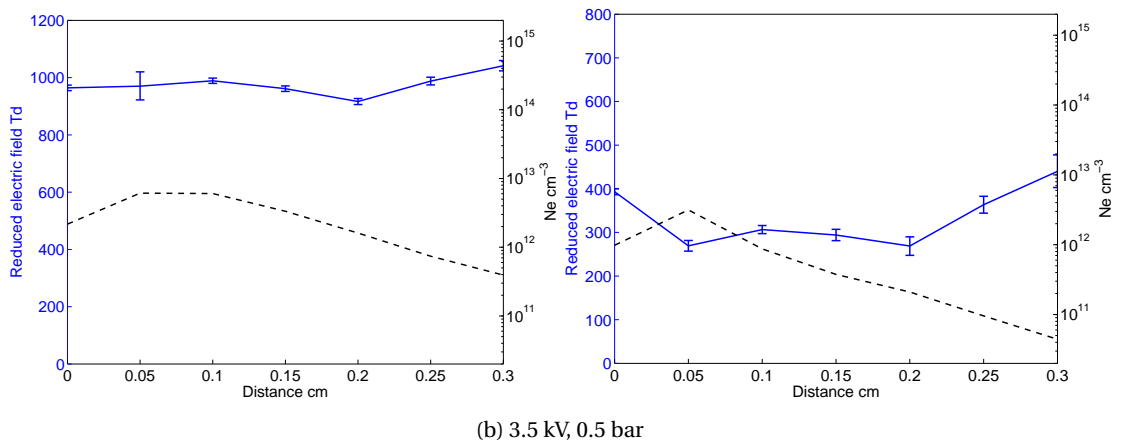
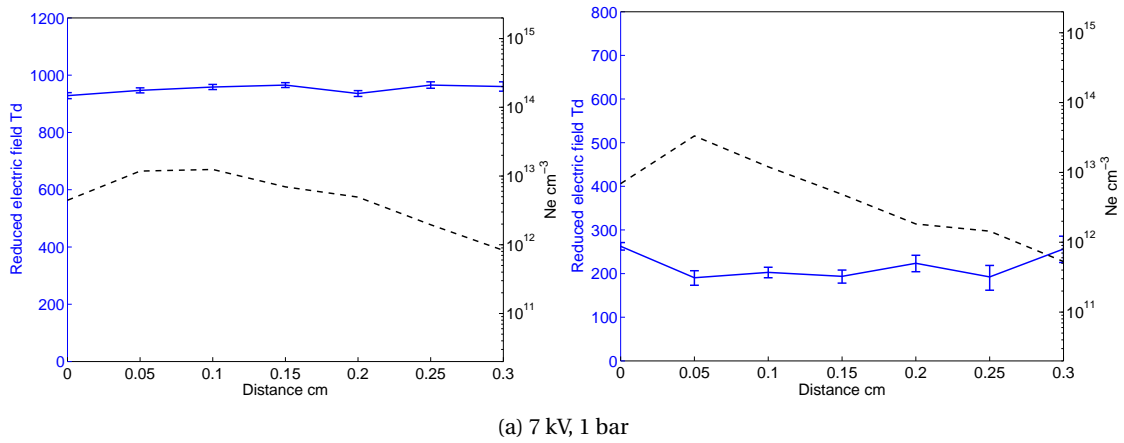


Figure 3.34: Spatial profile of the averaged electric field and normalized electron density in the direction of propagation of the streamer, for the ascending phase (left) and the decaying phase (right). The applied voltage and corresponding pressure are: 7kV, 1 bar (a) and 3.5 kV, 0.5 bar (b).

### 3.3. Experimental results

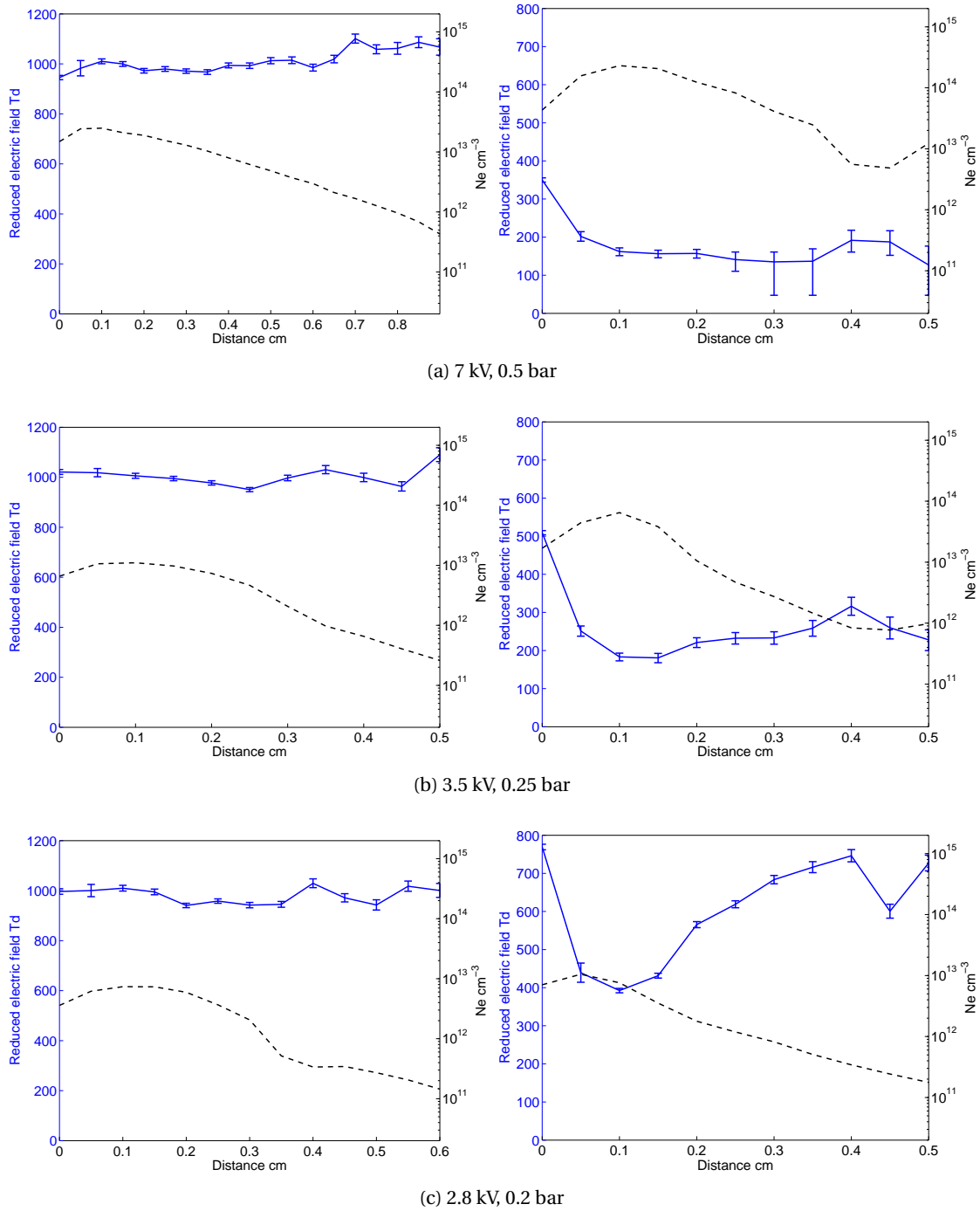


Figure 3.35: Spatial profile of the averaged electric field and normalized electron density in the direction of propagation of the streamer, for the ascending phase (left) and the decaying phase (right). The applied voltage and corresponding pressure are: 7kV, 0.5 bar (a), 3.5 kV, 0.25 bar (b), 2.8 kV, 0.2 bar (c).

### 3.3.7 Comparison with sinusoidal applied voltage

For comparison purposes, AC sinusoidal voltage has been applied to the actuator. Two different configurations were tested at two different pressures, namely 1 bar and 0.25 bar. The applied voltage and the frequency were set at 10 kV modulated at a frequency of 2.5 kHz for 1 bar and 2.5 kV at 10 kHz at 0.25 bar. These values were chosen in order to respect both  $V/p$  and the slope of the voltage increase with time (slew rate),  $V \nu$  where  $\nu$  is the frequency.

The evolution of the excited species in function of time (normalized to one cycle) are shown in figure 3.36. Two zones can be seen, which correspond to the positive slope and to the negative slope of the sinusoidal voltage. The fact that the plasma forms at these moment in time is well known. The interesting feature is that the same distribution of excited species corresponding to ascending and decaying phases, as seen in the above sections, can be clearly distinguished as well for the sinusoidal case. The comparison between the two pressures reveal the shorter duration of the plasma during both phases for a lower pressure. If the same interpretation made in subsection 3.3.6, the streamers should develop later in the cycle (= for a larger voltage) at a lower pressure, which is what is observed. The reduced electric field as computed with transitions B+/C and the average electron density obtained by the exponential fit are shown for both pressures in figure 3.37. Once again the high reduced electric field and low electron density associated with the ascending phase (positive streamers) and the low reduced electric field and high electron density associated with the decaying phase can be clearly seen, even though the streamers seen are only an average over several  $\mu s$ . Also, due to the duration of light collection, the averaged electron density is much lower than in the case of the nanosecond pulse. The integration time for the 1 bar and 0.25 bar cases are 80 and 20 times longer respectively than for the nanosecond pulse case (50 ns). If the light collected during the AC experiments is assumed to be produced by a single streamer event, the averaged electron density is of the same order in the nanosecond pulse and in the AC cases.

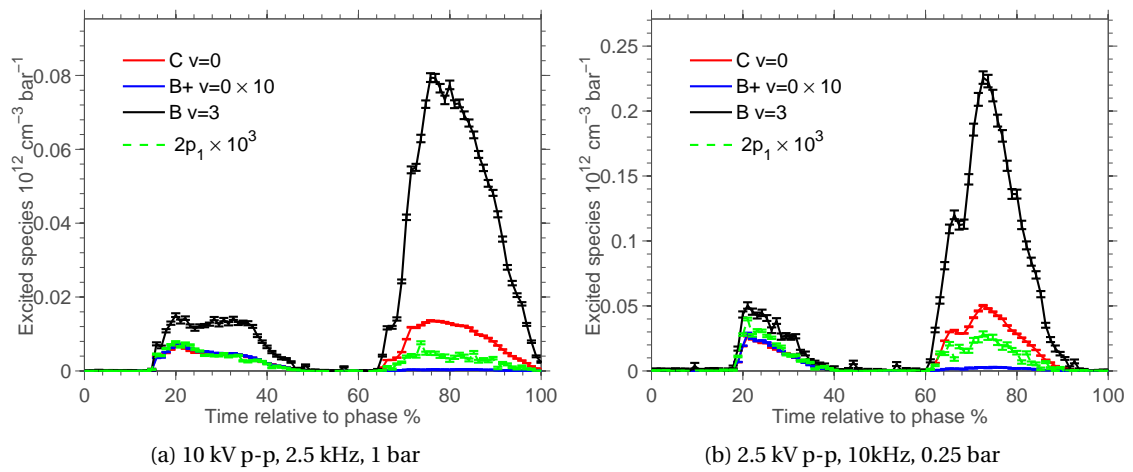


Figure 3.36: Spatial profile of the excited species populations, for one cycle. The applied voltage and corresponding pressure are: 1 bar, 10 kV p-p and 2.5 kHz (a), 0.25 bar, 2.5 kV p-p and 10 kHz (b).

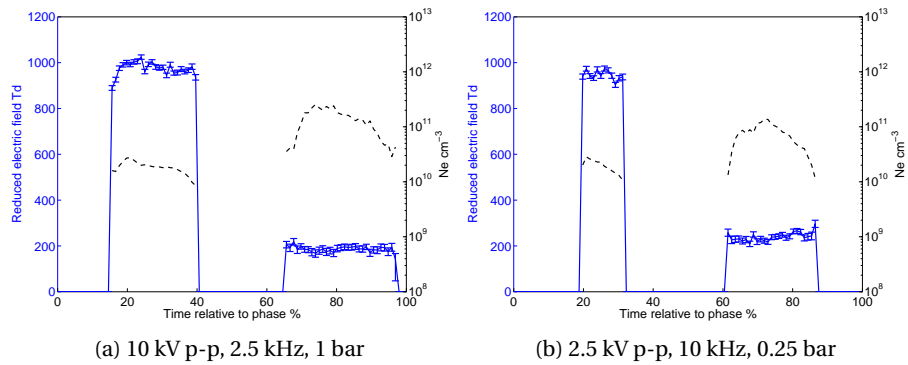


Figure 3.37: Spatial profile of the averaged electric field and normalized electron density, in the direction of propagation of the streamer, for one cycle. The applied voltages and corresponding pressures are: 1 bar, 10 kV p-p and 2.5 kHz (a), 0.25 bar, 2.5 kV p-p and 10 kHz (b).

### 3.4 Conclusions

The plasma produced by a 200 ns voltage pulse applied to a SDBD actuator was analyzed with electrical and optical diagnostics. Two distinct phases of the plasma were found, one at the beginning of the pulse and one at the end.

The electrical diagnostics permitted to determine the order of magnitude of the energy input to the plasma, which was of the order of 0.5 mJ per cm of electrode for 10 kV. The current input to the plasma was found to be of the order of the 500 mA.

The optical diagnostics were the fast camera footages and the time-averaged and time-resolved

### Chapter 3. Experimental Characterization of the Plasma

---

optical emission spectroscopy. The fast camera confirmed that the plasma emits light during two phases corresponding to the voltage rise (ascending phase) and fall (decaying phase). The light is emitted in the form of small filaments, which develops from the upper electrode to the direction of the lower electrode, for both phases. These filaments are readily associated with a positive streamer for the ascending phase and the decaying phase, for the case of a positive applied voltage and the reverse for the case of a negative applied voltage.

Time averaged emission spectroscopy allowed the determination of the main transitions occurring in the plasma. These were found to belong mainly to the first and second positive system of  $N_2$ , to the first negative system of  $N_2^+$ , to argon and oxygen lines and some features were associated with NO gamma bands but were difficult to interpret. The missing features of the spectrum were also investigated, namely emission from water vapor, from nitrogen lines and from the Meinel system of  $N_2^+$ .

The spectral code presented in chapter 2.6 allowed the unambiguous determination of excited species populations corresponding to the emission spectra for all but the NO gamma spectra recorded.

The effect of the voltage on the plasma was investigated by electrical measurement of the energy input to the plasma, which was found to vary quadratically with the applied voltage, as the electric power. Time-integrated OES was used to determine the variation of the spatial profile of the excited species production with respect to the applied voltage. The length of the plasma was found to be insensitive to the voltage. The intensity emitted was found to vary in a complicated manner with the voltage, with two regimes of a regular increase in intensity with applied voltage up to about 6 kV, a sudden increase between 6 and 8 kV and then a stagnation of the intensity.

The absolute calibration of the optical setup was performed. It allowed the estimation of actual excited species densities, which are only an estimate due to the unknown thickness of the plasma. The thickness of the plasma can be estimated as  $p/0.02$ , with  $p$  the pressure, and allowed a good approximation of the population densities.

Time-resolved spectroscopy with a temporal resolution  $\geq 2$  ns allowed separating the contribution to the emission spectrum due to the ascending and decaying phase. The former exhibits a very strong FNS and strong emission from argon lines, when compared to the decaying phase, which exhibits weak FNS and argon lines, and slightly stronger SPS and FPS, depending on the conditions. The difficulty to determine the spatio-temporal structure of the passing streamers is noted. This stems from the finite temporal and spatial resolution of the optical system. A deconvolution method was investigated in order to retrieve the true variation of excited species in time, but was unsuccessful due to the large sensitivity of the method on the



noise in the signal. Analysis of the relative populations of vibrational states demonstrated that initial populations follow the Franck-Condon principle and change over time due to different quenching rates associated with vibrational states.

The determination of the reduced electric field and average electron density were performed with the methods presented in chapter 2.6 based on phase-averaged emission spectroscopy. The reduced electric field was determined on the basis of the intensity emitted by several pairs of transitions. The spatial evolution of the reduced electric field and averaged electron density was characterized for both phases. It was found that the reduced electric field does not vary much with respect to the distance, apart for reduced electric fields determined from transitions involving the  $N_2(B^3\Pi_g)$  state, which was found to increase as distance increased. This effect is attributed to the overpopulation of this state by processes other than electron-impact from the ground state. This effect was considerably more pronounced during the ascending phase.

The reduced electric field was found to be much stronger during the ascending phase compared to the decaying phase. The reduced electric fields determined from different transitions were found to have very different values, especially in the case of the ascending phase.

The average electron density was determined using two methods, one presented in chapter 2.6 and the second presented in chapter 4.5. For the ascending phase, the first one was found to give very low values, of the order of  $10^{12} \text{ cm}^{-3}$  while with the second method values of the order of  $10^{13} \text{ cm}^{-3}$  were determined. For the decaying phase the difference was of the same order, but the absolute values were slightly higher with a maximum of  $10^{14} \text{ cm}^{-3}$ .

The investigation of the effect of the polarity of the applied voltage was investigated with the same diagnostic methods. It was shown that the plasma is very similar to the positive polarity, with only the order of the ascending and decaying phases inverted. The ascending phase is correspondingly weaker, with lower populations and reduced electric fields and the decaying phase is correspondingly stronger.

The effect of the pressure on the plasma was investigated at 1, 0.5, 0.3, 0.25 and 0.2 bar. The applied voltage was in the ratio of voltage over pressure 7 kV/bar for 1 and 0.5 bar and 14 kV/bar for 0.5, 0.3, 0.25 and 0.2 bar.

For pressures above 0.25 bar, the reduced electric field was found to be once again not significantly affected and remained almost constant to a value of approximately 1000 Td for the ascending phase and to a value ranging from 200 to 300 Td for the decaying phase, apart on the location of the upper electrode, where it is slightly higher (300 to 500 Td). The average electron density scales approximately with the pressure as expected from similarity laws for the ascending phase but not for the decaying phase, where the scaling was more than quadratic

### Chapter 3. Experimental Characterization of the Plasma

---

with the pressure. The length of the streamers during the ascending phase increases mainly with the applied voltage, thus diminishes with pressure for a same reduced electric field. The length of the streamers for the decaying phase was found to remain approximately constant for all conditions, with values between 3 and 5 mm. At 0.2 bar, the decaying phase exhibits a much larger reduced electric field. This trend is similar to the literature.

The comparison with a sinusoidal applied voltage was performed, at pressures 1 and 0.25 bar. The frequency/voltage and the voltage/pressure ratio were respected in order to isolate pressure effects not predicted by similarity laws. The high reduced electric field and low average electron density typical of positive streamers as well as low field and high average electron density typical of negative streamers were clearly observed during the rise of the positive half cycle and during the fall of the negative half cycle respectively.

## 4 Numerical Model of the Plasma

### 4.1 Introduction

The numerical modelling of the plasma produced by a SDBD actuator to which a short high voltage pulse is applied is described in this chapter. The characterization of the plasma by experimental means described in chapter 3.4 provided measurements representative of the whole plasma, which were useful to determine global characteristics such as the temporal evolution of the current and voltage, the energy input in the plasma and the temperature of the gas. These informations, while giving means to compare different configurations of the plasma actuator, does not permit to determine precisely the magnitude of actuating forces or the global heat release. A numerical model offers the advantages of a detailed description of the plasma, providing the spatial and temporal evolution of the charged species and allowing the computation of electrohydrodynamic forces and heat release to the gas. However, these outputs are meaningful only if the the model is able to describe the physics accurately. This last point is the main challenge with the numerical modelling of the plasma at atmospheric pressure, since the experimental validation is difficult to perform for other than very global characteristics of the plasma, such as the velocity of streamers or its spatial extent. To assess the validity of the numerical model, the reduced electric field and the electron density determined during the experiments are compared to the numerical simulations.

This chapter is structured as follows: A succinct literature review is given in subsection 4.1.1. The numerical methods employed are described in the second section. In the third section, the results of the simulations for the conditions investigated in chapter 3 are analyzed. The validity of the experimental methods employed in the experiments is discussed in the next section. The last section presents the global output of the actuators for flow-control applications and for plasma assisted combustion applications.

### 4.1.1 Literature review for plasma modelling

Streamer modelling is treated by several researchers, most of whom are using the same basic physical model, with difference only in their implementation. The following authors can be cited: J.P. Boeuf et al. ([Boeuf and Pitchford, 2005, Unfer and Boeuf, 2009]), Soloviev et al. ([Soloviev and Krivtsov, 2009]), Pancheshnyi et al. ([Pancheshnyi, 2005]), Likhanskii et al. ([Likhanskii et al., 2007]), Aleksandrov ([Aleksandrov and Bazelyan, 1996]), Morrow et al. ([Morrow and Lowke, 1997]), Bourdon et al. ([Bourdon et al., 2007, Bonaventura et al., 2011]).

The literature review reveals a necessary condition for the streamer to develop: the electric field must exhibit a gradient. This requirement leads to the necessity to solve the electric field in a two-dimensional geometry (or at least the so-called 1.5 D).

For example, in [Morrow and Lowke, 1997], the electric field is computed in a 2D geometry but the plasma dynamics is computed in one dimension along the axis of symmetry of the electrode.

The implementation of a two-dimensional model implies that relatively efficient numerical methods are employed, as the size of the problem to be solved is getting larger (typically several hundred thousand nodes). An overview of the different ways to implement a streamer model is depicted in [Luque et al., 2007]. The numerical methods available to solve the Poisson's equations are numerous, but only a few seem to be used for this type of problem. These methods are LU factorization (direct method) and SOR (successive over-relaxation) (iterative method). Despite its simple aspect, the advection equation for the transport of species is the most difficult to implement numerically, and its implementation varies from one author to the other.

For example, in [Morrow and Lowke, 1997, Bourdon et al., 2007], a 3rd order FCT (see [Leonard, 1991]) scheme is employed, in [Boeuf and Pitchford, 2005, Bonaventura et al., 2011], a Scharfetter and Gummel scheme is used, and in [Soloviev and Krivtsov, 2009, Pancheshnyi, 2005] a simple upwind scheme is used.

Chemical reactions is a more complex and paradoxically less investigated topic. Indeed, the models used are usually taking into account either two [Pancheshnyi, 2005] or three [Morrow and Lowke, 1997, Unfer and Boeuf, 2009, Likhanskii et al., 2007] different species, namely electrons, positive ions and negative ions (for three component models). These species embed the properties of the most important species for air and their reaction rates depend on the local reduced electric field.

One reference for this kind of model is the one developed by Morrow [Morrow and Lowke, 1997, Lowke and Morrow, 1995].

In [Aleksandrov and Bazelyan, 1996], the simulation of a long (several centimeters) streamer in air is undertaken. A complex model involving different types of ions, excited species and coupling of the vibrational relaxation to the reaction rates is developed. The calculation is carried in 1.5 D, meaning that the radius of the streamer channel is a parameter. A comparison is made with models using only three species and the large differences are demonstrated not only in chemical species computed, but also on global characteristics of the streamer, such

as its velocity, maximum electron density and limiting propagation length. The difference between the simple three species model and the complex one is believed to be due to an important change in the electron-ion recombination. An example is given which shows a large difference in electron density due to the use of different electron-ion recombination rate ( $\beta_{ei} = 2 \cdot 10^{-6} \text{ cm}^3 \text{ s}^{-1}$  and  $2 \cdot 10^{-7} \text{ cm}^3 \text{ s}^{-1}$ ). Although the conclusions made on the basis of a 1.5 D model are difficult to extrapolate to a 2D model, it seems clear that the chemical processes play an important role in the propagation of a streamer at long distances.

The treatment of photoionization, a process known to be important notably for the propagation of the streamer, is treated in three major ways in the literature. The first and simplest one is to use a so-called background ionization, a certain number of electrons and positive ions present in the whole domain either just at the beginning, or during the whole simulation time (a minimum number of electrons and ions is set). This procedure is discussed in [Pancheshnyi, 2005] and in [Likhanskii, 2009]. The main problem with this method is that it modifies the velocity and the direction taken by the streamer, and also the magnitude of the electric field in the streamer head. The second way of treating photoionization is to compute explicitly the photoionization due to radiating excited nitrogen species. The energetic photons are produced in region of high reduced electric field and radiated isotropically, ionizing the surrounding gas. The contribution of photoionization to a particular point in space must be integrated over the whole volume [Zhelezniak et al., 1982]. This procedure being very time consuming (summation over the whole volume for each point in space), a third way to treat photoionization is to transform the integral photoionization problem into a partial differential form, which can be solved very efficiently [Bourdon et al., 2007]. It is to be noted that the implementation of the photoionization model does not permit to describe accurately the propagation of streamers at different pressures for every condition, and that a debate exists on the subject [Pancheshnyi, 2005, Naidis, 2006]. In the present thesis, the analysis made in [Pancheshnyi, 2005] on the initial concentration of charged particles coming from natural sources and from previous pulses was retained. Indeed, since most of the experiments presented in the this thesis were performed at a frequency of 1 kHz, the hypothesis of residual charges coming from previous pulses seemed appropriate. Moreover, the agreement of experimental and numerical calculations performed in [Pancheshnyi, 2005] was better for uniform initial density of charges (seed charges) when compared to photoionization, especially at lower pressures.

The role of surface processes, i.e. surface discharge deposition and secondary emission, on the development of the streamer is not yet clear. It is discussed notably in [Unfer and Boeuf, 2009, Soloviev and Krivtsov, 2009, Likhanskii, 2009]. It is hard to attribute an effect of surface processes on the propagation of the streamer because of differences in the model varying from one author to the other. However, the effects of the secondary emission are best seen in the models used by Boeuf and coworkers, because surface processes are the sole mechanism for seed electron production. Also, it is clear from calculations that the charges on the surface affect the whole propagation of the plasma due to the shielding of the electric field. Surface charges are also partly responsible for the reverse breakdown occurring when the positive

voltage of a pulse decreases to a lower value.

### 4.2 Numerical Model

The implementation of the physical model described in section 2.6 is not straightforward in many regards. First, the advection-diffusion type equations 2.11 must be solved with a scheme that preserves positivity of the densities and with good stability properties, in connection with the temporal discretization. Second, the coupling of the transport equations with Poisson's equation is not easily performed, and thus is completely decoupled (i.e. the potential is computed using the densities of the previous time step) in the vast majority of work on the topic. The uncoupling of the equations seems fully justified in regards to the very small time steps necessary to solve the transport problem. The main difficulty in the resolution of the discretized problem lay in the size of the system to solve, which is large even for small test problems such as employed in section 4.2.5 ( $200 \times 100$  cells) in 2 dimensions. The generalization to a computational domain of several cubic centimeters in 3D makes mandatory the use of parallel computing together with efficient computational methods. Some of the problems linked with the numerical resolution of the problem are addressed in section 4.2.4.

#### 4.2.1 Numerical Discretization

For simplicity, the same grid is used to solve the Poisson's equation and the transport equations. Of course it is possible to use different grids (e.g. [Morrow and Lowke, 1997]), but the implementation is more difficult. The requirements for the problem of plasma modelling at high  $p \cdot d$  are a very fine grid for regions of space where the gradients are high and a large enough domain to solve the potential correctly. These requirements imply a large amount of memory, which can be prohibitive. The problem is even more difficult for the modelling of streamers: the region where the highest gradients are located is the head, which is moving. Thus either a very fine grid for the whole region where the streamers passes must be used, or a moving/adaptive mesh (see [Unfer and Boeuf, 2009] for an example of adaptive mesh applied to streamer modelling). As the implementation of an adaptive mesh is difficult and complicates the implementation of the numerical schemes, the choice has been made to use a fixed grid.

In the first part of this section, the numerical schemes associated with a uniform grid (rectangular cells of the same size for the whole domain) are described. The second part of this section describes the non-uniform grid developed in order to decrease the computational cost. The validation of the numerical schemes developed for this non-uniform grid is made by comparison with the uniform case.

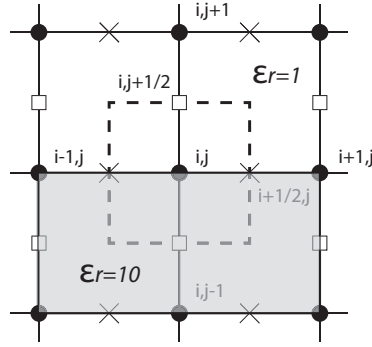


Figure 4.1: Computational cell with dielectric-gas interface located at the node.

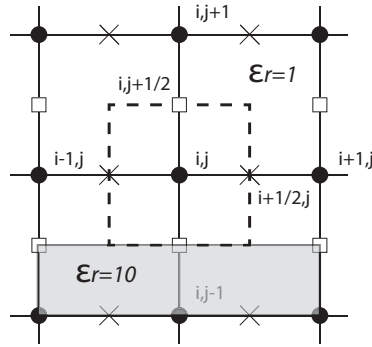


Figure 4.2: Computational cell with dielectric-gas interface located at the cell's boundary.

**Poisson's equation and electric fields**

There are several ways to set the computational grid within the finite volume method formula- tion: the properties of the material (dielectric constant, electrode) are defined:

- between nodes as shown in figure 4.1
- between cells as shown in figure 4.2

The latter choice was made for calculations shown in this thesis. A typical non-uniform grid cell is shown in figure 4.3. The dashed line shows the limit of the finite volume for the cell (i,j). The volume (surface in 2D) of this cell is given by  $\Delta x_{m,i} = 1/2(\Delta x_{i+1} + \Delta x_{i-1})$ . The gradients at the interface are computed as:

$$\nabla \Phi_{i+1/2} = \frac{\Phi_{i+1} - \Phi_i}{\Delta x_{i+1}}$$

while the divergence is computed as:

$$\nabla \cdot \Phi_i = \frac{\Phi_{i+1/2} - \Phi_{i-1/2}}{\Delta x_{m,i}}$$

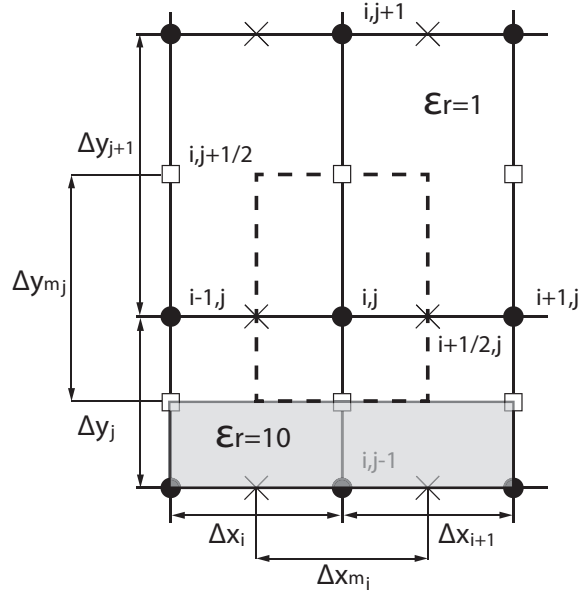


Figure 4.3: Computational cell with dielectric-gas interface located at the node.

Poisson's equation with varying dielectric is therefore written as:

$$\nabla \cdot (\epsilon \nabla V) = \frac{1}{\Delta x_{m,i}} \left( \epsilon_{i+1} \frac{(V_{i+1} - V_i)}{\Delta x_{i+1}} - \epsilon_i \frac{(V_i - V_{i-1})}{\Delta x_i} \right) + \frac{1}{\Delta y_{m,i}} \left( \epsilon_{j+1} \frac{(V_{j+1} - V_j)}{\Delta y_{j+1}} - \epsilon_j \frac{(V_j - V_{j-1})}{\Delta y_j} \right)$$

The scheme employed can be described using a toy problem of  $4 \times 4$  cells.

$$eM_x = \begin{pmatrix} 1 & 0 & 0 & 0 \\ -1 & 1 & 0 & 0 \\ 0 & -1 & 1 & 0 \\ 0 & 0 & -1 & 1 \\ 0 & 0 & 0 & -1 \end{pmatrix}$$

The boundary condition is applied to this matrix by setting the corresponding line to zero. For example the first line set equal to zero implies that the left of the computational domain has zero electric field along the  $x$  component. The natural boundary condition is  $V = 0$  at the boundaries.



$$dM_x = \begin{pmatrix} 1/\Delta x_i & 0 & 0 & 0 & 0 \\ 0 & 1/\Delta x_{i+1} & 0 & 0 & 0 \\ 0 & 0 & 1/\Delta x_{i+2} & 0 & 0 \\ 0 & 0 & 0 & 1/\Delta x_{i+3} & 0 \\ 0 & 0 & 0 & 0 & 1/\Delta x_{i+4} \end{pmatrix}$$

the full operator for the  $x$  component of the electric field is obtained using the tensor product:

$$EM_x = I_{jmax} \otimes dM_x EM_x$$

where  $I_{jmax}$  is the identity matrix of size  $jmax$  ( $y$  component). The same is made for the  $y$  component of the electric field. The dielectric permittivity being variable, a value of the dielectric permittivity is associated with each cell's face, in the following way (for  $y$  component faces):

$$\epsilon_y = \begin{pmatrix} \epsilon_{diel} & & \epsilon_{diel} & 1 & 1 & 1 \\ \epsilon_{diel} & & \epsilon_{diel} & 1 & 1 & 1 \\ \epsilon_{diel} & 2\epsilon_{diel}/(\epsilon_{diel} + 1) & & 1 & 1 & 1 \\ \epsilon_{diel} & 2\epsilon_{diel}/(\epsilon_{diel} + 1) & & 1 & 1 & 1 \end{pmatrix}$$

Notice that the permittivity is modified at the interface in order to take into account the discontinuity due to the interface gas-dielectric (the electrode is 2 cells long in this example).

In this matrix, the permittivities are set according to their physical locations, but must be put in a diagonal matrix in order to multiply it with the electric field matrix. This diagonal matrix  $\Delta_{\epsilon_{diel},x}$  is square and  $(i_{max} + 1)j_{max}$  long for the permittivities associated with the  $x$ -component of the electric field. The divergence operators are constructed as follows:

$$eDiv_x = \begin{pmatrix} -1/\Delta x_{m,i} & 1/\Delta x_{m,i} & 0 & 0 & 0 \\ 0 & -1/\Delta x_{m,i+1} & 1/\Delta x_{m,i+1} & 0 & 0 \\ 0 & 0 & -1/\Delta x_{m,i+2} & 1/\Delta x_{m,i+2} & 0 \\ 0 & 0 & 0 & -1/\Delta x_{m,i+3} & 1/\Delta x_{m,i+3} \\ 0 & 0 & 0 & 0 & -1/\Delta x_{m,i+4} \end{pmatrix}$$

$$Div_x = I_{jmax} \otimes eDiv_x$$

The dirichlet boundary conditions are implemented by constructing a matrix  $B_{Dirichlet}$  which is diagonal with zeros where the boundary conditions apply and ones otherwise. The actual value of the boundary condition is set in the right hand side of the equation. The final form of the Laplacian operator is:

$$\nabla \cdot (\epsilon \mathbf{E}) \equiv B_{Dirichlet} (Div_x \Delta_{epsilon,x} EM_x + Div_y \Delta_{epsilon,y} EM_y) + I_N - B_{Dirichlet}$$

where  $N = i_{max} j_{max}$  is the size of the system.

The Laplacian with homogeneous Dirichlet boundary conditions to compute the Helmholtz equations for the photoionization problem (see section [Bourdon et al., 2007]) is simply:

$$\nabla \cdot (\epsilon \mathbf{E}) \equiv B_{Dirichlet} (Div_x EM_x + Div_y EM_y) + I_N - B_{Dirichlet}$$

#### 4.2.2 Numerical Schemes

**Temporal discretization** An explicit Euler forward scheme (first order accurate) has been used throughout this study, and the accuracy of the results have been assessed by reducing the time steps for the test case. The advantages of using a second-order Runge-Kutta were found to be insignificant. In order to decrease the computational time, a semi-implicit procedure such as in [Lagmich et al., 2008] could be used. However, the accuracy associated with the semi-implicit procedure would have been harder to assess, especially for the computation of excited species.

The time steps are of variable duration and are computed according to stability conditions for the advection-diffusion problem (CFL condition) and for the dielectric relaxation time (Maxwell relaxation time) and the accurate calculation of the ionization source (see [Vitello et al., 1994]).

**Spatial discretization** The advection equations are discretized with the MUSCL scheme (second order in space).

The charged particle densities are defined at the center of the computational cell  $(i,j)$  as illustrated on figure 4.4. In the drift-diffusion equations, the charged particle fluxes directed towards the  $x$  and  $y$  axes are defined between the points  $(i,j)$  and  $(i+1,j)$ ,  $(i,j)$  and  $(i,j+1)$  respectively and therefore denoted by  $\Gamma_{x,i+1/2,j}$  and  $\Gamma_{y,i,j+1/2}$ .

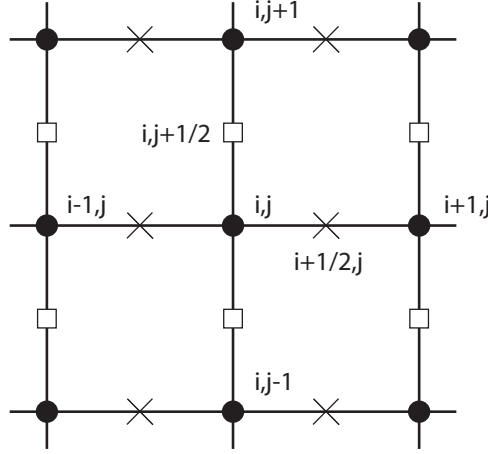


Figure 4.4: Representation of the computational cells implemented in the numerical model

The diffusion term is computed as follows:

$$\begin{aligned} & \int_{j-1/2}^{j+1/2} \int_{i-1/2}^{i+1/2} \nabla \cdot (D_e \nabla n_e) dx dy \cong \\ & D_e \frac{\partial n_e}{\partial x} \Big|_{i-1/2}^{i+1/2} \Delta y + D_e \frac{\partial n_e}{\partial y} \Big|_{j-1/2}^{j+1/2} \Delta x \cong \\ & \left( \frac{(D_{e_{i+1,j}} + D_{e_{i,j}})}{2} \frac{(n_{e_{i+1,j}} - n_{e_{i,j}})}{\Delta x} - \frac{(D_{e_{i,j}} + D_{e_{i-1,j}})}{2} \frac{(n_{e_{i,j}} - n_{e_{i-1,j}})}{\Delta x} \right) \Delta y \\ & + \left( \frac{(D_{e_{i,j+1}} + D_{e_{i,j}})}{2} \frac{(n_{e_{i,j+1}} - n_{e_{i,j}})}{\Delta y} - \frac{(D_{e_{i,j}} + D_{e_{i,j-1}})}{2} \frac{(n_{e_{i,j}} - n_{e_{i,j-1}})}{\Delta y} \right) \Delta x \end{aligned}$$

The MUSCL scheme is implemented for two purposes: the first one is to enable the comparison with the papers and thesis of [Unfer and Boeuf, 2009] and the second one is to have a spatial accuracy to the second order, which allows the use of larger cells. This scheme is defined as follows: A total variation diminishing (TVD) linear scheme is chosen (thus a first order scheme by Godunov's theorem), then the variables used to compute the fluxes or, alternatively, directly the fluxes, are assumed to be linear functions of space. These variables are then re-injected into the first order TVD fluxes. The numerical scheme is now second order in space. However, it is no more TVD and in particular will not preserve positivity. It is therefore necessary to limit the fluxes in order to achieve TVD. This is similar in concept with the Flux Corrected Transport (FCT) scheme. The scheme is described in [Hirsch, 2007] p.552-553. The limiter chosen is the minmod, in order to match [Unfer and Boeuf, 2009]. A better choice to capture steep gradients might be the superbee limiter [Ducasse et al., 2012], but this has not been tested.

$$\begin{aligned}\tilde{n}_{i+1/2}^L &= n_i + \frac{1}{2}\Phi^L(r^L)(n_i - n_{i-1}) \\ \tilde{n}_{i+1/2}^R &= n_{i+1} - \frac{1}{2}\Phi^R(r^R)(n_{i+2} - n_{i+1})\end{aligned}$$

with  $r^L = \frac{n_{i+1} - n_i}{n_i - n_{i-1}}$  and  $r^R = \frac{n_{i+1} - n_i}{n_{i+2} - n_{i+1}}$ . The complete scheme is then written:

$$\frac{dn_i}{dt} = -(v_{i+1/2}^+ \tilde{n}_{i+1/2}^L + v_{i+1/2}^- \tilde{n}_{i+1/2}^R - v_{i-1/2}^+ \tilde{n}_{i-1/2}^L + v_{i-1/2}^- \tilde{n}_{i-1/2}^R)$$

If this semi-discrete equation is resolved in time using an explicit first order (Euler) scheme, the stability condition for a minmod limiter is (Hirsch p.558)  $v\Delta t/\Delta x < 2/3$ .

The generalization to multidimensions is accomplished by applying the above scheme once for every direction. If the grid is orthogonal, this procedure is correct [Berger et al., 2005]. In order to generalize this scheme to a nonuniform grid, it is necessary to modify it slightly, as described in [Berger et al., 2005]. This scheme reads:

$$\begin{aligned}\tilde{n}_{i+1/2}^L &= n_i + \frac{1}{2} \left( \frac{\Delta x_{i+1} + \Delta x_i}{2} \right) \min\left(\frac{1}{\Delta x_i}, \frac{r^L}{\Delta x_{i+1}}\right)(n_i - n_{i-1}), \text{ if } r^L > 0 \\ &\tilde{n}_{i+1/2}^L = n_i, \text{ if } r^L \leq 0 \\ \tilde{n}_{i+1/2}^R &= n_{i+1} - \frac{1}{2} \left( \frac{\Delta x_{i+2} + \Delta x_{i+1}}{2} \right) \min\left(\frac{1}{\Delta x_{i+1}}, \frac{r^R}{\Delta x_{i+2}}\right)(n_{i+2} - n_{i+1}), \text{ if } r^R > 0 \\ &\tilde{n}_{i+1/2}^R = n_{i+1}, \text{ if } r^R \leq 0\end{aligned}$$

with  $\Delta x_i = x_i - x_{i-1}$ .

As a conclusion, the computational cost associated with different discretization schemes is studied in the context of streamers in [Ducasse et al., 2012], and shows that the MUSCL scheme is a good choice.

**Computation of the reduced electric field and the mobilities** The norm of the electric field is computed as follows:

$$|\mathbf{E}| = \sqrt{\frac{1}{2}(E_{x_{i+1/2}} + E_{x_{i-1/2}})^2 + \frac{1}{2}(E_{y_{j+1/2}} + E_{y_{j-1/2}})^2}$$

and then the reduced electric field is computed as:  $|E/N| \cdot 10^{-17}$  to obtain the reduced electric field in Townsend units ( $Vcm^2$ ). The mobilities necessary to compute the two components of the velocity is the average of the mobilities as follows:

$$\mu_{j+1/2} = \frac{1}{2}(\mu_j + \mu_{j+1})$$

except at the gas-dielectric interface, where a discontinuity in the electric field does not allow to perform an average, and thus the mobility is simply  $\mu_{j_{\text{diel}}+1/2} = \mu_{j_{\text{diel}}+1}$

**Photoionization** The photoionization problem [Bourdon et al., 2007] involves the solution of Helmholtz equations, which itself contains a Laplacian, which is identical to the Laplacian in Poisson's equation. The implementation of the other terms is straightforward.

### 4.2.3 Non-uniform Grid

In order to decrease the computational time, a non-uniform grid has been used. The grid is as shown in figure 4.5. Poisson's equation must be resolved with high accuracy especially near the discontinuities of the domain (gas-dielectric interface, upper electrode) and where the streamer develops. This is why a constant spacing block with the minimal  $\Delta y = \Delta y_0$  was defined, with thickness determined by trial and error (the maximal thickness of the streamer is of the order  $200 \mu m$ ). For the rest of the domain, a linearly decreasing grid size is used, where the maximum size is specified (e.g.  $\Delta y = 5\Delta y_0$ ). Very steep gradients of the electric field and of the species densities are located in the streamer head, which is moving. Thus a moving grid or an adaptive refinement technique would be necessary in order to refine the spatial region only where it is needed. This is why a constant grid spacing in the x direction is used ( $\Delta x = \Delta x_0$ ). Although very simple, this non-uniform grid allows the use of smaller grids, which decreases the memory usage and decreases the computing time significantly, especially for large dielectric thickness, as were used during the experiments.

### 4.2.4 Solver

The numerical resolution of the system of equation obtained from the discretized problem is discussed in the following.

Due to the explicit nature of the temporal discretization, the solution of the transport equations is very easy. The main challenge lies in the resolution of the Poisson's equation which is an elliptic problem and need the resolution of a large system of equations. They are two main class of methods used for the resolution of such systems in the framework of plasma modelling, the *direct* resolution of the system, which solves the problem exactly (within the precision of the computer) and the iterative resolution of the system, which uses a first guess to the

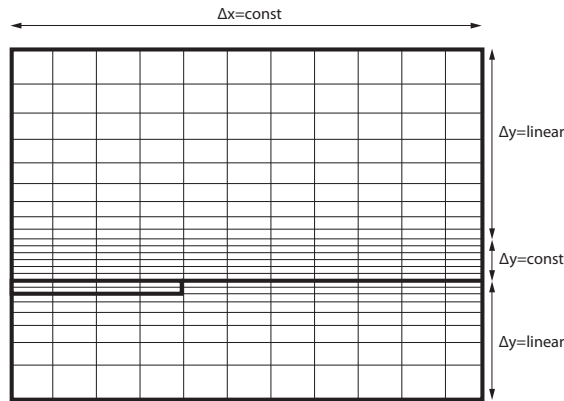


Figure 4.5: Typical non-uniform grid used for the computations.

solution and then iterates until the solution converges. The first class of methods is very time consuming for large systems, as it requires  $N^3$  operations (with  $N$  the number of unknowns) at least, while the iterative methods only needs  $N^2$  operations [Luque and Ebert, 2012]. However, for the particular case of streamer modelling, the LU factorization remains faster for small geometries (i.e. less than a million cells) due to the fact that once the system is factorized, the solution can be determined very quickly. If the number of time steps is large, which is true for streamer modelling ( $> 10^5$  time steps), then the initial factorization takes only a very small fraction of the overall computation time. Another issue with this method for large problems is the memory requirement. Another advantage of the direct methods over the iterative methods is their accuracy for any physical condition. The computational cost required for LU factorization and for the Successive Over-Relaxation (SOR) iterative method is compared in the context of streamer modelling in [Ducasse et al., 2012]. They conclude that the LU factorization is computational competitive with SOR methods with a good accuracy independently of the spatial gradients.

#### 4.2.5 Validation of the Numerical schemes

The validation of the numerical schemes used in the numerical code is presented in this section. The numerical schemes developed for the non-uniform grid are compared to the uniform grid case. The comparison between the present calculations and similar calculations performed in the literature is made.

The test calculation is carried out with parameters identical to those of [Unfer, 2008] (p.55 and following ones). The geometry is presented in figure 4.6, the height of the dielectric is  $50 \mu m$ , the length of the upper electrode is  $100 \mu m$ , the ground electrode covers the whole length of the dielectric. The height of the domain is  $200 \mu m$  and the length of the domain is  $400 \mu m$ . The gas used is  $N_2$ .

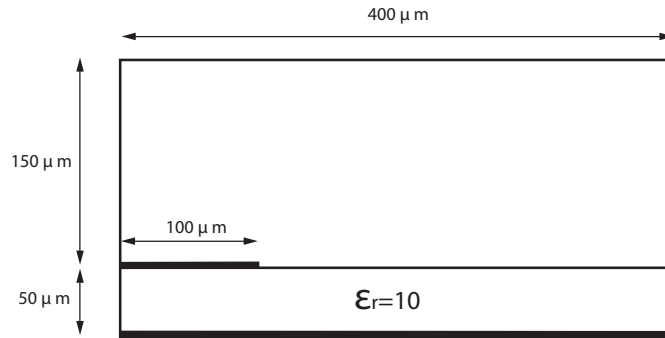


Figure 4.6: Computational domain used for the validation calculations.

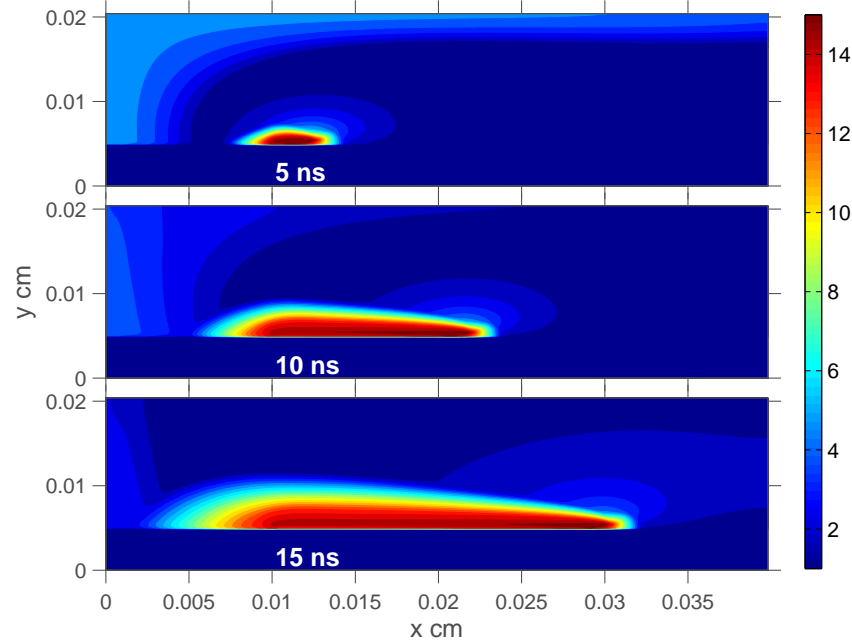
- Constant applied voltage on the upper electrode of 1200 V, 0 V on the lower electrode
- $\epsilon_r = 10$
- $\mathbf{E} \cdot \mathbf{n} = 0$  and  $\mathbf{\Gamma} \cdot \mathbf{n} = 0$  at the top, left and right boundaries
- $\gamma = 0.05$
- Constant temperatures  $T_e = 10^4$  K and  $T_{ion} = 350$  K
- Computed time: 150 ns
- initial concentration of  $n_e = N_2^+ = 10^4 \text{ cm}^{-3}$
- Gas temperature  $T_g = 300$  K and pressure  $P = 101300$  Pa and corresponding gas density  $N_g = 2.446 \cdot 10^{19} \text{ cm}^{-3}$

where  $\mathbf{n}$  is the vector normal to the boundary.

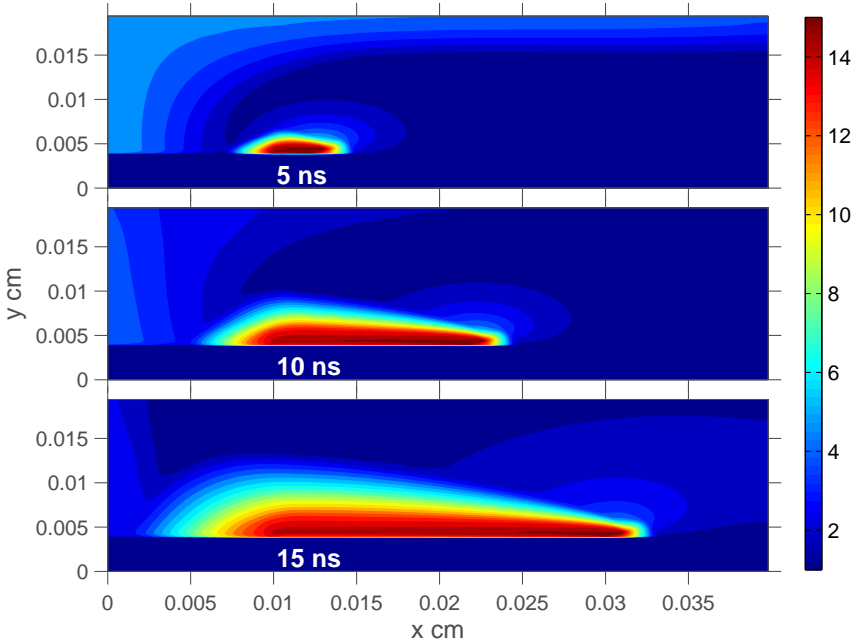
The explicit coefficients for the fits used in the code are shown in table A.1 in the appendix. The recombination coefficient is set to  $2 \cdot 10^{-7} \text{ cm}^3 \text{ s}^{-1}$ .

The comparison of the results of the test case are first compared between uniform and non-uniform grid. The spatial discretization scheme is the MUSCL scheme. The transport and source coefficients are the same as the ones used in the reference case [Unfer, 2008]. The results at 5, 10 and 15 ns are plotted in figure 4.7. The agreement between the two results is very good.

However the comparison with the reference case of the literature is less satisfactory. Even though the qualitative behavior of the plasma is identical for the present computation and the reference, a current of about a tenth of the present value is found in the reference (see figure 4.8). This difference is explained by the faster (about 4 times) propagation velocity of the plasma computed with the present code when compared to the reference. This is a large discrepancy and could be due to the neglect of the displacement current (conduction current to the anode only) performed in the present calculation. It is noted that this reference case



(a)



(b)

Figure 4.7: Density contours of the electron density computed at  $t=5, 15, 45$  and  $60$  ns. Uniform grid  $200 \times 100$  (a) and non-uniform grid  $200 \times 45$  (b).



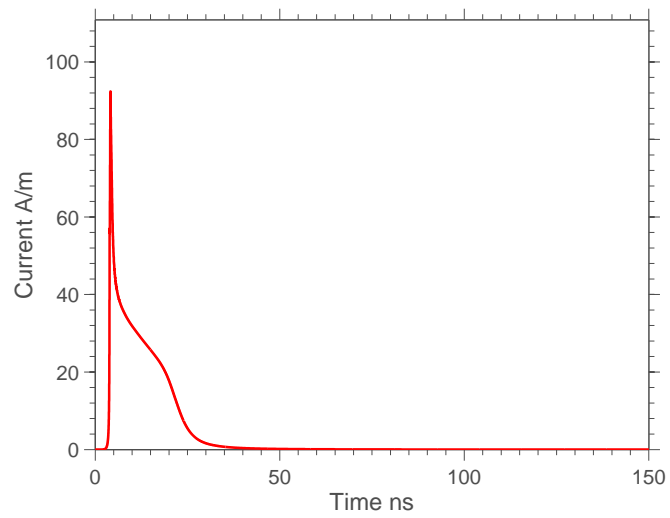


Figure 4.8: Conduction current computed for the uniform grid.

is very sensitive to the input parameters. The computations performed in air are in better agreement with the literature.

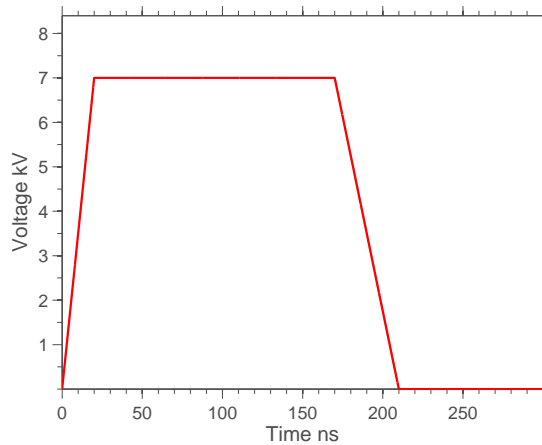


Figure 4.9: Voltage applied to the upper electrode in function of time.

### 4.3 Numerical Results

The SDBD actuator was simulated numerically for the conditions of the experiments. The geometry of the computational domain is: dielectric layer of thickness  $800 \mu\text{m}$ , total height of the computational domain of 4 mm and total length equal to 6 mm. The length of the upper electrode was  $500 \mu\text{m}$  and the length of the lower electrode was equal to the length of the computational domain. The cell sizes were set to  $5 \mu\text{m}$  for all voltages and the pressures. The applied voltage comprises a rise of 20 ns with linear slope, a plateau of 150 ns and a decay of 40 ns similar to the experiments. A typical applied voltage pulse is shown in figure 4.9. The voltage and pressure were set as in the experiments, i.e. 7 at 1 bar, 7 kV and 3.5 kV at 0.5 bar, 4.2 kV at 0.3 bar, 3.5 kV at 0.25 bar and 2.8 kV at 0.2 bar respectively. The computations were performed with the photoionization model described in [Bourdon et al., 2007]. The comparison with similar computations performed with a uniform pre-ionization of  $10^8 \text{ cm}^{-3}$  (see [Pancheshnyi, 2005]) has shown no significant differences.

#### 4.3.1 Positive Pulse

The simulated plasma for the case of a positive pulse of 7 kV at 1 bar is shown for the ascending phase in figure 4.10. The general structure of a streamer with steep variations in the reduced electric field and in the charged particles densities (electron density shown). These computations were made with the photoionization model. The difference in behavior for the ascending and decaying phases is clearly seen in figure 4.11. The plasma propagates to a distance of approximately 5 mm during the ascending phase and 1.5 mm during the decaying phase.

#### 4.3.2 Influence of the Polarity

The simulated plasma for the case of a positive pulse of 7 kV at 1 bar is shown in figure 4.12 for the ascending and decaying phases respectively. These computations show similar features

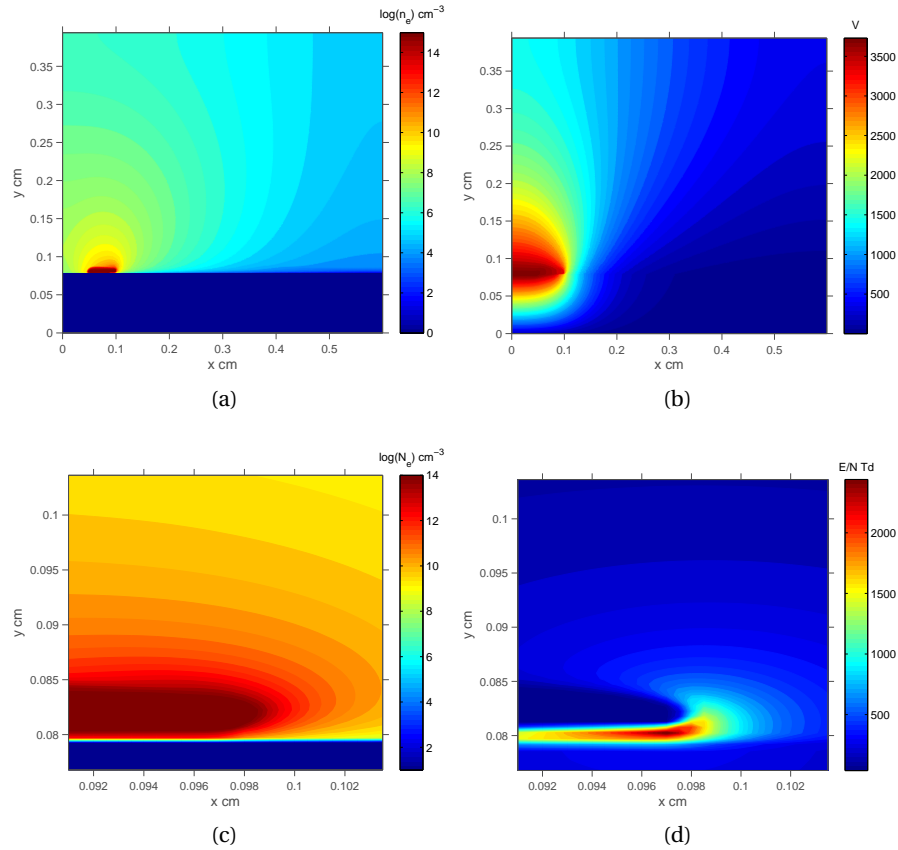
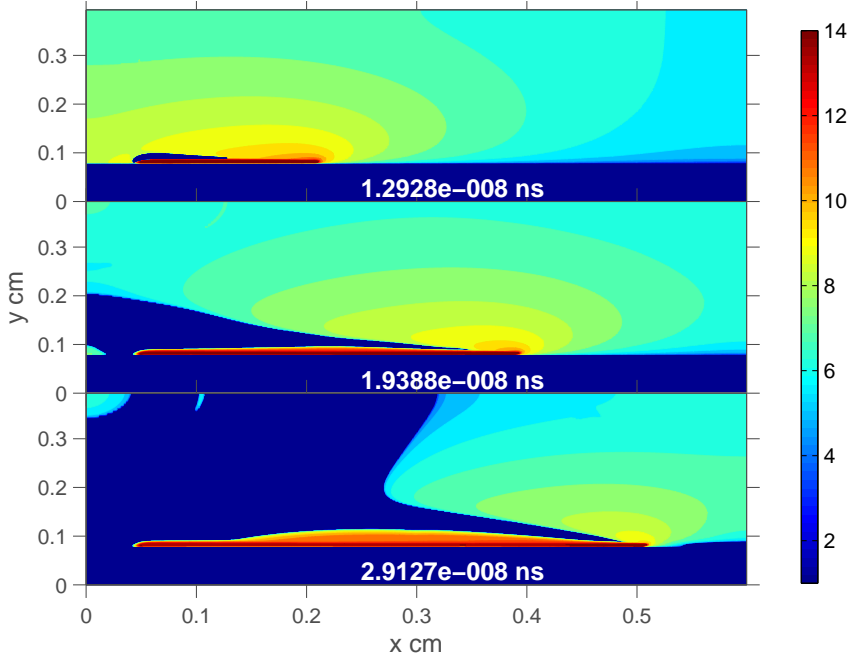


Figure 4.10: Contour plot of the electron density (a) and the potential (b) at time  $t=13 \text{ ns}$  (ascending phase). Enlarged view of the electron density (c) and of the reduced electric field (d). The conditions for the computation are: 7 kV applied voltage at 1 bar.

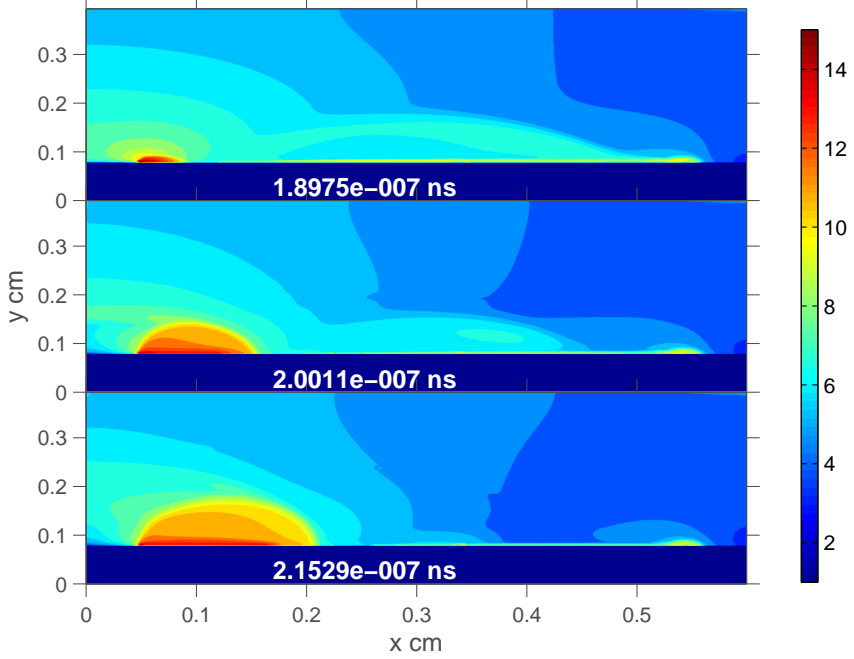
when compared to the positive pulse, with only a stronger and longer plasma formed during the decaying phase, and a weaker and shorter plasma during the ascending phase.

### 4.3.3 Influence of the Applied Voltage

The applied voltage is certainly the most important parameter of the SDBD. In reality, the maximum voltage cannot be applied instantly to the electrode and is a function of time. This aspect is very important for nanosecond pulsed SDBD, as the state of the plasma depends to a large extent on the slope of the voltage rather than on the maximum value of the applied voltage. In order to investigate the different streamers generated as a function of slope, the following calculation was performed: the geometry is  $1 \times 1 \text{ mm}$  and the dielectric thickness is  $0.2 \text{ mm}$ , with a dielectric constant of 10 as usual. The minimum cell size is  $dx = dy = 2 \mu\text{m}$ . The maximum voltage is fixed at 10 kV and the voltage rises linearly with time, as determined by the rise times, which are 1.25, 2.5, 5, 10 and 20 ns for each calculation respectively. The results are shown in figure 4.13 and the total number of electrons, the maximum reduced electric



(a)



(b)

Figure 4.11: Contour plot of the electron density and reduced electric field for different times during the ascending (a) and decaying (b) phases. The conditions for the computation are: 7 kV applied voltage at 1 bar.

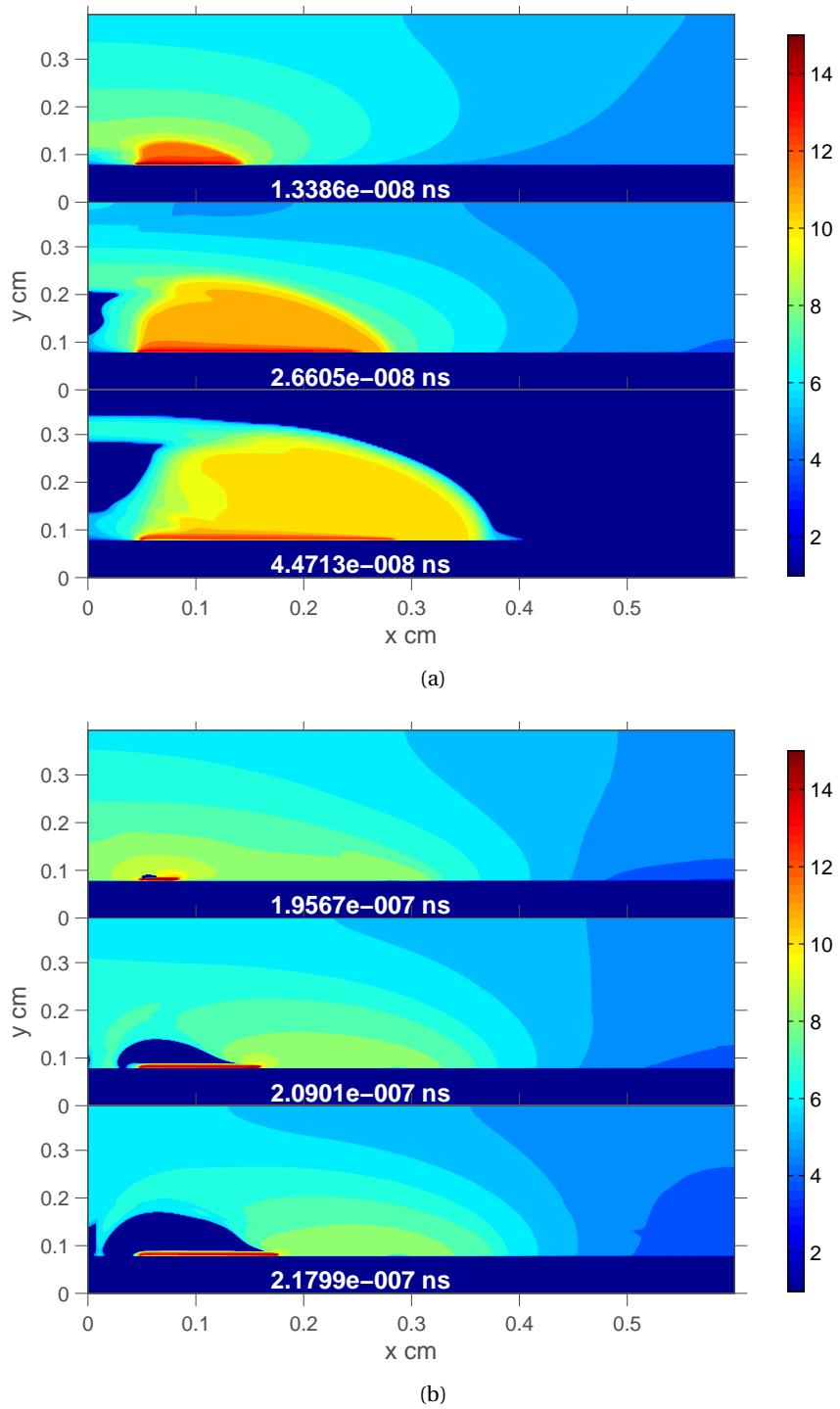


Figure 4.12: Contour plot of the electron density and reduced electric field for different times during the ascending (a) and decaying (b) phases. The conditions for the computation are: -7 kV applied voltage at 1 bar.

field together with the starting time of the streamer are shown in figure 4.14 as a function of the voltage slope. The starting time of the streamer is arbitrarily defined as the moment the current reaches 1 A/cm.

A first remark concerning the distribution of the electron density for high voltages: it exhibits denser regions in the vicinity of the upper electrode. This denser region seems to correspond to the bright spots that are noticeable in plasma imaging, for sufficient voltages.

It can be seen in figure 4.14 (a) that the total number of electrons and the maximum reduced electric field decrease as the rise time diminishes. The maximum power density varies accordingly (see figure 4.14 (b)) and follows the same trend as the energy input in the plasma measured during the experiments. However, the electron density varies under linearly with the rise time, as seen in figure 4.13. This is explained by the development of the streamer which occurs once the space charge field has reached a value close to the applied electric field, which occurs at a certain threshold value of the reduced electric field. For larger applied electric fields, the streamer will only develop faster. This faster development can be seen by plotting the velocity of the streamer and the time at which it starts, as shown in figure 4.14 (a) and (b) respectively.

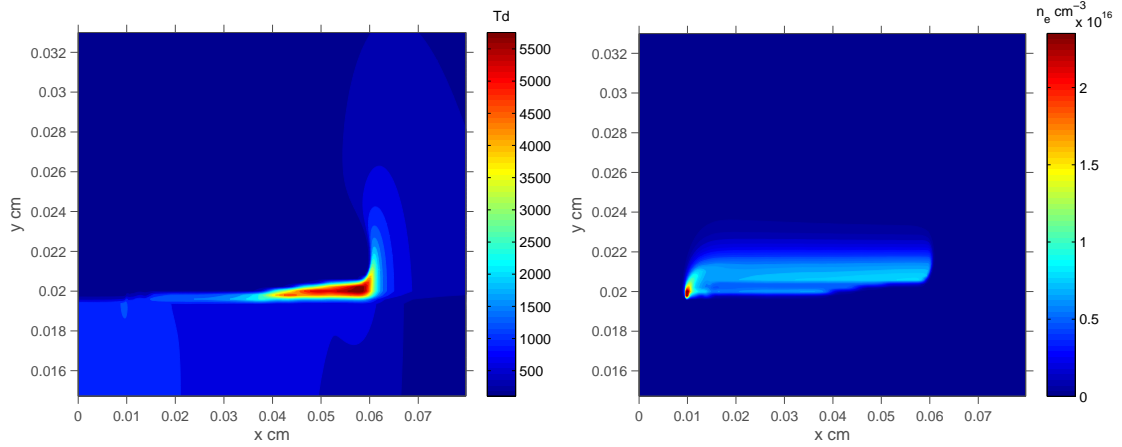
The maximum value of the voltage is associated with the total energy available for the streamer. It will therefore influence mostly the maximum length that the streamer can reach, which depends also on the charging of the dielectric and the length of the lower electrode. The current computed for different voltages are shown in figure 4.16. The maximum amplitude of the current increases slightly with the voltage. The plasma forms earlier with higher voltages since the breakdown voltage is reached sooner. This behavior is also shown in figure 4.17, where the evolution of the plasma for increasing applied voltages is plotted at the end of the ascending voltage phase (20 ns) and decaying phase (210 ns).

### 4.3.4 Influence of the Pressure

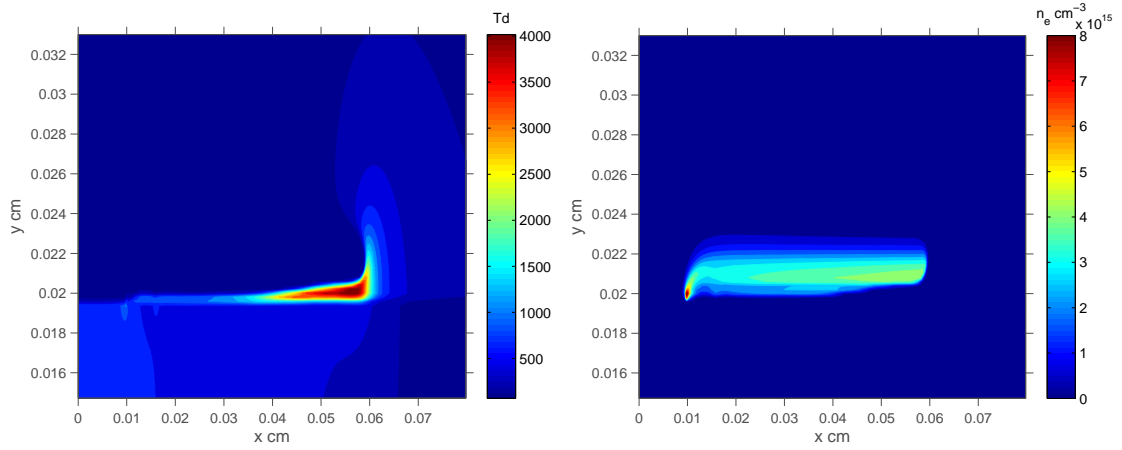
**Influence of the pressure** The influence of the pressure on the propagation of the streamers for the ascending and decaying phase is shown in figure 4.18. The increase in length with decreasing pressures as predicted by similarity laws is well seen.

**Breakdown voltages** The theory on breakdown voltages depicted in section 2.2 can be employed in order to interpret the experimental results obtained at different pressures. The application of Meek's criterion in the case of non-uniform electric field reads:

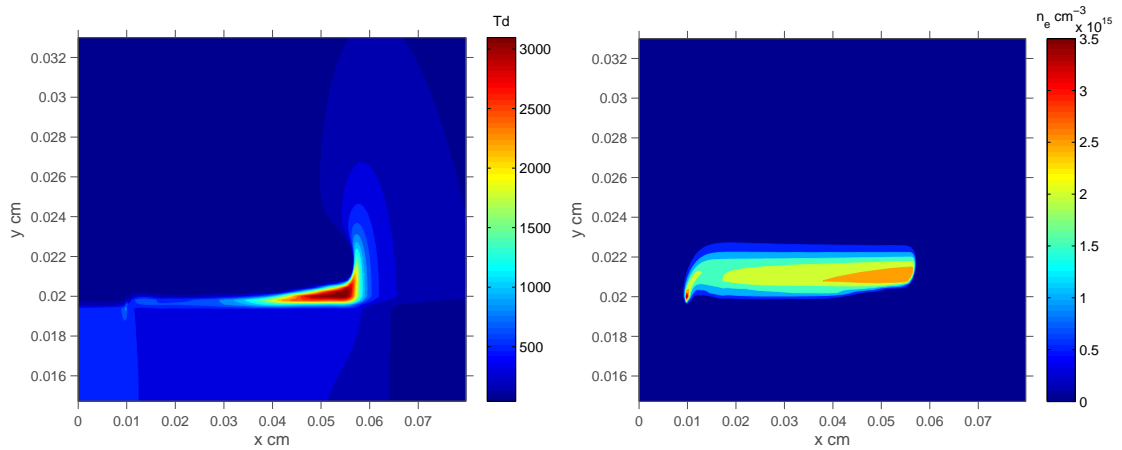
$$\oint \alpha_{\text{eff}}(E(\mathbf{r})) d\mathbf{r} = 16 - 21 \quad (4.1)$$



(a) 10 kV, 1.25 ns rise time



(b) 10 kV, 5 ns rise time



(c) 10 kV, 20 ns rise time

Figure 4.13: Influence of the voltage slope on the reduced electric field (left) and on the electron density (right).

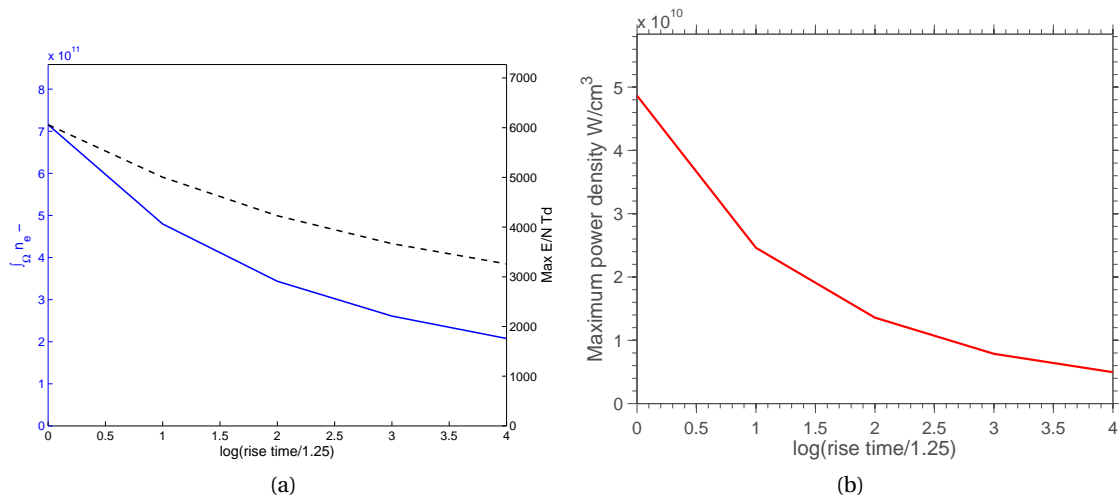


Figure 4.14: Maximum reduced electric field and total number of electrons as a function of the voltage slope (a). Maximum power density in the streamer (b).

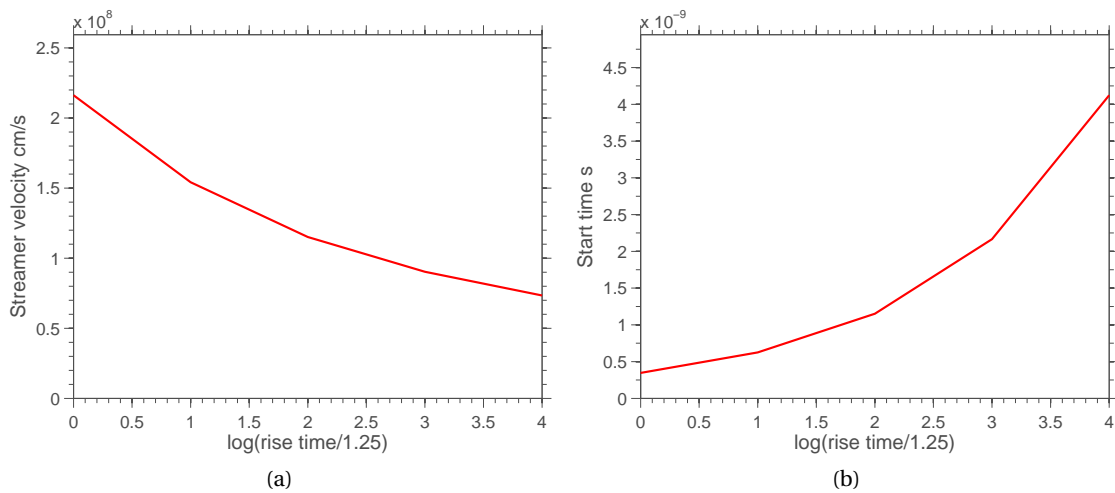


Figure 4.15: Maximum streamer velocity (a) and starting times of the streamer (b) as a function of the voltage slope.



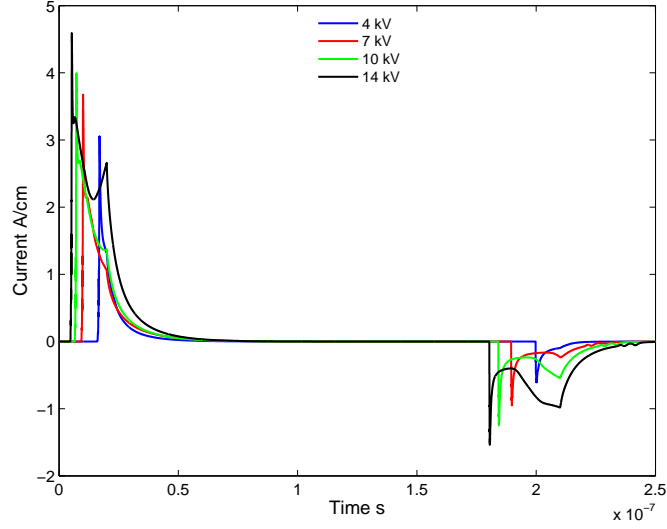


Figure 4.16: Conduction current collected at the anode for applied voltages: 4, 7, 10 and 14 kV.

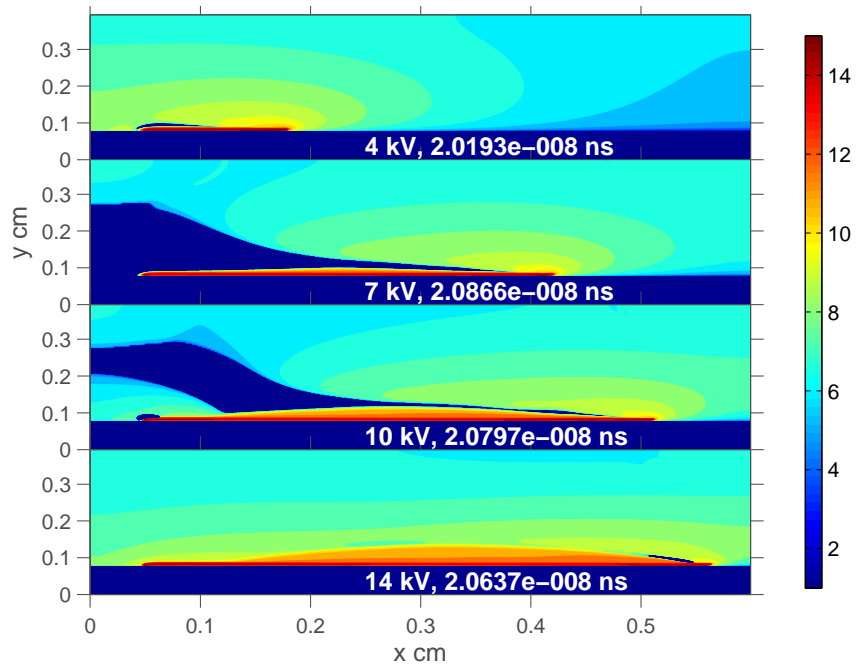
Table 4.1: Amplification coefficient  $\int \alpha_{\text{eff}} dr$  for the SDBD configuration at atmospheric pressure

Voltage $U_0$	$\int \alpha_{\text{eff}} dr$
$U_0=14$ kV	162
$U_0=10$ kV	97
$U_0=7$ kV	54
$U_0=3.5$ kV	16
$U_0=3$ kV	12

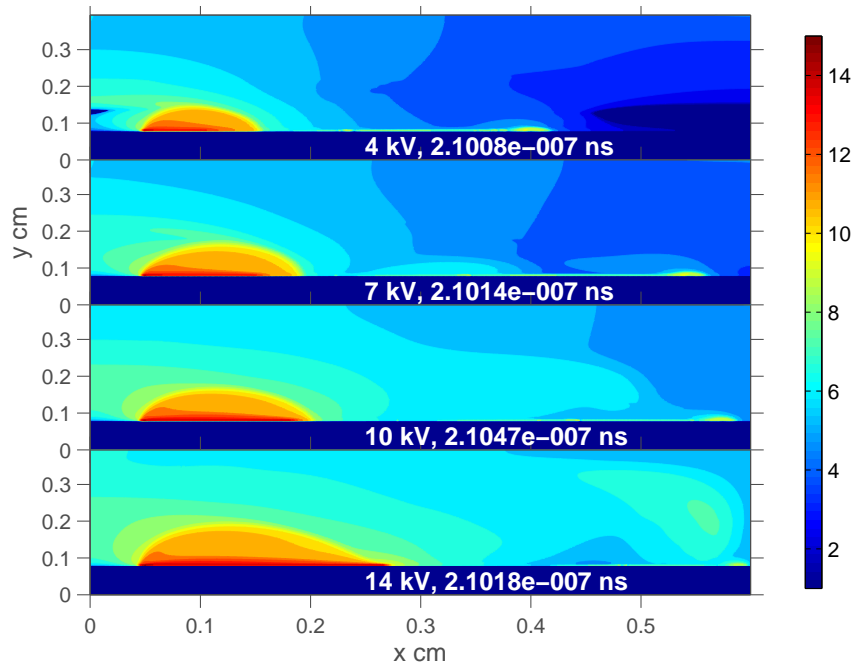
which can be computed using the numerical code described in this chapter. The integral is taken from each point of the dielectric and follows the electric field. In the case that the Townsend breakdown mechanism is the effective criterion, the formula 4.1 must be modified as follows:

$$\oint \alpha_{\text{eff}}(E(\mathbf{r})) d\mathbf{r} = \ln(1 + 1/\gamma)$$

The results of the integral in the lhs of the formula 4.1 are shown in table 4.1: These results indicate that at atmospheric pressure, the breakdown voltage should be about 3.5 kV. In order to extend these calculation to other pressures, we can consider the following reasoning: The electric field in the SDBD geometry is linearly related to the applied voltage, i.e.  $\mathbf{E}(x, y) = U_0 \tilde{\mathbf{E}}(x, y)$ . An  $\alpha$  of the form given by [Raizer, 1991] p.56 can be assumed.  $\alpha = A p \exp(-B p / E)$  where  $E$  is the norm of the electric field  $\mathbf{E}$  (the attachment is neglected here). Therefore, if the ratio  $U_0/p$  is kept constant, the value of the reduced electric field  $E/p = \|\mathbf{E}\|/p = U_0/p \|\tilde{\mathbf{E}}\|$  will be constant throughout the whole geometry with respect to pressure, and the values of  $\oint \alpha_{\text{eff}}(E(\mathbf{r})) d\mathbf{r}$  will consequently be  $\oint A p \exp(-B p / U_0 \tilde{E}) d\mathbf{r}$ , which exponential part is constant with respect to pressure and which varies therefore only linearly with pressure. We

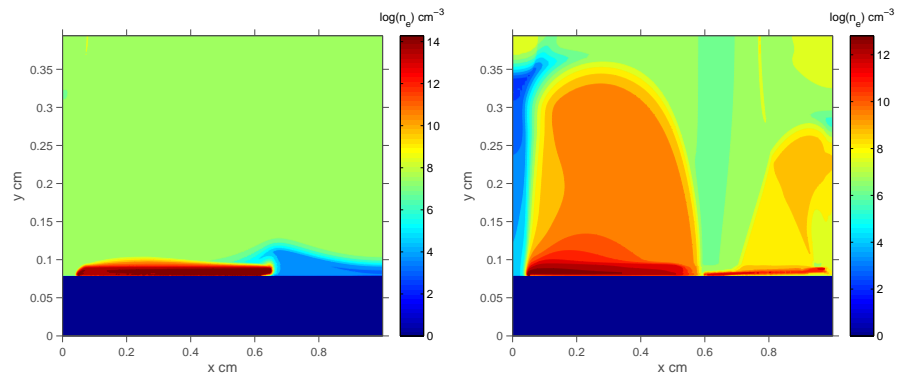


(a)

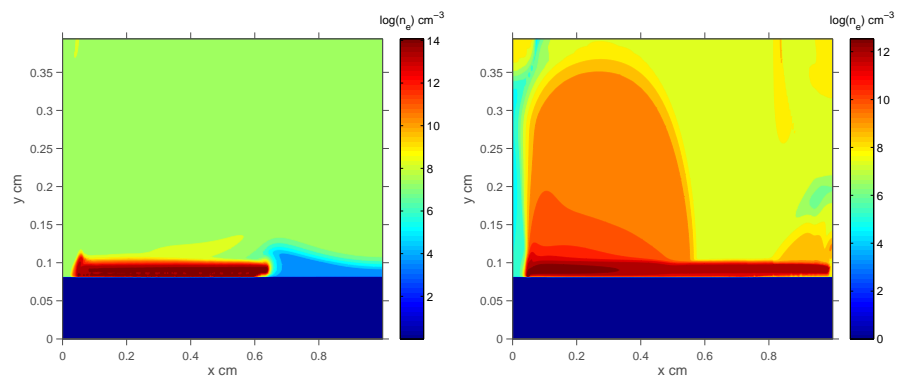


(b)

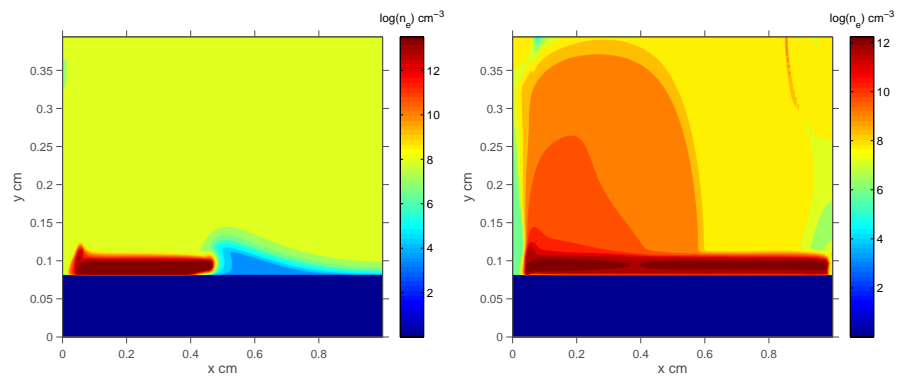
Figure 4.17: Contour plot of the electron density and reduced electric field for different applied voltages during the ascending (a) and decaying (b) phases. The conditions for the computation are: 4,7,10 and 14 kV applied voltages at 1 bar.



(a) 0.5 bar, 7 kV

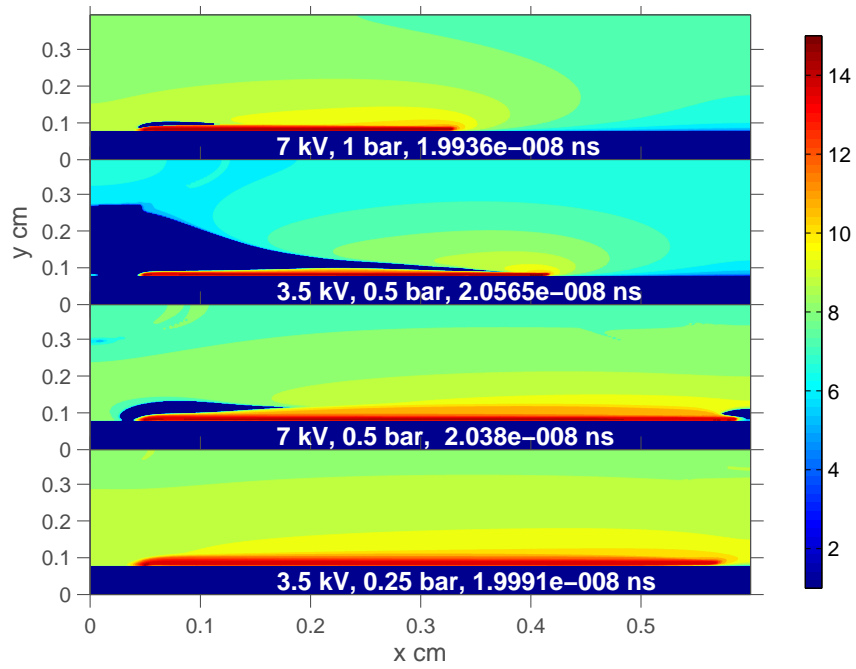


(b) 0.3 bar, 4.2 kV

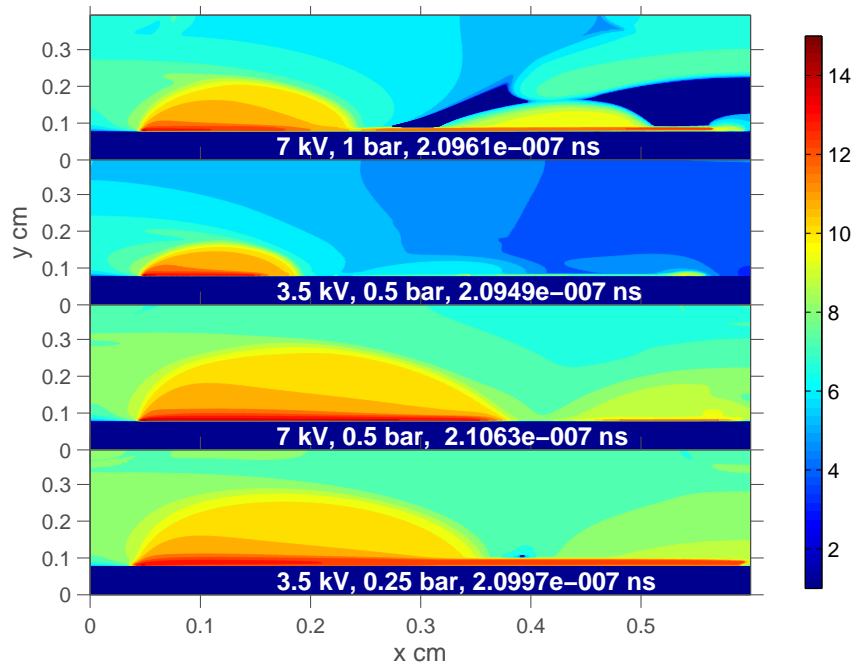


(c) 0.2 bar, 2.8 kV

Figure 4.18: Contour plot of the electron density for different pressures and voltages. Left figures correspond to the ascending phase, 20 ns after the pulse and right figures to the decaying phase, 240 ns after the pulse. The pressures and applied voltages are: 0.5 bar, 7 kV, 0.3 bar, 4.2 kV and 0.2 bar, 2.8 kV.



(a)



(b)

Figure 4.19: Contour plot of the electron density and reduced electric field for different voltages and pressures during the ascending (a) and decaying (b) phases.

Table 4.2: Breakdown pressure for the SDBD configuration for different values of  $U_0/p$ 

Voltage $U_0/p$ kV/bar	$p_{breakdown}$ Torr	$p_{breakdown}$ bar
14	75	0.10
10	125	0.17
7	225	0.30
3.5	760	1.00
3	1013	1.35

can then deduce the breakdown pressures for varying values of  $U_0/p$  (using the lower bound of Meek's criterion  $\oint \alpha_{\text{eff}}(E(\mathbf{r}))d\mathbf{r} = 16$ ). The breakdown pressures found are summarized in table 4.2.

These results present some difference when compared to experimental breakdown voltages. During the experiments, it was noticed that at 0.1 bar, the plasma ignites for a voltage of 1.75 kV. The plasma produced was however not stable. This is to be compared with the theoretical value obtained in this section, which gives 1.4 kV, underestimating the breakdown voltage. The breakdown voltage was measured even higher in some experiments, with a breakdown voltage at 2 kV. If the higher bound of Meek's criterion is used, which is justified due to the lower electric field (see [Montijn and Ebert, 2006]), the value of breakdown pressure ( $U_0/p = 17$  kV/bar) is 0.13 bar at 1.8 kV. This value is in good agreement with the behavior observed during the experiments, which was an unstable (= not very intense) plasma at 2.1 kV at 0.12 bar. On the other hand, the breakdown voltage at higher pressures was found to be very low, of the order of 2 kV. These discrepancies with the model can be explained at high pressure, where inhomogeneities in the electrode could produce locally enhanced fields, thus reducing the voltage necessary to attain the breakdown field.

#### 4.3.5 EHD Force and Heat Released by the Actuator

The time and space averaged EHD force  $f_x(t) = \int \int F_x dx dt$  is plotted for the computations performed. The effect of the variation of the polarity is show in figure 4.22. The positive pulses transfer most of the momentum during the formation phase of the plasma, increases slightly during the voltage plateau to reach its maximum at  $3.4 \cdot 10^{-1}$  nNs/cm. Then the value of the momentum transfer decreases, due to the reverse breakdown transferring momentum in the opposite direction due to the change in electric field's orientation (from the positively charged dielectric to the upper electrode charged negatively with respect to the dielectric). However, the positive streamer transfers more momentum than the reverse breakdown (negative streamer). This lower intensity of the reverse breakdown is also evidenced by examining the energy consumption, which is lower during the decaying phase compared to the ascending phase. The energy consumption is approximately 0.5 mJ/cm, which is to be compared to the experimental value of 0.2 mJ/cm. As noted above, the 2D model of the streamer is overestimating the current and thus the energy transferred to the gas, due to the finite length of the plasma along the coordinate normal to the computational plane. Moreover, the method to

compute the energy deposited in the gas overestimates the energy by more than 50 percents, as noted in section 3.3.1. Consequently, the two numbers seem in relatively good agreement. Interestingly, the negative pulse transfers a net positive momentum to the gas, the reverse breakdown being stronger in this case. The energy consumption is also lower than for the positive pulse.

The effects of the variation of the applied voltage from 4 to 14 kV is shown in figure 4.20 for positive polarity at atmospheric pressures. The momentum transferred during the ascending phase increases regularly with the voltage, but the amount of momentum transferred during the decaying phase does not vary similarly. The overall effect is a total momentum transferred weakly dependent on the voltage. The efficiency is thus better for smaller voltages (close to the breakdown field).

These results can be compared with [Unfer and Boeuf, 2010] and with [Likhanskii et al., 2007]. In [Unfer and Boeuf, 2010], the comparison between the EHD force and energy output was performed for different pulses. For a pulse similar to the one computed in this thesis, i.e. 10 ns rise and fall time, 1  $\mu$ s plateau and 15 kV applied voltage. The space and time integrated force was found to be 5.5 nNs/cm per pulse, which compares to the present results of  $2 \cdot 10^{-1}$  nNs/cm. This difference could be due partly to the duration of the plateau. Indeed, the momentum transfer is seen to increase during the plateau. With a plateau being 5 times longer, the momentum should increase by  $5 \cdot 10^{-1}$  nNs/cm. In [Unfer and Boeuf, 2010], the integrated energy was found to be  $3.6 \cdot 10^{-5}$  J/cm per pulse. This order of magnitude difference when compared to the present case can be explained by the discrepancy found when comparing the present numerical model to the model of Unfer et al. The current is stronger in the present case, with shorter duration. The typical momentum generated by a pulse plus bias computed in [Likhanskii et al., 2007] was approximately  $10^{-1}$  nNs/cm, which is very close to the present calculations.

The results for varying operating pressures are shown in figure 4.21. The momentum transferred is smaller as pressure decreases and higher for higher reduced electric fields, for the ascending phase. The momentum transferred during the decaying phase is again stronger for higher reduced electric fields, reducing the overall momentum transferred. The energy deposition is higher for higher pressures and higher reduced electric field, following a non linear dependence. It is to be noted that the computational domain was restricted to 6 mm in length in order to save memory and computational time. The plasma propagates further for the high reduced electric fields conditions, possibly leading to a higher momentum and energy transfer. These results does not present a similar trend as in [Benard et al., 2008], where a maximum ionic wind was found to occur at 0.6 bar. From these calculations, it can be deduced that higher voltages do not lead to higher momentum transfer, rather the contrary. The detrimental contribution from the decaying phase should be avoided. One possibility seems to be the use of a low applied voltage. On the other hand, high energy deposition is achieved at high applied voltages and high pressures. This complex behavior does not allow to determine the effect of the pressure for different applied voltages forms. Indeed, these results

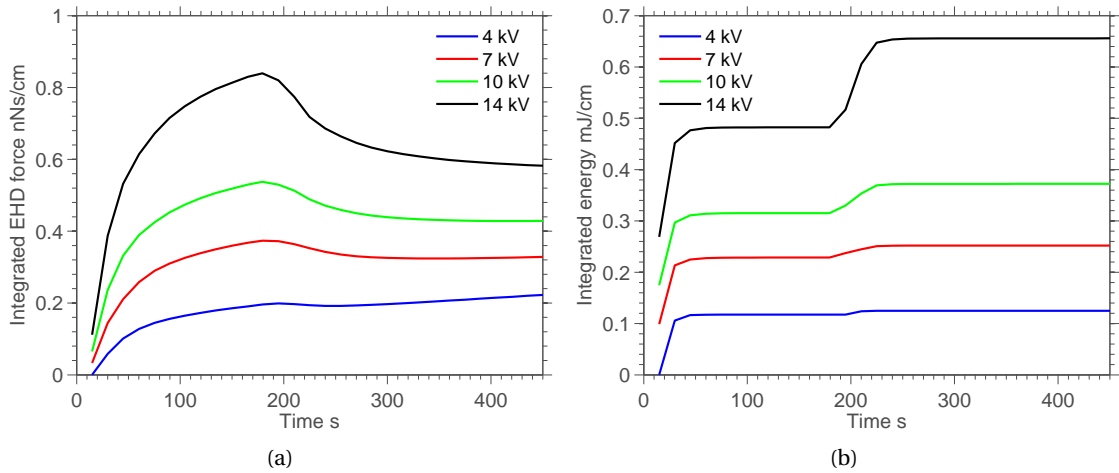


Figure 4.20: Temporal evolution of the time and space integrated parallel EHD force (a) and energy density (b) in function of the applied voltage.

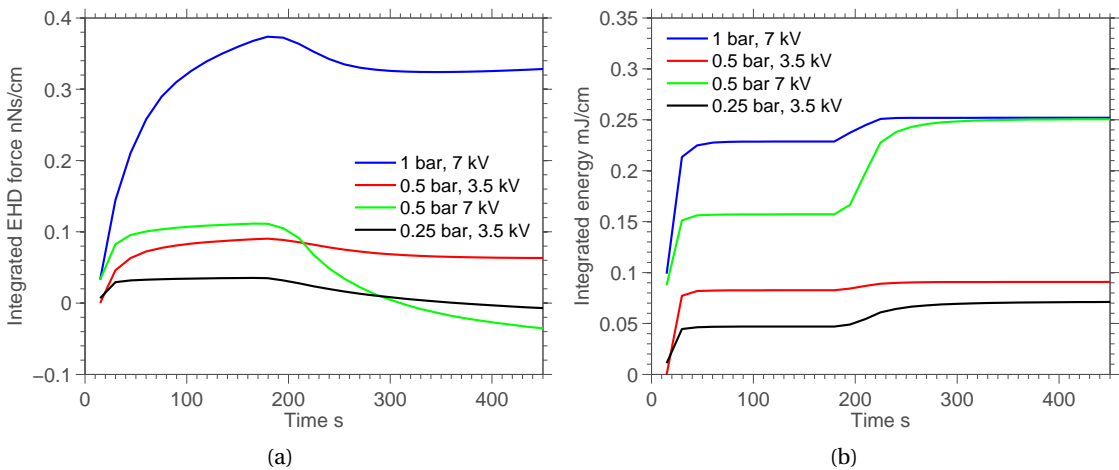


Figure 4.21: Temporal evolution of the time and space integrated parallel EHD force (a) and energy density (b) for different voltages and pressures.

do not follow the trend reported in [Benard et al., 2008], where a sinusoidal applied voltage was applied to the SDBD. Moreover, the global momentum and energy transferred to the gas cannot be linked in a simple manner to the plasma characteristics as measured with OES. It is to be noted that the present calculations does not take any saturation effects into account. Indeed, the net charge deposited in one pulse is positive, meaning that it will accumulate from pulse to pulse. The total charge remaining in the gas or on the surface will therefore screen the applied voltage and decrease the overall efficiency of momentum transfer. This point was shown experimentally in [Opaits et al., 2008b]. In order to prevent this effect, a negative pulse should be applied from time to time in order to remove the positive charges.

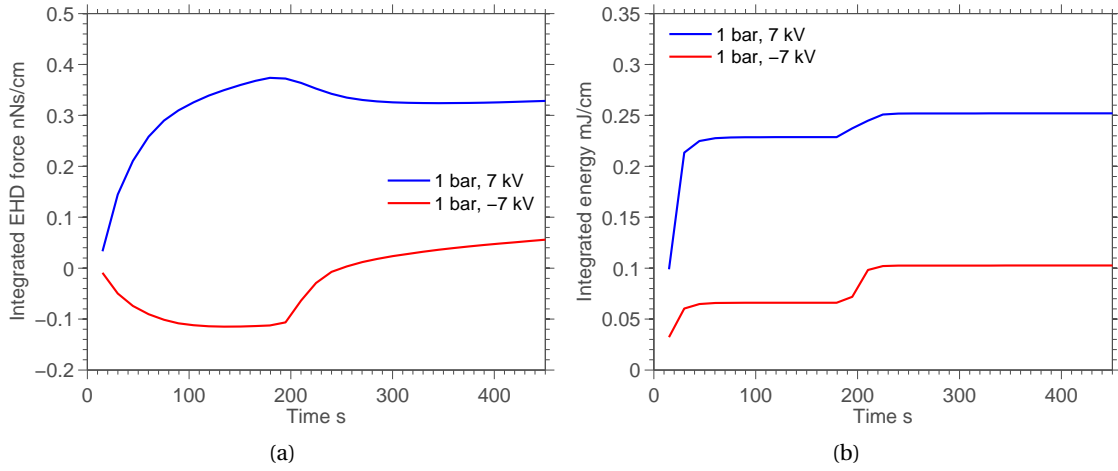


Figure 4.22: Temporal evolution of the time and space integrated parallel EHD force (a) and energy density (b) for positive and negative voltages.

#### 4.4 Comparison with the Experiments

In order to compare the spectroscopic measurements performed during the experiment with the numerical code, excited species are computed using the collisional-radiative discussed in section 2.4.1 and described by equation 2.19. The excited species are computed using the electron density and reduced electric field from the numerical solution of streamer, they are not computed in the streamer code. The kinetic processes involving excited species is very complex [Kossyi et al., 1992] in atmospheric pressure cold plasmas, and their detailed modelling is outside the scope of this thesis. The coupling of excited species might be important to the general dynamics of the discharge, as step-ionization, notably from vibrationally excited species [Guerra et al., 2004], and associative ionization [Popov, 2009] can occur under certain conditions. Nevertheless, these effects are believed to be insignificant at high reduced electric fields typical of the streamer head, which dominates the general features of the streamer propagation. In order to validate this assumption, step-excitation from the ground state of  $N_2^+(X^2\Sigma_g^+)$  has been computed, assuming that the population density of  $N_2^+(X^2\Sigma_g^+)$  is equal to the positive ion density. The case with step excitation was compared to the case of excitation from the ground state of  $N_2$  only. Step-excitation is particularly important for spectroscopy-based measurements of the reduced electric field because it would make the measured reduced electric field overestimated for situations where the ion density is high and the reduced electric field is low. Fortunately, the real population of  $N_2^+$  is not equal to the population of positive ions  $n_p$  computed in the streamer code, because of ion-ion conversion and charge exchange processes.

To reproduce the light output as would be recorded by an optical system, the density of radiating species is multiplied by the sensitivity function of the optical system (approximated



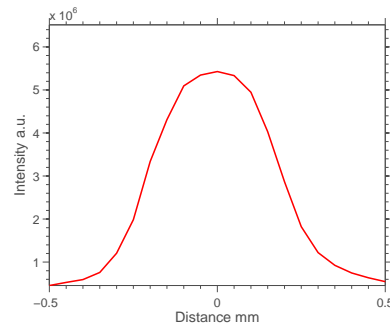


Figure 4.23: Response of the optical system to a point source in the 385-415 nm wavelength range.

by a normalized Gaussian of 250  $\mu\text{m}$  HWHM) and integrated in space. Due to the finite exposure time (gate width of the camera), the space integrated intensity is integrated in time for the duration of the gate width.

The sensitivity of the optical system has been estimated by measuring the light coming from an optical fiber connected to the calibration lamp. The location of maximum intensity has been located and measurement of the spectrum for the two spectral zones has been performed while displacing the optical system in steps of 500  $\mu\text{m}$  from -0.5 to 0.5 mm in the direction of propagation of the streamer. The resulting function is shown in figure 4.23.

The temporal evolution of the excited species is presented in figure 4.24 as would be recorded by a fast camera with gate width 2ns. The plot for the ascending phase starts at 7 ns after the beginning of the pulse. The plot for the decaying phase starts after 170 ns from the beginning of the pulse. These computations are to be compared with the corresponding experiments presented in section 3.3, and shown once more in figure 4.25 for convenience.

First the ascending phase is analyzed. The agreement between the computed and measured absolute densities of excited species is good. However, this agreement must not be overestimated, as the numerical model supposes an uniform streamer in the direction normal to the computational plane. This is not what is observed in reality, at least at high pressure, where the streamers are well separated. The overall intensity recorded is therefore lower than would be measured if a single streamer was recorded. This difference is also noticed in the magnitude of the current computed, which is at least an order of magnitude higher in the computation than estimated in the experiments. The absolute densities computed should therefore be higher than the measured ones. For the decaying phase, the agreement between experiment and computation is slightly less good. The relative magnitude between ascending and decaying phase is not the same in the experiments and in the computations.

The relative magnitude of the populations of excited species is very similar to the experiments. The population density of the  $\text{N}_2(B^3\Pi_g, \nu = 3)$  and  $\text{Ar}(2p_1)$  are slightly lower in the experiments than in the computation, with respect to the population density of the  $\text{N}_2(C^3\Pi_u, \nu = 0)$

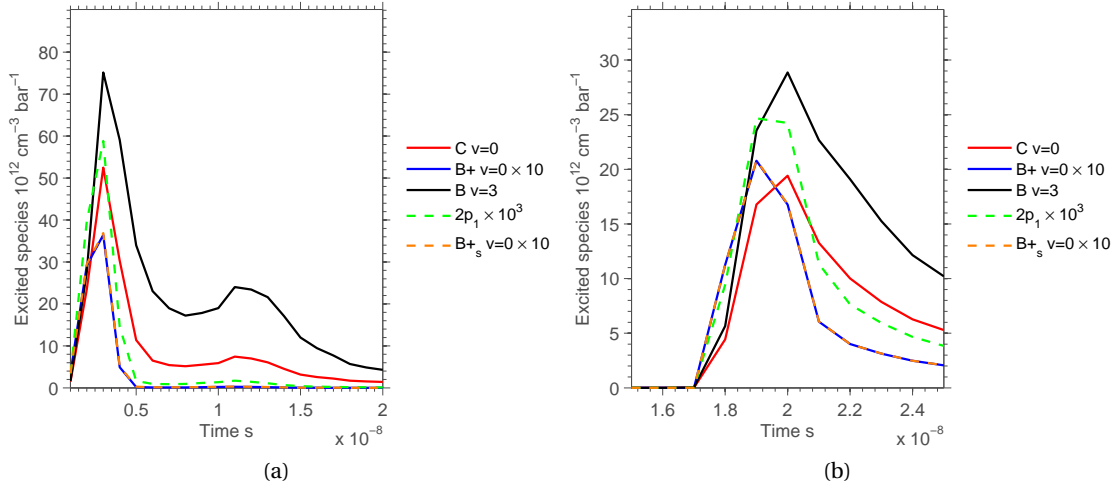


Figure 4.24: Temporal evolution of the excited species as would be recorded with a gate width of 2 ns. Ascending phase (a) and decaying phase (b).

state. Also, the  $N_2^+(B^2\Sigma_+, \nu = 0)$  is larger in the experiments than in the computation. This indicates a slightly higher electric field in the experiments than in the computation, which is confirmed by the computation of the reduced electric field shown in figure 4.28.

The width of the pulse of intensity computed (the increase and decrease of the excited species populations) for both the ascending and decaying phases is smaller than in the experiment, which most likely to be due to a faster propagation of the plasma in the computation.

A last interesting point is the contribution of step-excitation to the population of  $N_2^+(B^2\Sigma_+, \nu = 0)$ , which is found to be insignificant for both phases. This was confirmed during the experiments.

It is informative to compare the shape of the integrated intensity to the shape of the contour of the corresponding excited species density. These are plotted in figure 4.26. The spread of the species having a large quenching rate and a high excitation threshold is much smaller than for species with lower quenching rates and low excitation threshold. The integrated intensities of the more spread out species will reach their maximum when the maximum amount of excited species is “seen” by the optical system. That is when the head of the streamer reaches the end of the Gaussian. The maximum intensity of the more concentrated species on the other hand will occur when the head of the streamer reaches the maximum of the Gaussian. This is why the maximum of the intensities recorded in experiments is recorded at a different time. The maxima will occur at different moments in time also due to the velocity of the streamer, which is smaller in the case of the decaying phase. This fact is accentuated when the pressure diminishes, because the quenching decreases linearly with pressure. The spread of the maxima is therefore larger for lower pressures, as is seen in experiments.

#### 4.4. Comparison with the Experiments

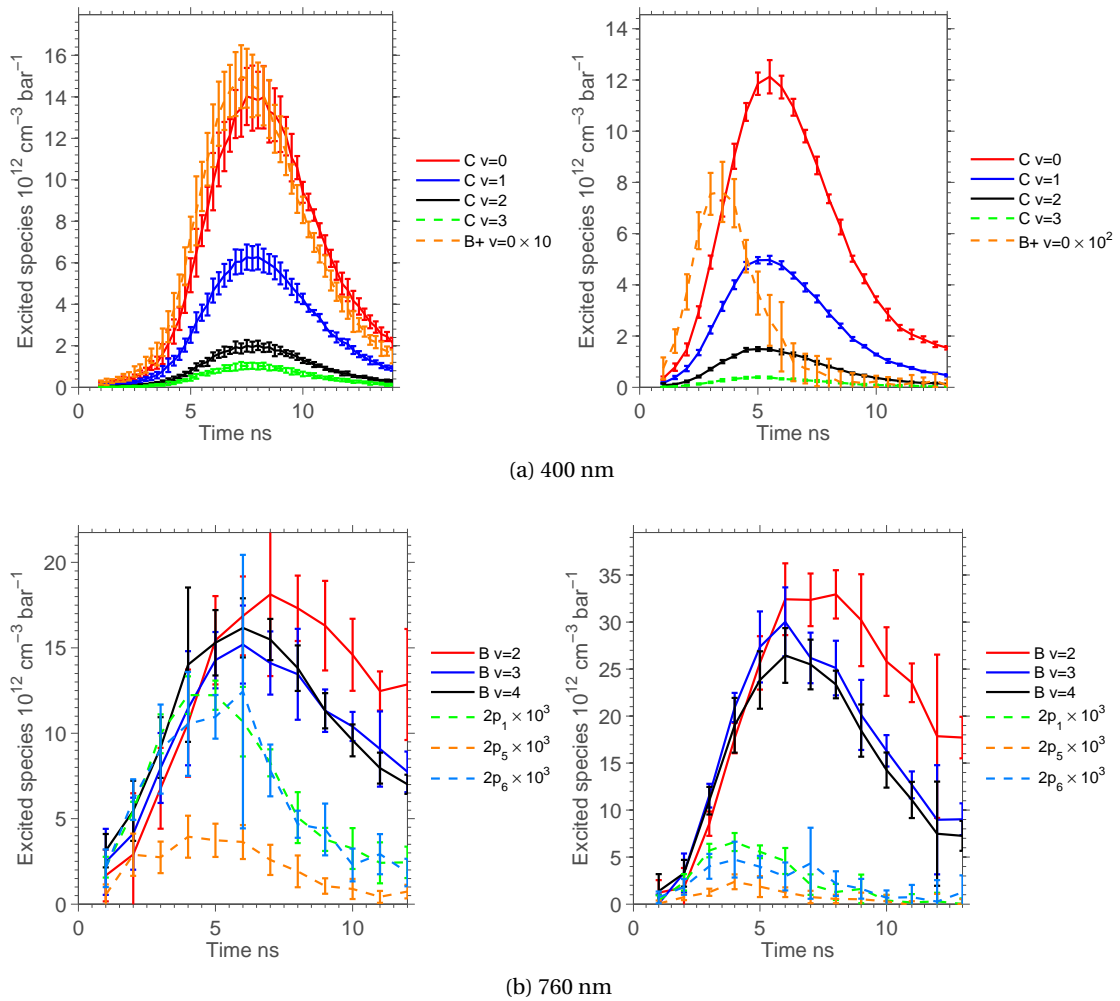


Figure 4.25: Temporal evolution of the excited species populations, for the ascending phase (left) and the decaying phase (right) for a 7 kV pulse at 1 bar. The excited species are inferred from emission spectroscopy in the 400 nm spectral zone (a) and in the 760 nm spectral zone (b).

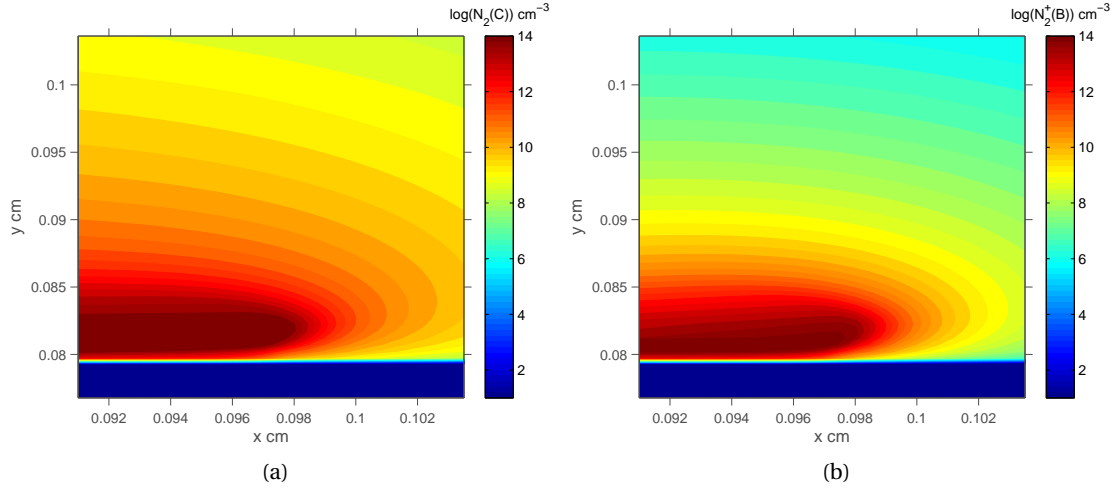


Figure 4.26: Contour plot of the density of  $N_2(C^3\Pi_u, \nu = 0)$  (a) and  $N_2^+(B^2\Sigma_+, \nu = 0)$  (b).

The spatial evolution of the integrated excited species is shown in figure 4.27. The distance is measured from the edge of the upper electrode (located at  $x=0.5$  mm).

The spatial evolution of the reduced electric field is shown in figure 4.28. The qualitative agreement for the ascending phase can be seen to be correct. The distinct values taken by the reduced electric fields determined from different lines is clearly seen. For the decaying phase, the agreement is poor.

The comparison of the estimated electron densities and metastable excited species as computed with equations 2.23 and 2.24 respectively is shown in figure 4.29.

The agreement between computed and estimated population densities of metastable states is relatively bad, with a factor of 4 underestimation for the worst part, which is the small distance. This discrepancy can be understood as follows: the production of metastable states is inferred from the population of radiating species, which are produced in the head of the streamer. Therefore, the metastable states estimated with this method are also assumed to be produced only in the streamer head. As the streamer propagates, the validity of this assumption degrades. More importantly, the averaged electron density is about two orders of magnitude lower than the electron density computed directly. These discrepancies can be easily understood when considering the graph of the electron density and of the reduced electric field along a line, as is shown in figure 4.30. The production rate leading to the production of excited species is a function of the electron density and the reduced electric field. The shape of this production rate for  $N_2(C^3\Pi_u)$  and  $N_2^+(B^2\Sigma_+, \nu = 0)$  is also plotted in figure 4.30. The production rate is maximum at a point in space where neither the electron density nor the reduced electric field is maximum. This is a well known fact about the streamer's head as discussed in [Naidis, 2009]. Therefore the electron density as estimated with equation 2.23 is necessarily lower than the maximum electron density and is also lower than the averaged electron density computed

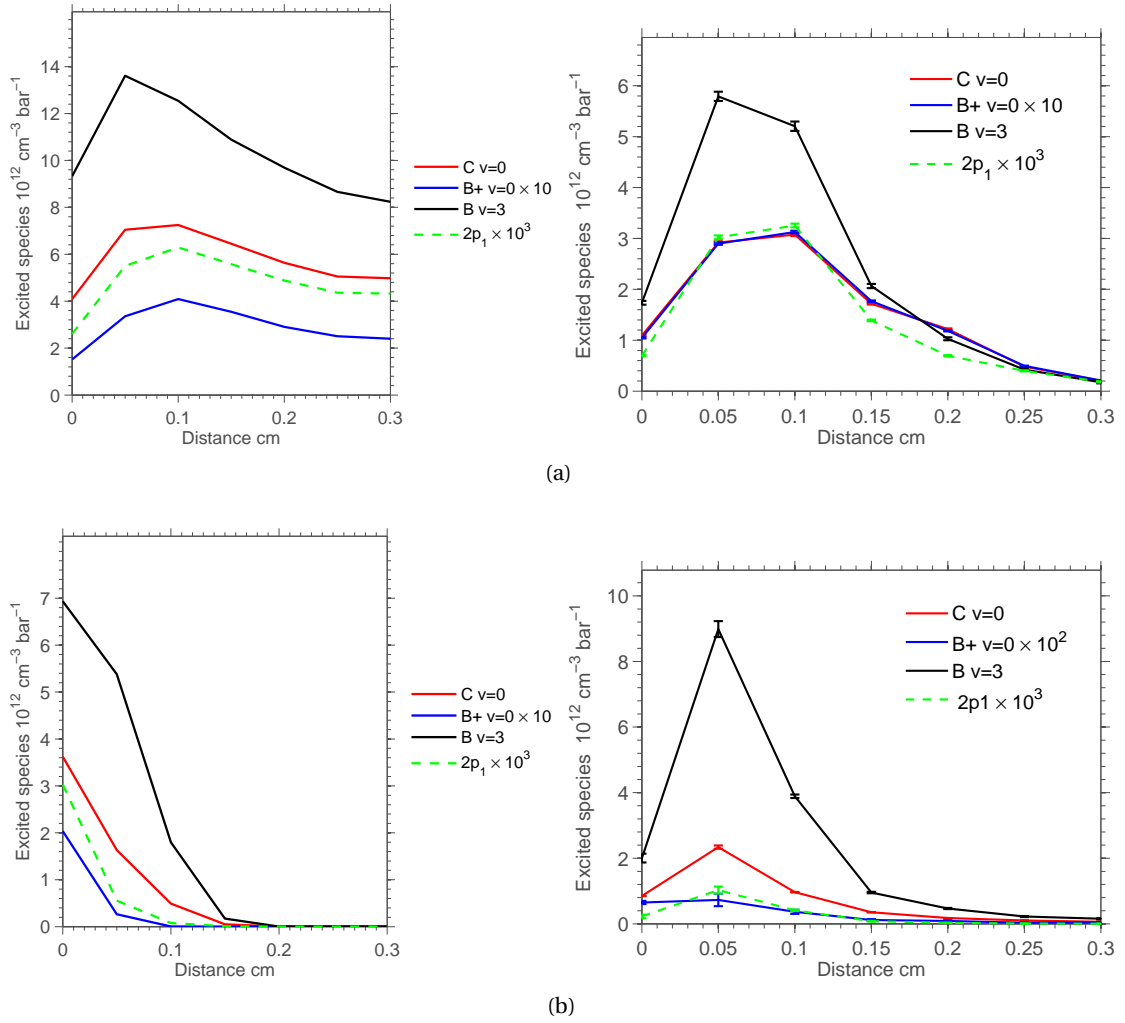


Figure 4.27: Comparison of the spatial profiles of the excited species computed with the numerical model (left) and measured during the experiments (right). Ascending phase (a) and decaying phase (b).

within the code. It is to be noted that the determination of the electron density in a streamer is particularly difficult, and even if Stark broadening measurements could be performed, it would be affected by the difference between maximum excitation electron density and maximum electron density. The true maximum electron density could be measured only if a laser would excite the transition used for Stark broadening measurement in the body of the streamer.

**Exponential fit** In order to improve the quality of those estimations, the shape of the electron density and of the reduced electric field can be approximated by exponentials, which take the form:

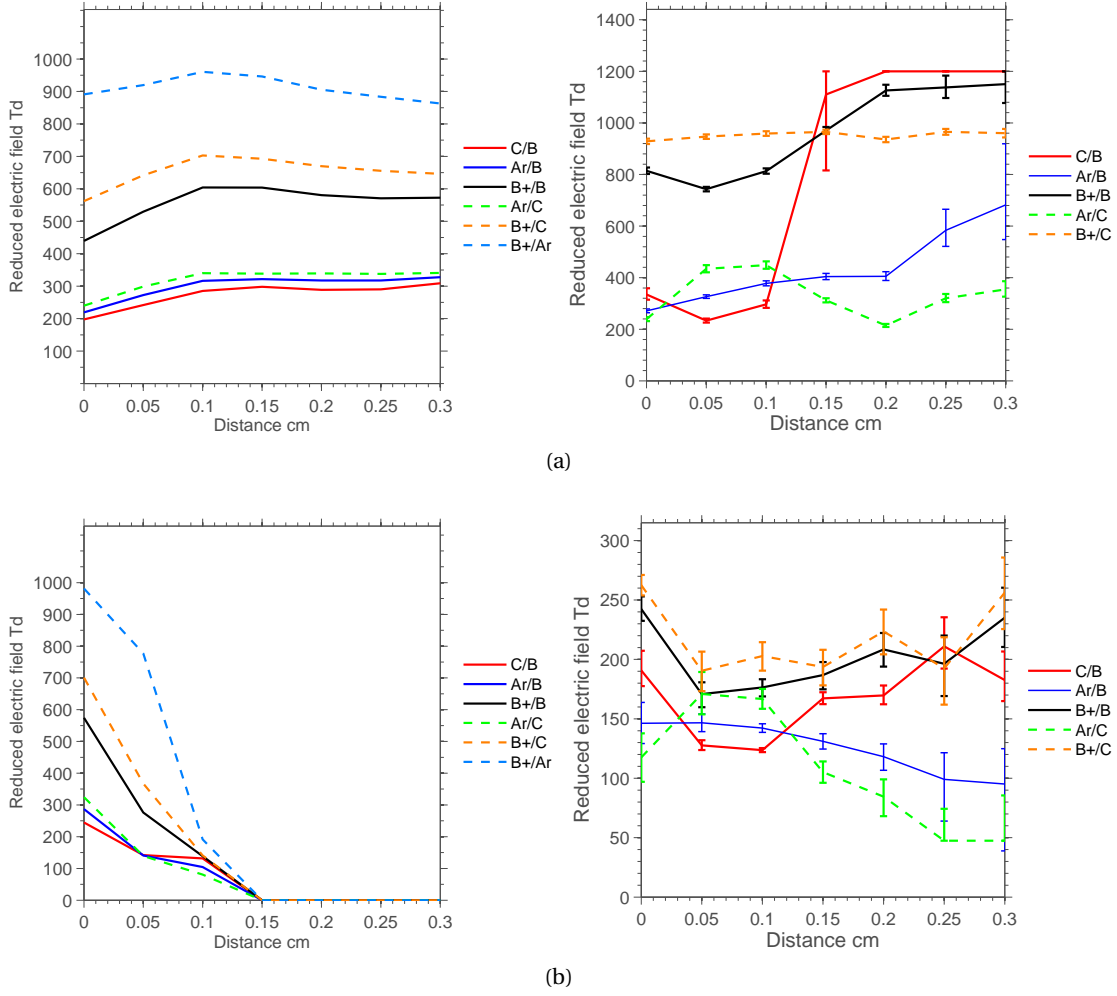


Figure 4.28: Comparison of the spatial profile of the reduced electric field computed with the numerical code (left) and measured during the experiments (right). Ascending phase (a) and decaying phase (b).

$$\frac{E}{N}(x) = E_0 \exp(x)$$

$$N_e(x) = N_{e0} \exp(-sx)$$

where  $E_0$ ,  $N_{e0}$  and  $s$  are fitting parameters. If these approximations are used to compute the ratio of excited species, the following equation is obtained:

$$\frac{\int_0^t \int_{-\infty}^{\infty} \int_0^{x_{\max}} T \exp(-sx) X_i K_i (E_0 \exp(x)) dx dy dt}{\int_0^t \int_{-\infty}^{\infty} \int_0^{x_{\max}} T \exp(-sx) X_j K_j (E_0 \exp(x)) dx dy dt} = \frac{\bar{n}_i \tau_j}{\bar{n}_j \tau_i}$$

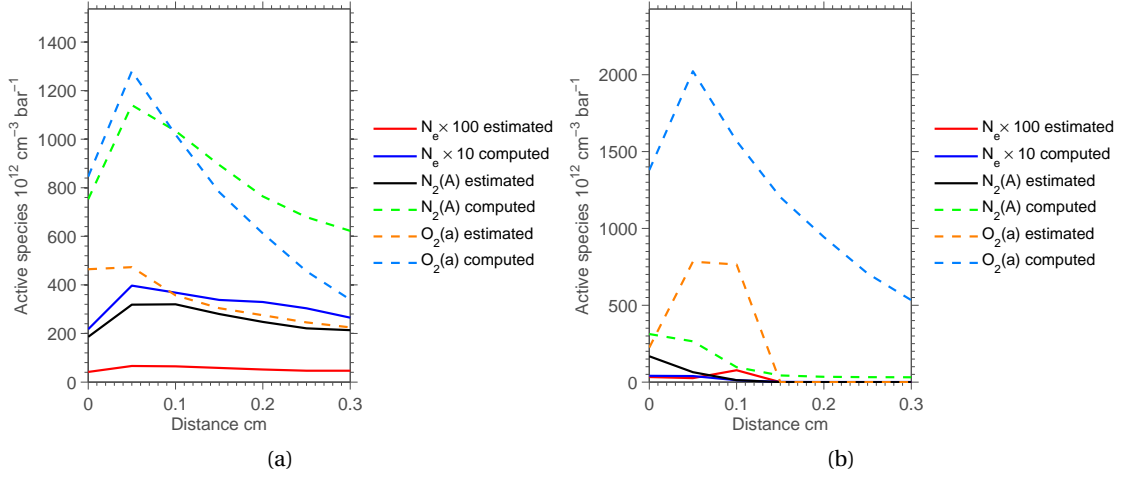


Figure 4.29: Spatial evolution of the average electron density and average metastable states  $N_2(A^3\Sigma_u^+)$  and  $O_2(a^1\Delta_g)$ . The comparison is made between population densities estimated and directly computed. Ascending phase (a) and decaying phase (b).

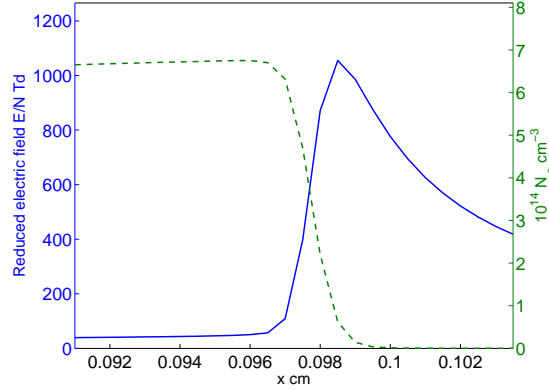


Figure 4.30: One dimensional profile of the electron density and reduced electric field along the streamer.

where the  $\bar{\phi}$  represent the space average of the function  $\phi$ , and  $x_{\max}$  is the upper limit of the integration. In practice it is chosen as the value when  $N_e(x_{\max}) = N_{e0}/100$ . The  $N_{e0}$ s can be taken out of the integral and simplified. If the problem is assumed one dimensional, then the integration with respect to  $y$  simplifies as well. If the structure of the streamer head is assumed to remain constant in time, then the integration in time can also be simplified. The values of the electron densities and reduced electric fields represent therefore averaged quantities in time and take into account also the optical sensitivity function  $T$ . The equation to be solved is then only:

$$\frac{\int_0^{x_{\max}} \exp(-sx) X_i K_i (E_0 \exp(x)) dx}{\int_0^{x_{\max}} \exp(-sx) X_j K_j (E_0 \exp(x)) dx} = \frac{\bar{n}_i \tau_j}{\bar{n}_j \tau_i} \quad (4.2)$$

To determine the two unknown parameters  $E_0$  and  $s$ , two equations need to be solved, involving at least three excited species.

Once these parameters are calculated, the electron density  $N_{e0}$  can be found using equation 4.3 and the population of metastable excited species with equation 4.4.

$$N_{e0} = \frac{\bar{n}_i}{\tau_i \left( \int_0^{x_{\max}} \exp(-sx) X_i K_i (E_0 \exp(x)) dx / x_{\max} \right)} \quad (4.3)$$

$$\bar{n}_i(\Delta t) = \frac{X_i \int_0^{x_{\max}} \exp(-sx) X_i K_i (E_0 \exp(x)) dx \bar{n}_j \Delta t}{X_j \int_0^{x_{\max}} \exp(-sx) X_j K_j (E_0 \exp(x)) dx \tau_j} \quad (4.4)$$

The estimation of the population of metastable excited species and of the electron density made with the exponential fit are shown in figure 4.31. It can be seen that there is no improvement on the estimation of the metastable populations. However, the average electron density estimated with the exponential fit is much better. This method provides a rough estimates, and it requires further investigation to determine its applicability.

**Variation of the pressure** The spatial evolution of the integrated excited species with varying pressure is shown in figures 4.32, 4.33, 4.34 and 4.35. The distance is measured from the edge of the upper electrode (located at  $x=0.5$  mm). The qualitative behavior is relatively good for both ascending and decaying phases, with the same weaknesses noted for the atmospheric pressure case. The profile of excited species is flatter than in the experiments for the ascending phase, and stems from the wrong propagation speed of the streamer. The quantitative agreement between experiments and computations is very good for the ascending phase. Comparatively, the quantitative agreement during the decaying phase is not good. The absolute populations are not the same and the trends with respect to the pressure are not the same. The population of the  $N_2^+(B^2\Sigma_+, \nu = 0)$  state in the decaying phase is largely overestimated in the computation and moreover does not follow the same trend compared to the experiments with decreasing



#### 4.4. Comparison with the Experiments

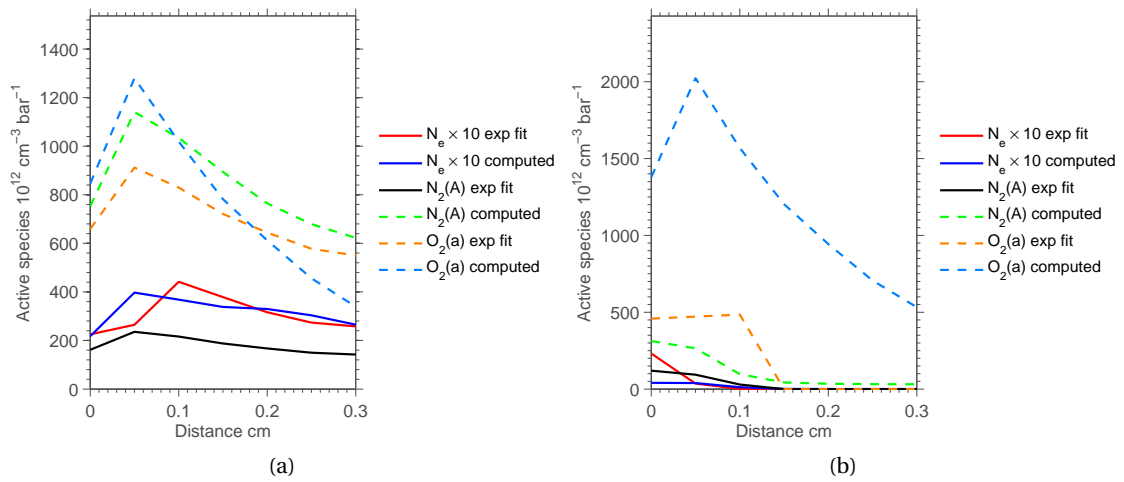


Figure 4.31: Spatial evolution of the average electron density and average metastable states  $N_2(A^3\Sigma_u^+)$  and  $O_2(a^1\Delta_g)$  for the ascending phase. Comparison between population densities estimated with the exponential fit and directly computed (a). Comparison between population densities estimated with equation 2.24 and directly computed (b).

pressure.

## Chapter 4. Numerical Model of the Plasma

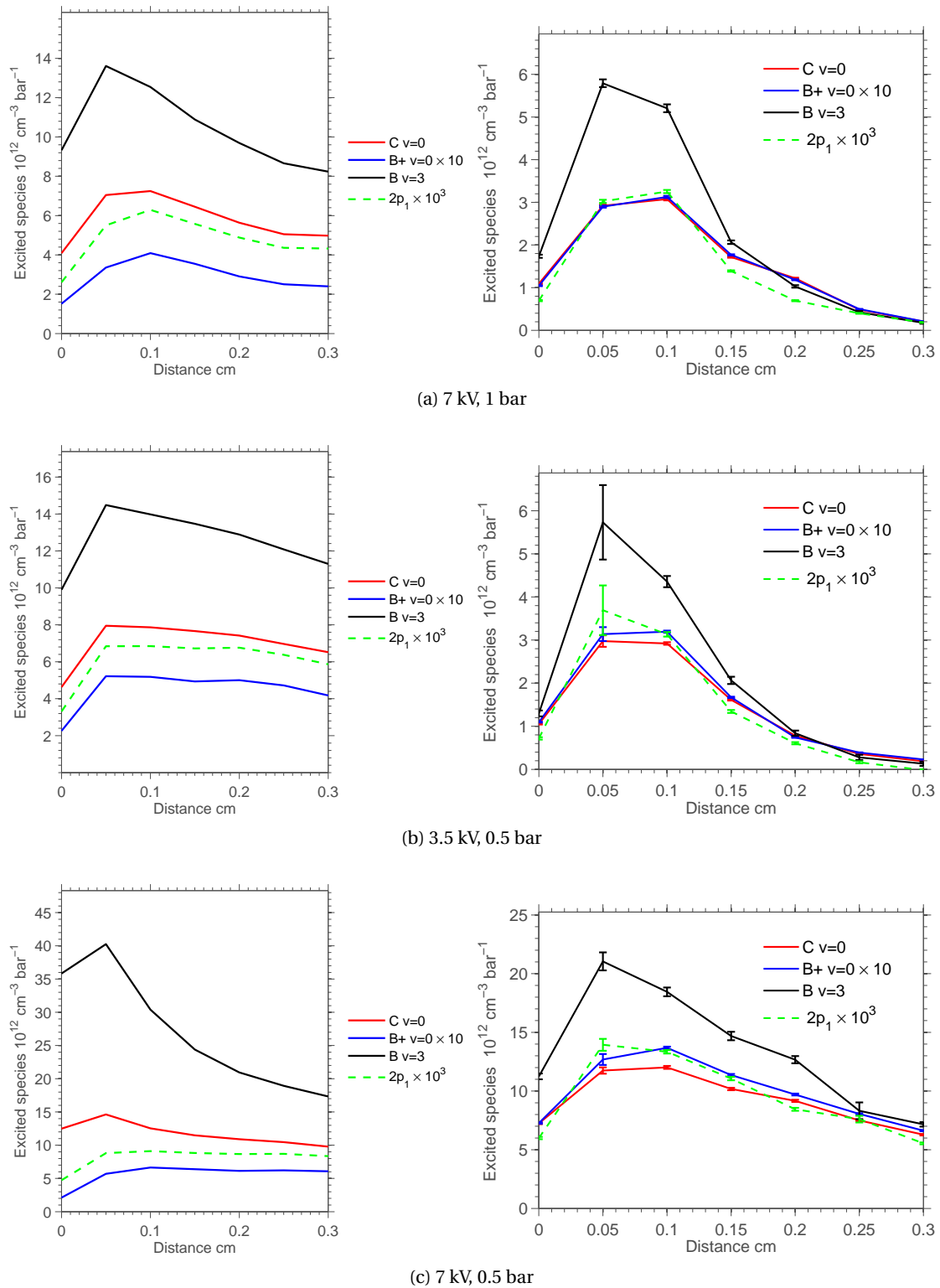


Figure 4.32: Comparison of the spatial profiles of the excited species populations, for the ascending phase. Numerical model (left) and the experiments (right). The applied voltages and corresponding pressures are: 1 bar, 7 kV (a), 0.5 bar, 3.5 kV (b) and 0.5 bar, 7 kV (c).

#### 4.4. Comparison with the Experiments

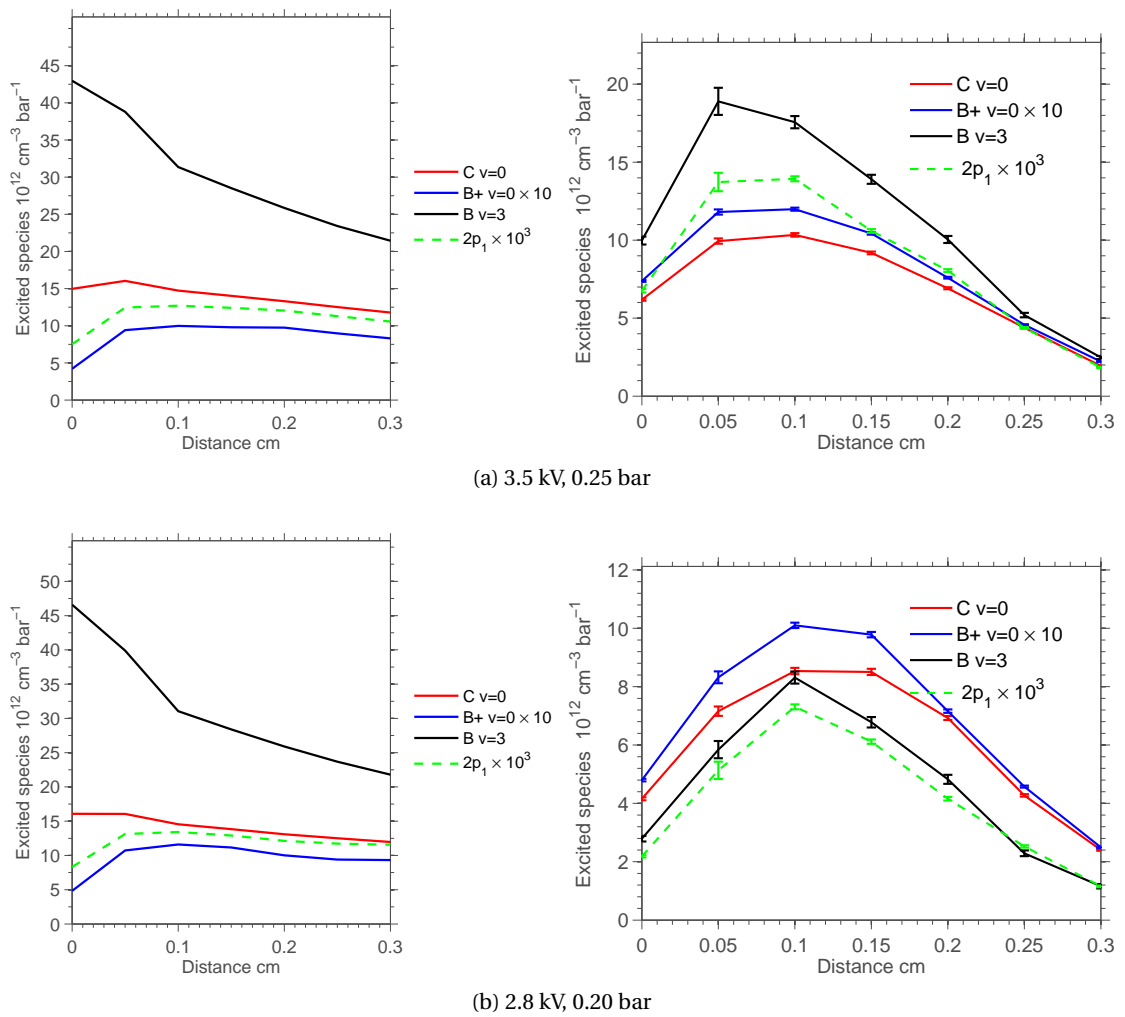


Figure 4.33: Comparison of the spatial profiles of the excited species populations, for the ascending phase. Numerical model (left) and the experiments (right). The applied voltages and corresponding pressures are: 0.25 bar, 3.5 kV (a) and 0.2 bar, 2.8 kV (b).

## Chapter 4. Numerical Model of the Plasma

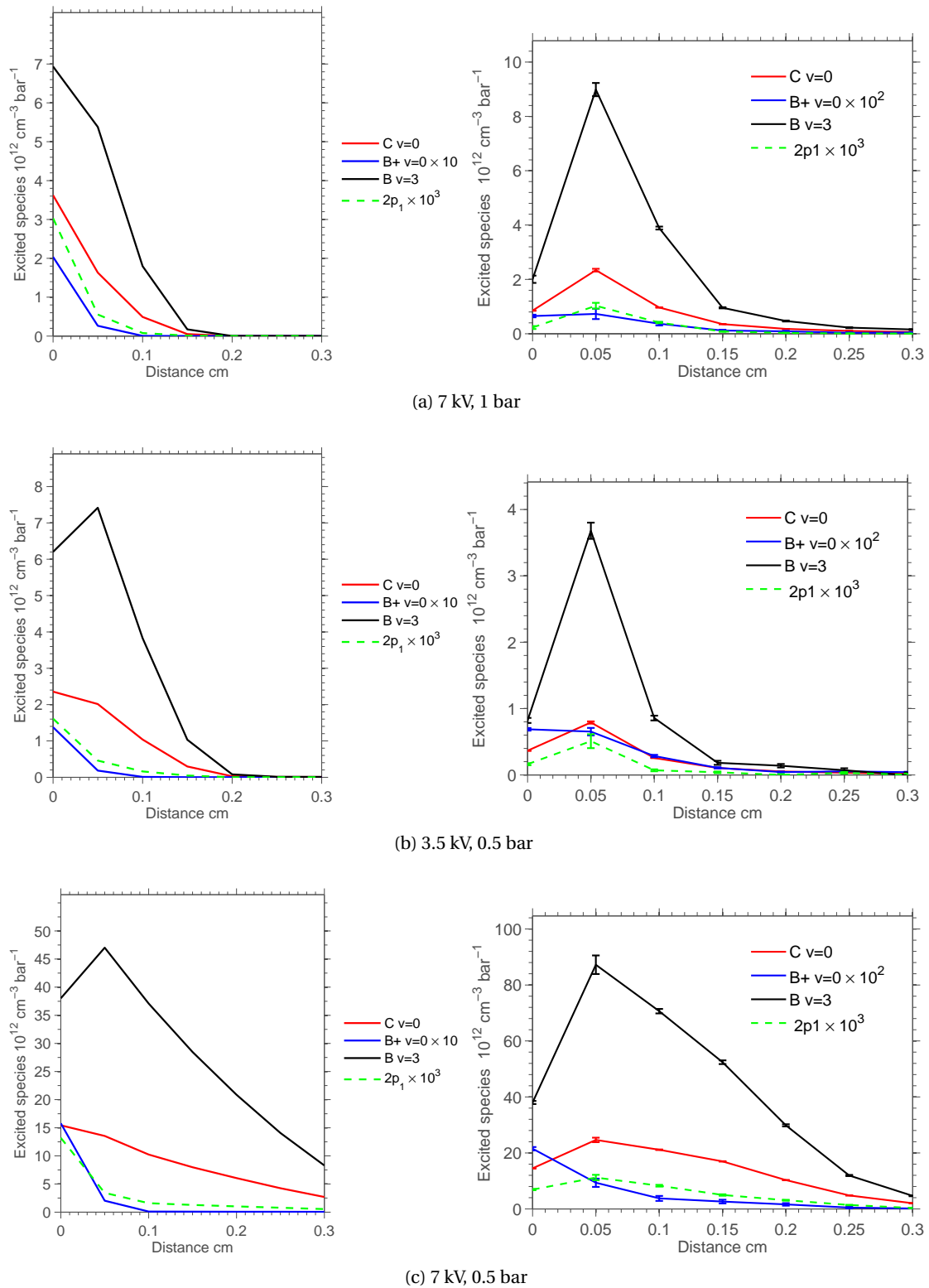


Figure 4.34: Comparison of the spatial profiles of the excited species populations, for the decaying phase. Numerical model (left) and the experiments (right). The applied voltages and corresponding pressures are: 1 bar, 7 kV (a), 0.5 bar, 3.5 kV (b) and 0.5 bar, 7 kV (c).

#### 4.4. Comparison with the Experiments

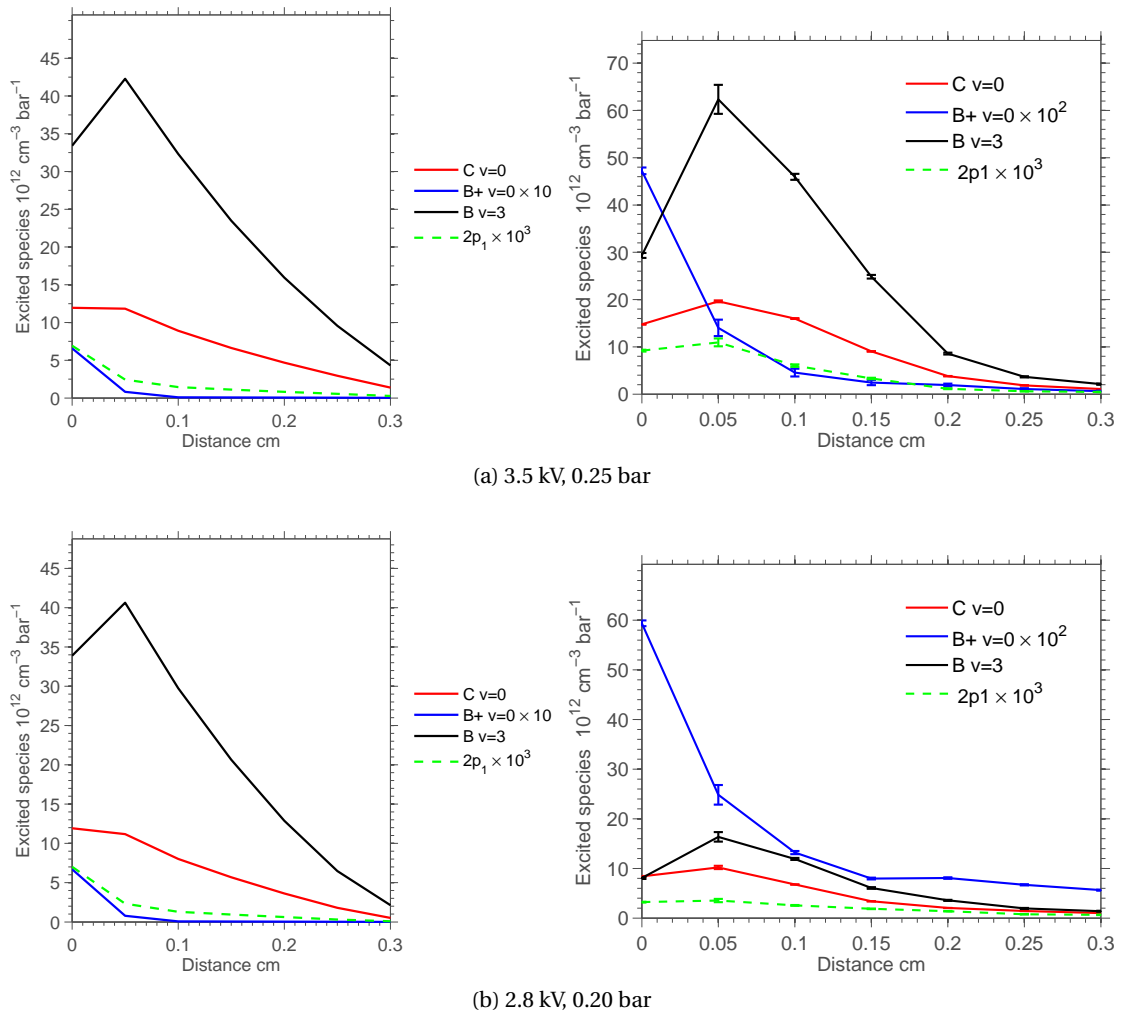


Figure 4.35: Comparison of the spatial profiles of the excited species populations, for the decaying phase. Numerical model (left) and the experiments (right). The applied voltages and corresponding pressures are: 0.25 bar, 3.5 kV (a) and 0.2 bar, 2.8 kV (b).

### 4.5 Conclusions

The numerical modelling of the plasma was discussed in this chapter. First the discretization methods and their implementation were described. A non-uniform grid was implemented in order to decrease both the memory and computational time requirements. A reference computation performed in pure nitrogen was performed and compared to an existing calculation available in the literature. It showed a large discrepancy, notably in the propagation speed and in the current of the streamer simulated, which is believed to be due to a different implementation. Real case computations in air exhibit a smaller difference compared to the literature. The plasma was simulated for a positive pulse at atmospheric pressure, using a photoionization source term to account for seed charges. The ascending phase was shown to correspond to a positive streamer propagating at a maximum distance of 5.5 mm. The decaying phase corresponds to a negative streamer, or reverse breakdown, initiated from the positive charges accumulated from the positive pulse, and propagating to a maximum distance of approximately 2 mm. The same computation was performed with an uniform seed charges density of  $10^8 \text{ cm}^{-3}$ . The results were very similar for both cases.

The simulation of the plasma was performed to investigate the influence of the polarity, the applied voltage and the pressure on the characteristics of the plasma. The polarity was shown to reverse simply the ascending and decaying phases. The size of the plasma was found to increase with decreasing pressures, as expected from similarity laws. An analysis of the breakdown voltages at different pressures was conducted, and showed an overestimation of the breakdown voltage with respect to the experiments, at high pressures. An underestimation of the breakdown voltage was predicted by the model for low pressures if the lower bound of Meek's criterion was used, but was in good agreement with experiments if the upper bound was used for low pressures. The discrepancy found at high pressure is attributed to the inhomogeneities of the electrode surface, which enhance the electric field locally.

Excited species were computed within the numerical code and served for comparison purposes with the experimental measurements. The excited species were considered to emit light vertically, and were integrated in the vertical direction after convolution with a numerical optical sensitivity function of Gaussian shape, matching the sensitivity function measured during the experiments.

The excited species were then integrated in time for a duration of 2 ns and the resulting time-resolved evolution of the excited species could be directly compared to the experiments. Differences were noted which allowed to determine that the propagation speed of the computed streamer was about two times too fast when compared to the experiments.

The approximate shape of the spatial distribution of the reduced electric field and of the electron density along the streamer was assumed to be of exponential form. This assumption was then used to determine more accurately the active species produced. Taking into account the shape of the electron density and reduced electric field proved to be beneficial for the estimation of high lying states, efficiently produced in the head of the streamer. One important

application of this method is the estimation of the electron density based on spectroscopy. This method was not found to be beneficial for the determination of the metastable states populations, when compared to the estimation made without spatial dependence of the electron density and reduced electric field.

The general behavior of the plasma was found to be very similar between experiments and computations. The quantitative agreement compared to the experiments was found to be very good for the ascending phase and poor for the decaying phase. Other parameters such as the reduced electric field showed that the plasma was not correctly predicted during the decaying phase, which exhibits too high reduced electric fields. The validity of the computations for the case of the decaying phase is therefore questionable for this model.

The overall momentum transfer and energy deposition to the gas was computed for different voltages and different pressures. It was shown that the positive pulse was more efficient to transfer momentum to the gas than negative pulses. The effect of the decaying phase was detrimental for the momentum transferred by positive pulses. The effect of the pressure on the momentum transferred was found to be complex and different between the ascending and decaying phases. The overall momentum and energy transferred to the gas was mainly decreasing with pressure.





## 5 Final Conclusions

The experimental and numerical investigation of nanosecond pulsed SDBD actuators was conducted. The general experimental investigation of the plasma produced was conducted by electrical and optical diagnostics, comprising fast camera imaging of the discharge and time-averaged emission spectroscopy. Preliminary investigations showed that the plasma was formed during two phases corresponding to the rise and fall of the voltage. The plasma was shown to evolve in the form of a streamer (propagating plasma). Emission spectroscopy revealed the vibrational non-equilibrium state of the plasma and the absence of  $H_\alpha$  lines, preventing the use of some common diagnostic tools for the determination of the densities of excited species and of the electron density. The detailed investigation of plasma characteristics such as the temperature of the gas, the reduced electric field and the average electron density was performed using emission spectroscopy. The interpretation of the emission spectrum was performed with a dedicated spectral code, which is able to simulate the spectra from spin-allowed transitions. It allowed the determination of the population densities corresponding to different vibrational states of excited species. The knowledge of these population levels allowed the determination of the reduced electric field based on 4 transitions, namely the first and second positive systems of  $N_2$ , the first negative system of  $N_2^+$  and argon lines. These four transitions permitted to determine the reduced electric field with different ratios of excited species, which revealed not to have the same values. This feature was explained by the different values of both the electric field and the electron density which produce the different species. Indeed, due to the spatial inhomogeneity of the electron density and electric field in a streamer, excited species with higher threshold excitation energies are efficiently produced only in the highest electric field regions at the very tip of the streamer head, whereas excited species with lower threshold excitation energies are efficiently produced also further behind in the direction of the body of the streamer.

The determination of the reduced electric field in conjunction with the absolute measurement of population densities allowed an estimation of the electron density and of metastable states  $N_2(A^3\Sigma_u^+)$  and  $O_2(a^1\Delta_g)$ . The effect of the applied voltage on the plasma was examined and found to mainly increase its length and the emitted intensity. The intensity was found to vary

almost linearly with the applied voltage. The gas temperature was measured with emission spectroscopy at times 200 ns and 1000 ns after the beginning of the pulse, and was found to increase slightly by approximately 50-100 K. The effect of the polarity on the plasma was found to merely inverse the ascending and decaying phases. The only other effect was a stronger intensity for the voltage fall and a weaker intensity for the voltage rise with respect to the positive pulse.

The effect of the operating pressure was investigated for 1, 0.5, 0.3, 0.25 and 0.2 bar. The similarity number  $E/N$  was respected but not the pressure times distance  $p \cdot d$  similarity number. Despite that one of the similarity numbers was not respected, the plasma was found to approximately follow the similarity laws for the ascending phases, but not for the decaying phases. The reduced electric field remained almost constant during the ascending phase, for the whole propagation distance, at a value of approximately 1000 Td. During the decaying phase, the reduced electric field was found to be relatively strong ranging from 300 to 800 Td for 1 to 0.2 bar respectively, but only for a very short distance (0.5 mm). After this short distance, the reduced electric field reaches an almost constant value ranging from 200 to 300 Td, apart for the 0.2 bar case, which exhibits a larger value reaching 700 Td. This increase in reduced electric field for pressures below 0.3 bar was also reported in [Starikovskii et al., 2009]. A comparison with sinusoidal voltage was also performed for two different pressures with a constant voltage/frequency ratio. The plasma was found to be comprised also of positive and negative streamers, corresponding to ascending and decaying phases of the nanosecond pulsed actuator. The effect of the pressure was shown to reduce the duration of the streamer phases, in accordance with similarity laws. From these observations, it was concluded that the similarity laws are useful to describe plasmas generated by SDBD actuators at pressures above 0.2 bar.

Numerical modelling of the plasma was conducted and provided useful insights in the structure of the streamers. It notably allowed to verify some hypothesis made during the experiments. The computation for different applied voltages, polarity and pressures were performed. The influence of the applied voltage was investigated by varying the slope of the applied voltage. The trend for the power input was found to follow the trend measured experimentally. The increase in voltages revealed hot spots at the location of the upper electrode, which were also seen during the experiments when the applied voltage was sufficiently high. The breakdown voltages were estimated using Meek's criterion and were found to describe well the breakdown voltages measured during the experiments at low pressures, but not at high pressures. This discrepancy was attributed to protrusion in the upper electrode, thereby enhancing the electric field locally. The diagnostic methods were applied on the simulated results as they would be in a real experiment, in order to validate the methods. It was shown that the numerical model was reproducing correctly most of the features of the plasma for the ascending phase, but was not as satisfactory for the decaying phase. Distinct values of the reduced electric fields were observed, when computed on the basis of different transitions, as was also observed during the experiments. The overpopulation of the  $N_2(C^3\Pi_u)$  state was not noticed during the computations, which supports the assumption that the overpopulation of

---

this state was due to physical processes which were not modeled (e.g. step-excitation). The electric field computed during the decaying phase was found to be too high, and the plasma did not extend sufficiently when compared to the experiments. The spatial distribution of the reduced electric field and of the electron density were approximated as exponentials in the vicinity of the head of the streamer. These approximations were then used to determine a more accurate estimation of the active species, such as the electron density and metastable states. The approximation was found to be suitable for the determination of the electron density, but not for the metastable states.

The global momentum transferred by the plasma to the gas was computed, together with the energy deposition. Both were found to be relatively well in accordance with the literature. The positive pulse was found to be more efficient than the negative pulse. Moreover, the decaying phase during the positive pulse was found to be detrimental to the momentum output of the actuator. The efficiency was found to drop with increasing voltages, due to the stronger decaying phase transferring momentum in the other direction. The momentum was found to increase during the plateau, which suggests to use longer plateau to maximize the momentum throughput of the actuator. The momentum transferred at different operating pressures was found to decrease with decreasing pressure in a non-linear way, which is in addition different during the ascending and decaying phase. These results show that the effect of the pressure on the global output momentum may vary significantly with different applied voltage forms, which does not allow drawing any definite conclusion on a global trend.

In conclusion, the use of emission spectroscopy was found to be a powerful tool to investigate the streamers produced by a nanosecond pulsed SDBD. Insights on fundamental processes occurring in the plasma were revealed, providing many experimental data. The innovative approach for the measurement of the reduced electric field allowed the determination of the production mechanisms of some active species. The development of an approximate method to determine both electron density and metastable concentration in conditions of relatively low intensity of light emitted was presented and the potential of the method was demonstrated using a numerical model of the plasma. The numerical modelling of the plasma was found to be suitable to describe the plasma produced during the ascending phase. The model was found appropriate for both polarities and at different pressures. The validity of the numerical model for the decaying phase was found to be limited. Therefore more investigations on the modelling of surface streamers produced in the reverse breakdown regime are necessary. The global momentum and energy deposition were computed and the positive pulse was found to transfer more energy and momentum to the gas than the negative. The reverse breakdown was found to decrease the overall momentum transferred. The effect of the pressure on the overall output was found to be complex, but mainly decreases with decreasing pressure. It was concluded on the basis of these computations that the momentum transferred was not proportional to the total number of electrons produced in the streamer, and thus OES cannot be used for the purpose of EHD force estimation.

The use of emission techniques for the investigation of fundamental plasma parameters is well

## Chapter 5. Final Conclusions

---

suited for the streamer phase, but is not suited to describe the decaying phase, which plays an essential role for the generation of ionic wind. Indeed, since the plasma decays and reaches a quasi stationary density of charged species after a few microseconds, most of the charges produced during the streamer are lost by recombination. Therefore, the use of absorption techniques are required to study experimentally the relaxation phase of the plasma.

The application of the nanosecond pulsed SDBD for flow control is thought to be possible through both mechanisms of pressure wave generation and momentum transfer at different operating pressures. The switching between modes is possible by varying the shape and strength of the applied voltage, making the plasma actuator a very versatile device for flow control. The possibility to use this actuator for the generation of active species is thought to be very promising. The possibility to produce a large amount of active species in air at atmospheric or lower pressures makes the SDBD a promising tool for plasma-assisted combustion. The use of a SDBD actuator for both purposes has not yet been investigated, and could be very interesting in internal flow applications, such as in the mixing zone of a combustion chambers, where both flow control authority to enhance turbulence levels and the production of active species could be beneficial for the combustion.

# A Appendix

Numerical values used for the source terms and transport coefficients used in the numerical model:

The value taken outside the specified range is indicated in brackets.

Table A.1: Fitting coefficients for N<sub>2</sub> computed with Bolsig+

Source/transport terms	A	B	C	D	E	F	G	range in Td (value taken outside the range)
Townsend ionization coefficient $\alpha/N_g$	-49.08	0.5812	-694	-4936	97170	-	-	15 (0)-1500 (cst)
Electrons mobility $\mu_e N_g$	56.04	-0.1666	12.04	-57.67	46.64	-	-	10 (700) - 1500 (100)
Positive ion mobility $\mu_p N_g$	2.8388	-0.4408	-40.7528	818.6970	-9752.3	56908	-125330	30 (1.9) - $\infty$

The coefficients for the electron ionization townsend coefficient and electron mobility where obtained to fit the data from:

- BOLSIG+ solver, [www.lxcat.net](http://www.lxcat.net), retrieved on November 17, 2013.
- SIGLO database, [www.lxcat.net](http://www.lxcat.net), retrieved on November 17, 2013.

and the coefficients for the positive ion N<sub>2</sub><sup>+</sup> from: Phelps database, [www.lxcat.net](http://www.lxcat.net), retrieved on November 17, 2013.

Conditions for air:

Angular field frequency / N (m3/s)	0.000
Gas temperature (K)	300.0
Ionization degree	0.1000E-04
Electron density (1/m3)	0.1000E+21
Wave number / N (m2)	0.000
Energy sharing	1.000
Growth model	2.000

## Appendix A. Appendix

---

Maxwellian mean energy (eV)	0.000
# of grid points	300.0
Grid type	3.000
Precision	0.1000E-09
Convergence	0.1000E-05
Maximum # of iterations	100.0
Mole fraction Ar	0.9300E-02
Mole fraction N2	0.7807
Mole fraction N2 <sup>+</sup>	0.1000E-04
Mole fraction O2	0.2100

Table A.2: Fitting coefficients for Air computed with Bolsig+

Process	A	B	C	D	E	range in Td (value taken outside the range)
Townsend ionization coefficient for N <sub>2</sub> component	-44.8	0.01023	-968.7	6202	176400	30 (0)-3000 (cst)
Townsend ionization coefficient for O <sub>2</sub> component	-45.66	0.1036	-796.5	14170	-117200	30 (0)-3000 (cst)
Townsend two-body attachment coefficient	-42.01	-1.276	-243.2	-1341	122900	30 (0)-3000 (cst)
Electrons mobility	56.43	-0.2185	0.9911	9.950	-9.959	15 (700) - ∞
Electrons diffusion	54.34	0.4264	-0.4032	58.32	58.32	10 (100) - 3000 (700)

Townsend three-body attachment fit:  $10^4 \text{O}_2 (-0.1556 \cdot z^9 + 0.1424 \cdot z^8 + 0.8363 \cdot z^7 - 0.6176 \cdot z^6 - 1.585 \cdot z^5 + 0.9924 \cdot z^4 + 0.902 \cdot z^3 - 0.1404 \cdot z^2 - 1.114 \cdot z - 99.81)$  with  $z = ((E/N) \cdot 10^{-17} - 750) / 440$ .

Positive ion mobility:  $\mu_p = 2 \text{cm}^2 \text{V}^{-1} \text{s}^{-1}$ , negative ion mobility:  $\mu_n = 2 \text{cm}^2 \text{V}^{-1} \text{s}^{-1}$ .

# Bibliography

- [Aleksandrov and Bazelyan, 1996] Aleksandrov, N. L. and Bazelyan, E. M. (1996). Simulation of long-streamer propagation in air at atmospheric pressure. *J. Phys. D: Appl. Phys.*, 29(3):740.
- [Babaeva and Kushner, 2013] Babaeva, N. Y. and Kushner, M. J. (2013). Reactive fluxes delivered by dielectric barrier discharge filaments to slightly wounded skin. *J. Phys. D: Appl. Phys.*, 46(2):025401.
- [Bachmann et al., 1992] Bachmann, R., Li, X., Ottinger, C., and Vilesov, A. E. (1992). Molecular-beam study of the collisional intramolecular coupling of  $N_2(B^3\Pi_g)$  with the  $N_2(A^3\Sigma_u^+)$  and  $N_2(W^3\Delta_u)$  states. *The Journal of Chemical Physics*, 96(7):5151–5164.
- [Benard et al., 2008] Benard, N., Balcon, N., and Moreau, E. (2008). Electric wind produced by a surface dielectric barrier discharge operating in air at different pressures: aeronautical control insights. *J. Phys. D: Appl. Phys.*, 41(4):042002.
- [Benesch and Fraedrich, 1984] Benesch, W. and Fraedrich, D. (1984). The role of intersystem collisional transfer of excitation in the determination of  $N_2$  vibronic level populations. Application to  $B'^3\Sigma_u^- - B^3\Pi_g$  band intensity measurements. *The Journal of Chemical Physics*, 81(12):5367–5374.
- [Berger et al., 2005] Berger, M., Murman, S. M., and Aftosmis, M. J. (2005). *Analysis of Slope Limiters on Irregular Grids*.
- [Bibinov et al., 1998] Bibinov, N. K., Kokh, D. B., Kolokolov, N. B., Kostenko, V. A., Meyer, D., Vinogradov, I. P., and Wiesemann, K. (1998). A comparative study of the electron distribution function in the positive columns in  $N_2$  and  $N_2/He$  dc glow discharges by optical spectroscopy and probes. *Plasma Sources Science and Technology*, 7(3):298–309.
- [Boeuf et al., 2007] Boeuf, J. P., Lagmich, Y., Unfer, T., Callegari, T., and Pitchford, L. C. (2007). Electrohydrodynamic force in dielectric barrier discharge plasma actuators. *J. Phys. D: Appl. Phys.*, 40(3):652.
- [Boeuf and Pitchford, 2005] Boeuf, J. P. and Pitchford, L. C. (2005). Electrohydrodynamic force and aerodynamic flow acceleration in surface dielectric barrier discharge. *Journal of Applied Physics*, 97(10):103307–103307–10.

## Bibliography

---

- [Boffard et al., 2007] Boffard, J. B., Chiaro, B., Weber, T., and Lin, C. C. (2007). Electron-impact excitation of argon: Optical emission cross sections in the range of 300–2500nm. *Atomic Data and Nuclear Data Tables*, 93(6):831–863.
- [Bonaventura et al., 2011] Bonaventura, Z., Bourdon, A., Celestin, S., and Pasko, V. P. (2011). Electric field determination in streamer discharges in air at atmospheric pressure. *Plasma Sources Science and Technology*, 20(3):035012.
- [Bourdon et al., 2007] Bourdon, A., Pasko, V. P., Liu, N. Y., Célestin, S., Ségur, P., and Marode, E. (2007). Efficient models for photoionization produced by non-thermal gas discharges in air based on radiative transfer and the helmholtz equations. *Plasma Sources Science and Technology*, 16(3):656.
- [Briels et al., 2008] Briels, T. M. P., Veldhuizen, E. M. v., and Ebert, U. (2008). Positive streamers in air and nitrogen of varying density: experiments on similarity laws. *J. Phys. D: Appl. Phys.*, 41(23):234008.
- [Cartwright, 1978] Cartwright, D. C. (1978). Rate coefficients and inelastic momentum transfer cross sections for electronic excitation of  $N_2$  by electrons. *Journal of Applied Physics*, 49(7):3855.
- [Chang and Setser, 1978] Chang, R. S. F. and Setser, D. W. (1978). Radiative lifetimes and two-body deactivation rate constants for  $Ar(3p_5, 4p)$  and  $Ar(3p_5, 4p')$  states. *The Journal of Chemical Physics*, 69(9):3885–3897.
- [Chen and Sekiguchi, 1965] Chen, S.-L. and Sekiguchi, T. (1965). Instantaneous Direct-Display system of plasma parameters by means of triple probe. *Journal of Applied Physics*, 36(8):2363–2375.
- [Dilecce et al., 2007] Dilecce, G., Ambrico, P. F., and Benedictis, S. D. (2007). New  $N_2(C^3\Pi_u, \nu)$  collision quenching and vibrational relaxation rate constants: 2. PG emission diagnostics of high-pressure discharges. *Plasma Sources Science and Technology*, 16(1):S45–S51.
- [Dilecce et al., 2010] Dilecce, G., Ambrico, P. F., and Benedictis, S. D. (2010). On the collision quenching of  $N_2^+(B^2\Sigma_u^+, \nu = 0)$  by  $N_2$  and  $O_2$  and its influence on the measurement of E/N by intensity ratio of nitrogen spectral bands. *J. Phys. D: Appl. Phys.*, 43(19):195201.
- [Ducasse et al., 2012] Ducasse, O., Eichwald, O., and Yousfi, M. (2012). Finite volume method for streamer and gas dynamics modelling in air discharges at atmospheric pressure. In Petrova, R., editor, *Finite Volume Method - Powerful Means of Engineering Design*. InTech.
- [Ebert et al., 2010] Ebert, U., Nijdam, S., Li, C., Luque, A., Briels, T., and van Veldhuizen, E. (2010). Review of recent results on streamer discharges and discussion of their relevance for sprites and lightning. *Journal of Geophysical Research*, 115. arXiv:1002.0070 [physics].
- [Ferreira and Loureiro, 2000] Ferreira, C. M. and Loureiro, J. (2000). Electron kinetics in atomic and molecular plasmas. *Plasma Sources Sci. Technol.*, 9(4):528.



- [Germany et al., 1988] Germany, G. A., Anderson, R. J., and Salamo, G. J. (1988). Electron impact excitation of the  $3p(^5P)$  state of atomic oxygen. *The Journal of Chemical Physics*, 89(4):1999–2002.
- [Gilmore et al., 1992] Gilmore, F. R., Laher, R. R., and Espy, P. J. (1992). Franck–Condon factors, r-centroids, electronic transition moments, and einstein coefficients for many nitrogen and oxygen band systems. *Journal of Physical and Chemical Reference Data*, 21(5):1005–1107.
- [Grundmann and Tropea, 2007] Grundmann, S. and Tropea, C. (2007). Experimental transition delay using glow-discharge plasma actuators. *Experiments in Fluids*, 42(4):653–657.
- [Guerra et al., 2004] Guerra, V., Sá, P. A., and Loureiro, J. (2004). Kinetic modeling of low-pressure nitrogen discharges and post-discharges. *The European Physical Journal Applied Physics*, 28(2):125–152.
- [Hagelaar et al., 2000] Hagelaar, G. J. M., de Hoog, F. J., and Kroesen, G. M. W. (2000). Boundary conditions in fluid models of gas discharges. *Phys. Rev. E*, 62(1):1452–1454.
- [Hagelaar and Pitchford, 2005] Hagelaar, G. J. M. and Pitchford, L. C. (2005). Solving the boltzmann equation to obtain electron transport coefficients and rate coefficients for fluid models. *Plasma Sources Science and Technology*, 14(4):722–733.
- [Hayashi, 2003] Hayashi, M. (2003). Bibliography of electron and photon cross sections with atoms and molecules published in the 20<sup>th</sup> century - argon -. Technical report, National Institute for Fusion Science.
- [Henrist, Bernard et al., 2002] Henrist, Bernard, Hilleret, Noël, Vorlauffer, G, Tadorelli, M, Jiménez, M, and Scheuerlein, C (2002). Secondary electron emission data for the simulation of electron cloud.
- [Herzberg, 1950] Herzberg, G. (1950). *Molecular Spectra and Molecular Structure*. Krieger Publishing Company.
- [Hirsch, 2007] Hirsch, C. (2007). *Numerical Computation of Internal and External Flows: The Fundamentals of Computational Fluid Dynamics*. Butterworth-Heinemann.
- [Hornkohl et al., 2005] Hornkohl, J. O., Parigger, C. G., and Nemes, L. (2005). Diatomic Hönl-London factor computer program. *Appl Opt*, 44(18):3686–3695. PMID: 15989043.
- [Hougen, 1970] Hougen, J. T. (1970). The calculation of rotational energy levels and rotational line intensities in diatomic molecules. *NBS Monograph*, [http://physics.nist.gov/Pubs/Mono115/chap1\\_05.html](http://physics.nist.gov/Pubs/Mono115/chap1_05.html), 115.
- [Itikawa, 2005] Itikawa, Y. (2005). Cross sections for electron collisions with water molecules. *Journal of Physical and Chemical Reference Data*, 34(1):1.

## Bibliography

---

- [Kirillov, 2008] Kirillov, A. S. (2008). The study of intermolecular energy transfers in electronic energy quenching for molecular collisions;  $N_2 - N_2$ ,  $N_2 - O_2$ ,  $O_2 - O_2$ . *Annales Geophysicae*, 26(5):1149–1157.
- [Kosarev et al., 2012] Kosarev, I. N., Khorunzhenko, V. I., Mintousov, E. I., Sagulenko, P. N., Popov, N. A., and Starikovskaia, S. M. (2012). A nanosecond surface dielectric barrier discharge at elevated pressures: time-resolved electric field and efficiency of initiation of combustion. *Plasma Sources Sci. Technol.*, 21(4):045012.
- [Kossyi et al., 1992] Kossyi, I. A., Kostinsky, A. Y., Matveyev, A. A., and Silakov, V. P. (1992). Kinetic scheme of the non-equilibrium discharge in nitrogen-oxygen mixtures. *Plasma Sources Science and Technology*, 1(3):207.
- [Kovacs, 1969] Kovacs, I. (1969). *Rotational Structure in the Spectra of Diatomic Molecules*. Adam Hilger LTD, London.
- [Lagmich, 2007] Lagmich, Y. (2007). *Diagnostic et modélisation d'une décharge à barrière diélectrique pour le contrôle d'écoulement*. phd, Université de Toulouse, Université Toulouse III - Paul Sabatier.
- [Lagmich et al., 2008] Lagmich, Y., Callegari, T., Pitchford, L. C., and Boeuf, J. P. (2008). Model description of surface dielectric barrier discharges for flow control. *J. Phys. D: Appl. Phys.*, 41(9):095205.
- [Lagmich et al., 2007] Lagmich, Y., Callegari, T., Unfer, T., Pitchford, L. C., and Boeuf, J. P. (2007). Electrohydrodynamic force and scaling laws in surface dielectric barrier discharges. *Applied Physics Letters*, 90(5):051502–051502–3.
- [Laher and Gilmore, 1991] Laher, R. R. and Gilmore, F. R. (1991). Improved fits for the vibrational and rotational constants of many states of nitrogen and oxygen. *Journal of Physical and Chemical Reference Data*, 20(4):685–712.
- [Laux, 2002] Laux, C. O. (2002). Radiation and nonequilibrium collisional-radiative models. *VKI Special course on physico-chemical models for high enthalpy and plasma flows modeling*.
- [Laux et al., 2003] Laux, C. O., Spence, T. G., Kruger, C. H., and Zare, R. N. (2003). Optical diagnostics of atmospheric pressure air plasmas. *Plasma Sources Science and Technology*, 12(2):125–138.
- [Leonard, 1991] Leonard, B. (1991). The ULTIMATE conservative difference scheme applied to unsteady one-dimensional advection. *Computer Methods in Applied Mechanics and Engineering*, 88(17-74).
- [Lieberman, 2005] Lieberman, M. A. (2005). *Principles of plasma discharges and materials processing*. Wiley-Interscience, Hoboken, N.J, 2nd ed edition.

- [Likhanskii, 2009] Likhanskii, A. (2009). *STUDY OF PLASMA PHENOMENA AT HIGH ELECTRIC FIELDS IN APPLICATIONS FOR ACTIVE FLOW CONTROL AND ULTRA-SHORT PULSE LASER DRILLING*. PhD thesis, The Pennsylvania State University, The Graduate School, Department of Engineering Science and Mechanics.
- [Likhanskii et al., 2007] Likhanskii, A. V., Shneider, M. N., Macheret, S. O., and Miles, R. B. (2007). Modeling of dielectric barrier discharge plasma actuators driven by repetitive nanosecond pulses. *Physics of Plasmas*, 14(7):073501–073501–8.
- [Liu and Pasko, 2006] Liu, N. and Pasko, V. P. (2006). Effects of photoionization on similarity properties of streamers at various pressures in air. *J. Phys. D: Appl. Phys.*, 39(2):327.
- [Lowke and Morrow, 1995] Lowke, J. and Morrow, R. (1995). Theoretical analysis of removal of oxides of sulphur and nitrogen in pulsed operation of electrostatic precipitators. *IEEE Transactions on Plasma Science*, 23(4):661–671.
- [Luque and Ebert, 2012] Luque, A. and Ebert, U. (2012). Density models for streamer discharges: Beyond cylindrical symmetry and homogeneous media. *Journal of Computational Physics*, 231(3):904–918.
- [Luque et al., 2007] Luque, A., Ebert, U., Montijn, C., and Hundsdorfer, W. (2007). Photoionization in negative streamers: Fast computations and two propagation modes. *Applied Physics Letters*, 90(8):081501.
- [Macheret et al., 2002] Macheret, S., Shneider, M., and Miles, R. (2002). Modeling of air plasma generation by repetitive high-voltage nanosecond pulses. *IEEE Transactions on Plasma Science*, 30(3):1301–1314.
- [Montijn and Ebert, 2006] Montijn, C. and Ebert, U. (2006). Diffusion correction to the Raether–Meek criterion for the avalanche-to-streamer transition. *J. Phys. D: Appl. Phys.*, 39(14):2979.
- [Moreau, 2007] Moreau, E. (2007). Airflow control by non-thermal plasma actuators. *J. Phys. D: Appl. Phys.*, 40(3):605.
- [Morrow and Lowke, 1997] Morrow, R. and Lowke, J. J. (1997). Streamer propagation in air. *Journal of Physics D: Applied Physics*, 30(4):614–627.
- [Naidis, 2009] Naidis, G. (2009). Positive and negative streamers in air: Velocity-diameter relation. *Physical Review E*, 79(5).
- [Naidis, 2006] Naidis, G. V. (2006). On photoionization produced by discharges in air. *Plasma Sources Sci. Technol.*, 15(2):253.
- [Naidis, 2010] Naidis, G. V. (2010). Evaluation of  $N_2(A^3\Sigma_u^+)$  density in nitrogen streamer discharges. *Plasma Sources Sci. Technol.*, 19(5):055010.

## Bibliography

---

- [Nicholls et al., 2001] Nicholls, R. W., Amani, M., and Mandelman, M. (2001). The  $r$ -centroid concept revisited. *Canadian Journal of Physics*, 79(2-3):611–622.
- [Nudnova et al., 2010] Nudnova, M. M., Aleksandrov, N. L., and Starikovskii, A. Y. (2010). Influence of the voltage polarity on the properties of a nanosecond surface barrier discharge in atmospheric-pressure air. *Plasma Phys. Rep.*, 36(1):90–98.
- [Opaits et al., 2008a] Opaits, D. F., Likhanskii, A. V., Neretti, G., Zaidi, S., Shneider, M. N., Miles, R. B., and Macheret, S. O. (2008a). Experimental investigation of dielectric barrier discharge plasma actuators driven by repetitive high-voltage nanosecond pulses with dc or low frequency sinusoidal bias. *Journal of Applied Physics*, 104(4):043304.
- [Opaits et al., 2008b] Opaits, D. F., Shneider, M. N., Miles, R. B., Likhanskii, A. V., and Macheret, S. O. (2008b). Surface charge in dielectric barrier discharge plasma actuators. *Physics of Plasmas (1994-present)*, 15(7):073505.
- [Orlov et al., 2006] Orlov, D., Corke, T., and Patel, M. (2006). Electric circuit model for aerodynamic plasma actuator. American Institute of Aeronautics and Astronautics.
- [Pancheshnyi, 2005] Pancheshnyi, S. (2005). Role of electronegative gas admixtures in streamer start, propagation and branching phenomena. *Plasma Sources Sci. Technol.*, 14(4):645.
- [Pancheshnyi et al., 2005] Pancheshnyi, S., Nudnova, M., and Starikovskii, A. (2005). Development of a cathode-directed streamer discharge in air at different pressures: Experiment and comparison with direct numerical simulation. *Physical Review E*, 71(1).
- [Pancheshnyi et al., 2000] Pancheshnyi, S. V., Sobakin, S. V., Starikovskaya, S. M., and Starikovskii, A. Y. (2000). Discharge dynamics and the production of active particles in a cathode-directed streamer. *Plasma Phys. Rep.*, 26(12):1054–1065.
- [Pancheshnyi et al., 1998] Pancheshnyi, S. V., Starikovskaia, S. M., and Starikovskii, A. Y. (1998). Measurements of rate constants of the  $N_2(C^3\Pi_u, v' = 0)$  and  $N_2^+(B^2\Sigma_u^+, v' = 0)$  deactivation by  $N_2$ ,  $O_2$ ,  $H_2$ ,  $CO$  and  $H_2O$  molecules in afterglow of the nanosecond discharge. *Chemical Physics Letters*, 294(6):523–527.
- [Paris et al., 2004] Paris, P., Aints, M., Laan, M., and Valk, F. (2004). Measurement of intensity ratio of nitrogen bands as a function of field strength. *J. Phys. D: Appl. Phys.*, 37(8):1179.
- [Paris et al., 2005] Paris, P., Aints, M., Valk, F., Plank, T., Haljaste, A., Kozlov, K. V., and Wagner, H.-E. (2005). Intensity ratio of spectral bands of nitrogen as a measure of electric field strength in plasmas. *J. Phys. D: Appl. Phys.*, 38(21):3894.
- [Pavón et al., ] Pavón, S., Thome, J. R., and Ott, P. Interaction between a surface dielectric barrier discharge and transonic airflows.

- [Peschke, 2014] Peschke, P. (2014). *Experimental investigation of pulsed DBD plasma actuators for aerodynamic flow control*. PhD thesis, Ecole polytechnique fédérale de Lausanne, Lausanne.
- [Peschke et al., 2011] Peschke, P., Goekce, S., Hollenstein, C., Leyland, P., and Ott, P. (2011). Interaction between nanosecond pulse DBD actuators and transonic flow. In *42nd AIAA Plasmadynamics and Lasers Conference*. American Institute of Aeronautics and Astronautics.
- [Phelps and Pitchford, 1985] Phelps, A. V. and Pitchford, L. C. (1985). Anisotropic scattering of electrons by  $\text{N}_2$  and its effect on electron transport. *Phys. Rev. A*, 31(5):2932–2949.
- [Piper, 1992] Piper, L. G. (1992). Energy transfer studies on  $\text{N}_2(X^1\Sigma_g^+, \nu)$  and  $\text{N}_2(B^3\Pi_g)$ . *The Journal of Chemical Physics*, 97(1):270–275.
- [Popov, 2001] Popov, N. A. (2001). Investigation of the mechanism for rapid heating of nitrogen and air in gas discharges. *Plasma Phys. Rep.*, 27(10):886–896.
- [Popov, 2009] Popov, N. A. (2009). Associative ionization reactions involving excited atoms in nitrogen plasma. *Plasma Physics Reports*, 35(5):436–449.
- [Raizer, 1991] Raizer, Y. P. (1991). *Gas discharge physics*. Springer-Verlag, Berlin ; New York.
- [Roth et al., 1998] Roth, J. R., Sherman, D. M., and Wilkinson, S. P. (1998). Boundary layer flow control with a one atmosphere uniform glow discharge surface plasma. *AIAA Meeting*, pages 98–0328.
- [Roupassov et al., 2009] Roupassov, D. V., Nikipelov, A. A., Nudnova, M. M., and Starikovskii, A. Y. (2009). Flow separation control by plasma actuator with nanosecond pulsed-periodic discharge. *AIAA Journal*, 47(1):168–185.
- [Rusterholtz et al., 2013] Rusterholtz, D. L., Lacoste, D. A., Stancu, G. D., Pai, D. Z., and Laux, C. O. (2013). Ultrafast heating and oxygen dissociation in atmospheric pressure air by nanosecond repetitively pulsed discharges. *Journal of Physics D: Applied Physics*, 46(46):464010.
- [Sadeghi et al., 2001] Sadeghi, N., Setser, D. W., Francis, A., Czarnetzki, U., and Döbele, H. F. (2001). Quenching rate constants for reactions of  $\text{Ar}(4p'[1/2]0, 4p[1/2]0, 4p[3/2]2, \text{ and } 4p[5/2]2)$  atoms with 22 reagent gases. *The Journal of Chemical Physics*, 115(7):3144–3154.
- [Schadee, 1978] Schadee, A. (1978). Unique definitions for the band strength and the electronic-vibrational dipole moment of diatomic molecular radiative transitions. *Journal of Quantitative Spectroscopy and Radiative Transfer*, 19(4):451–453.
- [Soloviev and Krivtsov, 2009] Soloviev, V. R. and Krivtsov, V. M. (2009). Surface barrier discharge modelling for aerodynamic applications. *Journal of Physics D: Applied Physics*, 42(12):125208.

## Bibliography

---

- [Stancu et al., 2010] Stancu, G. D., Janda, M., Kaddouri, F., Lacoste, D. A., and Laux, C. O. (2010). Time-Resolved CRDS Measurements of the  $N_2(A^3\Sigma_u^+)$  Density Produced by Nanosecond Discharges in Atmospheric Pressure Nitrogen and Air. *J. Phys. Chem. A*, 114(1):201–208.
- [Starikovskaia et al., 2010] Starikovskaia, S. M., Allegraud, K., Guaitella, O., and Rousseau, A. (2010). On electric field measurements in surface dielectric barrier discharge. *J. Phys. D: Appl. Phys.*, 43(12):124007.
- [Starikovskaia et al., 2002] Starikovskaia, S. M., Anikin, N. B., Pancheshnyi, S. V., and Starikovskii, A. Y. (2002). Time-resolved emission spectroscopy and its applications to the study of pulsed nanosecond high-voltage discharges. pages 63–73.
- [Starikovskii et al., 2009] Starikovskii, A. Y., Nikipelov, A. A., Nudnova, M. M., and Roupasov, D. V. (2009). SDBD plasma actuator with nanosecond pulse-periodic discharge. *Plasma Sources Sci. Technol.*, 18(3):034015.
- [Starikovskiy and Aleksandrov, 2013] Starikovskiy, A. and Aleksandrov, N. (2013). Plasma-assisted ignition and combustion. *Progress in Energy and Combustion Science*, 39(1):61–110.
- [Tabata et al., 2006] Tabata, T., Shirai, T., Sataka, M., and Kubo, H. (2006). Analytic cross sections for electron impact collisions with nitrogen molecules. *Atomic Data and Nuclear Data Tables*, 92(3):375–406.
- [Tanaka et al., 2009] Tanaka, D., Matsuoka, S., Kumada, A., and Hidaka, K. (2009). Two-dimensional potential and charge distributions of positive surface streamer. *J. Phys. D: Appl. Phys.*, 42(7):075204.
- [Tatum, 1967] Tatum, J. B. (1967). The interpretation of intensities in diatomic molecular spectra. *The Astrophysical Journal Supplement Series*, 14:21.
- [Unfer, 2008] Unfer, T. (2008). *Méthode asynchrone pour la modélisation d'actuateurs plasma destinés au contrôle d'écoulement*. phd, Université de Toulouse, Université Toulouse III - Paul Sabatier.
- [Unfer and Boeuf, 2009] Unfer, T. and Boeuf, J. P. (2009). Modelling of a nanosecond surface discharge actuator. *Journal of Physics D: Applied Physics*, 42(19):194017.
- [Unfer and Boeuf, 2010] Unfer, T. and Boeuf, J.-P. (2010). Modeling and comparison of sinusoidal and nanosecond pulsed surface dielectric barrier discharges for flow control. *Plasma Phys. Control. Fusion*, 52(12):124019.
- [Valk et al., 2010] Valk, F., Aints, M., Paris, P., Plank, T., Maksimov, J., and Tamm, A. (2010). Measurement of collisional quenching rate of nitrogen states  $N_2(C^3\Pi_u, \nu = 0)$  and  $N_2^+(B^2\Sigma_g^+, \nu = 0)$ . *J. Phys. D: Appl. Phys.*, 43(38):385202.
- [Vitello et al., 1994] Vitello, P. A., Penetrante, B. M., and Bardsley, J. N. (1994). Simulation of negative-streamer dynamics in nitrogen. *Physical Review E*, 49(6):5574–5598.

- [Whiting and Center, 1973] Whiting, E. E. and Center, A. R. (1973). *Computer program for determining rotational line intensity factors for diatomic molecules*. National Aeronautics and Space Administration.
- [Whiting and Nicholls, 1974] Whiting, E. E. and Nicholls, R. W. (1974). Reinvestigation of rotational-line intensity factors in diatomic spectra. *The Astrophysical Journal Supplement Series*, 27:1.
- [Whiting et al., 1980] Whiting, E. E., Schadee, A., Tatum, J. B., Hougen, J. T., and Nicholls, R. W. (1980). Recommended conventions for defining transition moments and intensity factors in diatomic molecular spectra. *Journal of Molecular Spectroscopy*, 80(2):249–256.
- [Zhdanov et al., 2001] Zhdanov, B. V., Neumann, D., Knize, R., and Murdough, M. P. (2001). Direct measurement of the deactivation rate of excited singlet sigma and singlet delta molecular oxygen by oxygen. In *Quantum Electronics and Laser Science Conference, 2001. QELS '01. Technical Digest. Summaries of Papers Presented at the*, pages 182–183.
- [Zhelezniak et al., 1982] Zhelezniak, M. B., Mnatsakanian, A. K., and Sizykh, S. V. (1982). Photoionization of nitrogen and oxygen mixtures by radiation from a gas discharge. *Teplofizika Vysokikh Temperatur*, 20:423–428.





Sami Goekce

E-mail : samigoekce@gmail.com

### Highlights

- Research engineer, PhD in Mechanical Engineering (July 2014)
- Expertise in experimental and numerical methods
- Strong interests and skills in the field of plasma physics and fluid mechanics

## Education

2009-2014	EPF Lausanne, Switzerland PhD Thesis: completion by July 2014 Topic: Flow control by surface Dielectric Barrier Discharge actuators
2009	<b>EPFL Master's degree in Mechanical Engineering, speciality: Fluid Mechanics</b>
2004-2009	EPF Lausanne, Switzerland Mechanical Engineering <b>Master thesis at University of Queensland, Australia</b>
2002-2004	EPF Lausanne, Switzerland Special mathematical course (CMS)
2001-2002	ERACOM Lausanne <b>Maturité professionnelle technique</b>
1997-2001	ETML Lausanne <b>CFC auto mechanic</b>

## Projects

### PhD thesis

Ionized molecules produced in a gas discharge can acquire and transfer momentum to the surrounding gas. This principle is used in the context of Aerodynamics to perform air-flow actuation. The plasma actuator was analysed experimentally by optical emission spectroscopy and theoretically with numerical modelling. The overall effect of the plasma on the flow was also measured by the LDA technique. The actuator is shown to be most efficient at higher pressures.

### Master thesis

Development of a Langmuir probe for the measurement of the electron temperature and density behind a strong ionizing shock wave produced in the expansion tube facility X2 at the Centre for Hypersonic, University of Queensland, Australia. The design of the probes, operation in the expansion tube and analysis of the results were performed. The applicability of the probe was shown.

## Language skills

French	Mother tongue
English	Fluent (5 months at the University of Queensland, Australia)
German	Basics (B1)

## Skills

**Experimental techniques:**

- Time resolved optical emission spectroscopy (operation and calibration of the spectroscope and the fast camera)
- Handling and mounting of high-voltage devices (high-voltage MOSFET switch) and measurements equipment (high voltage probe, oscilloscope)
- Laser Doppler Anemometry (used to map velocity vectors)

**Numerical modelling:**

- Development of a spectroscopy code that allows modelling of the emission spectra of several molecular and atomic transitions (N<sub>2</sub> FPS & SPS, N<sub>2</sub><sup>+</sup> FNS, Ar 2p-1s)
- Development of a 2D code that models the evolution of a non-equilibrium plasma produced by a high voltage pulse in air at different pressures, including the effect of photoionization.

**Coding languages:** Matlab, Fortran 90, C, C++, Java

**Sofwares:** Matlab, Word, Excel, Latex, Fluent, Catia

**Personal informations**

Personal situation: Age 32, father of one child

Nationality and military obligations: Swiss and Turkish nationality, military duties completed

Swiss driving licences: A, B, D1, BE, D1E